Multichannel Rydberg spectroscopy of complex atoms

Mireille Aymar

Laboratoire Aimé Cotton, Centre National de la Recherche Scientifique II, Bâtiment 505, 91405 Orsay Cedex, France

Chris H. Greene

Department of Physics and JILA, University of Colorado, Boulder, Colorado 80309-0440

Eliane Luc-Koenig

Laboratoire Aimé Cotton, Centre National de la Recherche Scientifique II, Bâtiment 505, 91405 Orsay Cedex, France

Multichannel atomic spectra frequently exhibit such extraordinary visual complexity that they appear at first glance to be uninterpretable. The present review discusses how to unravel such spectra through the use of theoretical multichannel spectroscopy to extract the key dynamical implications. Moreover, this class of techniques permits a quantitative prediction or reproduction of experimental spectra for some of the more challenging atomic systems under investigation. It is shown that multichannel spectroscopy marries the techniques of multichannel quantum-defect theory to the eigenchannel R-matrix method (or related methods). It has long been appreciated that multichannel quantum-defect theory can successfully use a collision-theory framework to interpret enormously complicated Rydberg spectra. However, the capabilities of multichannel quantum-defect theory have increased dramatically during the past decade, through the development of nearly *ab initio* methods for the calculation of the short-range scattering parameters that control the interactions of closed and open channels. In this review, emphasis is given to the alkaline-earth atoms, for which many different observables have been successfully compared with experiment over broad ranges of energy and resolution. Applications of the method to describe the photoionization spectra of more complex open-shell atoms are also discussed. [S0034-6861(96)00504-1]

CONTENTS

I. INTRODUCTION

The sharpest signature of any microscopic quantum-mechanical system is its pattern of resonances. This predominant importance of resonances provides a thread that unifies much of physics from the birth of quantum mechanics all the way to the present. Some of the early studies of resonances were conducted in the field of nuclear physics, where the first questions were fairly simple: Why are there resonances in the first place? What shapes can be expected in spectra exhibiting resonances? What information do those shapes convey about the internal dynamics of the system? The answers to these questions emerged from the work of Bohr (1936), Breit and Wigner (1936), Breit (1959), and others.

This review concentrates on showing how resonant spectra of many-electron atoms provide a highly detailed window on the complicated, nonseparable motions of atomic electrons. Capabilities of current theory have grown so rapidly in the past decade that tremendously complicated experimental spectra can now be accurately described quantitatively from first principles, or for heavy atoms from nearly first principles. Despite our focus on atomic spectra, many of the concepts have potentially wider applicability to other fields in physics and chemistry. Immediate examples include low-energy (up to a few MeV) nuclear scattering and photofragmentation processes, molecular photoionization and photodissociation, low-energy collisions (up to a few eV) between an atom or molecule and an electron or another atom, or any resonant reactive scattering process such as $AB+C\rightarrow A+BC$, to name only a few.

Whereas the earliest studies treated resonances phenomenologically on a state-by-state basis, the emphasis here will be on viewing a family of resonances with simular character, along with an adjoining fragmentation continuum, as consisting of one channel. This view of the resonance physics thus links immediately to a scattering-theory point of view, as the indices labeling channels are the same indices occurring in the scattering matrix. For instance, the set of all s states (with $l=0$) of atomic hydrogen, from the $1s$ state up to the ionization threshold ($\epsilon=0$), and including the continuum at $\epsilon>0$, constitutes a single channel. In most complex atoms, several interacting channels are present simultaneously, and their spectra are correspondingly multichannel in character. In fact, the only real difference between the channel description of resonances and the ''conventional'' form of scattering theory is the use of matrices (such as the collision or scattering matrix $\underline{S}$) with indices referring to closed channels (in which fragmentation all the way to asymptopia is energetically forbidden). This closed-channel description of resonances will be referred to in the following as the multichannel spectroscopy viewpoint. Elsewhere it has been called the quantum-defect theory viewpoint, reflecting the fact that the formulation of Seaton (1966, 1983) is the context in which closed channels arise most naturally and persistently. However, similar ideas originated in Wigner's nuclear studies (Wigner, 1946a, 1946b) long before quantum-defect theory was formulated [as stressed by Lane (1986)]. For this reason, and also because the term ''quantum defect'' masks the generality of this physical description to contexts far wider than atomic Rydberg spectra, we prefer the more descriptive term, multichannel spectroscopy.

The quantum-defect theory description of atomic Rydberg-state resonances arose from the work of Ham (1955) and Seaton (1955, 1966, 1983). Fano (1970) contributed the important and general concept of frame transformation. This dramatically broadened the scope of quantum-defect methods, as is manifested by applications ranging from the work of Jungen and co-workers (Jungen and Dill, 1980; Raoult and Jungen, 1981; Jungen, 1984) on molecular Rydberg spectra to that of Watanabe and Komine (1991) and of O'Mahony and Mota-Furtado (1991) on the amazing Rydberg spectra of atomic hydrogen in a magnetic field.

One of the goals of this review is to convey the unifying interpretive power of multichannel spectroscopic theory. The success of this theory is twofold. First, multichannel spectroscopy offers a powerful practical approach to the calculation of real spectra having extreme complexity. In this respect there are effectively no competing theoretical methods at present that rival the power of quantum-defect ideas, at least in the realm of autoionizing atomic spectra. Second, multichannel spectroscopy provides a complete way of visualizing the qualitative physics involved, and in particular a way of interpreting dense and seemingly irregular resonant spectra, allowing simple conclusions to be drawn about the underlying dynamics of the system.

A. Origins in nuclear physics

In the historical development of nuclear physics, the first step toward understanding resonant spectra was the development of semiempirical formulas, such as the formula of Breit and Wigner (1936), which described a

Lorentzian-shaped enhancement of the cross section for any reactive process in the vicinity of the resonance. These were initially based on physically plausible assumptions, such as Bohr's concept (Bohr, 1936) of the compound nucleus, in which a reactive process had two independent stages: formation of a compound (i.e., resonant) system, followed by its fragmentation into reaction products. This phenomenological approach successfully accounted for the existence of resonances and for their symmetrically-peaked profiles. Even earlier, Fano (1935) had shown, in the seemingly different physical context of atomic autoionization, how a discrete state interacting with a continuum produced a resonance profile that could exhibit a dip or an asymmetrical shape. Fano (1961) reformulated the approach much later to give a sharper derivation of these asymmetrical profiles arising from any type of discrete-continuum interaction. Equivalent formulations of discrete-continuum interactions carried out in different fields include the so-called "Anderson model" in condensed-matter physics [see, for example, Sec. 4.2 of Mahan (1981)] and the "unified theory of nuclear reactions" of Feshbach (1958). A simplification of this type of phenomenological theory, and ultimately a key limitation, was its assumption of a single isolated resonance state (or, at any rate, a finite number of such states) whose interactions with fragmentation continua had to be characterized on a state-by-state basis.

Wigner (1946a, 1946b), Wigner and Eisenbud (1947), and Teichmann and Wigner (1952) created the first systematic formulation capable of treating general resonant processes in reactive systems. Their work has generally gone under the name of R-matrix theory, as it focuses on the formal properties of the logarithmic derivative matrix (or R matrix) characterizing a complicated many-particle, multichannel system within some finite radius r_0. The indices of the R matrix label the different possible modes of breakup of the system, which we shall call the fragmentation channels throughout this review. These channel indices are the same ones that label the more familiar scattering matrix $\underline{S}$. Although the scattering matrix is generally referred to as the "Heisenberg matrix $\underline{S}$" (Heisenberg, 1943), it had been introduced earlier by Wheeler (1937), who called it the matrix $\underline{c}$. The main result of Wigner's R-matrix formulation was his demonstration that the Hermitian matrix $\underline{R}(E)$, which is simply related to the matrix $\underline{S}$and is a meromorphic (i.e., analytic except near simple poles) function of the energy E. Moreover, its poles on the real energy axis can (often) be associated with resonance energies E_λ, i.e.,

$$R_{ij}=\sum_\lambda \frac{\gamma_{i\lambda}\gamma_{j\lambda}}{E_\lambda - E}. \tag{1.1}$$

(The actual correspondence between poles E_λ and resonance states of the compound system confined to short range $r<r_0$ involves a few additional subtleties.) In this picture, each term in the summation of Eq. (1.1) was identified as a separate resonance, with the factors in the numerator $\gamma_{i\lambda}$ being related to the partial decay widths of resonance λ into channel i. This equation also shows how, in the immediate vicinity of any given resonance, a single term dominates the summation, whereby the R matrix becomes approximately separable and so has unit rank, as does the S matrix.

Equation (1.1) has been used widely in nuclear physics, and to some degree in high-energy physics, to account semiempirically for resonance features in a variety of measurements. The typical calculation attempts to fit an experimental spectrum by varying the parameters E_λ and $\gamma_{i\lambda}$ in a least-squares sense to optimize agreement between calculation and experiment. This semiempirical fitting procedure is what most nuclear physicists today associate with the term "R-matrix theory," even though R-matrix theory has come to mean something rather different in atomic and molecular physics, namely, the explicit numerical calculation of the R matrix. In the semiempirical approach, the R matrix is regarded as containing all the relevant information about the reaction zone within $r<r_0$, where all inelasticities occur. This reaction zone is thus regarded as a "black box" and most of the physics within it is neither understood in detail nor is plausibly calculable.

The absence of a detailed microscopic formulation that could predict the R matrix from first principles was not regarded as a problem in nuclear physics for many years. The attitude in the community was reflected in a quote from the influential textbook of Blatt and Weisskopf (1952): "We do not really need to know all the details of the motion within the compound nucleus in order to obtain all relevant information about nuclear reactions. A complete description of the internal motion within the compound nucleus is neither necessary nor desirable." In the present review, we emphasize that such a complete description is necessary if the goal is to perform spectroscopically useful calculations of complex spectra. We show below that in many cases it does not require laborious calculations. Moreover, the complete description is desirable in the sense that one thereby attains far greater confidence in the underlying theory and also great predictive power.

A few attempts were made, mainly in the 1960s, to determine the R matrix by explicit calculation, notably by Lane and Thomas (1958), by Lane and Robson (1966, 1969) and Chatwin (1970), and in effect by Brueckner (1955), among others. After a specific model of the nucleon-nucleon interaction potential was adopted, these methods gave R matrices to varying degrees of accuracy and showed that, at least in principle, one can calculate the detailed microscopic properties without being restricted by the difficulty and nonuniqueness of fitting the R matrix to reproduce experimental spectra. Such explicit calculations were not pursued very widely in nuclear physics, however. The poor theoretical understanding of the nucleon-nucleon interaction made it difficult to interpret discrepancies between theory and experiment as being attributable to an unconverged or otherwise inaccurate method for solving the many-particle Schrödinger equation for R_{ij}, or to an inadequate description of the nucleon-nucleon interaction.

As a result, the nuclear applications of Wigner's R-matrix formulation never progressed very far beyond its widespread use in the semiempirical analysis of experimental spectra (see, for example, Mo and Hornyak, 1969). Other aspects of the semiempirical work that were unsatisfactory to some included the fact that the fitted parameters E_λ and $\gamma_{i\lambda}$ depend on the reaction-zone radius r_0, and on the number of terms retained in the summation in Eq. (1.1). This dependence of the R matrix on the radius r_0 has been argued (see, for example, Feshbach, 1958) to be a somewhat unphysical aspect of R-matrix theory, and is in contrast to the physical scattering matrix $\underline{S}$, which is independent of any such radius. In fact, most of the competing formulations for calculating scattering or photoabsorption processes have a similar boundary either explicitly or implicitly present. For example, the complex Kohn (1948) variational principle, which has gained in popularity (McCurdy *et al.*, 1987; Miller, 1988; Robicheaux, 1989) does not seem at first glance to specify any boundary radius. But a truncated basis set is always used to expand the L^2 or short-range part of the variational solution. Consequently, a Kohn calculation will always have an "outermost" basis function that defines an effective radius, although it is a softer boundary radius than is used in R-matrix calculations. Similar remarks apply to other methods used currently, such as the Schwinger (1947) variational principle (for references see Watson, 1988).

B. Developments in atomic physics

The first atomic calculations of multichannel spectra, aside from early configuration-interaction studies, were conducted in the early 1960s within a framework called the close-coupling method (Burke and Smith, 1962). This method expands the full energy eigenfunctions Ψ_E of an N-electron atomic complex in terms of "channel functions" Φ_i that obey the time-independent Schrödinger equation for the $(N-1)$-electron system. The Φ_i are multiplied by unknown solutions $F_i(r)$ for the "outermost" electron and are then fully antisymmetrized with respect to all electrons. The channel functions Φ_i normally include spin and angular dependences of the outermost electron also, so that they form a complete orthonormal set in all degrees of freedom except the radial coordinate r. These close-coupling-type solutions are usually written as

$$\Psi_E = \mathcal{A} \sum_i \frac{1}{r} \Phi_i(\omega) F_i(r), \tag{1.2}$$

in which the symbol $\mathcal{A}$ indicates the antisymmetrization operation. Projection onto each of the channel functions results in an infinite set of coupled integrodifferential equations for the $F_i(r)$. This set is in principle continuously infinite, but is normally truncated to a finite number of equations on physical grounds and solved numerically. Burke and McVicar (1965) used this procedure to calculate doubly excited resonance states of helium that had been observed by Madden and Codling (1965) in early synchrotron radiation experiments.

These early close-coupling calculations enjoyed remarkable success. When the number of truncated channels is kept small, the calculations are reasonably fast, but they rapidly become laborious as the number of channels increases. A disadvantage arose, however, upon direct integration of the close-coupling equations on an energy grid sufficiently fine to reproduce narrow autoionizing states. This stemmed from the fact that the entire integration had to be repeated over and over, virtually from the beginning, at every energy for which the solutions were desired. To treat the extremely narrow resonances that are commonly seen in multichannel spectra, it was highly desirable to overcome this roadblock.

Two independent theoretical developments greatly enhanced the power of these calculations. First, Seaton formulated the multichannel quantum-defect theory (Seaton, 1955, 1966, 1983). This formulation, to be discussed at length in Sec. II, describes much of the complicated energy dependences of multichannel spectra analytically. In this paper, the abbreviation MQDT will be used for this theory. After implementation of multichannel quantum-defect theory in the context of atomic close-coupling calculations, the equations could then be solved on a very coarse energy mesh. The strongly energy-dependent spectra emerged in a subsequent rapid MQDT calculation (involving the solution of a modest-sized system of linear algebraic equations).

The second key development that led to an extremely efficient method of solving the close-coupling-type equations was Burke's implementation of the Wigner-Eisenbud R-matrix approach (Burke and Robb, 1975; Burke and Berrington, 1993). Here the basic idea was that the energies E_λ and the partial decay width factors $\gamma_{i\lambda}$ of Eq. (1.1) could be obtained after a single diagonalization of the full Hamiltonian H inside the box $r<r_0$. Once the eigenvectors and eigenvalues of H were known, Eq. (1.1) allowed a nearly instantaneous calculation of the R matrix at all energies for which the basis set converged adequately. Calculations based on this *ab initio* technique reproduced measured multichannel photoabsorption spectra for a number of atoms, including closed-shell species such as argon (Burke and Taylor, 1975), and open-shell atoms such as aluminum (Tayal and Burke, 1987). These studies made little or no use of multichannel quantum-defect techniques, opting instead to solve the long-range close-coupling equations by direct numerical integration.

Fano's (1970) paper on molecular hydrogen sparked a period of extraordinary progress in the interpretation of atomic and molecular spectra. It combined multichannel quantum-defect theory with the novel concept of a frame transformation to extract a detailed description of H_2 rotational-channel interactions. Subsequent studies by Jungen, Dill, and others extended these capabilities to include vibrational-channel interactions in diatomic molecules (Jungen and Dill, 1980; Jungen, 1984; Greene

and Jungen, 1985; Gauyacq, 1987), and in triatomics (Child and Jungen, 1990; Stephens and Greene, 1995). This body of work was able to account for a number of examples of rich molecular spectra with unprecedented quantitative accuracy. Some types of electronic-channel interactions in diatomics were also treated successfully in this approach (Ross and Jungen, 1994).

Fano's concept of a frame transformation was soon adapted to the spectra of atoms (Lu, 1971; Lee and Lu, 1973; Fano, 1975) and of negative ions (Rau and Fano, 1971; Lee, 1975). The emphasis of these studies was the semiempirical interpretation of experimentally observed spectra. A manageable set of energy-independent parameters was adjusted to reproduce observations. These fits proved to have much more physical content than mere "curve-fitting": the same parameters were used to generate predictions of completely new observables (Dill, 1973; Lee, 1974b) that had not been fitted initially, and were subsequently verified by experiments. Many more examples (Aymar, 1984a) of the predictive power of multichannel quantum-defect analysis, both with and without frame-transformation techniques, established it as a crucial tool for understanding multichannel Rydberg spectra.

While the examples just discussed demonstrated the potential power of techniques based on multichannel quantum-defect theory, multichannel effective-range theory, and their generalizations, some limitations of this semiempirical analysis became increasingly apparent. When the number of channels exceeded a number in the range 5–10, the number of fitted parameters became so large that the fits become nonunique and unsatisfactory. As increasingly complex systems were subjected to experimental study, it became imperative to develop ways to calculate the smooth, short-range parameters of multichannel spectroscopy directly, i.e., without relying on semiempirical fits. Fano and Lee (1973) took one of the first steps in that direction when they proposed the eigenchannel R-matrix method, which Lee (1974a) used to calculate argon MQDT parameters near the ionization threshold. The relativistic random-phase approximation was extremely successful in determining MQDT scattering parameters and numerous associated photoabsorption observables for every rare-gas atom (Johnson *et al.*, 1980; Lee and Johnson, 1980).

The extensive development of nearly *ab initio* multichannel spectroscopy in the last decade has largely bypassed the difficulties of semiempirical quantum-defect treatments alluded to above. This enhancement of theoretical capabilities was driven largely by a reformulation of the eigenchannel R-matrix treatment into a noniterative form (Greene, 1983; Le Rouzo and Raseev, 1984), which dramatically improved on the iterative version proposed and implemented by Fano and Lee (1973). Another key contribution to the improved ability of theory to describe complicated spectra to near-experimental precision has been the use of model potentials that approximately describe screening and polarization effects of the inner closed electron shells. For instance, to describe Ca spectra, one first finds a model one-electron Hamiltonian h that represents the Ca^+ energy spectrum to reasonable precision. Next, one "hammers" the two-electron problem variationally within the finite radius $\max\{r_1,r_2\}\leqslant r_0$, typically using the model Hamiltonian for the valence-electron pair: $H=h_1+h_2+1/r_{12}$. The resulting variational solutions are now matched to a channel expansion in terms of linear Coulomb functions (or whatever are the relevant long-range solutions) at the surface of this reaction volume. The matching coefficients then determine the short-range scattering parameters, which can in turn be used to calculate experimental observables on an arbitrarily fine energy mesh with great efficiency. Moreover, the parameters can then be used to classify and interpret the spectra, which can be surprisingly complicated even for "simple" atoms such as He .

The basic procedure just outlined has been applied extensively to many systems, especially in the alkaline-earth atoms where a vast amount of data exists. The precision of the resulting calculations has been surprisingly good. Many experiments that had remained "uninterpreted" are now completely understood, thanks to these methods. Nearly *ab initio* calculations have predicted a number of new, highly detailed spectra, achieving agreement in most cases to near-spectroscopic accuracy. In several cases, calculations based on this theoretical scheme have improved significantly over the accuracy of earlier experimental work. A number of examples are described in Sec. IV below. These methods have also been extended to treat the spectra of open-shell atoms, including some transition metals which exhibit impressive complexity. Recent applications to open-shell atomic systems are discussed in Sec. V.

Another area of current interest is the development of techniques for the analysis of complex spectra in the time domain rather than the energy domain. A time-domain spectrum is simply the Fourier transform of the corresponding energy-domain spectrum. While this review will consider energy spectra almost exclusively, some interpretive aspects are useful to consider from the temporal point of view. Time analysis can be performed using an outgrowth of Wigner's (1955) identification of

$$\tau_l(E)=2\hbar\frac{d\delta_l(E)}{dE} \tag{1.3}$$

as the time delay in scattering associated with the partial-wave scattering phase shift $\delta_l(E)$ at energy E. This concept of the time delay was generalized to multichannel scattering theory by Smith (1960). Section II below presents some additional generalizations that are useful in the multichannel quantum-defect approach, some of which have not been previously published. These further generalizations relate to the interpretive value of Smith's delay-time matrix in the presence of weakly closed channels (i.e., bound-state channels).

C. Other related reviews

A number of other published reviews and monographs touch on subjects relevant to this paper. Discus-

sions of multichannel quantum defect-theory can be found in the books by Gallagher (1994), by Fano and Rau (1986), and by Friedrich (1990). Gallagher (1994) also discussed experimental aspects of importance for measurements of multichannel spectra. A collection of original articles on the formulation and application of R-matrix methods in atomic physics was published by Burke and Berrington (1993). In a review with a much more general flavor, Gerjuoy *et al.* (1983) showed how to develop new variational principles for a broad range of applications. Buckman and Clark (1994) reviewed experimental and theoretical work on negative ions, emphasizing collision processes. Gauyacq (1987) adopted techniques similar to those used in Sec. II of this paper, in a pedagogical treatment of several different processes that involve negative ions. Semiempirical applications of multichannel quantum-defect theory to the analysis of experimental atomic Rydberg spectra were reviewed by Aymar (1984a). Greene and Jungen (1985) and Jungen (1988) have reviewed molecular applications of quantum-defect techniques. Molecular studies require the introduction of some key additional concepts in order to deal with the rotational and vibrational degrees of freedom.

(Our convention in denoting matrices is to underline them. We denote the transpose matrix by the superscript t, and the Hermitian conjugate matrix by a dagger (†); for spectroscopic notations, we use superscripts e and o to denote even and odd parity states.)

II. OVERVIEW OF THE IDEAS AND EQUATIONS OF MULTICHANNEL SPECTROSCOPY

The basic ideas of quantum-defect theory have remained mysterious to many, partly because its starting point already differs from the more widely familiar independent-electron approach to atomic structure. The philosophy of the Hartree-Fock method—and its improvements multiconfiguration Hartree-Fock or configuration-interaction methods—begin by assuming that all atomic electrons move independently in a mutually screened central potential. This approximation is made throughout all of configuration space. When the atomic wave function can be accurately represented by one or at most a handful of configurations, as is frequently true for low-lying states, this independent-electron scheme describes the dynamics efficiently. Its utility decreases for highly perturbed or correlated states that require extensive configuration mixing, especially when continuum configurations play a crucial role.

Multichannel spectroscopy adopts a philosophy closer to that of the nuclear R-matrix theory of Wigner (Wigner, 1946a, 1946b). Specifically, an independent-electron-type approximation is adopted only in an "outer region" $r>r_0$, where, aside from perturbative electrostatic multipole interactions, it is virtually exact. In this large-r region, a matrix equivalent to the scattering matrix $\underline{S}$, generalized to incorporate energetically closed channels, characterizes the solutions "exactly." As shown below in Sec. II.D, the large-r solutions can be also characterized by a reaction matrix $\underline{K}$ connected to the matrix $\underline{S}$. Quantum-defect theory (Seaton, 1983) for a long-range Coulomb potential, effective-range theory (Fermi, 1934; Fermi and Marshall, 1947; Bethe, 1949; Blatt and Jackson, 1949; Delves, 1958; Ross and Shaw, 1961; Rau and Fano, 1971; Lee 1975) for long-range purely centrifugal potentials, and their variants predict the energy dependence of these matrices $\underline{S}$ and $\underline{K}$, permitting analytic continuation of the key scattering information above or below fragmentation thresholds and giving the shape of complex spectra in analytical or semianalytical form. What quantum-defect theory cannot provide, by itself, are the actual values of scattering parameters such as $\underline{S}$ or $\underline{K}$ for any specific atom, symmetry and energy range.

In simple cases having a relatively small number of channels, one can hope to adjust the scattering parameters semiempirically until an experimental spectrum is reproduced. Most of the early applications of multichannel quantum-defect theory used this semiempirical approach. Even though the fitting procedure falls short of being a comprehensive atomic theory, it is useful for organizing extremely complicated spectra in terms of relatively few parameters. It also has nontrivial predictive power. Thus, for example, Dill (1973) and Lee (1974b) used parameters fitted to the bound energy levels and oscillator strengths of atomic xenon to predict the angular distribution and spin polarization of photoelectrons. Indeed, the first applications of effective-range theory showed similar predictive power in relating a low-energy scattering phase shift to the energy of a bound state lying just below a fragmentation threshold.

For systems having a large number of channels, more than about five, normally there is not sufficient experimental information to permit an unambiguous determination of the scattering parameters by using the semiempirical fitting procedure. In the presence of electronically excited perturbing energy levels, like the doubly excited states common in the alkaline-earth atoms, the unknown energy dependence of the scattering parameters also complicates the fitting; the resulting nonuniqueness of the fits has plagued some studies. More recently, it has become possible to calculate the scattering parameters in an *ab initio* or nearly *ab initio* calculation. Such calculations have most frequently been performed using R-matrix methods (Fano and Lee, 1973; Lee 1974a; Burke and Robb, 1975; O'Mahony and Greene, 1985; Hamacher and Hinze, 1989, 1991; Greene and Aymar, 1991), but they have also been carried out using the relativistic random-phase approximation (Johnson *et al.*, 1980), hyperspherical coordinate methods (Greene 1981; Watanabe, 1982, 1986; Fano, 1983; Tang *et al.*, 1992), and the Schwinger variational principle (Goforth *et al.*, 1987; Goforth and Watson, 1992). These techniques for calculating multichannel scattering parameters and spectra have improved dramatically in recent years, both in their accuracy and in their efficiency.

Below in Sec. II.A we attempt to remove some of the mystery surrounding these methods by presenting the

basic qualitative ideas of multichannel spectroscopy. While it is developed in a somewhat heuristic fashion, this section does give a useful way of thinking about multichannel spectra. Most of the qualitative phenomenology present in multichannel Rydberg spectra can, in principle, be deduced from these pictures. Moreover, we regard this development as fundamental in the sense that it requires hardly any approximations, in contrast to widely applied independent-electron models. The quantitative formulation of these ideas awaits Sec. II.B. below, which will begin to give the flavor of their nontrivial power and utility.

A. Visualizing atomic photoabsorption

Imagine that an atomic system swallows an incident photon of frequency ω and in the process an atomic electron gains kinetic energy $\hbar\omega$. This language already relies on an independent-electron viewpoint, which is frequently inappropriate since a single electron in a many-electron atom does not have "its own energy." More precisely, only the total energy E of the atom has a definite value in the stationary final state reached by photoabsorption, since the electrons are continually exchanging energy with each other via their Coulombic interaction $1/r_{12}$. Similarly, the electrons frequently exchange spin and orbital angular momentum with each other, while the total squared spin $\vec{S}^2$ and orbital momentum $\vec{L}^2$ have conserved eigenvalues (neglecting fine-structure effects). The possibility for exchange of energy and angular momentum between electrons diminishes as the outermost electron moves outward to a distance r, owing to the decay of the inner electron's wave function and to the falloff of $1/r_{12}$. Eventually a radius r_0 is reached, such that beyond $r>r_0$ the probability of any such exchange process diminishes to a negligible value. For all practical purposes the outermost electron is now distinguishable from the electrons of the residual ion that are confined to the region $r<r_0$.

1. Single-channel processes

Figure 1(a) gives a picture of the photoabsorption process reaching a singly excited Rydberg state of a two-electron atom. The inner electron is confined to $r_1<r_0$, in a stationary state of energy E_1, by the steeper (unscreened) attraction to the nucleus. When electron 2 moves beyond this radius r_0, its own energy ϵ is conserved at the value $\epsilon=E-E_1$, determined by the atomic final-state energy E. Classically, the outermost electron is reflected from the outer turning point if $\epsilon<0$, while it escapes uninhibited to infinity if $\epsilon>0$. The former process is called photoabsorption to a discrete state, while the latter is called direct or nonresonant photoionization. Quantum mechanics modifies this statement in the usual way. Specifically, in the case where the outermost electron is reflected classically (at $\epsilon<0$) only a discrete set of energies is allowed. These are energies for which the Schrödinger wave function decays exponentially at $r_2\to\infty$, and they are known to obey a Rydberg formula

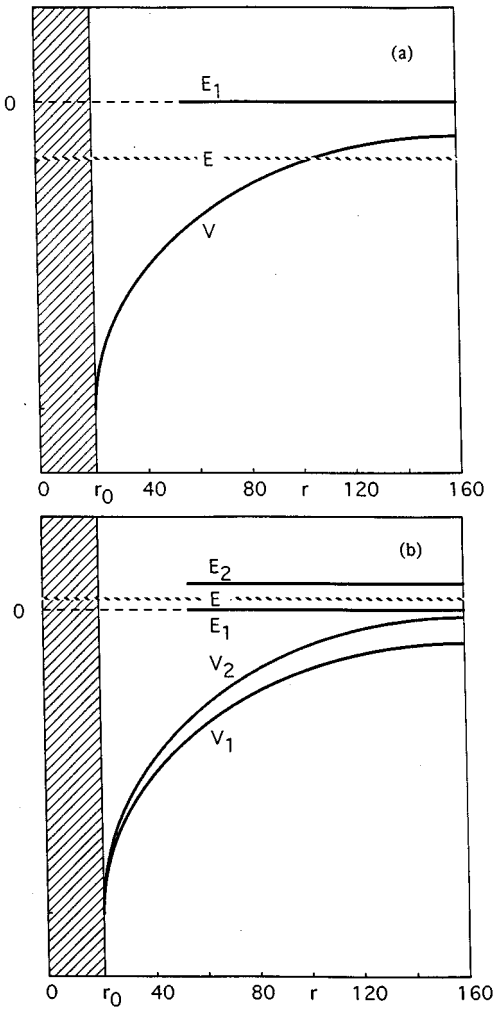

FIG. 1. Coulombic potentials (V) and total energies (E) for an electron outside an ionic core (shaded zone): (a) single-channel photoabsorption process with total energy E corresponding to a situation in which the electron is bound with respect to the ionization limit E_1; (b) two-channel photoionization process for final energy E between the first and second ionization limits E_1 and E_2. The radial position of the electron is denoted by r, in atomic units.

$$E_{nl}=E_1-\frac{R_y}{(n-\mu_l)^2}. \tag{2.1}$$

Here R_y is the Rydberg constant and the positive integer n is the principal quantum number. The parameter μ_l is a dimensionless quantity, roughly constant in energy but dependent on the atomic-state quantum numbers such as l. Historically μ_l has been called the quantum defect. Section II.B describes the origin of this energy expression and the reinterpretation of $\pi\mu_l$ as a scattering phase shift.

2. Two-channel processes

A less trivial situation is depicted in Fig. 1(b), where now the inner electron e_1^- can be in one of two different states, with energies E_1 or E_2. This two-channel proto-

type atom begins to show the main features characteristic of more complex atoms. Again, the radius r_0 marks a boundary beyond which the exchange of energy and angular momentum can be neglected. Below the first ionization threshold E_1, all energy eigenstates are discrete bound levels. Except for the ground state, each normally has a small natural linewidth due to spontaneous emission that we ignore for the purpose of this review.

Between the first and second thresholds $E_1<E<E_2$, all energies are allowed eigenvalues of the Hamiltonian, but the continuum is "lumpy" in that the density of states is enhanced at a sequence of autoionizing Feshbach resonances converging to the upper threshold. The resonance energies approximately obey a Rydberg formula

$$E_{nLS}^{\rm res}=E_2-\frac{R_y}{(n-\mu_{LS})^2}, \tag{2.2}$$

where μ_{LS} is nearly energy independent. The widths of these resonances decay with principal quantum number roughly as n^{-3}, which can be represented by incorporating a nearly constant imaginary part into the quantum defect μ_{LS} (Seaton, 1969). We show below how this imaginary part of μ can be extracted in terms of basic scattering information, mainly the scattering probability $|S_{21}|^2$ for the outer electron to induce a transition between inner-electron states E_2 and E_1 in a single collision.

Above the upper threshold, $E>E_2$, the continuum becomes smooth and is no longer lumpy since there are no more Feshbach resonances. Because two continuum channels are open, however, two physically distinguishable final states are reached. These simply add incoherently to the total photoionization cross section, but the relative strength of their contributions can in principle be sorted out experimentally. This could be accomplished, for instance, by measuring the state of the ionic residue following the photoionization, or by resolving the detected photoelectron energy in a spectrometer. The branching ratio of cross sections σ_2/σ_1 into these two alternative channels is generally a smooth, nearly flat function of energy. Observation of a sharp departure from near constancy of σ_2/σ_1 implies the presence of a shape resonance or else perhaps the presence of a third channel contributing a Feshbach resonance. (Long-range field effects can cause σ_2/σ_1 to vary even in the absence of resonances, when the long-range potential is non-Coulombic.)

In the discrete energy range below the first threshold, $E<E_1$, another common phenomenon occurs. The levels belonging to the two different channels can interfere and mutually perturb each other. A simple way to see whether a particular bound level lies within this "perturbed" energy regime is to extrapolate the sequence of autoionizing Feshbach resonances down from the region $E_1<E<E_2$ into the range $E<E_1$. The "influence" of each perturber extends over an energy range roughly equal to the width it would have were it an autoionizing state, namely

$$\Gamma_{nLS}^{\rm res}\approx\frac{4R_y{\rm Im}(\mu_{LS})}{[n-{\rm Re}(\mu_{LS})]^3}. \tag{2.3}$$

While the energy spectrum remains discrete for $E<E_1$, all levels E that fall within the range $E_{nLS}^{\rm res}\pm\frac{1}{2}\Gamma_{nLS}^{\rm res}$ will be perturbed. The perturbation causes the photoabsorption intensity to depart from the usual n^{-3} Rydberg scaling law and it induces a shift in the energy of levels lying within this width. The energy perturbation takes a very well-defined form: the quantum defects of all bound levels, referred to the lower threshold, rise by one unit across the perturber's width.

3. Properties in the time domain

Viewed in real time, for instance when a subpicosecond laser pulse excites the atom, there are three characteristic time scales in the internal dynamics of a two-channel atom. Two of these are the Rydberg orbital periods $\tau_1=2\pi(-\epsilon_1/R_y)^{-3/2}$ in channel 1 and $\tau_2=2\pi(-\epsilon_2/R_y)^{-3/2}$ in channel 2. Notice that a great disparity in these periods arises at an energy just below the threshold E_1, where $\tau_1\gg\tau_2$. The third relevant time scale is the average time required for a Rydberg electron in channel 2 to scatter into channel 1. This is essentially the autoionization lifetime $\tau_{12}=|S_{12}|^{-2}\tau_2$. Time-dependent wave-packet calculations show that when a fast laser pulse coherently excites several autoionizing states just below the threshold E_2, the ejected electrons do not emerge in a smooth exponentially decaying curve such as $\exp(-t/\tau_{12})$. Instead, a sequence of autoionizing electron pulses is seen, with the temporal separation between electron pulses equal to the Rydberg orbital period τ_2 and their relative heights governed by the anticipated exponential decay factor. This reflects a key property of multichannel Rydberg states, always to be kept in mind: energy exchange between the Rydberg electron and other electrons is possible only once per orbital period when the Rydberg electron enters the reaction zone $r<r_0$. Another point to bear in mind is that the reaction zone does not have a sharply defined radius r_0. Rather, it should be thought of as being smeared out to some extent, even though some methods (such as R-matrix method) choose a specific value.

B. Single-channel properties

Theoretical techniques commonly denoted as "quantum-defect theories" stress particularly the fact that Feshbach-type resonances represent excitations of closed channels. Other names for this general class of techniques include multichannel effective-range theory (Ross and Shaw, 1961; Lee, 1975), and the specific formulation of R-matrix theory developed by Teichmann and Wigner (1952) to include closed channels. We develop below the quantitative formulation that corresponds to the viewpoint described in the previous subsection. We begin by treating motion in a single channel

and then describe, in the following sections, the considerations appropriate to an arbitrary number of interacting channels.

When a system is confined to a single relevant channel, this implies the existence of just one possible two-body breakup mode. Beyond some distance r_0 we suppose that the system has a well-defined effective local potential energy $v(r)$ in the fragmentation coordinate r. Here we deal explicitly only with a long-range Coulomb potential, as the generalization to other potentials is fairly straightforward and has been described elsewhere. The effective potential for a Rydberg electron in any channel depends on its orbital quantum number l. In atomic units,

$$v(r)=\frac{l(l+1)}{2r^2}-\frac{1}{r}. \tag{2.4}$$

In the region of configuration space $r>r_0$ where this potential energy adequately describes that of the atomic electron, the atomic wave function, rescaled by r, can always be written as a linear combination of two linearly independent solutions (f,g) of the second-order radial Schrödinger equation $-\frac{1}{2}u''(r)+v(r)u(r)=\epsilon u(r)$. Considerable flexibility exists in choosing (f,g), but following Seaton (1966, 1983), some simplicity and convenience are gained by choosing them such that

(1) $f\to 0$ as $r\to 0$;

(2) $f\to(2/\pi k)^{1/2}\sin\left(kr+\frac{1}{k}\ln r+\eta\right)$ as $r\to\infty$

for $\epsilon\equiv\frac{1}{2}k^2>0$, which includes the logarithmic phase accumulation appropriate for an attractive Coulomb field of unit charge, and a long-range phase shift η that is given explicitly for the Coulomb field in Eq. (2.39) below.

(3) $g\to-(2/\pi k)^{1/2}\cos\left(kr+\frac{1}{k}\ln r+\eta\right)$ as

$r\to\infty$ for $\epsilon\equiv\frac{1}{2}k^2>0$.

(4) (f,g) for $\epsilon<0$ join smoothly onto the positive energy solutions obeying conditions (1)–(3).

Briefly, (1) is desirable so that a state with very high orbital angular momentum l in any atom will reduce to one solution $f_{\epsilon l}$ alone without requiring any superposition with $g_{\epsilon l}$. Condition (2) ensures that f is energy normalized, i.e., $\langle f_\epsilon|f_{\epsilon'}\rangle=\delta(\epsilon-\epsilon')$. Condition (3) guarantees that (f,g) are always linearly independent to the maximum extent. Finally, condition (4) ensures that any rapid energy variations in the calculated scattering parameters reflect dynamics of the atom rather than the arbitrary choice made for the reference functions. We stress that these criteria are only adopted to obtain maximum simplicity in the eventual formulas to be derived below. There is nothing magical or mysterious about these stipulations, as in fact any two linearly independent solutions of the radial long-range equation would serve as well as (f,g). In fact it is sometimes useful to discuss another pair of outgoing/incoming radial waves $f^{\pm}\equiv(-g\pm if)/\sqrt{2}$, where $i=\sqrt{-1}$. (Avoid throughout this section, the confusion between $i=\sqrt{-1}$ and the channel index i.)

The analytical properties of the solutions (f,g) are detailed completely by Seaton (1983) [who calls them $(s,-c)$] and by Greene *et al.* (1979, 1982), although the derivations involve somewhat laborious properties of the confluent hypergeometric equation. The main results needed below follow far more simply from approximate WKB (see, for example Messiah, 1958) solutions of the radial Coulombic Schrödinger equation, along the lines sketched by Greene *et al.* (1982). In particular, in the classically allowed range with positive kinetic energy, we have

$$f_{\epsilon l}(r)=\left(\frac{2}{\pi k(r)}\right)^{1/2}\sin\left(\int_a^r k(r')dr'+\frac{1}{4}\pi\right), \tag{2.5a}$$

$$g_{\epsilon l}(r)=-\left(\frac{2}{\pi k(r)}\right)^{1/2}\cos\left(\int_a^r k(r')dr'+\frac{1}{4}\pi\right). \tag{2.5b}$$

Here the Langer (1937) corrected local wave vector is

$$k(r)=\left(2\epsilon-\frac{(l+\frac{1}{2})^2}{r^2}+\frac{2}{r}\right)^{1/2}, \tag{2.6}$$

and a is the inner classical turning point, i.e., the zero of $k(r)$ that lies closest to the nucleus. For positive energies, the above expressions for (f,g) are valid all the way to $r\to\infty$. At $\epsilon<0$, however, the standard WKB connection formulas must be applied to give the corresponding solutions beyond the outermost turning point, $r\gg b$. After setting $\kappa\equiv(-2\epsilon)^{1/2}=1/\nu$, where ν is the effective quantum number, the asymptotic forms of these solutions can be written as

$$f_{\epsilon l}(r)\to(\pi\kappa)^{-1/2}(\sin\beta D^{-1}r^{-\nu}e^{\kappa r}-\cos\beta D r^{\nu}e^{-\kappa r}), \tag{2.7a}$$

$$g_{\epsilon l}(r)\to-(\pi\kappa)^{-1/2}(\cos\beta D^{-1}r^{-\nu}e^{\kappa r}+\sin\beta D r^{\nu}e^{-\kappa r}), \tag{2.7b}$$

where β and D are constants depending on ϵ and l. In the WKB approximation, for a Coulomb potential of unit charge, they can be evaluated explicitly and are given by Greene *et al.* (1982). Of greatest interest for our purposes is the phase parameter

$$\beta=\frac{1}{2}\pi+\int_a^b k(r)dr=\pi(\nu-l). \tag{2.8}$$

This phase (divided by π) measures the number of de Broglie half wavelengths in the radial solution between $r=0$ and $r=\infty$.

The asymptotic expressions (2.7) derived from a WKB approach are, remarkably enough, identical to the form of Seaton's (1966, 1983) exact nonrelativistic solutions. Moreover, the WKB approximation to β in Eq. (2.8) coincides precisely with the full quantum solution. Only the parameter D in Eq. (2.7) is changed. Milne's (1930) phase-amplitude method provides a different exact quantum treatment, which can be viewed (Greene *et al.*, 1982) as an alternative to Seaton's (1983) deriva-

tions based on complicated special-function properties. The Milne approach readily shows how a phase parameter such as β and an amplitude such as D arise for solutions of the time-independent Schrödinger equation with any one-dimensional potential. This general point of view permits us to generalize Seaton's basic approach to any long-range reference field. A detailed description of these generalizations would take us far afield from the aims of this review, but an interested reader can find discussions in the existing literature (Greene *et al.*, 1979, 1982; Mies and Julienne, 1984; Fano and Rau, 1986).

For many purposes, the interaction between an electron and a closed-shell atom or ion can be described by a local, central potential $V(r)$. Such a model-potential description has considerable utility and some limitations, both of which are discussed below in Sec. III. Consider the problem of finding energy levels of an electron with partial wave l moving in this potential field. The exact radial solution, rescaled by r in order to eliminate the first derivative term in the usual way, obeys

$$-\frac{1}{2}F''(r)+\left(\frac{l(l+1)}{2r^2}+V(r)\right)F(r)=\epsilon F(r). \tag{2.9}$$

To within an arbitrary proportionality constant, the solution at any chosen energy ϵ is uniquely specified by regularity at the origin $r=0$, although numerical methods may be required to solve Eq. (2.9) for $F(r)$. This differential equation coincides with the equation determining (f,g), because the effective potential in Eq. (2.4) was understood to coincide with the true atomic effective potential in Eq. (2.9), at sufficiently large distances $r>r_0$. This, combined with the fact that a second-order differential equation has just two linearly independent solutions, ensures that for $r>r_0$ the atomic solution $F(r)$ is a linear combination of (f,g) with constant coefficients. Characterizing the two coefficients by an amplitude N_l and a phase $\pi\mu_l$, we have

$$F_{\epsilon l}(r)=N_l[f_{\epsilon l}(r)\cos\pi\mu_l-g_{\epsilon l}(r)\sin\pi\mu_l], \quad r>r_0. \tag{2.10}$$

If $F(r)$ has been determined by numerically integrating Eq. (2.9) from $r=0$ to $r=r_0$ or beyond, the phase shift $\pi\mu_l$ can be calculated from a ratio of radial Wronskians:

$$\tan\pi\mu_l=\left.\frac{fF'-f'F}{gF'-g'F}\right|_{r\geq r_0}. \tag{2.11}$$

The real constants N_l and μ_l depend on energy, but for the most part this dependence is very smooth. Boundary conditions at $r\to\infty$ still remain to be applied. At any negative energy $\epsilon<0$, insertion of the asymptotic forms (2.7) into Eq. (2.10) shows that the solutions $F_{\epsilon l}(r)$ diverge exponentially at $r\to\infty$,

$$F_{\epsilon l}(r)\to N_l(\pi\kappa)^{-1/2}[\sin(\beta+\pi\mu_l)D^{-1}r^{-\nu}e^{\kappa r} -\cos(\beta+\pi\mu_l)Dr^{\nu}e^{-\kappa r}]. \tag{2.12}$$

Accordingly, the bound-state quantization condition, needed to kill the exponential growth at infinity, reads simply

$$\sin(\beta+\pi\mu_l)=0, \tag{2.13}$$

or $\nu-l+\mu_l=n_r$, an integer. Defining the principal quantum number $n\equiv n_r+l$, the allowed energy values fit the empirical formula proposed by Rydberg (1889), in atomic units (a.u.),

$$\epsilon_{nl}=-\frac{1}{2(n-\mu_l)^2}. \tag{2.14}$$

The term "quantum defect" for μ_l stems from the view that μ_l measures how "defective" an alkali atom is compared to the "perfect" atom (from the perspective of the "old" quantum theory) hydrogen, whose quantum defects all vanish. A single key result initiated the so-called "quantum-defect theory" of Ham (1955), Seaton (1955, 1958, 1966, 1983), and their successors: the smooth manner in which below-threshold bound-state quantum defects evolve with increasing energy into above-threshold scattering phase shifts $\delta_l=\pi\mu_l$. Seaton (1958) further showed that μ_l suffers from a mild nonanalyticity right at the ionization threshold $\epsilon=0$, but this singularity is so weak that it is inconsequential for an attractive Coulomb potential. Some further remarks on a few difficult properties of Coulomb functions are deferred to Sec. II.D below.

For other long-range potentials, such as the purely centrifugal potential or the repulsive Coulomb potential so important in nuclear physics, the energy-normalized solutions (f,g) become highly energy dependent at small distances. This strong energy dependence can be factored out analytically by expressing (f,g) in terms of two new solutions (f^0,g^0) that are (entire) analytic functions of the energy at any finite radius. It is convenient (and permissible) to choose $f^0(r)$ to be proportional to the regular solution $f(r)$, but $g^0(r)$ need not be proportional to $g(r)$ in general. This point has been discussed elsewhere (Greene *et al.*, 1979, 1982; Seaton, 1983; Fano and Rau, 1986). In case the analytic solutions are needed, the transformation between (f^0,g^0) and (f,g) requires two r-independent parameters $\mathcal{A}$ and $\mathcal{G}$ that are functions of ϵ and l:

$$f_{\epsilon l}(r)=\mathcal{A}_{\epsilon l}^{1/2}f^0_{\epsilon l}(r), \tag{2.15a}$$

$$g_{\epsilon l}(r)=\mathcal{A}_{\epsilon l}^{-1/2}[g^0_{\epsilon l}(r)+\mathcal{G}_{\epsilon l}f^0_{\epsilon l}(r)]. \tag{2.15b}$$

Rau (1988) has derived many revealing interrelationships between all of these parameters at positive and negative energies.

ASIDE: For the special problem of a purely centrifugal long-range potential, these solutions are given in terms of spherical Bessel functions: $f_{\epsilon l}(r)=(2k/\pi)^{1/2}rj_l(kr)$, $g_{\epsilon l}(r)=(2k/\pi)^{1/2}rn_l(kr)$. The transformation (2.15) to analytic solutions (f^0,g^0) involves coefficients $\mathcal{A}_{\epsilon l}=k^{2l+1}$ and $\mathcal{G}_{\epsilon l}=0$ in this simple case. In examples such as this, for which (f,g) depend strongly on the energy at small distances, the phase shift $\pi\mu_l^0$ of $F(r)$ relative to (f^0,g^0) is a smooth, analytic function of energy across the relevant fragmentation threshold. Thus, taking $l=0$ as a specific example, one sees at once that the tangent of the analytic phase shift

$$\tan\pi\mu_l^0=\left(\frac{f_l^0F'-f_l^{0'}F}{g_l^0F'-g_l^{0'}F}\right)\Bigg|_{r\geq r_0} \tag{2.16}$$

determines the energy of a high-lying s-wave bound state at $\epsilon<0$. The analog to the Rydberg formula, applicable for zero long-range potential and $l=0$, is readily derived to be $\tan\pi\mu_{l=0}^0+\kappa^{-1}=0$, or

$$\epsilon=-\tfrac{1}{2}\kappa^2=-\tfrac{1}{2}\cot^2\pi\mu_{l=0}^0, \tag{2.17}$$

provided $\tan\pi\mu_{l=0}^0$ is negative and "large" in absolute value. The physical phase shift $\delta_{l=0}$ entering the scattering matrix $S_l=\exp(2i\delta_l)$ in this s-wave example becomes

$$\delta_{l=0}=\pi\mu_{l=0}=\arctan(k\tan\pi\mu_{l=0}^0), \tag{2.18a}$$

and

$$S_{l=0}=\frac{1+ik\tan\pi\mu_{l=0}^0}{1-ik\tan\pi\mu_{l=0}^0}. \tag{2.18b}$$

Equations (2.16)–(2.18) constitute the basic formulas of single-channel effective-range theory, which relates bound-state properties to low-energy scattering properties. The connection can be made complete by identifying the zero energy value of $\tan\pi\mu_{l=0}^0$ as the usual "scattering length," while its energy derivative is related to the "effective range." In this sense, the generalized form of quantum-defect theory encompasses both single-channel and multichannel effective-range theories as special cases (Blatt and Jackson, 1949; Ross and Shaw, 1961).

C. Nonseparable quantum mechanics in several dimensions

An enormous class of physical problems of current interest requires the solution of a nonseparable, time-independent Schrödinger equation in more than one dimension. No single theoretical approach is known that can solve all such problems. In fact for many systems, such as the double continuum states of two electrons interacting with each other and with another charged particle, only relatively crude approximations are presently available. Moreover, even these crude solutions typically apply over small ranges of energy, angular momentum, and other quantum numbers.

Dramatic progress has been achieved in recent years in developing powerful techniques capable of handling physical systems of unprecedented complexity, provided their fragmentation involves no more than one coordinate at a time. A famous problem of this category, which has only been solved quite recently (Iu *et al.*, 1991; O'Mahony and Mota-Furtado, 1991; Watanabe and Komine, 1991), is the near-threshold photoionization spectrum of hydrogen or of an alkali atom in an uniform magnetic field. In that three-dimensional problem, the fragmentation coordinate is $|z|$, the projection of the electron-nucleus separation $\vec{r}$ onto the magnetic field direction $\vec{B}=B\hat{z}$. Motion in the two remaining coordinates (ρ,ϕ) or (x,y) is bounded at any finite energy, and is therefore quantized. (Here we suppose that the usual choice of vector potential has been made, $\vec{A}=\frac{1}{2}\vec{B}\times\vec{r}$.) Also in the atomic two-electron problem, at energies below the threshold for double escape, a single fragmentation coordinate can be identified, either the distance r_2 of the outermost electron from the nucleus or the hyperspherical radius $R=\sqrt{r_1^2+r_2^2}$ (Fano, 1983). Another example that, in contrast, seems to involve more than one coordinate is Jungen's (1984) description of competing ionization and dissociation channels in H_2; because only one of these processes occurs in any given asymptotic fragmentation channel, this last problem fits into the same category as well.

1. Characterizing the solutions

We restrict our attention now to solving the stationary-state Schrödinger equation for such systems where one fragmentation coordinate, to be written as r, is assumed to be identifiable. As Fano (1981) has stressed, a generalized hyperspherical radius or moment of inertia coordinate can serve quite generally in this capacity. Other choices may be more computationally convenient depending on the problem at hand and on the solution method adopted. The main point we need for now is that the d-dimensional configuration space can be separated into mutually orthogonal coordinates: one fragmentation coordinate r and $d-1$ "surface" coordinates ω. The coordinates ω are interpreted to include the spin degrees of freedom as well as true spatial coordinates.

Because the multidimensional Schrödinger equation is homogeneous, with up to second-order derivatives, knowledge of a particular rescaled solution $\{r\psi_\beta(r,\omega)\}$ and its radial derivative $\partial\{r\psi_\beta(r,\omega)\}/\partial r$ uniquely determines $\psi_\beta(r,\omega)$ at all large distances $r\geq r_0$. The subscript β distinguishes different linearly-independent solutions that are degenerate in energy, angular momentum, parity (denoted by π), and any other "exact" quantum numbers. [Note that, throughout this section, the index β should not be confused with the quantum-defect-theory phase parameter of Eq. (2.8).] In fact it would be inconvenient to tabulate the wave function and normal derivative at the continuously infinite set of points ω representing this surface. Fortunately, such a table is not really needed anyway for the following reason: a discrete set of functions $\Phi_i(\omega)$ can always be found that spans the fixed r surface. These functions might be, as described in this section, a set of r-independent eigenstates [frequently appropriate at $r\to\infty$ as in the close-coupling representation (Burke and Smith, 1962)], or a set of "adiabatic" eigenfunctions of the fixed-r Hamiltonian (Born and Oppenheimer, 1927).

In any case, the surface Fourier decompositions of $\{r\psi_\beta(r,\omega)\}$ and $\partial\{r\psi_\beta(r,\omega)\}/\partial r$ in terms of this basis can for practical purposes be truncated to a finite number N at any chosen energy, on physical grounds. In the special case that $\Phi_i(\omega)$ are independent of r, we can write the decompositions as

$$\psi_\beta(r,\omega)=\sum_i \frac{1}{r}\Phi_i(\omega)F_{i\beta}(r), \tag{2.19a}$$

$$\frac{\partial[r\psi_\beta(r,\omega)]}{\partial r}=\sum_i \Phi_i(\omega)F'_{i\beta}(r). \tag{2.19b}$$

Knowledge of $F_{i\beta}(r)$ and $F'_{i\beta}(r)$ in Eqs. (2.19), along with the Schrödinger equation itself, provides enough information to uniquely determine ψ_β at all distances larger than r_0. We focus on this large-r region because that is where the scattering information will eventually be extracted.

Quite generally, if the Fourier decompositions (2.19) of the Schrödinger solutions regular at $r\to 0$ involve N terms or channels i, one expects to find also N linearly-independent solutions, $\beta=1,\ldots,N$. Thus we can speak of $F_{i\beta}(r)$ as representing an $(N\times N)$ solution matrix. This is a square matrix prior to imposing boundary conditions at $r\to\infty$, each column of which represents a separate independent solution as indicated by Eq. (2.19). The ith row gives the projection of the ith surface harmonic or channel function $\Phi_i(\omega)$ onto each independent solution. The phases of $F_{i\beta}$ and Φ_i can be chosen such that $F_{i\beta}(r)$ is a real matrix for almost all problems in atomic and molecular physics.

Any linear combination of the degenerate Schrödinger eigenfunctions ψ_β is also a valid eigenfunction. This implies that considerable nonuniqueness exists in the choice of the $F_{i\beta}(r)$. Stated in mathematical terms, any constant nonsingular $(N\times N)$ linear transformation matrix $X_{\beta\gamma}$ can be used to transform $F_{i\beta}(r)$ into an equally acceptable set of solutions—for example,

$$\psi_\gamma=\sum_\beta \psi_\beta X_{\beta\gamma}=\sum_i \frac{1}{r}\Phi_i(\omega)M_{i\gamma}(r), \tag{2.20a}$$

where

$$M_{i\gamma}(r)=\sum_\beta F_{i\beta}(r)X_{\beta\gamma}. \tag{2.20b}$$

Prior to imposing physical boundary conditions at $r\to\infty$, nothing in the mathematics or physics "prefers" one set of independent solutions $\{\psi_\beta\}$ over another set $\{\psi_\gamma\}$. However one can identify a "minimal" amount of information regarding the solution at smaller distances $r<r_0$ that provides enough information to determine the scattering matrix. This follows upon recognizing that the matrix

$$\underline{R}\equiv\underline{F}(r)[\underline{F}'(r)]^{-1}=\underline{M}(r)[\underline{M}'(r)]^{-1} \tag{2.21}$$

is invariant under transformations such as $\underline{X}$. Following Wigner (1946b), we call this fundamental invariant quantity the matrix $\underline{R}$. It is real and symmetric, and will be seen below to determine the scattering matrix $\underline{S}$ and its close relative, the reaction matrix $\underline{K}$.

2. Modified form of the close-coupling method without exchange

For readers not already familiar with multichannel, multidimensional problems in quantum mechanics, the preceding discussion may seem somewhat nebulous. In order to make it more concrete, we turn to a specific example—the atomic close-coupling equations for a distant electron in the field of a residual ion or neutral atom with a single valence electron. To simplify our notation somewhat, the distant electron is assumed to move in a region having no overlap with the residual electrons. This permits us to neglect all exchange effects. We further neglect fine-structure effects; this permits us to write the exact solutions in LS coupling, omitting reference to the spin degrees of freedom for the sake of brevity. For this example a convenient choice for the fragmentation coordinate r is the distance between the outermost electron and the nucleus. Accordingly, the set of coordinates ω orthogonal to r consists of all spatial coordinates of the inner residue, and the angular coordinates $\hat{r}\equiv(\theta,\phi)$ of the distant electron. The surface harmonics or channel functions $\Phi_i(\omega)$ are eigenfunctions of the inner-electron Hamiltonian h_1, the inner-electron squared orbital angular momentum operator $\vec{l}_1^{\,2}$, the distant electron squared orbital momentum $\vec{l}_2^{\,2}$, the squared total orbital angular momentum $\vec{L}^2$, and the z component L_z. The detailed eigenvalue equations read

$$h_1\Phi_i(\omega)=E_i\Phi_i(\omega), \tag{2.22a}$$

$$\vec{l}_1^{\,2}\Phi_i(\omega)=l_{1i}(l_{1i}+1)\Phi_i(\omega), \tag{2.22b}$$

$$\vec{l}_2^{\,2}\Phi_i(\omega)=l_{2i}(l_{2i}+1)\Phi_i(\omega), \tag{2.22c}$$

$$\vec{L}^2\Phi_i(\omega)=L(L+1)\Phi_i(\omega), \tag{2.22d}$$

$$L_z\Phi_i(\omega)=M\Phi_i(\omega). \tag{2.22e}$$

Aside from possible degeneracies of these eigenvalues and routine phase ambiguities, these equations uniquely determine the channel functions. The total Hamiltonian (that includes electrostatic interactions only) is

$$H=h_1-\frac{1}{2}\frac{1}{r}\frac{\partial^2}{\partial r^2}r+\frac{\vec{l}_2^{\,2}}{2r^2}-\frac{Z_{\rm net}}{r}+\sum_{k=1}^{\infty} r^{-k-1}r_1{}^k P_k(\hat{r}_1\cdot\hat{r}). \tag{2.23}$$

The term $P_k()$ represents a Legendre polynomial and $Z_{\rm net}$ is the asymptotic (screened) net charge of the residue that is seen by the distant electron.

At this point we depart in a crucial way from the usual formulations of the close-coupling method (Burke and Smith, 1962). Our motivation for this departure follows from Fig. 2, which depicts the radial portion of configuration space for the two electrons.

Because we consider energies below the "Wannier" (1953) threshold for double escape, one can identify a radius r_0 such that the wave function $\psi=0$ when $r_1>r_0$ and $r_2>r_0$ simultaneously. More accurately, of course, the true wave function decays exponentially in that region, but the exponential falloff is sufficiently rapid that neglect of ψ altogether in region IV can be made arbitrarily precise by increasing the value of r_0. In

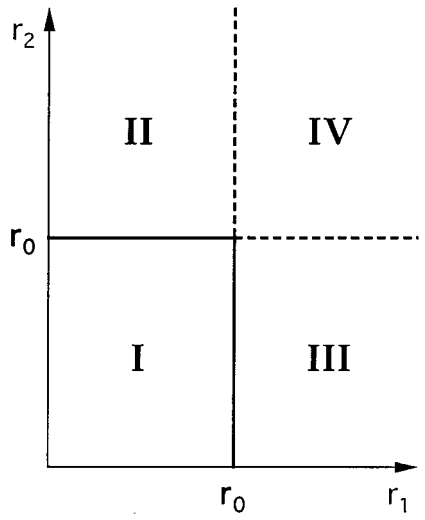

FIG. 2. Radial configuration space for two electrons with regions I, II, III, and IV marked.

this spirit, we seek to construct solutions in regions II and III alone, subject to the (nonstandard) boundary condition that $\psi=0$ at the boundary of each region with region IV. To be specific, we treat region II only, where $r_2>r_1$, and require that $\psi=0$ for $r_1=r_0$. In region II the fragmentation coordinate r coincides with r_2. With this boundary condition, the energy spectrum of the inner electron in Eq. (2.22a) is entirely discrete. The close-coupling expansion (2.19) is likewise discrete, whereas in the conventional close-coupling method the summation Σ_i in Eq. (2.19) implies an integral over the inner-electron continuum energy eigenstates. Without this integral the $\Phi_i(\omega)$ do not form a complete set. In conventional calculations this continuum integral is usually ignored or else it is approximated by a discrete summation using so-called "pseudostates" (Burke, Gallaher, and Geltman, 1969). The critical role of continuum contributions can be seen from the fact that the continuum contributes roughly half of the hydrogen atom ground-state polarizability in a second-order perturbation theory calculation. In fact, this correct description of the polarizability was the initial motivation for the introduction of discrete pseudostates (Burke, Gallaher, and Geltman, 1969) that approximately describe the effect of the neglected continuum. Another recent study (Bray and Stelbovics, 1993) has developed a systematic way to incorporate continuum coupling effects by using Sturmian functions to represent the inner-electron wave function. This method appears to offer similar advantages to the present systematic scheme for generating a complete set of discrete solutions that can represent the inner-electron degrees of freedom.

A physically relevant point to keep in mind is the fact that the boundary condition $\psi=0$ at $r_1=r_0$ causes the inner electron's radial orbitals to differ from the usual orbitals calculated over $0<r<\infty$. This difference might appear to be undesirable at first glance. The entire treatment for the present example, however, is only intended for an electron interacting with a residual fragment state confined within $r<r_0$. The modified boundary condition consequently introduces no further errors. More to the point, though, the convergence of the expansion (2.19) improves dramatically as a result of confining the inner-electron eigenstates to a "box" of radius r_0. There is consequently no mathematical or physical need for additional pseudostates of any type.

Insertion of Eq. (2.19) into the time-independent Schrödinger equation at energy E, followed by projection onto $\langle\Phi_j|$, leads to the following infinite but discrete set of coupled differential equations,

$$F''_{i\beta}(r)+2\sum_j [\epsilon_i\delta_{ij}-V_{ij}(r)]F_{j\beta}(r)=0. \tag{2.24}$$

Here $\epsilon_i\equiv E-E_i$ is the asymptotic electron kinetic energy in the ith channel. The potential matrix $V_{ij}(r)$ includes a diagonal centrifugal term in addition to an electrostatic coupling matrix element:

$$V_{ij}(r)=\left(\frac{l_i(l_i+1)}{2r^2}-\frac{Z_{\rm net}}{r}\right)\delta_{ij} + \sum_{k=1}^{\infty} r^{-k-1}\langle\Phi_i|{r_1}^k P_k(\hat{r}_1\cdot\hat{r})|\Phi_j\rangle. \tag{2.25}$$

In matrix notation, Eq. (2.24) becomes more succinct,

$$\underline{F}''(r)+2[\underline{\epsilon}-\underline{V}(r)]\underline{F}(r)=0. \tag{2.26}$$

Upon truncating the infinite set of second-order coupled differential equations (2.24) to a finite number N, one can find, in general, $2N$ linearly independent solutions at each energy E. After boundary conditions at the origin are imposed, $F_{i\beta}(0)=0$, N solutions remain mathematically acceptable prior to enforcing boundary conditions at asymptotic distances.

We present a few more detailed aspects of the truncated system of N close-coupling equations [(2.24), (2.26)]. The first important property is constancy of the "Wronskian matrix" of two different solution matrices $\underline{F}$ and $\underline{M}$, provided that each of them obeys Eq. (2.26). The Wronskian is defined for this system to be

$$W(\underline{M},\underline{F})\equiv\underline{M}^t\underline{F}'-\underline{M}'^t\underline{F}. \tag{2.27}$$

By matrix-multiplying $\underline{M}^t$ to Eq. (2.26) from the left, and subtracting its analog with $\underline{M}$ and $\underline{F}$ interchanged, one finds that the Wronskian of any two solution matrices is a constant. This statement is independent of boundary conditions and reflects mainly the absence of first-derivative terms in Eq. (2.26) and the symmetry of the potential matrix $\underline{V}$. A second useful property of solutions of Eq. (2.26) is the simple first-order differential equation obeyed by their matrix $\underline{R}$. This can be obtained by differentiating the definition (2.21) and then using Eq. (2.26) to eliminate the second-derivative matrix that occurs. The resulting equation reads

$$\underline{R}'(r)=\underline{1}+2\underline{R}(\underline{\epsilon}-\underline{V})\underline{R}, \tag{2.28}$$

where $\underline{1}$ is the $(N\times N)$ identity matrix. (Note that the identity matrix is denoted by $\underline{1}$ through this review.) This differential equation could be solved numerically, for instance, to calculate long-range multipole corrections to the matrix $\underline{R}$. Ideas along the lines of the first-order nonlinear differential equation were pursued in the context of single-channel and multichannel problems by Calogero (1967).

For a variety of reasons, including the fact that $\underline{R}(r)$ typically has numerous poles, direct solution of Eq. (2.28) is not the most efficient way to solve for the matrix $\underline{R}$. One further useful property emerges from an inspection of Eq. (2.28), namely the fact that symmetry of the matrix $\underline{R}$ at one value of r immediately guarantees symmetry at all r values. In most problems the matrix $\underline{R}(r)$ is diagonal in some region of space, often at small distances, which is enough to prove that it will remain real and symmetric at all radii.

D. Long-range treatment using multichannel quantum-defect theory

For the purposes of this section, we suppose that the R matrix has been calculated for an atomic system within the small-r region in which all electrons overlap each other and exchange could be important. For an atom with two valence electrons, this corresponds to region I in Fig 2. Section III below discusses efficient methods for accomplishing this small-r part of the calculation in practice. Our goal now is to discuss the motion of a single electron when it emerges from this small-r region (or R-matrix "box"). For a two-electron atom, this amounts to solving the Schrödinger equation in regions II or III in Fig. 2. One possible approach is to simply adopt the close-coupling equations without exchange in those regions, as presented in Eq. (2.26). Several algorithms and computer programs have been published to accomplish this numerically. This direct numerical solution of the long-range coupled equations can be rather time consuming. However, recent rapid developments in computational power and in computational algorithms have improved the power of this numerical approach for dealing with the outer-field calculation.

Another approach has received widespread use owing to its great efficiency. Seaton's multichannel quantum-defect theory can be used to solve the long-range part of the problem in closed analytical form, at the price of making an approximation to the close-coupling equations at large distances. In its simplest form, which coincides with Seaton's initial formulation, this approximation neglects all anisotropic multipole contributions $(k>0)$ to the interaction between an outermost electron and the inner residue. This means neglecting the entire $\Sigma_{k=1}^{\infty}$ in the potential matrix [Eq. (2.25)] that enters the long-range close-coupling equations (2.26). In some problems, where this approximation seems dubious, one can increase somewhat the size of the box radius r_0, since we assume that all multipole interactions are correctly treated within. In any case, this approximation implies that the channels are completely decoupled beyond $r=r_0$. In physical terms, this amounts to neglect the scattering of an electron from one channel into another whenever it moves in the outer region.

Mathematically, the absence of off-diagonal coupling matrix elements in the outer region (in this approximation) implies that a simple attractive Coulomb plus centrifugal potential applies within every channel individually, at all radii $r>r_0$. This diagonal potential in each channel coincides with the form of Eq. (2.4), if we take $Z_{\rm net}=1$, as would be appropriate for describing states of a neutral atom or molecule. The generalization of these results to arbitrarily ionized (nonrelativistic) species is straightforward. We start from the assumed known values of the wave function and derivative at $r=r_0$, or more conveniently their projections on the ith channel function:

$$F_{i\beta}(r_0)=\langle\langle\Phi_i|(r\psi_\beta)\rangle\rangle, \tag{2.29a}$$

$$F'_{i\beta}(r_0)=\left\langle\left\langle\Phi_i\left|\frac{\partial(r\psi_\beta)}{\partial r}\right.\right\rangle\right\rangle. \tag{2.29b}$$

Here the double bracket notation is used to denote an integral over only the surface of the reaction volume, while single brackets will imply the usual integral over all space.

These surface properties of the previously calculated inner-region solutions serve as boundary conditions that uniquely determine the $(N\times N)$ solution matrix $F_{i\beta}(r)$ in the outer region, in conjunction with Eq. (2.26). Specifically, in view of the relevance of Eq. (2.4) as the potential within each channel, the ith channel component of the βth independent solution is a linear combination of regular and irregular Coulomb functions $f_i(r)\equiv f_{\epsilon_i l_i}(r)$ and $g_i(r)\equiv g_{\epsilon_i l_i}(r)$. This follows because $F_{i\beta}(r)$ obeys the same differential equation as (f_i,g_i), whereby

$$F_{i\beta}(r)=f_i(r)I_{i\beta}-g_i(r)J_{i\beta}, \tag{2.30}$$

and the matrices $\underline{I}$ and $\underline{J}$ are independent of r. They can be calculated by taking the Wronskian of both sides of Eq. (2.30) with respect to f_i and then with respect to g_i, which gives explicitly

$$I_{i\beta}=W(g_i,F_{i\beta})/W(g_i,f_i), \tag{2.31a}$$

$$J_{i\beta}=W(f_i,F_{i\beta})/W(g_i,f_i). \tag{2.31b}$$

Since these Wronskians are independent of r, they can be evaluated at any $r\geq r_0$. They are usually calculated right at the boundary $r=r_0$, however, where a variational or other type of calculation has provided $F_{i\beta}$ and its derivative with respect to r.

So far very little has been specified about the particular choice of independent solutions represented by ψ_β and the corresponding radial-channel components $F_{i\beta}(r)$ beyond the boundary r_0. Normally, these calculated independent solutions do not yet obey physically relevant boundary conditions. Alternative sets of lin-

early independent solutions, corresponding to alternative boundary conditions at $r\to\infty$, can be used to describe the stationary states at a definite energy E. The asymptotic solutions for $r\geqslant r_0$ are characterized by either the reaction matrix $\underline{K}$ or the scattering matrix $\underline{S}$ referring to open and closed channels. First, we introduce the solutions characterized by the reaction matrix $\underline{K}$, which is simply connected to the matrix $\underline{R}$. Then, below in Secs. II.D.1 and II.D.2, the basic derivations of multichannel quantum-defect theory are presented in terms of the scattering matrix $\underline{S}$.

A first standard set of linearly independent solutions that satisfy standing-wave boundary conditions is given by a linear transformation of the solutions $\underline{F}$:

$$\underline{M}(r)=\underline{F}(r)(\underline{I})^{-1}, \tag{2.32}$$

where the ith channel component of this i'th independent solution is

$$M_{ii'}(r)=f_i(r)\delta_{ii'}-g_i(r)K_{ii'}. \tag{2.33}$$

The asymptotic solutions $M_{ii'}(r)$ are characterized by an $(N\times N)$ matrix $\underline{K}\equiv\underline{J}(\underline{I})^{-1}$ which is real and symmetric. Because this matrix $\underline{K}$ usually includes closed-channel indices (i.e., for channels that are energetically forbidden as $r\to\infty$), its energy dependence is normally quite smooth and this matrix can frequently be assumed to be energy independent over limited energy intervals such as across an ionization threshold. We refer to $\underline{K}$ as the "smooth short-range reaction matrix," and we call the particular set of independent solutions (2.33) the "short-range reaction-matrix solutions." When an attractive Coulomb potential describes the long-range motion in every channel, $\underline{K}$ coincides with the matrix $\underline{\mathcal{R}}$ of Seaton (1983). Recalling expressions (2.31) and (2.21), the $\underline{K}$ and $\underline{R}$ matrices at $r=r_0$ are related by

$$\underline{K}=(\underline{f}-\underline{f}'\underline{R})(\underline{g}-\underline{g}'\underline{R})^{-1}. \tag{2.34}$$

The radial functions f, g, f', g' here are the Coulomb functions and derivatives appropriate to each channel, evaluated at $r=r_0$ for the appropriate orbital angular momentum l_i and channel energy ϵ_i, and arranged into diagonal matrices.

Practical quantum-defect calculations are frequently conducted using $\underline{K}$ rather than $\underline{S}$, as this permits the entire calculation of total cross sections to be carried out using real arithmetic. Another real representation is the eigenchannel version of multichannel quantum-defect theory introduced by Fano (1970), which utilizes the eigenvalues $\tan\pi\mu_\alpha$ and eigenvectors $U_{i\alpha}$ of the matrix $\underline{k}$,

$$K_{ij}=\sum_\alpha U_{i\alpha}\tan\pi\mu_\alpha U^\dagger_{\alpha j}. \tag{2.35}$$

The independent eigenchannel solutions have the following form outside the reaction volume:

$$\Psi_\alpha=\mathcal{A}\sum_i \frac{1}{r}\,\Phi_i(\omega)U_{i\alpha}[f_i(r)\cos\pi\mu_\alpha-g_i(r)\sin\pi\mu_\alpha], \tag{2.36}$$

which corresponds to the multichannel generalization of Eq. (2.10). In Eq. (2.36), $\mathcal{A}$ is the antisymmetrization operator. The eigenchannel wave functions Ψ_α, $\alpha=1,\ldots,N$, have a common phase shift $\pi\mu_\alpha$ in each of the fragmentation channels i. The eigenchannel MQDT formulation has been widely used for studying atomic and molecular spectra. The techniques for obtaining physical solutions that remain well behaved at $r\to\infty$ and for calculating the observables, discussed in numerous papers (Fano, 1970; Lu, 1971; Lee and Lu, 1973; Fano and Rau, 1986), will not be detailed in this review; some relevant points will be discussed later in Secs. II.E and II.F. In particular, it will be shown that a great deal of semiempirical MQDT analyses are based on the eigenchannel formulation of multichannel quantum-defect theory.

1. Multichannel quantum-defect theory derivations for resonant continua

To describe a photoabsorption (or scattering) experiment, carried out with sufficiently high energy resolution that it effectively probes stationary states at a definite energy E, incoming-wave (or outgoing-wave) boundary conditions must be imposed. To find the linear combinations of the arbitrary Schrödinger solutions ψ_β that obey these boundary conditions, it is convenient to rewrite the radial solutions (f_i,g_i), defined above in Sec. II.B, in terms of outgoing/incoming waves $f_i^\pm$

$$\begin{Bmatrix} -if \\ g \end{Bmatrix}=\frac{1}{\sqrt{2}}(-f^+\pm f^-). \tag{2.37}$$

(In this section, take care not to confuse $i=\sqrt{-1}$ and the channel index i.) The solutions $f^\pm$ are convenient, with simple asymptotic forms:

$$f^\pm(r)\to\begin{cases}(\pi k)^{-1/2}r^{\pm i/k}e^{\pm ikr\pm i\eta}, & \epsilon=k^2/2\geqslant 0;\\ (2\pi\kappa)^{-1/2}e^{\pm i\beta}(D^{-1}r^{-\nu}e^{\kappa r}\mp iDr^{\nu}e^{-\kappa r}), & \epsilon=-\kappa^2/2<0,\end{cases} \tag{2.38}$$

where the long-range phase shift for a long-range attractive Coulomb potential of unit charge is known analytically:

$$\eta=\frac{1}{k}\ln(2k)+\arg\Gamma\left(l+1-\frac{i}{k}\right)-\frac{1}{2}l\pi. \tag{2.39}$$

The solutions $f^{\pm}(r)$ defined here are identical to the $\varphi^{\pm}(r)$ functions of Seaton (1983). In contrast, they are proportional, at $\epsilon>0$ only, to those with the same notation in Greene *et al.* (1982) and in Greene *et al.* (1979). The particular independent solutions beyond $r=r_0$ now have the form

$$F_{i\beta}(r)=\frac{1}{i\sqrt{2}}f_i^{+}(r)(I_{i\beta}+iJ_{i\beta})-\frac{1}{i\sqrt{2}}f_i^{-}(r)(I_{i\beta}-iJ_{i\beta}). \tag{2.40}$$

In this form it is evident that there exists a linear transformation that will transform the solutions ψ_β into new solutions, each of which has an outgoing-wave component in a single channel only. We now apply from the right side of Eq. (2.30) the inverse of the matrix $\underline{I}+i\underline{J}$, giving a new set of linearly independent solutions:

$$\underline{M}(r)=\underline{F}(r)(\underline{I}+i\underline{J})^{-1}. \tag{2.41}$$

One obtains for the ith channel component of the i'th independent solution

$$M_{ii'}(r)=\frac{1}{i\sqrt{2}}f_i^{+}(r)\delta_{ii'}-\frac{1}{i\sqrt{2}}f_i^{-}(r)S^{\dagger}_{ii'}. \tag{2.42}$$

The asymptotic solutions $M_{ii'}(r)$ are characterized by an $(N\times N)$ matrix $\underline{S}^{\dagger}\equiv(\underline{I}-i\underline{J})(\underline{I}+i\underline{J})^{-1}$. In the special case that all channels are open, $\underline{S}^{\dagger}$ coincides, aside from phase factors, with the Hermitian conjugate of the usual scattering matrix. (The phase factors will be given below.) It is the Hermitian conjugate $\underline{S}^{\dagger}$ that appears rather than $\underline{S}$ itself, because these incoming-wave states are the time-reversed versions of the outgoing-wave states that are used to describe particle-scattering experiments (Breit and Bethe, 1954). This scattering matrix $\underline{S}$ is related to the short-range reaction matrix $\underline{K}$ through the relation

$$\underline{S}=\frac{\underline{1}+i\underline{K}}{\underline{1}-i\underline{K}}. \tag{2.43}$$

In fact, the omission of some phase factors, coupled with the fact that $\underline{S}$ usually includes closed-channel indices, leads to important differences between $\underline{S}$ and the usual "physical scattering matrix" that we denote by $\underline{S}^{\rm phys}$ throughout this paper. Like the smooth, short-range reaction matrix, this matrix $\underline{S}$, referred to as the "smooth, short-range scattering matrix," has a weak energy dependence. When an attractive Coulomb potential describes the long-range motion in every channel, $\underline{S}$ coincides with the matrix $\underline{\chi}$ of Seaton (1983). The solutions of Eq. (2.42) are not acceptable if one or more channels is closed, because the radial wave functions $M_{ii'}(r)$ diverge exponentially at $r\to\infty$ for all closed-channel components i.

It may be helpful to describe qualitatively the meaning of the solutions constructed in Eq. (2.42). Imagine forming a wave packet by performing an energy integral over $\exp(-iEt)$ multiplying the i'th independent solution of Eq. (2.42) with an additional energy envelope reflecting the bandwidth of the exciting laser. (This would be the state excited if the dipole matrix element reaches only this particular solution from the ground state. We should point out that this is not normally the case, as more frequently all or most of the solutions i' will be excited coherently, with relative amplitudes given by a dipole matrix element $d_{i'}$.) The resulting wave packet describes a *gedanken* experiment in which photoabsorption occurs at time $t\approx 0$, exciting a Rydberg wave packet that will be found moving outward at positive times, in channel i' only. While this outgoing wave packet would look more or less sensible in the classically allowed region, it would eventually acquire unphysical behavior in any channels that are closed, owing to the divergence of the large-r stationary-state solutions. In particular, the packet would not be reflected backward from the outermost classical turning point, as one expects.

To find solutions with the correct physical behavior, we must impose boundary conditions at large r. Most importantly, we need to superpose the stationary solutions given by Eq. (2.42) to determine linear combinations that, for closed channels, decay exponentially in the asymptotic region. This can be accomplished rather simply by using a compact partitioned matrix notation borrowed from Seaton (1983). The notation was developed earlier in the nuclear-physics resonance studies of Teichmann and Wigner (1952) and of Breit (1959), and the idea is simple. At any energy E, we collect all of the open channels (for which $E\geqslant E_i$) and label the entire set by a subscript o. We call the number of open channels N_o. Similarly, we collect all closed channels ($E<E_i$) into a set labeled c, and label their number N_c. Since the total number of long-range channels is assumed to remain a fixed number N over an appreciable energy range, we have $N_o+N_c=N$. Next, we arrange the $(N\times N)$ outer-region solution matrix $\underline{M}(r)$ into open and closed partitions accordingly:

$$\begin{pmatrix}\underline{M}_{oo} & \underline{M}_{oc}\\ \underline{M}_{co} & \underline{M}_{cc}\end{pmatrix}=\frac{1}{i\sqrt{2}}\underline{f}^{+}(r)-\frac{1}{i\sqrt{2}}\underline{f}^{-}(r)\begin{pmatrix}\underline{S}^{\dagger}_{oo} & \underline{S}^{\dagger}_{oc}\\ \underline{S}^{\dagger}_{co} & \underline{S}^{\dagger}_{cc}\end{pmatrix}. \tag{2.44}$$

In Eq. (2.44), $\underline{f}^{\pm}(r)$ indicate diagonal matrices containing the radial solutions appropriate to each channel along the diagonal, whose asymptotic forms were given in Eq. (2.38).

In this partitioned matrix notation, we can simply construct the solutions needed. Because there are only N_o open channels at this energy, we anticipate only N_o linearly independent "physical" incoming-wave solutions. Each of these is a different linear combination of the

solutions $\underline{M}(r)$. We represent the transformation taking us from the N "smooth short-range" $\underline{S}$-matrix solutions $\underline{M}(r)$ to the N_o "physical" incoming-wave solutions by $\underline{\underline{M}}^{(-)}(r)=\underline{M}\ \underline{B}$. The transformation matrix is an $(N\times N_o)$ constant matrix that will itself be partitioned

$$\underline{B}\equiv\begin{pmatrix}\underline{B}_o\\ \underline{B}_c\end{pmatrix}. \tag{2.45}$$

Combining these quantities gives the open- and closed-channel components:

$$\begin{pmatrix}\underline{M}^{-}_{oo}\\ \underline{M}^{-}_{co}\end{pmatrix}=\frac{1}{i\sqrt{2}}\begin{pmatrix}\underline{f}^{+}_{o}\underline{B}_o-\underline{f}^{-}_{o}(\underline{S}^{\dagger}_{oo}\underline{B}_o+\underline{S}^{\dagger}_{oc}\underline{B}_c)\\ -\underline{f}^{-}_{c}\underline{S}^{\dagger}_{co}\underline{B}_o+(\underline{f}^{+}_{c}-\underline{f}^{-}_{c}\underline{S}^{\dagger}_{cc})\underline{B}_c\end{pmatrix}. \tag{2.46}$$

Using now the asymptotic forms of $f^{\pm}(r)$ from Eq. (2.38), we find that the large-r wave function components in the closed channels approach

$$\underline{M}^{(-)}_{co}(r)\rightarrow(\cdots)e^{\kappa r}e^{-i\beta}[-\underline{S}^{\dagger}_{co}\underline{B}_o-(\underline{S}^{\dagger}_{cc}-e^{2i\beta})\underline{B}_c]. \tag{2.47}$$

Exponential growth in the closed channels must be eliminated by choosing the closed part $\underline{B}_c$ of the coefficient matrix to be

$$\underline{B}_c=-(\underline{S}^{\dagger}_{cc}-e^{2i\beta})^{-1}\underline{S}^{\dagger}_{co}\underline{B}_o\,. \tag{2.48}$$

If we choose the open-channel subspace coefficients to be a diagonal matrix of long-range phase parameters $\underline{B}_o=\exp(-i\underline{\eta})$, the physical states obeying the incoming-wave boundary condition are obtained; these have the following asymptotic form in the open channels [i.e., $\underline{M}^{(-)}_{oo}(r)$]:

$$M^{(-)}_{ii'}(r)\rightarrow i^{-1}(2\pi k_i)^{-1/2}(e^{ik_ir}\delta_{ii'}-e^{-ik_ir}S^{\dagger\,\mathrm{phys}}_{ii'}). \tag{2.49}$$

The Hermitian conjugate of the $(N_o\times N_o)$ physical scattering matrix introduced here is

$$\underline{S}^{\dagger\,\mathrm{phys}}=e^{-i\underline{\eta}}[\underline{S}^{\dagger}_{oo}-\underline{S}^{\dagger}_{oc}(\underline{S}^{\dagger}_{cc}-e^{2i\beta})^{-1}\underline{S}^{\dagger}_{co}]e^{-i\underline{\eta}}. \tag{2.50}$$

The general expression for the closed-channel components in the physical solution follows from Eq. (2.48), for $r>r_0$,

$$\underline{M}^{(-)}_{co}(r)=\frac{i}{\sqrt{2}}[-\underline{f}^{-}_{c}\underline{S}^{\dagger}_{co}e^{-i\underline{\eta}}-(\underline{f}^{+}_{c}-\underline{f}^{-}_{c}\underline{S}^{\dagger}_{cc})(\underline{S}^{\dagger}_{cc}-e^{2i\beta})^{-1}\underline{S}^{\dagger}_{co}e^{-i\underline{\eta}}]. \tag{2.51}$$

A somewhat more useful expression follows after introducing a solution $W(r,\nu,l)$ proportional to the Whittaker Coulomb function (Whittaker and Watson, 1927) that decays exponentially as $r\rightarrow\infty$ for all negative energies. This solution will be written in each channel as

$$W(r,\nu_i,l_i)=\frac{i}{\sqrt{2}}e^{-i\beta_i}f^{+}-\frac{i}{\sqrt{2}}e^{i\beta_i}f^{-}. \tag{2.52}$$

More precisely, our solution $W(r,\nu,l)$ is given by

$$W(r,\nu,l)=\nu^{3/2}[\nu^2\Gamma(\nu+l+1)\Gamma(\nu-l)]^{-1/2}\times W_{\nu,l+1/2}\left(\frac{2r}{\nu}\right), \tag{2.53}$$

where $W_{\nu,l+1/2}$ is the Whittaker function, Γ denotes a gamma function, and the multiplicative factor in front is a constant. $W(r,\nu,l)$ has an "energy-normalized" amplitude $(2/\pi k(r))^{1/2}$ in the classically allowed region, like the solutions in Eq. (2.5), but it decays properly asymptotically. For non-Coulombic long-range fields, Eq. (2.52) remains a valid generalization of the Whittaker-type function. Whereas both $f^{\pm}_{c}$ diverge exponentially at infinity in Eq. (2.51), the divergence is cancelled in $\underline{\underline{M}}^{(-)}(r)$ owing to the choice of coefficients [Eq. (2.48)]. However, this is not so apparent from inspecting Eq. (2.51). We cancel the exponentially growing terms analytically, giving the long-range closed-channel component wave functions in a form involving $W(r,\nu,l)$ that now explicitly gives the coefficient $\underline{Z}_{co}$ in front of the exponential decay,

$$\underline{M}^{(-)}_{co}=\underline{W}\ \ \underline{Z}_{co}\,, \tag{2.54a}$$

where the closed-channel coefficients are given by

$$\underline{Z}_{co}=e^{i\beta}(\underline{S}^{\dagger}_{cc}-e^{2i\beta})^{-1}\underline{S}^{\dagger}_{co}e^{-i\underline{\eta}}. \tag{2.54b}$$

Next, Eqs. (2.49) and (2.54) can be combined to give the i'th energy-normalized physical incoming-wave state:

$$\psi^{(-)}_{i'}=\mathcal{A}\sum_{i\in o}\frac{1}{r}\Phi_i(\omega)i^{-1}(2\pi k_i)^{-1/2}(e^{ik_ir}\delta_{ii'}-e^{-ik_ir}S^{\dagger\,\mathrm{phys}}_{ii'})+\sum_{i\in c}\frac{1}{r}\Phi_i(\omega)W_i(r,\nu_i,l_i)Z_{ii'}. \tag{2.55}$$

The i'th such stationary state has outgoing waves asymptotically only in channel i' and can be used to describe a photoionization experiment that detects electrons emerging in channel i'. We denote by d_β the reduced dipole matrix elements connecting a specific initial state ψ_0 of total angular momentum J_0 to the real states ψ_β in Eq. (2.19) having total angular momentum quantum number J, i.e.,

$$d_\beta=\langle\psi_\beta||r^{(1)}||\psi_0\rangle. \tag{2.56}$$

Viewing the d_β as a column vector of N real numbers, the linear transformation (2.41) determines a smooth set of N dipole matrix elements

$$d^{S}_{i'}=\sum_{\beta}\ (\underline{I}+i\underline{J})^{-1\,\dagger}_{i'\beta}d_\beta\,. \tag{2.57}$$

This column vector of amplitudes can be partitioned in the usual way into open- and closed-channel contributions $\underline{d}^{S}\equiv\begin{pmatrix}\underline{d}^{S}_{o}\\ \underline{d}^{S}_{c}\end{pmatrix}$.

Next, Eqs. (2.45) and (2.48) can be combined to give reduced dipole matrix elements connecting the initial state ψ_0 to the N_o physical incoming-wave states. These matrix elements generally exhibit very rapid energy dependences reflecting closed-channel resonances and are given by

$$\underline{d}^{(-)}=\underline{d}_o^S e^{-i\eta}-\underline{d}_c^S(\underline{S}_{cc}^{\dagger}-e^{2i\beta})^{-1}\underline{S}_{co}^{\dagger}e^{-i\eta}. \tag{2.58}$$

The resonances occur when the closed-channel submatrix $\underline{S}_{cc}^{\dagger}-e^{2i\beta}$ is nearly singular; at these energies, the resonant dipole amplitudes can grow orders of magnitude larger than the background or nonresonant amplitudes.

Equation (2.58) gives the dipole amplitudes required by most standard formulations of total and partial photofragmentation cross sections, photofragment angular distributions, spin polarization, alignment, orientation, or various quantities that can be measured by coincidence experiments. For the moment, we give only the formulas for total and partial photoionization cross sections, in the simplest case in which the magnetic substates of the initial state ψ_0 are randomly populated. The partial photoionization cross section into channel i, in a.u., is

$$\sigma_i=\frac{4\pi^2\omega\alpha}{3(2J_0+1)}|d_i^{(-)}|^2, \tag{2.59}$$

where α is the fine-structure constant and ω the photon energy. The total photoionization cross section is the sum over all partial cross sections (a sum over total final-state angular momenta J is also implied):

$$\sigma_{\rm tot}=\frac{4\pi^2\omega\alpha}{3(2J_0+1)}\underline{d}^{(-)\dagger}\underline{d}^{(-)}. \tag{2.60}$$

Calculations of other observables, such as scattering cross sections, are equally straightforward using the physical scattering matrix $\underline{S}^{\rm phys}$ in Eq. (2.50).

The formalism developed in this section is based on channel expansions in terms of the energy-normalized Coulomb functions f and g. This formalism is not the most convenient for studying the systems in which the long-range potential experienced by the escaping electron is non-Coulombic. The (f^0, g^0) pair describing a long-range polarization potential is better adapted to the study of negative ions (Kim and Greene, 1989; Greene, 1990a) because this base pair and the resulting phase shifts μ^0 are analytic functions of the energy and exhibit no singularities at the photodetachment threshold (Watanabe and Greene, 1980). In a single-channel problem the quantum defect μ^0 of negative-ion bound states can be expressed easily in terms of the parameters $\mathcal{A}$, β, and $\mathcal{G}$ [Eqs. (2.8) and (2.15)] that characterize the long-range polarization potential (Greene, 1980; Watanabe and Greene, 1980; Kim and Greene, 1989). Matching the R-matrix eigenstates and their derivatives to a channel expansion with f^0 and g^0 Coulomb functions gives a short-range reaction matrix $\underline{K}^0$. This changes the equations of multichannel quantum-defect theory in a manner described by Greene (1990a).

For photoelectron energy ϵ less than $-1/2l^2$, the energy-normalized Coulomb functions ($f_{\epsilon l}$, $g_{\epsilon l}$) become complex and therefore inconvenient. We will show later in Secs. III and IV that some studies of doubly excited states of alkaline-earth atoms were performed using short-range reaction matrices $\underline{K}^0$ instead of short-range reaction matrices $\underline{K}$. Multichannel quantum-defect theory calculations can be carried out using R matrices that have a fixed number of fragmentation channels at all energies considered, even when, for some channels, $\epsilon\leqslant-\frac{1}{2}l^2$.

2. Bound-state properties

The formulas that were developed above to eliminate exponential growth in closed channels are not immediately applicable to bound states because there is no open-channel subspace. When all channels are closed, the energy-level spectrum becomes entirely discrete, whereas it is continuous if at least one channel is open. The first thing of interest in the discrete energy range is simply the position of the bound levels. For a single-channel problem the quantization of bound states was accomplished by Eqs. (2.13) and (2.14) above. The more general multichannel version can be derived by following similar logic.

We start from the radial solution matrix $M_{ii'}(r)$ outside the reaction volume, as expressed in Eq. (2.42) in terms of the smooth, short-range scattering matrix $S_{ii'}$. Since all channels i are now closed, $f_i^{\pm}(r)$ diverge at $r\to\infty$, according to Eq. (2.38). We attempt to construct a linear combination $M_{ii'}^{(n)}(r)=\Sigma_i' M_{ii'}(r)B_{i'}^{(n)}$ of the solutions (2.42), chosen to cancel this exponential divergence. The desired superposition follows from inspection of Eq. (2.47), recalling that B_o is now absent. The resulting MQDT form of the bound-state quantization condition reads

$$(\underline{S}_{cc}^{\dagger}-e^{2i\beta})\underline{B}^{(n)}=0. \tag{2.61}$$

This system of linear equations has at least one nontrivial solution if and only if

$$\det|\underline{S}_{cc}^{\dagger}-e^{2i\beta}|=0. \tag{2.62}$$

The energies E_n at which Eq. (2.62) has a solution are the bound-state energies of the system. Determination of the E_n normally requires a numerical search for roots. In this search the fastest energy dependence is normally confined to the quantity $e^{2i\beta}$. The scattering parameters $\underline{S}_{cc}^{\dagger}$ normally vary quite slowly with energy, and can frequently be regarded as constants over small spectral ranges. The column vector of superposition coefficients $\underline{B}^{(n)}$ is well defined only at the bound energy levels and is undefined at other energies. [It is sometimes useful to establish continuity of the eigenvectors of Eq. (2.62) even at nonbound energies, especially when trying to classify complex spectra. One useful method is to diagonalize the matrix on the left-hand side at any E, giving N_c eigenvalues and eigenvectors as continuous functions of energy. The bound-state search then amounts to finding energies at which at least one eigenvalue vanishes.] The bound-state eigenvector is needed to calculate other observable properties of the bound state at energy E_n, such as the probabilities of photon emission or absorption. As in Eq. (2.54a), the exponentially decaying function can be expressed in terms of the $W(r,\nu,l)$ function of Eq. (2.53),

$$\Psi^{(n)}=\sum_i \frac{1}{r}\Phi_i(\omega)W_i(r,\nu_i,l_i)Z_i^{(n)}, \tag{2.63}$$

where the closed-channel coefficient is

$$Z_i^{(n)}=e^{i\beta_i}B_i^{(n)}. \tag{2.64}$$

Normalization of the coefficients $\underline{B}^{(n)}$ remains unspecified, of course, by the homogeneous system (2.61). The normalization integral can be evaluated analytically using a flux conservation argument, along the lines sketched by Seaton (1983), Lee and Lu (1973), and Greene *et al*. (1979). The expression given in Eq. (6.49) of Seaton (1983) involves the energy derivative of the short-range reaction matrix $\underline{K}$. While the expression is formally correct, it is numerically inconvenient in some cases owing to the occurrence of poles of $\underline{K}(E)$ on the real energy axis. In the eigenchannel formalism of multichannel quantum-defect theory, this difficulty is avoided by using an alternative normalization expression that involves energy derivatives of the eigenquantum defects μ_α and eigenvectors $U_{i\alpha}$ of the K matrix (Lee and Lu, 1973). While this avoids differentiation of divergent quantities, another drawback of the resulting expression is that derivatives of an eigenvector matrix such as $U_{i\alpha}$ also require great care in practice owing to sharply avoided crossings between the μ_α.

We give instead an alternative normalization condition based on the short-range scattering matrix states, which has been derived by similar techniques. The resulting normalization integral can be cast into a form suitable for rapid and accurate numerical evaluation:

$$\int |\psi|^2 dV=(2\pi)^{-1}\underline{B}^{(n)\dagger}\left(2\frac{d\underline{\beta}}{dE}+ie^{-2i\underline{\beta}}\frac{d\underline{S}^\dagger}{dE}\right)\underline{B}^{(n)} =1. \tag{2.65}$$

Normalization of the bound-state eigenvector is completed by enforcing this requirement on the $\underline{B}^{(n)}$ calculated in the course of solving Eq. (2.61). In this form of the normalization constant, only smooth quantities that are free from poles on the real energy axis are differentiated. Oscillator strengths for electric dipole transitions from a lower level to a bound final state normalized according to Eq. (2.65) can be calculated using the same superposition coefficients $\underline{B}^{(n)}$ and dipole matrix elements $\underline{d}^S$ of Eq. (2.57). If the lower level has angular momentum J_0 and has an isotropic distribution of magnetic substates, this oscillator strength is given by

$$f_n=\frac{2\omega}{3(2J_0+1)}\sum_i |B_i d_i^S|^2. \tag{2.66}$$

Some insight into the qualitative meaning of the normalization condition (2.65) is gained by recasting it and Eq. (2.61) into another form. Note first that the bound-state condition and also most of the quantum-defect expressions of the preceding subsection involve the matrix difference $\underline{S}_{cc}^\dagger-e^{2i\underline{\beta}}$. Here $(e^{2i\underline{\beta}})_{ii'}\equiv S_{ii'}^{\rm LR}$ can be regarded as a "long-range scattering matrix," giving the amplitude that an electron fired outward from the origin into a particular channel i' will be reflected back toward small distances in channel i. In the strict "quantum-defect approximation" that ignores channel coupling in the outer region, this long-range scattering matrix is diagonal. This diagonality expresses the fact, for instance, that a Rydberg electron with a definite orbital angular momentum l does not scatter into a different orbital momentum l' in the course of its usual motion in the purely Coulombic outer field. Processes that change the Rydberg electron orbital momentum are embodied of course in the short-range scattering matrix $\underline{S}$. But an anisotropic long-range field, such as an external electric or magnetic field, produces a long-range field scattering matrix $\underline{S}^{\rm LR}$ that is nondiagonal in a spherical representation.

Condition (2.61) can be rewritten in another form which shows how an equilibrium must be established between short- and long-range scattering, in order to form a standing wave at a bound state:

$$(\underline{S}_{cc}^\dagger-\underline{S}^{\rm LR})\underline{B}^{(n)}=0. \tag{2.67}$$

This expression, with a few manipulations, gives a more general form for the normalization condition as well:

$$(2\pi)^{-1}\underline{B}^{(n)\dagger}\left(i\underline{S}^{\rm LR}\frac{d\underline{S}^{\rm LR\dagger}}{dE}+i\underline{S}\frac{d\underline{S}^\dagger}{dE}\right)\underline{B}^{(n)}=1. \tag{2.68}$$

In this form the normalization integral involves two matrices that are in some sense average values of Smith's "quantum time operator" id/dE, with the "average" being taken over the long-range and short-range scatterings, respectively. These quantities are closely related conceptually to the time-delay matrix (Wigner, 1955; Smith, 1960). We will denote the Hermitian time-delay matrix by $\underline{Q}^{\rm phys}$. This superscript is adopted in the same spirit as the notation in Eq. (2.50), because $\underline{Q}^{\rm phys}$ is defined in terms of the physical scattering matrix,

$$\underline{Q}^{\rm phys}=i\underline{S}^{\rm phys}\frac{d\underline{S}^{\rm phys\dagger}}{dE}. \tag{2.69}$$

Note in particular that $\underline{Q}^{\rm phys}$ has indices relating to open channels only, whereas the matrices in the normalization expression (2.68) have only closed channel indices. Nevertheless, they have the same structure, so we identify the first matrix in the parentheses of Eq. (2.68) as the "long-range time-delay matrix" $\underline{Q}^{\rm LR}$ and the second as the "short-range time-delay matrix" $\underline{Q}$.

Having established the connection between the normalization constant or "density of states," and the long- and short-range time-delay matrices, we can give a more detailed interpretation of the structure of Eqs. (2.65) and (2.68). In particular, the long-range contribution to the density of states in Eq. (2.68) is given analytically for an attractive Coulomb field by $\pi^{-1}(d\underline{\beta}/dE)_{ii'}=\delta_{ii'}\nu_i^3$. For any high Rydberg state this contribution is huge and it normally dominates strongly over the short-range time-delay contribution. It is also worth considering the expression (2.50) for the physical scattering matrix, where the fastest energy dependence (except possibly for threshold effects or shape resonances) comes from

the closed-channel phase parameter β. For this reason we anticipate that the strongest energy dependences of the scattering matrix, for systems of the kind treated in this review, tend to come from the closed channels that have been "eliminated" in the quantum-defect sense. Deflection into such channels introduces appreciable time delays in the emergence of a scattered wave packet, when viewed in the time domain. When viewed instead in the energy domain for stationary scattering states, such effects appear in the corresponding density of states or time-delay matrix $\underline{Q}(E)$. Accordingly, we interpret qualitatively the long-range part of the normalization integral (i.e., $\pi^{-1}|B_i|^2 d\beta_i/dE$) as mainly reflecting the portion of the density residing within the ith closed channel. On the other hand, the short-range part $(2\pi)^{-1}\underline{B}^{\dagger}\underline{Q}\ \underline{B}$ in Eq. (2.68) reflects density in other channels whose indices are not included in the N_c explicit closed channels treated in the short-range scattering matrix, but whose effects have been included in the course of solving the time-independent Schrödinger equation.

3. Resonance analysis

The poles of the matrix $\underline{S}$ occur at the complex energies for which Eq. (2.62) is satisfied. Several theoretical methods have been proposed for determining the resonance positions and widths in the complex energy plane from the poles of the complex matrix $\underline{S}$ (see, for example, Siegert, 1939; Humblet and Rosenfeld, 1961; Noble *et al.*, 1993).

The fact that $\underline{S}^{\dagger}_{cc} - e^{2i\underline{\beta}}$ becomes singular at bound levels can help us to understand the origin of autoionizing resonances in scattering amplitudes [Eq. (2.51)] or in dipole photoabsorption amplitudes [Eq. (2.58)]. In both of these expressions, such a singularity clearly causes the matrix inverse to become very large. At first glance, this divergence of the matrix inverse might seem to lead to infinite cross sections. But unitarity of the smooth, short-range S matrix ensures that the singularity remains finite at real energies, provided there is no closed-channel subspace that is totally decoupled from the continuum. (If such a subspace is identifiable, its bound spectra can be treated separately as in the previous subsection.) The following discussion is adapted to resonances with nonzero decay widths.

Near resonance energies, the closed part of the physical incoming-wave state of Eq. (2.55) has a significant amplitude at finite distance. Equation (2.55) shows that the wave-function components in closed channels take the form of a quasistable standing-wave pattern near these resonant energies, whose amplitude grows to a maximum as the energy reaches the resonance center. Following Lecomte (1987), the density of states can be expressed in terms of the closed-channel coefficients Z_{co} of Eq. (2.54b) as:

$$ds = \mathrm{Tr}\,(\underline{Z}^{\dagger}_{oc}\underline{Z}_{co}). \tag{2.70a}$$

The partial density of states in a particular closed channel i is given by

$$ds_i = \sum_{i'} Z^2_{ii'}, \tag{2.70b}$$

where the summation runs over the N_o linearly independent solutions [Eq. (2.55)].

Equations (2.70a) and (2.70b) can be adapted, as described by Luc-Koenig, Lecomte, and Aymar (1994), to multichannel-quantum-defect-theory calculations using the short-range reaction matrix $\underline{K}^0$ instead of $\underline{K}$. Resonance analysis in neutral atoms is performed (Luc-Koenig, Aymar, and Lecomte, 1994; Luc-Koenig, Lecomte, and Aymar, 1994), by defining "analytic" partial densities of states in closed channels i by

$$ds^0_i = \sum_{i'} (Z^0_{ii'})^2, \tag{2.71}$$

where now the closed-channel component in the physical incoming-wave state [Eq. (2.55)] is expressed as $\Sigma_{i\in c} r^{-1}\Phi_i(\omega)W(\nu_i,l_i,r)(\mathcal{A})_i^{-1/2}Z^0_{ii'}$. The introduction of the parameter $\mathcal{A}_i^{-1/2}$ [Eq. (2.15a)] eliminates the divergences occurring when the effective number ν_i in the closed channel i has an integer value less than or equal to l_i.

Another tool for analyzing resonance properties was provided by Smith's (1960) physical time-delay matrix $\underline{Q}^{\mathrm{phys}}$ of Eq. (2.69). In fact, Smith's symbol Q reflects the analogy he had in mind with resonating cavities that can trap an electromagnetic or sound wave for thousands or even millions of internal wave "bounces." One key property of an "isolated" resonance is its decay width. We consider now states whose width is dominated by autoionization, although other decay mechanisms such as light emission or predissociation can be incorporated when appropriate. The derivation of Eq. (2.69) for the physical time-delay matrix is rather complicated as presented by Smith (1960), as it involves determining the ratio of the density of particles within a finite volume to the flux of particles in and out of that volume in different channels. The derivation of Eq. (2.68), on the other hand, shows how a quantity having the structure of the time-delay matrix [Eq. (2.69)] arises naturally in a calculation of the normalization constant, or density of states contributed by different channels. As Smith (1960) proposed, this physical time-delay matrix can be used to interpret resonances as follows. At any isolated resonance in scattering or photoabsorption, a single eigenvalue q_α of $\underline{Q}^{\mathrm{phys}}$ is found to be far larger than all other eigenvalues, and is seen to trace out an approximate Lorentzian as a function energy (Burke, Cooper, and Ormonde, 1969). If we denote the corresponding dominant eigenvector as $C_{i\alpha}$, then the relative probabilities for decay of the resonance into the different possible open channels i are given by $|C_{i\alpha}|^2$. Moreover, the total decay width of the resonance (full width at half maximum) is given by $\Gamma = 4/\max\{\mathrm{Tr}(\underline{Q}^{\mathrm{phys}})\} \approx 4/q_\alpha$. In more complex situations involving overlapping resonances, the number of eigenvalues q_α of $\underline{Q}^{\mathrm{phys}}$ having a nonnegligible value amounts to the number of closed channels N_c ($N_c < N_o$) that have been eliminated when constructing $\underline{S}^{\dagger\ \mathrm{phys}}$ in Eq. (2.50). The density of states can

be analyzed from the evolution of $\{\mathrm{Tr}\,(\underline{Q}^{\mathrm{phys}})\}$ with the energy E, though, the branching ratios for autoionization can no longer be simply related to the eigenvectors of the time-delay matrix. As was shown by Dalitz and Moorhouse (1970), this quantity can be expressed in terms of the energy derivatives of the eigenphase shifts τ_ρ of the physical scattering matrix (Greene and Jungen, 1985),

$$ds' = \mathrm{Tr}\,(\underline{Q}^{\mathrm{phys}}) = 2\sum_{\rho\in o}\frac{d\tau_\rho}{dE}. \tag{2.72}$$

As was shown by Lecomte (1993) and Lecomte *et al.* (1994), the densities of states defined by Eqs. (2.70) and (2.72) are identical when the short-range S matrix is energy independent. This case corresponds to the short-range time-delay contribution being negligible compared to the long-range contribution. This approach permits calculation of the total decay width when only the widths and positions are of interest, and not the eigenvectors of $\underline{Q}^{\mathrm{phys}}$. This type of analysis of the time-delay eigenvectors and eigenvalues can be very helpful for interpretation of resonance properties, and in particular for isolating final-state resonance effects from the means of exciting them.

For more complicated situations, as illustrated later in Sec. IV, the characteristics and the identifications of the resonances can be obtained from the total and partial densities of states using Eqs. (2.70)–(2.72).

Another area of current interest in this field is the development of methods for resonance analysis in the time domain rather than in the energy domain. The time-domain spectrum can be calculated directly using semiclassical approximations to quantum mechanics. General ideas along these lines have been developed extensively by Gutzwiller (1967), and applied with success to problems in atomic and molecular physics by Du and Delos (1988a, 1988b), and numerous other groups. These techniques often end up calculating a semiclassical approximation to the ''density of states,'' and can be viewed accordingly as approximations to the trace of the time-delay matrix $\underline{Q}^{\mathrm{phys}}$. These methods are particularly useful in the short-time limit, where peaks in the ''time domain'' can be associated with the periods of closed, unstable classical trajectories. ''Short-time'' features in a complex spectrum can be regarded equivalently as the main features that show up in an experiment that does not have particularly high-energy resolution. The analysis of such short-time phenomena is often the simplest in this picture, as surprising subtlety can be extracted from the study of spectral features in the time domain.

Resonance analysis can also be performed using an alternative MQDT parametrization of the resonances, based on the commonly called phase-shifted MQDT method. This approach was introduced by Giusti-Suzor and Fano (1984) and Cooke and Cromer (1985) and then worked out in a more rigorous form by Lecomte (1987).

The development of this method has been motivated by an increasing number of experimental data on autoionizing resonances of alkaline earths obtained, during the last two decades, using the experimental isolated-core excitation method (Cooke *et al.*, 1978). Several illustrations will be given later in Sec. IV. We briefly sketch the basic ideas of the Lecomte's formulation. The phase-shifted multichannel quantum-defect theory reduces the general problem of N_c closed channels interacting with N_o open channels to a simpler problem involving closed channels only, the presence of the open channels being taken into account implicitly. From the short-range reaction matrix $\underline{K}$ one introduces a complex matrix $\underline{\kappa}_{cc}$ restricted to the closed channels,

$$\underline{\kappa}_{cc} = \underline{K}_{cc} - \underline{K}_{co}(i\underline{1}_{oo} + \underline{K}_{oo})^{-1}\underline{K}_{oc}. \tag{2.73}$$

This amounts to imposing Siegert-type boundary conditions with only outgoing waves in all open channels. As explained by Fano and Rau (1986) and illustrated later in Sec. IV, the real part of $\underline{\kappa}$ can be used to calculate the positions of the resonances and to identify them by using MQDT bound-state techniques.

The phase-shifted multichannel quantum-defect theory is based on a phase normalization of the Coulomb functions that consists of replacing the standard pair (f,g) by a phase-shifted pair $(f\cos\pi\tilde{\mu} - g\sin\pi\tilde{\mu},\ g\cos\pi\tilde{\mu} + f\sin\pi\tilde{\mu})$ followed by obtaining a set of phase-shifted quantum defects $\tilde{\mu}_i$ and a transformed reaction matrix $\underline{\kappa}'_{cc}$ whose elements can be written in the form

$$\kappa'_{ij} = r_{ij} + i\vec{R}_i.\vec{R}_j, \tag{2.74}$$

with $r_{ii}=0$. As detailed by Lecomte (1987), the nondiagonal real r_{ij} elements describe the direct coupling between the closed channels and can be diagonalized within a set of ''degenerate'' channels converging to the same threshold. The N_c vectors $\vec{R}_i$ involved in the imaginary part of the κ' matrix describe the coupling between the N_c closed channels and N_c effective continua. When the resonances pertaining to the ith channel are well separated from the others, $\tilde{\mu}_i$ and $|\vec{R}_i|^2$ characterize the positions and scaled autoionizing widths γ_i of the resonances in channel i. One has, in a.u.

$$\gamma_i = \Gamma_i(\nu_i)^3 = 2|\vec{R}_i|^2/\pi, \tag{2.75}$$

where Γ_i is the full width at half maximum for autoionization and ν_i is the effective quantum number in channel i. The explicit construction of the effective continua in terms of the jj-coupled open fragmentation channels permits the branching ratios for autoionization toward each open channel to be calculated for each closed channel. In addition, the calculation of the photoionization spectra requires dipole matrix elements connecting the initial level to the closed channels component and to the effective continua, as well as one additional dipole element corresponding to the excitation of the $N_o - N_c$ noninteracting continua.

E. Frame transformations

The key quantity characterizing the scattering and photoabsorption spectra of a multichannel system is the

smooth, short-range scattering matrix $\underline{S}$ (or the equivalent reaction matrix $\underline{K}$), and a set of smooth dipole transition amplitudes $\underline{d}$. The short-range scattering matrix $\underline{S}$ reflects a great deal of the system's dynamics; in fact Heisenberg (1943) regarded the physical scattering operator $\underline{S}^{\rm phys}$ as even more fundamental than the Hamiltonian itself. It is certainly true that essentially any interaction appearing in the Hamiltonian will be reflected at some level in the scattering matrix. For instance, the effect of a sufficiently small term in the Hamiltonian can be described by first-order perturbation theory, in which the matrix element of a perturbation V is proportional to a corresponding element of the reaction matrix (Rodberg and Thaler, 1967):

$$K_{ij} \approx -\pi \left\langle \frac{1}{r}\Phi_i f_i | V | \frac{1}{r}\Phi_j f_j \right\rangle + O(V^2). \tag{2.76}$$

Consequently, much quantum-mechanical intuition, which is initially sharpened for most students in the context of energy-level calculations, can be directly carried over and used to develop intuition about multichannel scattering processes and spectra. For example, if the dominant interactions present in the Hamiltonian are diagonal in a particular angular momentum coupling scheme, we expect the scattering matrix to be block diagonal in that same coupling scheme. The physical consequences of this viewpoint were first used profitably by Fano (1970) in the context of H_2 photoabsorption. Fano, Jungen, and their co-workers have been instrumental in developing and extending this picture to systematically describe a broad range of problems in atomic and molecular physics. (See, for example, Jungen and Dill, 1980; Raoult and Jungen, 1981; Greene and Jungen, 1985; Fano and Rau, 1986)

The basic idea of the recoupling frame transformation can be conveyed by developing a specific example. Consider the photoabsorption spectrum of a light atom. Because spin-orbit and other fine-structure perturbations are particularly weak in light atoms, most of the important physics is determined by the electrostatic interaction. Exchange is important, because Pauli antisymmetrization affects each symmetry differently. To the extent that electrostatic interaction and Pauli exchange effects dominate, the energy eigenstates can be characterized by L and S, the total orbital and spin angular momenta respectively, of all atomic electrons, since $\vec{L}^2$ and $\vec{S}^2$ both commute with the electrostatic Hamiltonian.

One might be tempted under these circumstances to complete the entire photoabsorption calculation assuming validity of LS coupling throughout. However, the basic logic developed by Lu (1971), and more systematically by Lee and Lu (1973), shows how frame transformation methods describe a large class of fine-structure effects. These effects are surprisingly important and nonperturbative in certain regions of the spectrum, even in light atoms. For definiteness, consider photoionization of the $^1S^e$ ground state of a two-electron atom such as beryllium, in an energy range that extends to final states close to the $Be^+(2p)$ ionization threshold. In a standard LS-coupling approximation, an electric dipole photon excites only $^1P^o$ final states. Focusing just on the ionization channels attached to the $2p$ ionic state, two relevant channels are specifically excited, namely $2pns\,^1P^o$ and $2pnd\,^1P^o$. Because the $2p$ ionic state would (artificially) have no spin-orbit splitting in a strict LS-coupled nonrelativistic calculation, the escaping s- or d-wave electron will move outward toward the detector at infinity if the final-state energy E lies above the $2p$ threshold E_{2p}. If the energy lies below, $E<E_{2p}$, a pattern of $2pns\,^1P^o$ and $2pnd\,^1P^o$ Rydberg levels will be formed just below the $2p$ threshold.

Now consider the physics of photoelectron escape from the real ionic $2p$ levels, which have a fine-structure splitting, $E_{2p_{3/2}}=E_{2p_{1/2}}+6.6\ \text{cm}^{-1}$. This splitting is tiny on the scale of the strongest interactions present in the atomic Be Hamiltonian. For reference, the exchange splitting between the $^1P^o$ and $^3P^o$ $2s2p$ levels is more than 21 000 cm^{-1}. While the fine-structure splitting thus seems to be negligible in comparison, at final-state energies close to the $Be^+(2p)$ thresholds it can have a nonperturbative effect on the asymptotic wave functions. With the atom at a final-state energy E, the electron escapes from these two possible ionic energy levels $E_{2p_{1/2,3/2}}$. Owing to energy conservation, the escaping electron energy is asymptotically different depending on the residual ionic energy,

$$\epsilon_{2p_{1/2}}=E-E_{2p_{1/2}}, \quad \epsilon_{2p_{3/2}}=E-E_{2p_{3/2}}. \tag{2.77}$$

The effect of these different energies of photoelectron escape in the two different channels can be summarized succinctly in terms of the de Broglie phase difference between the corresponding wave functions. A WKB analysis, which neglects the short-range phase contributions from electron correlations, gives for this phase difference as a function of r:

$$\Delta\phi = \int^r \left(\sqrt{2\epsilon_{3/2}+\frac{2}{r'}} - \sqrt{2\epsilon_{1/2}+\frac{2}{r'}} \right) dr' \approx \frac{\sqrt{2}}{3} r^{3/2} \Delta E. \tag{2.78}$$

(For the purposes of this qualitative analysis, we ignore the Langer-corrected centrifugal term and the small difference between the classical turning points at small distances.) Figure 3 shows how this small energy difference affects the corresponding radial ($l=0$) wave functions at a final-state energy in between the $2p_{1/2}$ and $2p_{3/2}$ threshold, such as $\epsilon_{2p_{3/2}}=-\epsilon_{2p_{1/2}}$. The key thing to note here is the way the wave-function components attached to the different fine-structure thresholds remain locked tightly in phase up to a radius $r_{\rm crit}$ of about 1000 a.u. But beyond that radius, the two orbitals lose their phase coherence and at larger distances they act like independent channels. Any property relating to electron motion at distances larger than 10^3 atomic units for this energy range of atomic Be can be expected to show nonpertur-

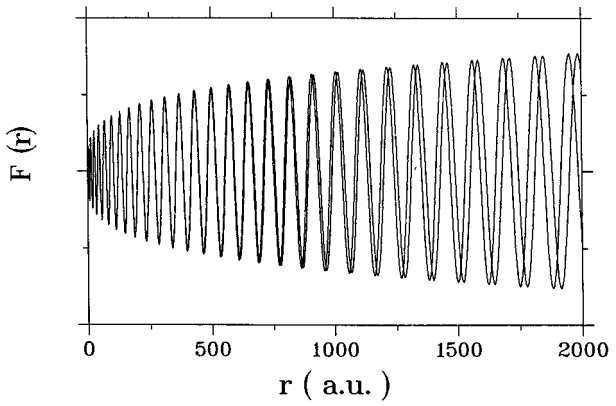

FIG. 3. Spin-orbit frame-transformation example with wave functions in two fine-structure-split Coulombic channels. Radial s orbitals of Be calculated at an energy equidistant from the $2p_{1/2}$ and $2p_{3/2}$ thresholds, i.e., for $\epsilon_{2p_{1/2}}>0$ and $\epsilon_{2p_{3/2}}<0$ such that $\epsilon_{2p_{3/2}}=-\epsilon_{2p_{1/2}}$.

bative effects of the spin-orbit interaction. One such property is the spectroscopy of high-lying $2pns$ Rydberg levels just below the $2p$ ionic threshold. Distances of this magnitude translate into principal quantum numbers in the range of $n_{\rm crit}\approx\sqrt{1000}\approx 30$. This critical value of n marks a transition region beyond which spin-orbit interaction is especially strong. An energy argument confirms this: the difference between the $2pns\ ^1P^o$ and $^3P^o$ energy levels should be approximately $(\Delta\mu)n^{-3}$ a.u. Here, $\Delta\mu$ is the difference between singlet and triplet quantum defects for this series, and its magnitude is expected to be less than 1. Simple arithmetic shows that $n\approx 30$ likewise marks the transition region in energy, where the exchange interaction becomes smaller than the ionic fine-structure splitting of 6.6 $\rm cm^{-1}$.

The observed capability (Fig. 3) of radial fine-structure components to remain phase locked at small distances provides the key toward a formulation of these nonperturbative spin-orbit effects. The first key is to recognize that LS-coupled asymptotic channels are fundamentally incapable of describing the fine-structure-dependent phase evolution depicted in Fig. 3. In particular, the asymptotic phase depends on J_c, the total angular-momentum quantum number of the ionic residue, with values $\frac{1}{2}$ and $\frac{3}{2}$ in this example. Because $\vec{J}_c^{\,2}$ commutes with neither $\vec{L}^2$ nor $\vec{S}^2$, LS-coupled channels can never suffice in the region $r>r_{\rm crit}$. The asymptotic channel indices i must therefore include J_c. Other than this absolute requirement, considerable flexibility remains in the choice of the other channel quantum numbers. For different systems, or for different observables, different asymptotic coupling schemes may be advantageous, although they will all produce the same spectra in the frame-transformation method. Examples of typical coupling schemes include J_cj-coupled channels (usually abbreviated as jj-coupled) $|i\rangle=|n_c(s_cl_c)J_c(sl)jJM\rangle$, J_cK-coupled channels $|i\rangle=|n_c[(s_cl_c)J_cl]KsJM\rangle$ (denoted as pair coupling, jK or jl coupling) and J_cJ_{cs}-coupled channels $|i\rangle=|n_c[(s_cl_c)J_cs]J_{cs}lJM\rangle$. For these three cases, a standard angular-momentum recoupling, diagonal in the total J and M, relates the asymptotic channels to the LS-coupled channel functions $|\bar{i}\rangle=|n_c(s_cs)S(l_cl)LJM\rangle$.

The recoupling formulas needed can be found in Sobel'man (1972) or other standard references such as Zare (1988). In the case of J_cj coupling, the real orthogonal transformation matrix $\underline{X}_{i\bar{i}}$ involves the recoupling matrix element $\langle(s_cl_c)J_c(s\bar{l})j|(s_cs)S(l_cl)L\rangle^{(J)}$. (A Kronecker delta function is implied in all channel quantum numbers other than J_cj,SL.) In problems in which the dominant interactions are the ionic fine-structure and multipole effects on the distant electron, the $i\equiv J_cK$ coupling scheme leads to short-range scattering matrices $\underline{S}$ that are more nearly diagonal. In this scheme the recoupling matrix $\underline{X}_{i\bar{i}}$ is $\langle[(s_cl_c)J_cl]Ks|(s_cs)S(l_cl)L\rangle^{(J)}$. An analogous formula is readily derived for the J_cJ_{cs} coupling scheme, which is advantageous, for instance, in calculation of photoelectron angular distributions because both $\vec{J}_c^{\,2}$ and $\vec{J}_{cs}^{\,2}$ commute with the observed ejection angle. We repeat, however, that the use of all three of these coupling schemes leads to identical results in a description of fine-structure effects by frame-transformation techniques. In fact, the true wave function is not assumed to be a single term in LS coupling, jj coupling, nor in any other coupling scheme. Rather, a linear combination of the different channels is ultimately selected in the course of solving the quantum-defect equations at each energy. To connect to a more familiar point of view, the MQDT description of spin-orbit effects using a recoupling frame transformation gives results similar to an intermediate-coupling calculation in traditional spectroscopy, for levels lying far below all ionization thresholds. However the MQDT version automatically includes continuum and high-Rydberg interactions that are difficult to describe in traditional intermediate-coupling calculations. Importantly, and perhaps surprisingly, the dynamics are correctly described even when fine-structure effects are ignored completely when calculating the short-range scattering matrix $\underline{S}_{LS}$, which is block diagonal in LS coupling.

The complete frame-transformation procedure requires one additional key point. In fact, the recoupling of the short-range matrix $\underline{S}_{LS}$ just described,

$$\underline{S}_{jj}=\underline{X}\,\underline{S}_{LS}\underline{X}^{\dagger}, \tag{2.79a}$$

and of the associated dipole matrix elements on the left-hand side of Eq. (2.57),

$$\underline{d}_{jj}=\underline{X}\,\underline{d}_{LS}, \tag{2.79b}$$

by themselves have no effect whatsoever on the calculated spectra. This can be seen by inspecting Eqs. (2.58) and (2.59), as the unitary transformation drops out of the total cross section. Importantly, in the spirit of Fig. 3, it is crucial to use the experimental J_c-dependent ionization thresholds when calculating the long-range diagonal phase matrix $e^{2i\underline{\beta}}$ needed to evaluate the MQDT formulas (2.50) and (2.58). A further note of clarification concerns the dipole matrix elements $\underline{d}_{LS}$ in Eq. (2.79b):

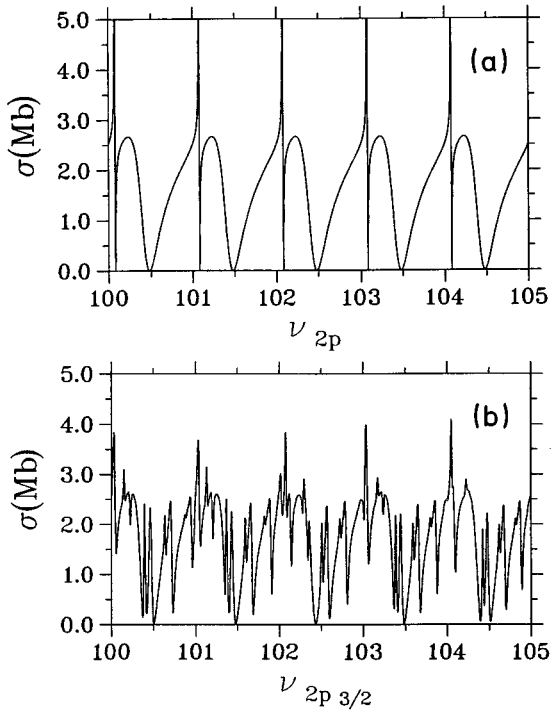

FIG. 4. Be photoionization spectrum near the $2p_j$ thresholds: (a) all fine-structure effects are neglected in the eigenchannel R-matrix and MQDT calculations performed in LS coupling; (b) results obtained with scattering and dipole matrices determined by LS-coupled R-matrix calculations combined with a recoupling jj-LS frame transformation and the use of experimental ionization $2p_j$ thresholds in the MQDT calculations.

these are understood to be coupled reduced dipole matrix elements determined from an LS-coupled calculation, i.e., $\underline{d}_{LS} \equiv \langle (SL)J || d^{(1)} || (S_0 L_0) J_0 \rangle$.

On top of the changed values of $e^{2i\beta_i}$, in different closed fine-structure channels, an equally important aspect is the fact that use of experimental thresholds affects the partitioning between open and closed channels at any chosen energy E. That is, before inclusion of fine-structure effects, the channels attached to the $2p$ threshold are either all open or all closed. Once the splitting into $2p_{1/2}$ and $2p_{3/2}$ thresholds is built into the calculation by using their experimental energies, a new regime arises at energies between the two thresholds where the $2p_{3/2}nl$ channels are closed while the $2p_{1/2}\epsilon l$ channels are open. In this energy range, a completely new physical process occurs that cannot be described in pure LS coupling, namely autoionization by a spin flip. Although it occurs in only a tiny energy range for this Be example, it can happen over larger energy ranges in other systems. In such energy regimes the physics is affected qualitatively and nonperturbatively by the inner-electron spin-orbit interaction.

These effects are illustrated in Fig. 4, which depicts the photoionization cross section of Be at final-state energies just below the $2p_{1/2}$ threshold. Neglecting all fine-structure effects throughout the calculation leads to the qualitatively incorrect spectrum shown in Fig. 4(a). Figure 4(b) shows how LS-coupled scattering and dipole matrices, combined with a recoupling jj-LS frame transformation and the use of experimental ionic $2p$ thresholds in the MQDT calculation, predict a rich multichannel spectrum. This particular system has not been studied experimentally at such high resolution, but such recoupling frame transformations are usually quite accurate, as will be seen in the comparisons of Sec. IV.

To interpret the dynamics involved in spectra like that in Fig. 4(b), we return to a heuristic time-dependent viewpoint. A light pulse incident on the $^1S^e$ ground state at time $t \approx 0$ excites an outgoing wave front of purely $^1P^o$ character at small distances. The outgoing $2pns\,^1P^o$ wave front is sheared into its two fine-structure components that accumulate radial phase at slightly different rates. If, in fact, the final-state energy reaches the small range between the fine-structure thresholds, eventually the portion of the packet in the closed $2p_{3/2}ns$ channel will be reflected back toward the nucleus, whereas the portion in the open $2p_{1/2}\epsilon s$ channel can continue outward to infinity uninhibited. This differential reflection, i.e., that occurring only for one fine-structure component $J_c = \frac{3}{2}$, couples the other LS symmetries into the photoabsorption process even though they are not connected to the ground state by an electric dipole matrix element. For this reason, the spectra in this energy range are sensitive also to the $^3P^o$ symmetry scattering matrix, as the wave front returning to the nucleus will have components in all relevant LS symmetries. In the case of the $2pnd$ channels, not only $^{1,3}P^o$ symmetries are coupled, but also the $^3D^o$ symmetry, whose Rydberg levels converging to the $2p$ threshold would have been true bound levels for our *gedanken* Be atom without spin-orbit interactions. The frame transformation couples the $2pnd\,^3D^o$ levels to the $L = 1^o$ channels in the real atom, thereby permitting these states to autoionize.

Note also that when the energy is above all thresholds relevant in the problem—just above $Be^+(2p_{3/2})$ in our example—the frame transformation has no effect on the total cross section, since there are no longer any β_i occurring in which to use the experimental thresholds. Our time-dependent argument shows why this is reasonable, namely because when all channels are open, no differential reflection is expected to occur semiclassically, and the wave fronts in the fine-structure channels can proceed outward indefinitely to infinity. In this energy range where all channels are open, the total photoionization cross section coincides with that which would be obtained in a purely LS-coupled calculation. [This is not generally true for long-range fields other than the attractive Coulomb field, owing to the energy-dependent parameters $\mathcal{A}$ and $\mathcal{G}$ discussed in the context of Eq. (2.15).] Finally, the dynamics of recoupling frame transformations have been discussed elsewhere by Watanabe *et al.* (1984), who point out that a fairly well-defined radius can be identified where the shearing of the $^1P^o$ wave function into its fine-structure components occurs. This is the radius at which a Landau-Zener-type transition

occurs, and it is roughly where the exponentially-decaying exchange energy is equal to the spin-orbit interaction energy.

The preceding considerations demonstrate that effects of the spin-orbit interaction on a highly excited Rydberg or continuum electron are felt primarily at large distances. This may seem surprising initially, since one normally thinks of the spin-orbit interaction as a short-range interaction, owing to the r^{-3} dependence of the spin-orbit term in the Hamiltonian, which is strongest near the nucleus. This apparent contradiction clarifies the origin of spin-orbit effects on atomic Rydberg electrons. They are mostly caused by the dephasing of different spin-orbit radial components as an indirect consequence of energy conservation, reflecting the spin-orbit splitting of the residual ionic core. In fact, the direct effect of the Rydberg electron's spin-orbit term in the Hamiltonian can usually be neglected. Examples in Sec. IV will probe the accuracy and limitations of this viewpoint.

F. Semiempirical analysis of multichannel spectra

The semiempirical approach of multichannel quantum-defect theory, in which short-range scattering parameters are adjusted to reproduce a particular set of experimental data, has enjoyed remarkable success in interpreting complex multichannel spectra. A great deal of empirical analyses were carried out using the eigenchannel MQDT formalism introduced by Fano and coworkers (Fano, 1970; Lu and Fano, 1970; Lu, 1971; Lee and Lu, 1973). The physical solutions and observables were calculated in terms of the μ_α and $U_{i\alpha}$ smooth scattering parameters obtained by diagonalizing the short-range reaction matrix of Eq. (2.35), and of the short-range dipole matrix elements D_α. Compared to the previous semiempirical analyses based on the Seaton's formalism, two aspects of the eigenchannel MQDT formalism greatly enhanced the power of such analyses. First, Fano and Lu (Fano, 1970; Lu and Fano, 1970; Lu, 1971) introduced a graphical method, based on the use of the so-called Lu-Fano plots, which has proved extremely useful in analyzing multichannel spectra. The second key development resulted from the introduction of the frame transformation between the short-range eigenchannels α and the long-range fragmentation channels i (Fano, 1970).

Earlier semiempirical studies dealt with channel interaction between Rydberg series converging to two different ionization limits. The first calculation (Fano, 1970) concerned the channel interaction between the $J=1$ odd-parity $1snp$ Rydberg series of H_2 converging to the $N^+=0$ and $N^+=2$ rotational levels of H_2^+, which were observed in the photoabsorption spectrum of H_2. Then diverse experimental data (energy positions and oscillator strengths in the discrete and autoionizing regions) observed in the photoabsorption spectra of Xe (Lu, 1971) and Ar (Lee and Lu, 1973) were interpreted in a compact form using the same procedure. The method was then applied to the photoabsorption spectra of

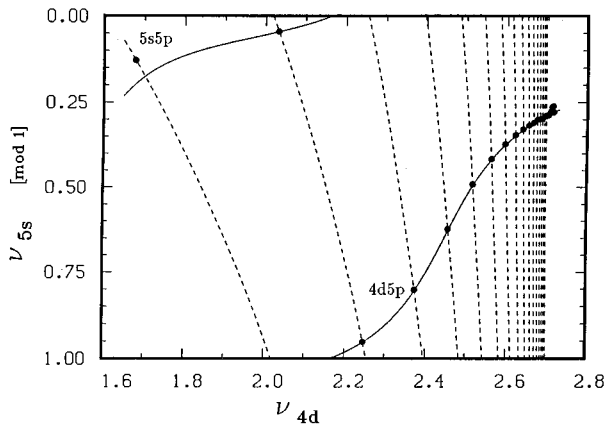

FIG. 5. Lu-Fano plot of the odd-parity $^1P_1^o$ bound levels of Sr, comparing experimental values—depicted by solid points—with the Lu-Fano plot of Eq. (2.81b), calculated using the eigenquantum defects μ_1, μ_2 and the mixing angle θ fitted to the experimental data by Armstrong *et al.* (1979). The theoretical energy levels are obtained at the intersections of the Lu-Fano plot and of the curve (dashed line) $-\nu_{5s}$ (mod 1) = f(ν_{4d}) defined by Eq. (2.80). The Sr $5snp$ $^1P_1$ Rydberg series is perturbed by the $4d5p$ $^1P_1$ doubly excited level.

carbon-group elements Si, Ge, Sn, and Pb (Brown *et al.*, 1977a, 1977b, 1977c; Ginter and Ginter, 1986; Ginter *et al.*, 1986). Simultaneously, in connection with the developmen t of laser spectroscopy, the method was extended to handle more complex spectra involving interacting Rydberg series converging to more than two ionization limits and numerous perturbed Rydberg series of alkaline earths were successfully interpreted (Armstrong *et al.*, 1977; Esherick, 1977; Lu, 1977; Aymar *et al.*, 1978; Armstrong *et al.*, 1979; and references in Aymar, 1984a). Since then, the analysis of atomic and molecular spectra has increasingly utilized this empirical approach but it is out of the scope of this review to quote all the corresponding studies.

Because the semiempirical fitting procedure based on the eigenchannel formalism of multichannel quantum-defect theory is described in detail in the above-mentioned papers, we will sketch only the main points and begin by illustrating a Lu-Fano plot in a simple two-channel system. Figure 5 deals with the perturbation of the Sr $5snp$ ^1P Rydberg series by the $4d5p$ ^1P doubly excited level, the lowest member of the $4dnp$ ^1P series converging to the upper $4d$ ionization limit. All $^1P^o$ bound levels are represented in a compact form by plotting them in the plane $-\nu_{5s}$ (mod 1) against ν_{4d}. The effective quantum numbers ν_{5s}, and ν_{4d} relative to the spin-orbit-averaged $4s$ and $4d$ limits are connected through the relation

$$E=I_{5s}-\frac{R_y}{\nu_{5s}^2}=I_{4d}-\frac{R_y}{\nu_{4d}^2}, \tag{2.80}$$

where R_y is the mass-corrected Rydberg constant. (Note that E, I_{5s}, and I_{4d}, expressed in cm^{-1}, are relative to the $5s^2$ ground state.) All experimental points (full points) except that corresponding to the lowest $5s5p$

level lie on the Lu-Fano plot (full line). Theoretically, this curve represents the solution of Eq. (2.62), which, in terms of eigenchannel short-range scattering parameters, is

$$\det|U_{i\alpha}\sin\pi(\nu_i+\mu_\alpha)|=0. \tag{2.81a}$$

For a two-channel problem, Eq. (2.81a) gives

$$\det\begin{pmatrix}\cos\theta\,\sin\pi(\nu_1+\mu_1) & \sin\theta\,\sin\pi(\nu_1+\mu_2)\\ -\sin\theta\,\sin\pi(\nu_2+\mu_1) & \cos\theta\,\sin\pi(\nu_2+\mu_2)\end{pmatrix}=0, \tag{2.81b}$$

where μ_1 and μ_2 are the two quantum-defect parameters and the angle θ characterizes the (2×2) orthogonal $U_{i\alpha}$ matrix.

The theoretical curve can be plotted continuously even though the true spectrum is discrete. Therefore, this approach determines the quantum defect even at energies at which there is no level because Eq. (2.80) is disregarded. The Lu-Fano plot depends only on the dynamical smooth scattering parameters, which are nearly independent of the energy. Thus the Lu-Fano plot can be viewed as a way to highlight the short-range dynamics common to all the levels. The theoretical energy levels are obtained at the intersections of the Lu-Fano plot $-\nu_{5s}\ (\mathrm{mod}\ 1)=f_1(\nu_{4d})$ defined by Eq. (2.81b) and of the curve (dashed line) $-\nu_{5s}\ (\mathrm{mod}\ 1)=f_2(\nu_{4d})$ defined by Eq. (2.80), where $-\nu_{5s}$ and ν_{4d} depend parametrical on the energy. The Lu-Fano plot of Fig. 5 was calculated using the eigenquantum defects $\mu_1=0.892$, $\mu_2=0.491$ and the mixing angle $\theta=0.196\pi$ fitted to the experimental data by Armstrong *et al.* (1979). The deviation between theory and experiment occurring for the $5s5p$ level results from the fact that Armstrong *et al.* (1979) introduced only a linear energy dependence for the μ_α whereas, as documented in Sec. IV, a more complicated energy dependence exists. It should be noted here that the Lu-Fano plot of Fig. 5 can be extended above the $5s$ threshold provided the effective quantum number ν_{5s} is replaced by δ_{5s}/π where δ_{5s} represents the phase shift in the $5s\epsilon p$ open channel.

From a practical point of view, for a two-limit problem, the intersections of the diagonal straight line $\nu_{5s}=\nu_{4d}$ with the Lu-Fano curve directly give the values of the two μ_α parameters. Moreover the slope of the Lu-Fano curve at each of these intersections is related to the angle θ (Fano, 1970). The gap between the two branches gives a visual estimation of the channel interaction strength. For an almost unperturbed $5snl$ Rydberg series characterized by an almost constant quantum defect μ, one should expect a sharp rise of $-\nu_{5s}$ (mod 1) near the perturbing level in order to keep $\mu=n-\nu_{5s}$ constant. The marked departure from a step function visible in Fig. 5 reflects a strong channel interaction. A quantitative measure of the channel coupling is given (Greene, 1981) by the S-matrix element

$$|S_{12}|^2=\sin^2 2\theta\,\sin^2\pi\Delta\mu, \tag{2.82}$$

which gives the probability that the Rydberg electron will scatter from one channel to the other when it collides with the ionic core. The fitted values $\Delta_\mu=|\mu_1-\mu_2|=0.401$ and $\theta=0.196\pi$ are not too far from the values $\Delta_\mu=0.5$ and $\theta=\pi/4$, which correspond to the strongest possible channel interaction.

Lu-Fano plots drawn through experimental points help the experimentalists in spectral analysis of perturbed series. It is possible to detect channel interactions and to estimate their strength without any calculation. However, more quantitative information on the identification of interacting levels and on the strengths of channel interactions requires the determination of the smooth scattering parameters. The fitting procedure consists of adjusting the parameters so that the theoretical and experimental energies agree. The determination of the channel coefficients $Z_i^{(n)}$ of Eq. (2.64), which measure the fractional admixture of each fragmentation channel i into a particular level n allows one to label the levels. In the Sr case discussed above, the empirical MQDT treatment has confirmed the suggestion of Garton and Codling (1968) concerning the identification of the $4d5p\ ^1P$ perturber: this level must be identified with the $5s8p\ ^1P$ level listed by Moore (1949).

For systems in which spin-orbit effects cannot be neglected (rare gases, heavy alkaline earths), the fragmentation channels should be described in jj or jK coupling. The number N of interacting channels corresponding to given J and parity can be large. The number of scattering parameters becomes important, the unitary $U_{i\alpha}$ matrix depending on $N(N-1)/2$ independent parameters. The use of the jj-LS frame transformation helps to greatly reduce the number of adjustable parameters. The semiempirical analyses of the Ar absorption spectrum (Lee and Lu, 1973) and of heavy alkaline earths (Aymar *et al.*, 1978; Armstrong *et al.*, 1979 Aymar and Robaux, 1979) introduced a set of LS-coupled channels $\bar{\alpha}$ and factorized the $U_{i\alpha}$ matrix, so that $U_{i\alpha}=\Sigma_{\bar{\alpha}}X_{i\bar{\alpha}}V_{\bar{\alpha}\alpha}$. The $X_{i\bar{\alpha}}$ matrix corresponding to the geometric jj-LS transformation accounts for most of the angular recoupling effects. Assuming that the short-range Hamiltonian is almost diagonal in LS coupling, the $V_{\bar{\alpha}\alpha}$ matrix elements are fitted to the experimental data by minimizing the departure of the $V_{\bar{\alpha}\alpha}$ matrix from the unit matrix. From a practical point of view, the $V_{\bar{\alpha}\alpha}$ matrix elements are often expressed in terms of generalized Euler angles, each of them describing a rotation between two particular channels (Lee and Lu, 1973). The empirical analysis of the odd-parity $J=1$ spectrum of Ar (Lee and Lu, 1973) showed that the jj-LS frame transformation accounts for much of the channel interaction. This was confirmed by the *ab initio* calculation performed by Lee (1974a) using the iterative eigenchannel R-matrix variational approach, the empirical and *ab initio* scattering parameters being in good agreement.

The graphical method of Lu-Fano is most useful for two-limit systems with a small difference between the two ionization limits. In such a case, the Rydberg series

converging to the lower limit I_1 is periodically perturbed by members of the series converging to the higher limit I_2. The clear pattern of periodicity not only in ν_1, but also in ν_2, can be easily visualized when data are plotted with respect to ν_2 (mod 1) instead of ν_2 itself. When the energy dependence of the short-range scattering parameters is negligible, all data drawn inside a $-\nu_1$ (mod 1) against ν_2 (mod 1) unit square come to lie on a single curve. This curve represents in a compact form all the perturbations arising from the interaction between the channels (see, for example, Lee and Lu, 1973, and Fano and Rau, 1986).

Such a situation occurs for Rydberg series converging to the doublet levels of a spin-orbit split core: Rydberg series of rare gases converging to the $p^5\ ^2P_{3/2,1/2}$ thresholds (Lu, 1971; Lee and Lu, 1973); series of the carbon-group elements converging to the $s^2p\ ^2P_{1/2,3/2}$ thresholds (Brown *et al.*, 1975, 1977a, 1977b, 1977c; Ginter and Ginter, 1986; Ginter *et al.*, 1986); autoionizing Rydberg series of Ba converging to the $5d_{3/2,5/2}$ or $6p_{1/2,3/2}$ thresholds (Aymar *et al.*, 1983; Gounand *et al.*, 1983). Note that the autoionizing series can be treated as bound series providing the autoionizing widths are small, the treatment being, of course, restricted to the positions of resonances. The advantages related to the periodicity of perturbing levels and to the use of the *jj*-*LS* frame transformation were fully exploited in all these studies.

Now we turn again to the analyses of the perturbations of bound Rydberg series m_0snl of alkaline-earth atoms by doubly excited levels, which are the lowest members of the Rydberg series converging to the $(m_0-1)d$ or/and m_0p thresholds ($m_0=4, 5, 6$ for Ca, Sr, and Ba, respectively). The semiempirical approach has helped greatly in analyzing much energy data obtained by laser spectroscopy measurements, allowing one to identify the newly observed levels and to analyze quantitatively the channel interactions. Moreover, various observables other than energy (lifetimes, g_J Landé factors, isotope shifts, hyperfine-structure measurements) provided by high-resolution laser spectroscopy were also interpreted semiempirically (see Aymar, 1984a, 1984b). In spite of its clear success, the semiempirical method encountered several difficulties:

(1) At the low end of each Rydberg series, the smooth scattering parameters acquire a strong energy dependence. The lowest levels of each m_0snl series cannot be correctly described empirically, even when a linear dependence is invoked for some parameters (see the $5s5p$ level on Fig. 5). More critical is the fact that it then becomes difficult and even sometimes impossible to identify unambiguously the low-lying perturbers by taking into account their Rydberg periodicity. The main difficulties arising for the $(m_0-1)d^2$ and m_0p^2 isolated perturbers of even-parity series will be further addressed in Sec. IV.

(2) For systems involving a large number of interacting Rydberg series, assumptions have to be made to reduce the number of free parameters. They mainly concern the construction of the $U_{i\alpha}$ matrix. As already mentioned, this matrix is generally constructed by assuming that the α channels are nearly LS coupled. Assumptions on the strength of channel interactions permit one to reduce the number of free parameters introduced in the fitting procedure by fixing the values of some angles generating the $V_{\tilde{\alpha}\alpha}$ matrix at zero. In particular, the interactions between some perturbing channels are neglected.

(3) The main difficulties arise from the fact that the energy values do not contain sufficient information to determine the complete $U_{i\alpha}$ matrix. More precisely, when more than one channel converges onto a given threshold, energies permit one to determine only some combinations of $U_{i\alpha}$ elements that are invariant under orthogonal transformation of these channels (Lu, 1971; Aymar, 1984a, 1984b). Experiments that distinguish between these channels are necessary to get the full matrix. Aymar (1984a, 1984b) discussed how g_J Landé factors and mainly hyperfine-structure data have been used to extend the Ba multichannel-quantum-defect-theory models deduced from energy data. In this way, the singlet-triplet mixing between $6snl\ ^1L$ and ^3L Rydberg levels have been correctly described (Aymar, 1984a, 1984b; Post *et al.*, 1986). In Sec. IV we will discuss the validity of the assumptions made in the semiempirical MQDT method and show that the difficulties arising in this approach are bypassed by calculating the scattering parameters with the R-matrix method.

In addition to the early studies of the photoabsorption spectra of rare gases between the $^2P_{3/2}$ and $^2P_{1/2}$ thresholds (Lu, 1971; Lee and Lu, 1973), a few semiempirical MQDT simulations of autoionizing resonances were performed with the eigenchannel MQDT formalism (see, for example, Aymar *et al.*, 1982; Gounand *et al.*, 1983). However, during the last two decades, experimental data on autoionizing resonances of alkaline earths have been obtained mainly by using the experimental isolated-core excitation method and the semiempirical MQDT simulations of the corresponding data were primarily performed using the phase-shifted MQDT approach of Cooke and Cromer (1985). The alternative MQDT parameters, quantum defects $\tilde{\mu}_i$ and matrix elements κ'_{ij} of Eq. (2.74) referring to the fragmentation channels can be more easily extracted from the observation than short-range eigenchannel MQDT parameters. Indeed, as is stated in Sec. II.D.3, for an isolated autoionizing Rydberg series, the positions of the resonances are characterized by the quantum defects $\tilde{\mu}_i$ and the scaled autoionizing widths are related to the κ'_{ij} matrix elements. An impressive number of experimental data on autoionizing Rydberg series were fitted using this approach (see, for example, Xu *et al.*, 1986; Abutaleb, de Graff, Ubachs, and Hogervorst, 1991; Hieronymus *et al.*, 1990; Jones *et al.*, 1991b; de Graaff *et al.*, 1992, and references therein). However, most of the MQDT models adjusted to a particular set of measurements introduced numerous assumptions in order to reduce the number of free parameters. A limited number of closed channels was accounted for and generally each closed channel was assumed to be coupled to only one effective continuum. Moreover, the fragmentation

channels were assumed to be purely jj- or jK-coupled and the energy dependence of the MQDT parameters was frequently neglected. These models permit a good simulation of the observations but have little or no predictive power.

III. EIGENCHANNEL R-MATRIX APPROACH

The preceding section showed how it is useful to characterize complicated spectra in terms of the smooth short-range scattering parameters of multichannel quantum-defect theory. While these have been obtained semiempirically by simply fitting to experimental spectra in a number of problems, the full power of this theoretical formulation emerged after when it became possible to extract these scattering parameters from *ab initio* or nearly *ab initio* calculations. In principle, a host of different theoretical approaches can be used to calculate the scattering matrix $\underline{S}$ and relevant dipole matrix $\underline{d}^S$. In the multichannel spectroscopy viewpoint, the main idea is to solve the time-independent Schrödinger equation at a chosen energy subject to scattering-type boundary conditions at large distances, which must be applied in all open and closed channels. Such calculations have been performed to treat argon photoabsorption by Lee (1974a), using an iterative form of the eigenchannel R-matrix approach developed by Fano and Lee (1973). Accurate MQDT parameters were subsequently calculated by Johnson *et al.* (1980), near the lowest ionization threshold(s) for all of the rare-gas atoms using the relativistic random-phase approximation, with the interesting difference that a relativistic version of multichannel quantum-defect theory (Zilitis, 1977; Johnson and Cheng, 1979; Johnson and Lin, 1979; Lee and Johnson, 1980; Chang, 1993; Goldberg and Pratt, 1987) was adopted in place of the nonrelativistic approach discussed in Sec. II. These calculations successfully accounted for numerous photoionization experiments in the rare-gas atoms, including integrated total and partial cross sections in addition to the angular distribution and spin polarization of the photoelectrons. Fink and Johnson (1990) used a time-dependent Dirac-Fock approach that is closely related to the relativistic random-phase approximation to predict Lu-Fano plots for the rare-gas atoms with $J=0,2$ close to the lowest threshold. The nonrelativistic random-phase approximation could similarly be applied to calculate the MQDT scattering parameters and photoabsorption amplitudes including closed as well as open channels, but apparently no nonrelativistic random-phase approximation calculations have yet been carried out in this manner.

While these and other methods such as the hyperspherical close-coupling approach (Greene, 1981; Watanabe, 1982, 1986; Tang *et al.*, 1992) and the Schwinger variational principle (Goforth *et al.*, 1987; Goforth and Watson, 1992) are capable of solving the Schrödinger equation and extracting the desired MQDT parameters, noniterative R-matrix methods appear to be among the most efficient. The majority of the nearly *ab initio* calculations of quantum-defect parameters have utilized a noniterative reformulation (Greene, 1983; Le Rouzo and Raseev, 1984) of the Fano-Lee eigenchannel R-matrix method (Fano and Lee, 1973; Lee, 1974a; Raseev and Le Rouzo, 1983). Because it has been used so extensively and successfully in recent years for such calculations, this particular (noniterative eigenchannel) formulation of the R-matrix approach will be the focus of our discussion in this section. [It should be noted that, like the Wigner-Eisenbud form of the R-matrix method, the eigenchannel R-matrix method was first introduced in nuclear physics to study resonance reactions (Danos and Greiner, 1966; Mahaux and Weidenmüller, 1968).] On the other hand, we stress that many other methods are available and have comparable strengths. A notable example is the Wigner-Eisenbud (Wigner and Eisenbud, 1947) form of the R-matrix method, which has many of the same advantages as the eigenchannel variant, provided a Buttle correction (Buttle, 1967) is introduced to offset its poor convergence properties. This method has been extensively used by the Belfast group (Burke and Robb, 1975; Berrington *et al.*, 1978); for references the readers are referred to the recent compilation of Burke and Berrington (1993). Moreover, a modified form of the Wigner-Eisenbud R-matrix theory (Wigner and Eisenbud, 1947) that has been used by Schneider (1975, 1995) appears to be formally equivalent (Robicheaux, 1991; Schneider, 1995) to the noniterative eigenchannel R-matrix method if the same variational basis sets are used in the two approaches.

A. General procedure

The eigenchannel R-matrix method is a variational approach that determines a set of eigenstates of the Schrödinger equation within a finite reaction volume V in configuration space. The reaction volume is a sphere of radius r_0, chosen such as $r_i \leqslant r_0$, r_i being the distance between the ith electron and the nucleus (see Sec. II and Fig. 2). The fragmentation coordinate r, introduced in Sec. II, is the radial coordinate of the outermost electron. In a multichannel problem, the boundary conditions on solutions at a finite boundary, on the surface Σ enclosing the reaction volume, are not uniquely specified. The word eigenchannel, which characterizes this method, refers to the fact that it calculates a particular set of linearly independent solutions that are the eigenstates of the R matrix at the energy E specified beforehand. This implies that each such eigenstate, for example, the βth solution $(r\Psi_\beta)$ has a normal logarithmic derivative

$$-b_\beta = \frac{\partial \ln(r\Psi_\beta)}{\partial r} \tag{3.1}$$

that is constant at every point on the surface Σ.

The variational principle for the eigenvalues b_β can be derived easily, starting from the exact expression for the Schrödinger energy eigenvalue that is calculated in terms of exact eigensolutions within the reaction volume only:

$$E=\frac{\int_V \Psi^\star(-\frac{1}{2}\nabla^2\Psi+U\Psi)dV}{\int_V \Psi^\star\Psi dV}. \tag{3.2}$$

Here, the integrals extend only over the reaction volume V. The $-\frac{1}{2}\nabla^2$ kinetic-energy operator is a shorthand notation for $-\frac{1}{2}\nabla^2=-\frac{1}{2}\Sigma_i\nabla_i^2$, where the sum runs over all electrons. The potential-energy operator U is assumed to be Hermitian.

Application of Green's theorem to the kinetic-energy operator integral transcribes Eq. (3.2) into

$$E=\frac{\int_V[\frac{1}{2}\vec{\nabla}\Psi^\star\cdot\vec{\nabla}\Psi+\Psi^\star U\Psi]dV-\frac{1}{2}\int_\Sigma \Psi^\star(\partial\Psi/\partial n)d\Sigma}{\int_V \Psi^\star\Psi dV}, \tag{3.3}$$

in which an additional integral over the reaction surface Σ now appears. Using Eq. (3.1), the expression (3.3) can be written, at a given energy E, as an equation for $b(E)$:

$$b=2\frac{\int_V \Psi^\star(E-\hat{H})\Psi dV}{\int_V \Psi^\star\delta(r-r_0)\Psi dV}, \tag{3.4}$$

where $\hat{H}$ denotes the Hamiltonian within the sphere, made Hermitian by addition of the Bloch operator (Bloch, 1957)

$$\hat{H}=H+\frac{1}{2r}\delta(r-r_0)\frac{\partial}{\partial r}r. \tag{3.5}$$

Strictly speaking, in Eq. (3.4) we have derived thus far only an identity obeyed by any exact Schrödinger eigenstate whose logarithmic derivative is constant across the reaction surface. However, by taking the first-order variation of this expression with respect to small deviations of Ψ from an exact solution, one can demonstrate that this is a variational principle for $b(E)$, the negative of the logarithmic derivative. This variational principle is typically used in practical calculations as follows. The trial functions Ψ are expanded in terms of a set of n arbitrary (but preferably physically motivated) basis functions y_k

$$\Psi=\sum_{k=1,n} y_k C_k, \tag{3.6}$$

where the superposition coefficients C_k are determined by the variational principle (3.4). Since the Hamiltonian is normally real, Ψ, C_k, and y_k will be assumed to be real without loss of generality.

In the Wigner-Eisenbud formulation (Burke and Robb, 1975; Burke and Taylor, 1975; Burke and Berrington, 1993), the procedure for calculating an R matrix starts from the variational expression (3.2) and determines a complete set of eigenvalues E_λ and eigenfunctions Ψ_λ for any fixed value of the boundary parameter b by solving the system of equations $\partial E/\partial C_k=0$. In contrast, the eigenchannel R-matrix approach (Greene, 1983, 1985, 1988; Hamacher and Hinze, 1989) uses the variational expression (3.4) to determine a complete set of eigenvalues b_β and eigenfunctions Ψ_β for any fixed value of the energy E. No constraint needs to be imposed on the basis functions y_k; in particular they need not be orthogonal and also they need not have any specified (common) logarithmic derivative on the reaction surface. The extremum condition $\partial b/\partial C_k=0$ leads to a generalized eigenvalue problem for b in the vector space of the coefficients C_k, namely

$$\underline{\Gamma}\vec{C}=\underline{\Lambda}\vec{C}b. \tag{3.7}$$

The matrix $\underline{\Gamma}$ is expressed as

$$\Gamma_{kl}=2\int_V y_k(E-H)y_l dV-\int_\Sigma \frac{1}{r}y_k\frac{\partial(ry_l)}{\partial r}d\Sigma. \tag{3.8}$$

The matrix $\underline{\Gamma}$ can be expressed in terms of a volume overlap matrix $\underline{O}$ and of a Bloch-operator matrix $\underline{L}$ in addition to the Hamiltonian,

$$\Gamma_{kl}=2(EO_{kl}-H_{kl}-L_{kl}). \tag{3.9}$$

The matrix $\underline{\Lambda}$ consists of a simple surface overlap integral

$$\Lambda_{kl}=\int_\Sigma y_k y_l d\Sigma. \tag{3.10}$$

Eigenvectors $\vec{C}_\beta$ and $\vec{C}'_\beta$ corresponding to distinct eigenvalues b_β and b'_β are orthogonal over the reaction surface

$$\vec{C}^t_\beta\underline{\Lambda}\vec{C}_{\beta'}=N^2_\beta\delta_{\beta\beta'}, \tag{3.11}$$

where N_β is a normalization factor. On physical grounds, the number of eigensolutions should equal the total number N of open or ''weakly closed'' channels, namely the number of channels having non-negligible amplitude on Σ. The remaining channels that have negligible amplitude on Σ but may contribute appreciably to the dynamics inside the reaction volume are referred to as ''strongly closed'' channels.

If the $(n\times n)$ matrix $\underline{\Lambda}$ is nonsingular there are n independent solutions of Eq. (3.7). In practice, however, the number of independent solutions is far smaller than the total number of variational basis functions included in Eq. (3.6), because $\underline{\Lambda}$ is singular. Le Rouzo and Raseev (1984) showed that the number of nontrivial eigensolutions of Eq. (3.7) equals the rank of the matrix $\underline{\Lambda}$.

We can clarify the concept of a channel function introduced in Sec. II.C.1 in this mathematical description by introducing a set of N real orthonormal surface harmonics $\Phi_i(\omega)$ which span the surface Σ:

$$\int_\Sigma \frac{1}{r_0^2}\Phi_i(\omega)\Phi_j(\omega)d\Sigma=\delta_{ij}, \tag{3.12}$$

where ω is the set of coordinates orthogonal to r (see Sec. II.C.1). In other words, N, the number of channels in which an electron can escape from V, corresponds to

the smallest number of surface harmonics needed to adequately represent the n basis functions on Σ. Each of the basis functions y_k can be expanded on Σ as a linear combination of the Φ_i, according to

$$y_k = \sum_{i=1,N} \frac{1}{r_0} \Phi_i(\omega) u_{ki}(r_0). \tag{3.13}$$

The matrix elements of $\underline{\Lambda}$ are then simply

$$\Lambda_{kl} = \sum_{i=1,N} u_{ki}(r_0) u^t_{il}(r_0). \tag{3.14}$$

It is now possible to complete the eigenchannel derivation of the R matrix itself (Greene, 1983, 1988). Recalling Eqs. (2.21) and (2.29), the R-matrix eigenvectors are the projections of the $(r\Psi_\beta)$ eigensolution

$$\Psi_\beta = \sum_{k=1,n} y_k C_{k\beta} \tag{3.15}$$

onto the ith surface harmonic

$$Z_{i\beta} = \int_\Sigma \Phi_i(\omega)(r\Psi_\beta) d\omega / N_\beta = \sum_{k=1,N} u_{ki}(r_0) C_{k\beta} / N_\beta . \tag{3.16a}$$

When N_β is chosen such that $(r\Psi_\beta)/N_\beta$ is normalized over the reaction surface, the eigenvector matrix $\underline{Z}$ is orthogonal. The projection of the radial derivative of $(r\Psi_\beta)$ onto the ith surface harmonic is simply

$$Z'_{i\beta} = -b_\beta Z_{i\beta}. \tag{3.16b}$$

[Note that the $Z_{i\beta}$ correspond to the $F_{i\beta}(r_0)$ defined in Eq. (2.19)]. The R matrix in the chosen representation of surface harmonics is now given by

$$R_{ij} = -\sum_\beta Z_{i\beta} b_\beta^{-1} Z_{j\beta}, \tag{3.17}$$

which is automatically symmetric.

Using Eqs. (3.7), (3.16), and (3.17), the matrix $\underline{R}$ matrix can be written in matrix form as

$$\underline{R} = -\underline{u}^t \underline{\Gamma}^{-1} \underline{u}. \tag{3.18}$$

This form of the matrix $\underline{R}$ is identical to that previously given by Nesbet (1980) and by Robicheaux (1991).

Robicheaux (1991) has shown how Eq. (3.17) can be expressed in the Wigner-Eisenbud form for $R(E)$, involving a sum of poles. He introduced a Hermitian matrix $\underline{\bar{H}}$ which is the sum of the Hamiltonian $\underline{H}$ and Bloch-operator $\underline{L}$ matrices. [Schneider (1995) has presented an alternative derivation that starts from the time-independent Schrödinger equation, after which the Bloch operator is added and subtracted.] This matrix $\underline{\bar{H}}$ can be diagonalized by an energy-independent transformation matrix $\underline{W}$:

$$\sum_l \bar{H}_{kl} W_{l\lambda} = \sum_l O_{kl} W_{l\lambda} E_\lambda , \tag{3.19}$$

where $W_{l\lambda}$ is normalized by the condition $\Sigma_{k,l} O_{kl} W_{k\lambda} W_{l\lambda'} = \delta_{\lambda\lambda'}$. [Note that the orthogonal transformation matrices W introduced in this section should not be confused with the decreasing Coulomb function of Eq. (2.52).] The R matrix determined by the variational principle (3.7) and by Eq. (3.18) is now given by the Wigner-Eisenbud-type form of Eq. (1.1):

$$R_{ij} = \frac{1}{2} \sum_\lambda \frac{Y_{i\lambda} Y_{j\lambda}}{E - E_\lambda}, \tag{3.20}$$

where

$$Y_{i\lambda} = \sum_k u_{ki} W_{k\lambda} . \tag{3.21}$$

The E_λ are the variational energy eigenvalues, while $Y_{i\lambda}$ is the surface projection of the λth eigenstate onto the ith surface harmonic. (Note that the factor before the summation differs depending on the authors; the factors ± 1, $\pm 1/2$, and $\pm 1/r_0$ are encountered in the literature.) Robicheaux's derivation explicitly connects the eigenchannel and Wigner-Eisenbud R matrix methods, showing how the well-known Wigner-Eisenbud form of the R matrix remains generally valid, even when the basis functions do not have a common logarithmic derivative on the surface. This fact has been recognized by some authors (see, for example, Nesbet, 1980; Schneider, 1975, 1995) but it has been rarely utilized in practical calculations. The flexibility of using basis functions with different surface logarithmic derivatives speeds up convergence of the calculation (with respect to basis set size) significantly. It is critically important to include an energy-dependent Buttle correction (Buttle, 1967) to the R matrix to obtain accurate results using the original Wigner-Eisenbud-type basis set with a common surface logarithmic derivative. On the other hand, calculations that use a basis set with a range of logarithmic derivatives exhibit sufficiently rapid convergence such that no Buttle correction is needed.

B. Specialization to two-electron systems. *R*-matrix calculations in *LS* coupling

Neglecting the spin-orbit terms within the reaction volume, a model Hamiltonian can be used to effectively describe the two outermost (valence) electrons of an alkaline-earth atom A. These two valence electrons move primarily outside of the closed shell A^{++}, with a total Hamiltonian

$$H = -\tfrac{1}{2}\nabla_1^2 - \tfrac{1}{2}\nabla_2^2 + V(r_1) + V(r_2) + \frac{1}{r_{12}}. \tag{3.22}$$

The interaction of each valence electron with the nucleus and inner-shell A^{++} core electrons is described by an effective potential $V(r)$.

1. Relationship between $V(r)$ and the energy levels of A^+

In the first eigenchannel R-matrix calculations carried out for Be and Mg (O'Mahony and Greene, 1985; O'Mahony, 1985; O'Mahony and Watanabe, 1985), an *ab initio* l-independent Hartree-Slater potential $v^{\mathrm{HS}}(r)$ was used as the model potential $V(r)$. The Hartree-Slater potential is a relatively crude type of

TABLE I. Semiempirical parameters describing the model potential experienced by the outermost (valence) electron in alkaline-earth atoms.

		(a) Potential of Eq. (3.25)			
		α_1	α_2	α_3	
Be^+		6.9010	8.9581	5.0798	
Mg^+		4.2499	11.0223	2.9417	
Ca^+		3.9557	12.8420	2.0039	
Sr^+		3.5515	6.0373	1.4389	
	l	(b) Potential of Eq. (3.26)			
		α_1	α_2	α_3	r_c
	0	4.0616	13.4912	2.1539	1.5736
Ca^+	1	5.3368	26.2477	2.8233	1.0290
α_{cp}=3.5	2	5.5262	29.2059	2.9216	1.1717
	$\geqslant$3	5.0687	24.3421	6.2170	0.4072
	0	3.4187	4.7332	1.5915	1.7965
Sr^+	1	3.3235	2.2539	1.5712	1.3960
α_{cp}=7.5	2	3.2533	3.2330	1.5996	1.6820
	$\geqslant$ 3	5.3540	7.9517	5.6624	1.0057
	0	3.0751	2.6107	1.2026	2.6004
Ba^+	1	3.2304	2.9561	1.1923	2.0497
α_{cp}=11.4	2	3.2961	3.0248	1.2943	1.8946
	$\geqslant$ 3	3.6237	6.7416	2.0379	1.0473
	0	3.7702	4.9928	1.5179	1.3691
Ra^+	1	3.9430	5.0552	3.6770	1.0924
α_{cp}=18	2	3.7008	4.7748	1.4956	2.2784
	$\geqslant$ 3	3.8125	5.0332	2.1016	1.2707

independent-electron model which is adequate for many purposes in light atoms, but for the heavier alkaline-earth atoms more sophistication is needed. In fact, the d orbitals of Ca, Sr, and Ba, as well as the f orbitals of Ba, depend sensitively on the accuracy of the potential. The potential used in Ca by Greene and Kim (1987) and by Kim and Greene (1987, 1988) included, in addition to a l-dependent Hartree-Slater screening potential $v_l^{\rm HS}(r)$, an additional polarization potential:

$$V_l(r)=v_l^{\rm HS}(r)-\frac{\alpha_{\rm cp}}{2r^4}\{1-\exp[-(r/r_c^l)^6]\}. \tag{3.23}$$

The core polarization $\alpha_{\rm cp}$ and the cutoff radius r_c^l were adjusted so that the eigenvalues ϵ_{nl} of the one-electron radial equation

$$\left(-\frac{1}{2}\frac{d^2}{dr^2}+\frac{l(l+1)}{2r^2}+V_l(r)-\epsilon_{nl}\right)u_{nl}=0 \tag{3.24}$$

coincided with the experimental (spin-orbit averaged) energies of Ca^+. Optimal values of the parameters can be found in the paper of Kim and Greene (1988).

More recently, a number of calculations have been carried out using a more convenient analytical model potential that depends on a few parameters that must be determined empirically. Simple l-independent potentials of the form

$$V(r)=-\frac{1}{r}\{2+(Z-2)\exp(-\alpha_1 r)+\alpha_2 r\exp(-\alpha_3 r)\} \tag{3.25}$$

were used in the lighter alkaline earths, where Z is the nuclear charge and the three empirical parameters α_i were fitted to known energy levels of the alkali-like ion. The parameters values optimized for the alkaline-earth ions from Be^+ to Sr^+ are given in Table I(a). Accurate two-electron spectra have been obtained, even in an atom as heavy as Sr (Aymar, 1987; Aymar *et al.*, 1987; Aymar and Lecomte, 1989), using such an l-independent potential. More sophisticated l-dependent potentials including a polarization term

$$V_l(r)=-\frac{1}{r}\{2+(Z-2)\exp(-\alpha_1^l r)+\alpha_2^l r\exp(-\alpha_3^l r)\}$$
$$-\frac{\alpha_{\rm cp}}{2r^4}\{1-\exp[-(r/r_c^l)^6]\} \tag{3.26}$$

are needed to describe Ba^+ and Ra^+ adequately (Aymar, 1990; Greene and Aymar, 1991). Here, $\alpha_{\rm cp}$ is the experimental dipole polarizability of the doubly charged positive ion (Fajans and Joos, 1924; Tessman *et al.*, 1953; Dalgarno, 1962; Johnson *et al.*, 1983). The empirical parameters α_i^l and r_c^l were adjusted until the result-

ing Schrödinger energy eigenvalues obtained from the potential agree with the experimental energies of the alkaline-earth ion. The values of the parameters obtained for Ca^+, Sr^+, Ba^+, and Ra^+, are given in Table I(b).

The extensive eigenchannel R-matrix calculations carried out in recent years using model potentials have shown one major result: accurate two-electron spectra are obtained provided the potential $V(r)$ gives accurate energies for the one-electron ionic system. This can be understood from the fact that the phase of the valence electron orbital as the electron emerges from the ionic core is virtually guaranteed to be correct if the model-potential energy levels agree with the experimental ionic levels. The detailed interactions of the two electrons outside this core depend sensitively on these phases, i.e., on the one-electron quantum defects of each emerging electron. The majority of recent calculations of complicated alkaline-earth atom spectra have used semiempirical model potentials such as those given by Eq. (3.26) and Table I(b). They have been successful mainly because they give a good description of the ionic (alkalilike) valence energy spectra.

2. Design of the basis set

The basis set used in the variational calculations consists of LS-coupled independent-particle numerical basis functions. An antisymmetric two-electron basis function, LS coupled to form a state of definite S, L, and parity, is expressed in terms of numerical one-electron orbitals $u_{nl}(r)$ and $F_{nl}(r)$ by

$$\begin{aligned} y_{n_1l_1n_2l_2}(\vec{r}_1,\vec{r}_2)=&\frac{1}{\sqrt{2}r_1r_2}[u_{n_1l_1}(r_1)F_{n_2l_2}(r_2)\\ &\times Y_{l_1l_2LM}(\Omega_1,\Omega_2)\\ &+(-1)^{l_1+l_2-L+S}F_{n_2l_2}(r_1)u_{n_1l_1}(r_2)\\ &\times Y_{l_2l_1LM}(\Omega_1,\Omega_2)]. \end{aligned} \tag{3.27}$$

An alternative form for Eq. (3.27) connects more naturally with the quantum-defect description of the outer region [Eq. (2.19a)],

$$\begin{aligned} y_{in_2}=&2^{-1/2}[\Phi_i(r_1,\Omega_1,\Omega_2)F_{n_2l_2}(r_2)/r_2\\ &+(-1)^S\Phi_i(r_2,\Omega_2,\Omega_1)F_{n_2l_2}(r_1)/r_1], \end{aligned} \tag{3.28}$$

where the channel index stands for $i\equiv\{n_1l_1l_2\}$ and where

$$\Phi_i(r_1,\Omega_1,\Omega_2)=\frac{u_{n_1l_1}(r_1)}{r_1}Y_{l_1l_2LM}(\Omega_1,\Omega_2). \tag{3.29}$$

The channels functions Φ_i are the functions for the ionic states including the angular wave functions of both electrons. (Note that, in the following, the open and weakly closed channels, with specific values of n_1, l_1, and l_2, will often be designated by $n_1l_1nl_2$, the notation $n_1l_1\epsilon l_2$ being used for open channels to emphasize that the channel is open.)

In some early R-matrix calculations performed for Be, Mg (O'Mahony, 1985; O'Mahony and Greene, 1985; O'Mahony and Watanabe, 1985), and Sr (Aymar, 1987; Aymar *et al.*, 1987) two different kinds of orbitals were introduced. The $u_{n_1l_1}$ orbitals in the channel functions [Eq. (3.29)] obey Eq. (3.24) using the potential $V(r)$ that describes the A^{++}-e interaction. However, the F_{nl} orbitals were chosen to correspond instead to "polarized" orbitals. These were still determined by solving Eq. (3.24) except with a different potential more appropriate to the A^+-e interaction.

The use of different types of orbitals complicates the calculations without providing any significant acceleration of the convergence. After this was recognized, the more recent two-electron R-matrix calculations have used orbitals generated from the A^{++}-e potential $V(r)$, which amounts to setting $F_{nl}\equiv u_{nl}$ in Eq. (3.27). With this choice, the two-electron basis functions in Eq. (3.27) are eigenfunctions of the independent-electron Hamiltonian $H_0=H-1/r_{12}$. [Note that with this choice the factor $1/\sqrt{2}$ in Eq. (3.27) should be replaced by $1/\sqrt{2(1+\delta_{n_1n_2}\delta_{l_1l_2})}$.] Because the ionic basis set is simple, convenient, and effective for two-electron systems, we consider only this type in the following. In Sec. III.D below we will show that for atoms with many open-shell electrons, this choice is highly inferior to the use of Löwdin's "natural orbitals" (Löwdin, 1955; Löwdin and Schull, 1956) or multiconfiguration Hartree-Fock-type (Froese-Fischer, 1977) orbitals (Robicheaux and Greene, 1992, 1993a, 1993b, 1993c; Chen and Robicheaux, 1994; Miecznik *et al.*, 1995; Miecznik and Greene, 1996).

In practice, a first set of orthogonal "closed-type" orbitals denoted u^c_{nl} is obtained by solving Eq. (3.24) numerically subject to the boundary condition that each orbital vanishes on the boundary $r=r_0$. Figure 6 shows a set of closed-type $l=0$ orbitals obtained for Ba with r_0 = 20 a.u. This first set is complemented by a second set of "open-type" orbitals (u^o_{nl}) by integrating Eq. (3.24) at several energies that differ from the ϵ^c_{nl} eigenvalues obtained in calculating the closed-type orbitals. These orbitals have a nonzero amplitude at $r=r_0$, and are neither orthogonal to one another nor to the u^c_{nl} orbitals in general. Two such s-wave open-type orbitals are shown in Fig. 6.

As presently implemented, the R-matrix approach treats the escape of (at most) one electron from the reaction volume. This is enforced by using only closed-type orbitals for the channel functions Φ_i [Eq. (3.29)]. The minimum possible value that can be used for the box size r_0 is therefore governed by the requirement that the most diffuse A^+ n_1l_1 ionic states relevant to the energy range under consideration must fit within the reaction volume.

The two-electron basis functions y_k retained in the R-matrix calculation are grouped into closed-type and open-type sets. Each "closed-type" basis function y^c_k consists of two closed-type orbitals and thus vanishes everywhere on the reaction surface Σ. Therefore, all the

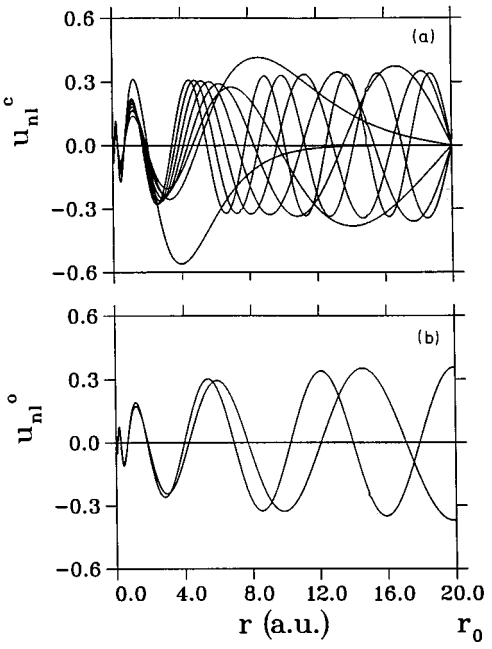

FIG. 6. Radial one-electron ns orbitals of Ba^+ used in the eigenchannel R-matrix calculations for Ba carried out with a reaction volume of radius $r_0 = 20$ a.u: (a) closed-type orbitals; (b) open-type orbitals.

coefficients $u_{ki}(r_0)$ associated with the y_k^c functions vanish in the expansion (3.13). Each "open-type" basis function y_k^o has a nonzero amplitude on Σ and is built from one open-type orbital $u_{n_2 l_2}^o$, for the outer electron and one closed-type orbital $u_{n_1 l_1}^c$ for the inner electron. For a given channel $i=\{n_1 l_1 l_2\}$, the coefficients $u_{ki}(r_0)$ associated with y_k^o functions in Eq. (3.13) reduce to $u_{n_2 l_2}^o(r_0)$. A set of closed-type functions alone forms an orthonormal set of eigenfunctions that spans the reaction volume. This set would be efficient only to describe a solution of the Schrödinger equation which vanishes on Σ. The open-type basis functions y_k^o are needed to allow the outermost electron to reach the surface Σ and to escape beyond it in an excited bound or continuum state. The use of y_k^o basis functions adds flexibility to the basis, although the number of such basis functions should be kept small (typically 1–3 per channel) to avoid numerical difficulties associated with linear dependence of the full basis set. The nonorthogonality of the full basis set causes no particular difficulties for two-electron systems. For atoms having more than two electrons in open shells, however, the calculation of matrix elements becomes tremendously complicated if the orbitals are not orthogonal, and consequently the open-type orbitals are orthogonalized to the closed-type orbitals.

No completely general algorithm for choosing the two-electron configurations has been identified, i.e., to select the basis functions to include in the variational calculation. The optimum basis set depends on details of the system being studied, such as the number of open and weakly closed channels relevant to the energy range, the size of the reaction volume, the degree of convergence desired, and the available computer memory. If any particular channel is to be treated as open or weakly closed in the MQDT calculation, both open-type and closed-type basis functions must be included for that channel. Trials with one to three open-type basis functions per channel have found very little sensitivity to their number. Experimentation has shown that, in heavy alkaline earths, a surprisingly large number of strongly closed channels (or equivalently, a large set of closed-type basis functions) is required to describe various electron correlation, relaxation, and polarization effects (Bartschat and Greene, 1993). In particular, the inner electron can "relax" or become polarized in response to the electric field of the outermost electron. This is the dominant contribution to core relaxation in the present model since the A^{++} core is treated as frozen. Polarization effects are neglected when an electron roams beyond the reaction volume V. The closed-type basis set should be sufficiently flexible to permit a description of polarization effects within V.

The choice of the basis set and of the reaction volume size, in calculations for two-electron atoms, will be documented further in Sec. III.G below.

C. Inclusion of nonperturbative spin-orbit effects: Two-electron *R*-matrix calculations in *jj* coupling

Because the eigenchannel R-matrix calculations in jj coupling proceed along the same lines as the R-matrix calculations in LS coupling, only the differences are outlined here. The model Hamiltonian used in R-matrix calculations carried out in jj coupling includes explicitly the spin-orbit terms, which are ignored in the Hamiltonian of Eq. (3.22),

$$H=-\frac{1}{2}\nabla_1^2-\frac{1}{2}\nabla_2^2+V(r_1)+V(r_2)+V_{so}^{s_1 l_1 j_1}(r_1)+V_{so}^{s_2 l_2 j_2}(r_2)+\frac{1}{r_{12}}. \tag{3.30}$$

The spin-orbit interaction between each valence electron and the screened nucleus can be approximated by a potential having the form

$$V_{so}^{slj}(r)=\frac{\alpha^2}{2}\vec{s}\cdot\vec{l}\frac{1}{r}\frac{dV}{dr}\left(1-\frac{\alpha^2}{2}V(r)\right)^{-2}, \tag{3.31}$$

in which α is the fine-structure constant in a.u. The last factor in Eq. (3.31) is suggested by the Dirac equation (see Condon and Shortley, 1935). While it is not needed in perturbative spin-orbit calculations, this factor is included, as in some previous studies, in order to ensure that solutions of the radial Schrödinger equation are well defined near the origin, $r\to 0$. Without this factor, the r^{-3} behavior of the spin-orbit potential near the origin leads to an ill-defined mathematical behavior of the radial wave functions.

The variational basis set consists of antisymmetrized two-electron functions whose angular momenta are jj

coupled to form a state of definite total angular momentum J and parity,

$$y_k(\vec{r}_1,\vec{r}_2)=\frac{1}{r_1 r_2\sqrt{2(1+\delta_{n_1 n_2}\delta_{l_1 l_2}\delta_{j_1 j_2})}} \times\{u_{n_1 l_1 j_1}(r_1)u_{n_2 l_2 j_2}(r_2) \times\{[\chi_{s_1}(1)Y_{l_1}(1)]^{j_1}[\chi_{s_2}(2)Y_{l_2}(2)]^{j_2}\}^{JM} -(-1)^{j_1+j_2-J}u_{n_2 l_2 j_2}(r_1)u_{n_1 l_1 j_1}(r_2) \times\{[\chi_{s_2}(1)Y_{l_2}(1)]^{j_2}[\chi_{s_1}(2)Y_{l_1}(2)]^{j_1}\}^{JM}\}, \tag{3.32}$$

where the basis-vector label k is a shorthand notation for the quantum numbers $n_1 l_1 j_1 n_2 l_2 j_2$. In Eq. (3.32), the electron spinors χ_s and spherical harmonics Y_l are standard. The j-dependent one-electron radial function u_{nlj} obeys the radial Schrödinger equation

$$\left(-\frac{1}{2}\frac{d^2}{dr^2}+\frac{l(l+1)}{2r^2}+V(r)+V_{so}^{slj}(r)-\epsilon_{nlj}\right)u_{nlj}=0. \tag{3.33}$$

All the jj-coupled eigenchannel R-matrix calculations performed in heavy alkaline-earth atoms use for the electron-core effective potential the empirical l-dependent model potential V_l of Eq. (3.26), also utilized in recent LS-coupled R-matrix calculations. Indeed, the semiempirical parameters listed in Table I(b) were adjusted to obtain optimum agreement between the eigenvalues ϵ_{nlj} of Eq. (3.33) and the experimental j-dependent energies of the alkaline-earth ions. Of course, if the spin-orbit term is neglected in the one-electron radial Schrödinger equation, one obtains ϵ_{nl} energies that agree well with the spin-orbit-averaged energies of alkaline-earth ions.

Some calculations (Lecomte *et al.*, 1994, Luc-Koenig *et al.*, 1995) were performed by adding to the two-electron Hamiltonian H of Eq. (3.30) a dielectronic polarization correction (Chisholm and Öpik, 1964; Hameed, 1972) to the $1/r_{12}$ interaction. Following Victor and Laughlin (1972), the dielectronic polarization term between the $l_1 l_2$ and $l_1' l_2'$ basis functions was taken to be

$$V_{\rm pol}^{(2)}(\vec{r}_1,\vec{r}_2)=-\frac{\alpha_{\rm cp}}{r_1^2 r_2^2}P_1(\hat{r}_1\cdot\hat{r}_2)[w(r_c^{l_1},r_1) \times w(r_c^{l_1'},r_1)w(r_c^{l_2},r_2)w(r_c^{l_2'},r_2)]^{1/4}, \tag{3.34}$$

where the cutoff function is $w(r_c^l,r)=1-\exp[-(r/r_c^l)^6]$. In Eq. (3.34), P_1 is a Legendre polynomial and $\alpha_{\rm cp}$ the dipole polarizability of the core. The l-dependent cutoff radii are given in Table I(b).

D. Specialization to open-shell atoms. *R*-matrix calculations in *LS* coupling

The LS-coupled eigenchannel R-matrix approach has been used to calculate photoionization cross sections and bound-states properties of some open p-shell atoms and of two open d-shell atoms, scandium and titanium. Calculations in open p-shell atoms dealt with Al (O'Mahony, 1985; Miecznik *et al.*, 1995), with halogens (Robicheaux and Greene, 1992, 1993a), with atoms in the carbon group (Robicheaux and Greene, 1993b), and in the oxygen group (Chen and Robicheaux, 1994). All of these atoms have a ground configuration of the type $m_0 s^2 m_0 p^q$, with $m_0=3$ and $q=1$ for Al. For the second-row elements ($m_0=2$), one has $q=2$ for C, $q=4$ for O, and $q=5$ for F. Scandium, the simplest transition-metal atom, with ground-state configuration $3d4s^2$, has been chosen to see whether the eigenchannel R-matrix method can reproduce the extremely complicated spectra of open d-shell atoms (Armstrong and Robicheaux, 1993; Robicheaux and Greene, 1993c, 1993d). The accurate results obtained in Sc have encouraged Miecznik and Greene (1996) to undertake eigenchannel R-matrix calculations in titanium, with ground state $3d^2 4s^2$.

1. Hamiltonian

Most of the eigenchannel R-matrix calculations in open-shell atoms were carried out with a Hamiltonian H that does not refer to the full atomic system. As in the alkaline-earth atoms, they utilized a model Hamiltonian of the valence electrons only, and approximated the effects of the closed-shell inner electrons and of the nucleus on the valence electrons through an effective potential $V(r)$. Neglecting the spin-orbit terms within the reaction volume, the valence-electron Hamiltonian, in a.u., is

$$H=\sum_i\{-\tfrac{1}{2}\nabla_i^2+V(r_i)\}+\sum_{\substack{i,j\\ i<j}}1/r_{ij}. \tag{3.35}$$

In Eq. (3.35), the sums over indices i and j run over the N_v valence electrons outside the rare-gas-like inert core. One has $N_v=3$ for Al and Sc, $N_v=4$ for the carbon-group atoms and for Ti, $N_v=6$ for the oxygen-group atoms, and $N_v=7$ for the halogens.

The first eigenchannel R-matrix study carried out in an atom with more than two valence electrons concerned Al (O'Mahony, 1985). As in the previous R-matrix calculation carried out in Be and Mg (O'Mahony and Greene, 1985), the interaction of each valence electron with the closed-shell core was described by an *ab initio* l-independent Hartree-Slater potential. The second calculation dealt with Si (Greene and Kim, 1988). A Hartree-Slater potential with an empirical polarization potential was used to describe the Si^{4+}-e interaction.

The techniques used in the recent calculations have been improved compared to those employed in Al (O'Mahony, 1985) and Si (Greene and Kim, 1988). A number of calculations (Robicheaux and Greene, 1992, 1993a, 1993b, 1993c, 1993d; Armstrong and Robicheaux, 1993; Miecznik *et al.*, 1995) have been carried out using more sophisticated analytical one-electron model poten-

tial including an l-dependent screened Coulomb potential and a polarization potential,

$$V_l = -\frac{1}{r}\{N_v + (Z-N_v)\exp(-\alpha_1^l r) + \alpha_2^l r \exp(-\alpha_3^l r)\} + V_{\rm pol}^{(1)}(r), \tag{3.36}$$

where the polarization potential has the form

$$V_{\rm pol}^{(1)}(r) = \frac{\alpha_{\rm cp}}{2r^4}\{1-\exp[-(r/r_c)^3]\}^2. \tag{3.37}$$

In Eq. (3.37), theoretical values were used for the dipole polarizability $\alpha_{\rm cp}$ (Johnson *et al.*, 1983). The parameters α_i^l and r_c were fitted to optimize agreement between the calculated energy levels of H_v and the experimental energy levels of the $(N_v-1)+$ ion. Complete lists of the parameters for the semiempirical potentials optimized in the open-shell atoms that were studied, as well as the references on the experimental levels included in the fits, can be found in the relevant papers (Robicheaux and Greene, 1992, 1993b, 1993c; Miecznik *et al.*, 1995). The one-electron Hamiltonian has the form:

$$H_v = -\tfrac{1}{2}\nabla^2 + V_l(r). \tag{3.38}$$

In addition, the dielectronic polarization interaction has been systematically introduced in the model Hamiltonian used in the recent eigenchannel R-matrix calculations of open-shell atoms. This consists in replacing the Hamiltonian of Eq. (3.35) by

$$H = \sum_i \{-\tfrac{1}{2}\nabla_i^2 + V_l(r_i)\} + \sum_{\substack{i,j \\ i<j}} (1/r_{ij} + V_{\rm pol}^{(2)}(\vec{r}_i,\vec{r}_j)), \tag{3.39}$$

with

$$V_{\rm pol}^{(2)}(\vec{r}_i,\vec{r}_j) = -2P_1(\hat{r}_i.\hat{r}_j)[V_{\rm pol}^{(1)}(r_i)V_{\rm pol}^{(1)}(r_j)]^{1/2}. \tag{3.40}$$

Formally, Eq. (3.40) is identical to Eq. (3.34) given in Sec. III.C above. Note that the dielectronic polarization interaction has not been systematically included in the calculations in alkaline earths. However, its effect has been analyzed in some particular cases (Lecomte *et al.*, 1994; Luc-Koenig *et al.*, 1995). As described below in Sec. IV, the dielectronic polarization interaction significantly influences the Ba $5d5g$ autoionization widths (Luc-Koenig *et al.*, 1995). In contrast, the influence of this interaction on the dynamics of open-shell atoms has not been studied in detail.

The calculations in open-shell atoms conducted with a parametrized model potential emphasize the need for accurate energy-level data for alkali-like ions. Some calculations for the heavier halogens Br and I and the heavier C-group atoms Ge and Sn have suffered from the limited amount of ionic-level information that was available. Errors could be introduced in the calculation through the parameters of the model potential. To bypass these difficulties, another approach was used recently by Chen and Robicheaux (1994) to study the oxygen-group atoms with the eigenchannel R-matrix approach. The Hamiltonian chosen by Chen and Robicheaux (1994) refers to the full atomic system. However it still contains the one- and two-electron polarization terms. One has

$$H = \sum_i \left(-\tfrac{1}{2}\nabla_i^2 - \frac{Z}{r_i} + V_{\rm pol}^{(1)}(r_i)\right) + \sum_{\substack{i,j \\ i<j}} (1/r_{ij} + V_{\rm pol}^{(2)}(\vec{r}_i,\vec{r}_j)). \tag{3.41}$$

In Eq. (3.41), the sums over indices i and j run over all electrons; $V_{\rm pol}^{(1)}(r_i)$ and $V_{\rm pol}^{(2)}(\vec{r}_i,\vec{r}_j)$ have the form given in Eqs. (3.37) and (3.40), respectively. Theoretical values (Johnson *et al.*, 1983) were used for the dipole polarizability $\alpha_{\rm cp}$ and the cutoff radius r_c was determined by evaluating the expectation value $\langle nl|r|nl\rangle$ for orbitals of the outermost closed shell. Comparison of eigenchannel R-matrix calculations carried out in S with the Hamiltonian of Eq. (3.41) referring to all 16 electrons and with a model potential and 6 electrons (Chen and Robicheaux, 1994) will be discussed later in Sec. V.

A full-electron description has been used also recently by Miecznik and Greene (1996) in titanium (22 electrons) for calculating photoabsorption and photoionization from excited states. However, in those calculations, the one- and two-electron polarization terms were not included.

2. Constructing basis functions

One major complication occurs in R-matrix calculations of open-shell atoms compared to those in two-valence-electron systems. This complication is related to the construction of basis functions used for the initial- and final-state atomic wave functions. A key requirement of any R-matrix calculation is an accurate description of the target-state wave functions, which correspond to the possible wave functions of the positive ion in the studied energy range. For two-electron systems, when a semiempirical model is used to describe the interaction of each valence electron with the closed-shell core, this aspect of the computation is easy since the target functions are simply orbitals of the one-electron ionic potential. More effort goes into determining multielectron target functions, which magnifies the amount of work needed to describe the full atomic dynamics. Configuration interaction is generally included in the target functions. It is very important in choosing target basis functions to try to work with the minimum number necessary to achieve convergence for the atomic dynamics because each target basis function translates to ~ 10 atomic functions. Different approaches have been used in open-shell atoms to describe ionic states.

First, consider the calculations that included a model potential to account for the effects of closed shells. In order to reduce the number of multielectron basis functions needed for convergence, the many-electron functions are not expanded in terms of the orbitals that are eigenstates of H_v [Eq. (3.38)] but in terms of orbitals that cause the core states to converge. Indeed, a more

compact description of target states could be obtained using "natural orbitals" (Löwdin, 1955; Löwdin and Shull, 1956; Froese Fischer, 1991). The natural orbitals can be obtained by diagonalizing a large configuration-interaction matrix constructed from orbital solutions of H_v for the target states of interest, and superposing the orbitals. Natural orbitals can also be chosen to minimize the total energies of selected target states. The $\bar{n}l$ natural orbitals are associated with the lowest n values occurring for $s, p, d, f, \ldots$ symmetries. Different techniques were sometimes used for a given atom to determine the $\bar{n}l$ natural orbitals associated with different l values (see, for example, Robicheaux and Greene, 1992). Natural orbitals can be more diffuse or more contracted than spectroscopic orbitals.

Because of the limited number of orbital solutions of Eq. (3.38) introduced in determining the natural orbitals, excited natural orbitals can have spurious nodes close to r_0. In order to eliminate this unphysical behavior, an l-dependent potential $\bar{V}_l$ that has these orbitals as eigenstates is optimized. Different forms were used for the potential $\bar{V}_l$. The potential used by Robicheaux and Greene (1992) has the same form as V_l [Eq. (3.36)] with N_v replaced by 2 and α_i^l replaced by $\bar{\alpha}_i^l$, whereas the potential used in Sc and Al (Robicheaux and Greene, 1993c; Miecznik *et al.*, 1995) has the form

$$\bar{V}_l(r)=V_l(r)+\frac{1-\exp(-\bar{\alpha}_1^l r)}{r}+\frac{\bar{\alpha}_2^l\{1-\exp[-\bar{\alpha}_3^l r]\}}{r^2}. \tag{3.42}$$

Lists of the parameters $\bar{\alpha}_i^l$ optimized in each open-shell system that was studied can be found in the corresponding papers (Robicheaux and Greene, 1992, 1993b, 1993c; Miecznik *et al.*, 1995). This potential is next used to generate $s, p, d, f, \ldots$ orbitals with higher quantum numbers.

Although the procedure used to generate natural orbitals, that we have just described, proved to be highly successful in previous applications (Robicheaux and Greene, 1992, 1993a, 1993b, 1993c, 1993d; Armstrong and Robicheaux, 1993; Miecznik *et al.*, 1995), it is not free of difficulties. As emphasized by Miecznik and Greene (1996), the form of natural orbitals (and thus the rate of convergence of configuration-interaction target states) depends strongly on the number of orbital solutions of H_v, as well as on the type and number of target configurations used to obtain the natural orbitals.

A different approach to describe the target states, based on the Hartree-Fock approximation, was used by Chen and Robicheaux (1994) in their full-electron calculation in oxygen-group atoms and by Miecznik and Greene (1996) in titanium. Indeed, while using orbital solutions of Eq. (3.38), it is necessary to include a large configuration-interaction basis, with singly excited, doubly excited, and triply excited configurations to get modest degree of convergence, whereas a fully variational (Hartree-Fock) calculation takes better care of such excitations, effectively minimizing the number of excitations to singly and doubly excited states. Radial orbitals needed to calculate short-range interaction parameters were obtained in the Hartree-Fock or multiconfiguration Hartree-Fock approximation (Froese Fischer, 1977, 1991). The natural orbitals incorporate screening and correlations associated with the ionic system. More precisely, in the oxygen-group atoms, Chen and Robicheaux (1994) performed first a Hartree-Fock calculation to obtain one-electron orbitals of the configuration-averaged ion. Next, a multiconfiguration Hartree-Fock calculation was performed to get the lowest d and f orbitals to describe correlation in the valence shell. A similar step procedure was used in Ti by Miecznik and Greene (1996). First the inner-electron orbitals as well as the valence $3d$ and $4s$ orbitals of Ti^+ were optimized on the $3d^2 4s$ configuration, after which $4p$ was optimized on $3d^2 4p$. Next, a multiconfiguration Hartree-Fock calculation of the $3d^3\ ^2G^e$ term was performed to generate $4d, 5s, 5p$, and $4f$ correlations orbitals.

Once target orbitals are obtained, higher-n orbitals needed to represent the outgoing electron are generated. In oxygen-group atoms (Chen and Robicheaux, 1994) and in Ti (Miecznik and Greene, 1996), higher-n orbitals were obtained by constructing a local screened potential $V_{\rm scr}(r)$ using the Hartree-Fock wave functions of both the inner shells and the valence s and p orbitals. The explicit form of $V_{\rm scr}(r)$ is

$$V_{\rm scr}(r)=-\frac{Z}{r}+\sum_i w_i \int_0^\infty \frac{1}{r_>} P_i^2(r')dr', \tag{3.43}$$

where $r_>$ is the larger of r and r', w_i is the number of electrons in subshell i described by the radial function P_i, and the summation runs over all subshells of the ion ground state. High-n orbitals are orthogonalized to the low-n input orbitals.

As for two-valence-electron systems, open-type orbitals (which have nonzero value on the R-matrix surface) and closed-type orbitals (which are zero on the boundary) are computed. Closed-type orbitals are automatically orthogonal. These orbitals are next used to construct open-type functions (where only one of the electron orbitals of the many-electron basis functions is of open type) and closed-type functions (where all orbitals are of closed type).

The basis functions used for a given open-shell atom to describe the initial-state and the different final-state LS symmetries incorporate configuration interaction in both the $(N_e\text{-}1)$ electron ionic states and the full N_e wave functions. (The notation N_e is used for the total number of electrons in order to avoid confusion with the number of open and weakly closed fragmentation channels, referred to as N throughout this paper.) Basis functions of close-coupling type are constructed by attaching an l wave of appropriate symmetry onto each component of the target states. Part of these functions describes relaxation of the orbitals due to the addition of the extra electron. As in two-valence electron systems, the open or weakly closed channels are described by closed-type and open-type functions. Multielectron matrix elements are considerably easier to evaluate when all orbitals are orthogonal to each other. Moreover, nu-

merical difficulties could occur in Gram-Schmidt orthogonalization of two orbitals with each other and with the closed-type orbitals. Thus, only one open-type orbital, orthogonalized to the closed-type orbitals, is used for each l value.

Correlation-type basis functions related to the close-coupling-type basis as well as various other correlation-type functions are also included. Such functions are needed, in particular, to represent the dipole polarization of the ionic states. For example, for the open p-shell atoms, correlation functions of the type $m_0 p^{q+2}$ were introduced for describing the $m_0 s^2 m_0 p^q$ ground states (with $q \leqslant 4$) and correlation functions of the type $m_0 s m_0 p^{q+1}$ for the final-state symmetries. No general rule has been identified to choose the correlation-type functions in open-shell systems. Some calculations in open p-shell atoms included only a restricted number of correlation-type functions. So, for example, as stated by Robicheaux and Greene (1992), these functions seem to play a smaller role in the halogen dynamics than they do in the dynamics of the alkaline earths, where a large number of strongly closed channels were found necessary to obtain converged results. In contrast, as shown later in Sec. V, it was found to be important for the convergence of Sc quantum defects (Robicheaux and Greene, 1993c) that numerous correlation-type functions and strongly closed channels be included. As in alkaline earths, all basis functions used to describe the correlation-type basis functions, as well as the initial states, are of closed-type.

A final remark concerns the choice of ionic orbitals to describe basis functions. These basis functions do not necessarily give the best convergence for the initial state; however, they tend to give better agreement between the length and velocity gauge cross sections than basis functions that are chosen to give the best convergence for the initial level.

The choice of the basis functions adapted to study each type of open-shell atoms that was investigated using the eigenchannel R-matrix approach will be further documented in Sec. V.

E. Streamlined solution of the generalized eigensystem

As discussed in the previous sections, eigenchannel R-matrix calculations may involve large sets of n two- or many-electron basis functions. For such large basis sets, the numerical solution of the generalized eigensystem [Eq. (3.7)] at many energies can become very time consuming. One way to bypass this difficulty and improve the efficiency of repeated R-matrix calculations at many different energies is to use Robicheaux's Wigner-Eisenbud-type (Robicheaux, 1991) reformulation of the eigenchannel R-matrix method, which was discussed above. For instance, this formulation was used by Chen and Robicheaux (1994) to study chalcogens. This approach lacks the flexibility to change the number of weakly closed channels as the energy is varied. Specifically, if one decides to add one more weakly closed channel when the energy increases above a certain value, it becomes necessary to enlarge the matrix $\underline{\bar{H}} = \underline{H} + \underline{L}$ to include the relevant open-type basis functions, and then rediagonalize $\underline{\bar{H}}$. For all energies having this fixed number (N) of open and weakly closed channels, the R matrix is then given analytically by Eq. (3.20) without requiring the numerical solution of another large matrix equation.

An alternative "streamlined" reformulation (Greene and Kim, 1988) casts the generalized eigenvalue equation of the eigenchannel R-matrix method into a form that can be rapidly solved at many energies, and which retains the flexibility to change the number of open or weakly closed channels as often as desired, without requiring the solution of a new large $(n \times n)$ matrix equation each time. The streamlined formulation relies on the fact that the size of the open-type basis set (typically of order N to $3N$) is always much smaller than the closed-type basis set. For a calculation involving N open and weakly closed channels, the number N of nontrivial solutions of the generalized eigensystem [Eq. (3.7)] is smaller than n by typically one or two orders of magnitude.

The streamlined reformulation partitions the basis functions y_k into n_o open-type (o) and n_c closed-type (c) subsets, depending on whether each basis function is nonzero on Σ or zero on Σ, respectively. With this partitioning, the matrices $\underline{\Gamma}$ and $\underline{\Lambda}$ in Eqs. (3.9) and (3.10) have the structure:

$$\underline{\Gamma} = \begin{pmatrix} \underline{\Gamma}_{cc} & \underline{\Gamma}_{co} \\ \underline{\Gamma}_{oc} & \underline{\Gamma}_{oo} \end{pmatrix} \tag{3.44}$$

and

$$\underline{\Lambda} = \begin{pmatrix} 0 & 0 \\ 0 & \underline{\Lambda}_{oo} \end{pmatrix}. \tag{3.45}$$

This partitioning allows us to write Eq. (3.7) as two coupled matrix equations,

$$\underline{\Gamma}_{cc}\vec{C}_c + \underline{\Gamma}_{co}\vec{C}_o = 0, \tag{3.46a}$$

and

$$\underline{\Gamma}_{oc}\vec{C}_c + \underline{\Gamma}_{oo}\vec{C}_o = \underline{\Lambda}_{oo}\vec{C}_o b. \tag{3.46b}$$

Using Eq. (3.46a) to eliminate $\vec{C}_c$ from Eq. (3.46b), the equation determining the eigenvalue b is now of much smaller dimension $n_o \times n_o$,

$$\underline{\Omega}\vec{C}_o = \underline{\Lambda}_{oo}\vec{C}_o b, \tag{3.47}$$

where

$$\underline{\Omega} = \underline{\Gamma}_{oo} - \underline{\Gamma}_{oc}(\underline{\Gamma}_{cc})^{-1}\underline{\Gamma}_{co}. \tag{3.48}$$

The closed components $\vec{C}_c$ of the eigenvector are deduced from the open components $\vec{C}_o$ by

$$\vec{C}_c = -(\underline{\Gamma}_{cc})^{-1}\underline{\Gamma}_{co}\vec{C}_o. \tag{3.49}$$

Here we have used the fact that the Bloch matrix $\underline{L}_{cc}$ vanishes, and have assumed that the closed-closed portion of the overlap matrix $\underline{O}$, namely $\underline{O}_{cc}$, is the unit matrix. (This can be accomplished, even for a nonorthogonal basis set, by orthogonalization of the closed-type basis functions.) The matrix $\underline{\Lambda}_{oo}$ reduces to N sepa-

rable blocks of nonzero elements, each of these blocks being of rank 1. This guarantees that the number of eigensolutions of Eq. (3.47) is N.

Inversion of the matrix $\underline{\Gamma}_{cc}$ at many energies E is efficiently accomplished by first transforming the closed portion of the basis set into the energy-independent representation in which $\underline{H}_{cc}$ is diagonal, with eigenvalues E_λ and orthonormal eigenvectors $X_{k\lambda}$. The matrix $\underline{\Omega}$ is then explicitly

$$\Omega_{kk'}=2(EO_{oo}^{kk'}-H_{oo}^{kk'}-L_{oo}^{kk'})-2\sum_\lambda \times\frac{(EO_{oc'}^{k\lambda}-H_{oc'}^{k\lambda}-L_{oc'}^{k\lambda})(EO_{c'o}^{\lambda k'}-H_{c'o}^{\lambda k'}-L_{c'o}^{\lambda k'})}{E-E_\lambda}. \tag{3.50}$$

In Eq. (3.50), the notation c' implies that the closed portion of the two-electron basis set is now in the transformed representation, i.e., $O_{oc'}^{k\lambda}=\Sigma_{k'}O_{oc}^{kk'}X_{k'\lambda}$, $O_{c'o}^{\lambda k}=\Sigma_{k'}O_{c'o}^{k'k}X_{k'\lambda}$, with the same transformation being applied also to the matrices $\underline{H}$ and $\underline{L}$. The semianalytic energy dependence of all matrices in Eq. (3.50), combined with the much smaller number of open-type basis functions than closed-type functions, now improves the speed of solving Eq. (3.47) on a fine energy mesh dramatically compared to the original Eq. (3.7).

To summarize, the eigenchannel R-matrix computational scheme in two-electron atoms consists of the following steps: (1) Choice of the reaction-volume size and of the fragmentation channels. (2) Choice of the two-electron basis set. (3) Numerical calculation of the one-electron orbitals. (4) Calculation of the matrix elements of $\underline{O}$, $\underline{H}$, $\underline{L}$, and $\underline{\Lambda}$. (5) Diagonalization of the Hamiltonian $\underline{H}_{cc}$. (6) Solution of the streamlined form of the generalized eigensystem (3.47) on a chosen energy mesh.

The eigenchannel R-matrix computation scheme in open-shell atoms proceeds along the same lines as that in two-electron atoms. However, major complications occur, mainly in steps (2)–(4). As was emphasized in Sec. D above, most difficulties occur in the construction of basis functions used for the initial- and final-state atomic wave functions. Effort goes into determining multielectron target functions and one-electron natural orbitals. The second major complication in R-matrix calculations of open-shell atoms compared to those in two-valence-electron systems concerns the computation of matrix elements. For two-electron atoms when the two-electron basis functions are chosen to be eigenfunctions of the independent-particle Hamiltonian $H_0=H-1/r_{12}$, the evaluation of matrix elements is especially straightforward and standard. The calculation of multielectron matrix elements is much more complicated and an efficient computer code has been developed to evaluate the angular parts of multielectron one- and two-particle operators (Robicheaux and Greene, 1992).

The evaluation of the $1/r_{ij}$ matrix elements and the diagonalization of the Hamiltonian $\underline{H}_{cc}$ are the most time consuming parts of the computation. However, these need to be done only once, after which the energy-dependent R matrix is determined semianalytically at all energies: this is the major advantage of both the eigenchannel and Wigner-Eisenbud formulations of R-matrix theory. A second advantage of the R-matrix method is the faster convergence achieved by limiting the variational calculation to as small a portion of configuration space as is possible.

F. Short-range reaction matrix K and parameters of multichannel quantum-defect theory

After the N eigenvalues b_β and corresponding N linearly-independent eigenvectors $C_{k\beta}$ have been obtained by solving Eqs. (3.47) and (3.49) at a given energy E, the solutions are matched to a linear combination of Coulomb functions in each open or weakly closed channel. Recalling Sec. II, we see that two alternative short-range reaction matrices can be determined. Matching to energy-normalized Coulomb functions $(f_{\epsilon_2 l_2}, g_{\epsilon_2 l_2})$ gives the short-range reaction matrix $\underline{K}(E)$ [Eq. (2.34)] or the equivalent smooth, short-range scattering matrix $\underline{S}(E)$. Matching the R-matrix eigenstates to analytic Coulomb functions $(f^0_{\epsilon_2 l_2}, g^0_{\epsilon_2 l_2})$ gives a $\underline{K}^0$ short-range reaction matrix. We restrict the following discussion to the $\underline{K}$ matrix, keeping in mind that the $\underline{K}^0$ short-range reaction matrix can also be used to solve the equations of multichannel quantum-defect theory.

Because the boundary conditions at infinity, which quantize the Rydberg energies in the closed channels, have not yet been applied, the short-range scattering matrix $\underline{S}(E)$, or the equivalent eigenchannel MQDT parameters μ_α and $U_{i\alpha}$ [Eq. (2.35)], vary relatively smoothly as functions of the energy E. The full energy dependence of $\underline{S}(E)$ is obtained by solving the generalized eigensystem of Eq. (3.47) on as fine an energy mesh as desired. When the spectrum is desired on an extremely dense energy mesh, for instance in an energy range that includes very high-lying Rydberg levels, it is more efficient to first solve Eq. (3.47) on a relatively coarse grid of selected energies. Interpolation of these smooth matrices then permits the equations of multichannel quantum-defect theory [Eqs. (2.44)–(2.46)] to be solved on an arbitrarily fine energy mesh to predict the relevant observables.

Calculation of the photoionization cross section from a low-lying level requires the additional determination of dipole matrix elements. The wave function of the initial state that will be exposed to incident radiation can be obtained by diagonalization of the Hamiltonian matrix constructed using closed-type two-electron basis functions only, provided the box is large enough to enclose its full probability density. The dipole matrix elements $\underline{d}^S$ [Eq. (2.57)] that connect the initial and final states can then be evaluated by restricting the integration volume to the interior of the R-matrix box. Likewise, the short-range matrix $\underline{S}$, the short-range dipole matrix elements $\underline{d}^S$ vary smoothly as functions of the

energy. Photoionization of an excited state, especially of a Rydberg state [as in isolated-core excitation experiments (Cooke *et al.*, 1978)], requires the inclusion of longer-range contributions to the dipole matrix elements. In many cases this can be performed analytically, as is discussed in Sec. IV below.

As illustrated later in Secs. IV and V, in energy domains involving sharp resonances, reliable comparison between theory and experiment should use a theoretical spectrum convolved with the experimental linewidth. To obtain a convolved cross section that can be compared to experiment, the cross section needs to be calculated on an extremely fine mesh before numerically convolving it. This is a wasteful procedure since the short-range MQDT parameters do not vary much with energy. Robicheaux (1993) developed a procedure to obtain a convolved total cross section directly from the smooth scattering parameters that avoids explicitly performing numerical convolution. The approximate formula derived for photoabsorption by neutral species is accurate to the extent that the short-range scattering parameters do not vary over the convolution width. This preconvolved technique was used in some recent works (Chen and Robicheaux, 1994; Miecznik and Greene, 1996).

Figure 7 illustrates the energy dependence of the MQDT parameters and the implication of this dependence on the final results. Figure 7 compares the eigenquantum defects μ_α and photoabsorption spectra of Ba obtained from R-matrix calculations using $r_0=15$ a.u. or 20 a.u. Figures 7(a) and 7(b) display the μ_α obtained for the $^1P^o$ symmetry as functions of the energy relative to the double-ionization limit, for a wide energy range from below the $6s$ threshold to above the $6p$ thresholds. The μ_α vary smoothly with the energy whatever the value of r_0, but comparison of curve (a) obtained with $r_0=15$ a.u. with curve (b) corresponding to $r_0=20$ a.u. shows that the energy dependence of the μ_α increases with r_0. Such r_0 dependence of the μ_α was encountered in all cases we considered, but disappeared in the final results. Photoionization cross sections for the photoabsorption spectrum between the $5d_{5/2}$ and $6p_{1/2}$ thresholds calculated, in the velocity form, by combining LS-coupled R-matrix calculations done for the $^1P^o$, $^3P^o$, and $^3D^o$ symmetries with the jj-LS frame transformation are displayed in Fig. 7(c). The differences between the full line ($r_0=15$ a.u.) and the dashed line ($r_0=20$ a.u.) are not significant, being of the same order of magnitude as the differences between length and velocity results for a given r_0. Note that the calculations were performed with small two-electron basis sets, resulting in poor convergence of the variational calculation.

In the nearly *ab initio* theoretical multichannel spectroscopy, three different kinds of MQDT calculations have been carried out using the dynamical quantities $\underline{S}$ and $\underline{d}^S$ obtained by eigenchannel R-matrix calculations.

1. R-matrix calculations in LS coupling

Calculations in LS coupling (denoted as LS calculations) neglect spin-orbit effects everywhere. These calculations start from the LS-coupled matrices $\underline{S}^{LS}$ and $\underline{d}^S_{LS}$ derived from the nonrelativistic Hamiltonian [Eq. (3.22)]. The MQDT fragmentation channels for this type of calculation are the LS-coupled channels $i=\{n_1 l_1 l_2\}$ introduced in Sec. III.B.2 above. We will see in Sec. IV that the nonrelativistic LS method is adequate for describing low-resolution photoabsorption spectra that are incapable of resolving fine-structure splittings.

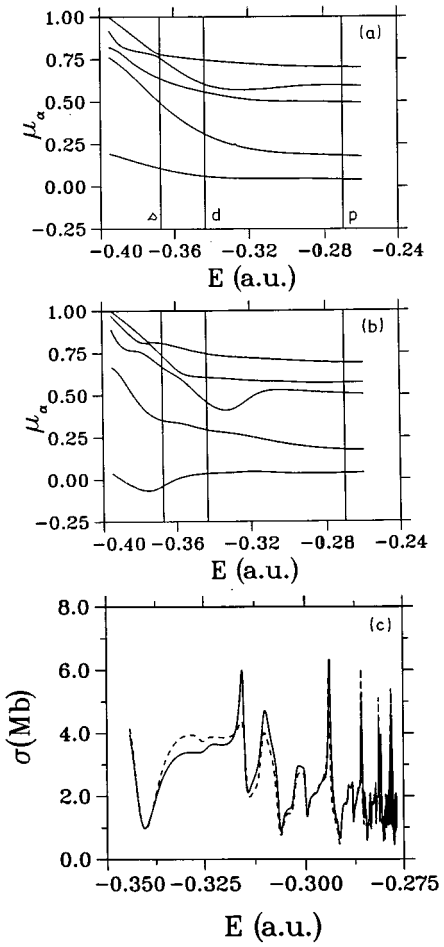

FIG. 7. Comparison of eigenquantum defects μ_α and photoabsorption spectra obtained in Ba with LS-coupled eigenchannel R-matrix calculations performed using different reaction-volume sizes and combined with the jj-LS frame transformation: (a) eigenquantum defects μ_α for the $^1P^o_1$ symmetry obtained with r_0 = 15 a.u.; (b) eigenquantum defects μ_α for the $^1P^o_1$ symmetry obtained with r_0 = 20 a.u.; (c) photoabsorption spectrum between the $5d_{5/2}$ and $6p_{1/2}$ ionization limits calculated using r_0 = 15 a.u. (solid line) and r_0 = 20 a.u. (dashed line). The vertical bars in (a) and (b) correspond to the $6s$, $5d$, and $6p$ ionization limits. The energies are referred to the double-ionization limit.

2. R-matrix calculations in LS coupling combined with the jj-LS frame transformation

Calculations start from the nonrelativistic LS-coupled quantities, but then apply the jj-LS frame transformation (see Sec. II.E) and perform the MQDT

calculation using experimental fine-structure ionization thresholds. These calculations are denoted as jj-LS (or frame-transformation) calculations. The MQDT fragmentations channels for this type of calculation are the jj-coupled channels $i=\{n_1 l_1 j_1 l_2 j_2\}$ introduced in Sec. III.C above.

The approximations embodied in the jj-LS frame transformation are accurate as long as $\underline{K}(E)$ does not vary appreciably over an energy range comparable to the fine-structure splitting of the A^+ core levels. As is visible on Fig. 7, at the low-energy end in each channel the MQDT parameters acquire a strong energy dependence. The use of experimental thresholds in strongly closed channels can adversely affect the MQDT calculation of observables, sometimes causing spurious resonances to appear or physical resonances to disappear. These instabilities are due to the exponential growth of Coulomb functions associated with the strongly closed channels. The use of the frame transformation in this energy range requires extra caution. It was found to be crucial that spin-orbit-averaged *theoretical* energies be introduced instead of *experimental* ones for the threshold energies associated with the strongly closed channels treated as weakly closed and also, as documented in Secs. IV and V, with some particular weakly closed channels supporting an isolated level at the low end of the channel. To minimize these difficulties it is also advisable to include only the weakly closed channels involved in the energy range under consideration. As shown later in Secs. IV and V, the jj-LS method can quantitatively describe a class of nonperturbative spin-orbit effects even in some atoms as heavy as barium or as complicated as scandium and titanium.

3. R-matrix calculations in jj coupling

We denote as jj calculations any jj-coupled R-matrix calculations based on the Hamiltonian that includes spin-orbit interactions both inside and outside the R-matrix box. At the present time, calculations using the jj-coupled eigenchannel R-matrix approach deal only with two-electron systems, and the discussion below concerns only alkaline earths.

The jj method is needed when the ionic fine-structure splittings become as large as 1 eV or more. The jj method is also recommended for calculations requiring a large reaction volume. Indeed, the energy dependence of MQDT parameters rapidly increases with r_0, and results obtained using the jj-LS method can drastically depend on the choice of either the experimental or the theoretical ionization thresholds for the closed channels.

Even using the jj method, some results, such as those obtained for $6d^2$ and $7p^2$ levels of Ba (Lecomte *et al.*, 1994), depend slightly on the choice of the threshold energies although the experimental threshold energies used in the MQDT calculations are very close to the theoretical energies introduced in the matching procedure. An adaptation of the streamlined eigenchannel method recently developed to circumvent these difficulties occurring at the bottom end of Rydberg series, where MQDT parameters acquire the strongest energy dependence, is presented in Sec. III.H below.

Finally, it is worth comparing the approximations used in eigenchannel R-matrix calculations to take into account relativistic effects to those used in Wigner-Eisenbud-type R-matrix calculations. To our knowledge, in the Wigner-Eisenbud R-matrix formalism, the frame-transformation treatment has been used for studying electron-atom scattering processes only. So, for instance, starting from LS-coupled reaction matrices obtained by LS-coupled R-matrix calculations, Saraph (1978) used the jj-LS frame transformation for computing collision strengths for transitions between fine-structure levels. Another way to include relativistic terms is to reduce the fully relativistic Dirac plus Breit equations to the Breit-Pauli form (Condon and Shortley, 1935) and to retain either all terms of the Breit-Pauli Hamiltonian or only the one-particle operators. This approach was developed by Scott and Burke (1980) and was first applied to the calculation of collision strengths in Be-like Fe XXIII. As further documented in Secs. IV and V, the same approach has also been employed by Bartschat and co-workers to investigate Sr, Ba, Zn, and Hg photoionization (Bartschat and Scott, 1985a, 1985b; Bartschat *et al.*, 1986, 1991; Bartschat, 1987; Mende *et al.*, 1995). The approximations embodied in the calculations that include only the one-particle terms of the Breit-Pauli Hamiltonian are comparable to those involved in the jj-coupled eigenchannel R-matrix calculations. To go beyond the approximations underlying the jj-coupled eigenchannel R-matrix method or the Breit-Pauli R-matrix method of Scott and Burke (1980), R-matrix calculations should be based on the Dirac Hamiltonian as was performed early by Chang (1975, 1977). This point will be further documented in Sec. VI.

G. Reaction volume size, basis functions, and fragmentation channels

This section focuses on practical considerations on the eigenchannel R-matrix technologies. Most of the calculations carried out using the eigenchannel R-matrix approach have dealt with alkaline earths. Moreover, the techniques used in open-shell atoms are dependent on the atom being studied. Accordingly, the following section is restricted to two-electron systems.

Prior to each eigenchannel R-matrix calculation, it is necessary to decide which channels should be treated as open, weakly closed, or strongly closed in the studied energy range. This choice is important in order to select the reaction-volume boundary r_0 and the two-electron functions to include in the variational calculation. However, the choice is not unique, as will be stressed later.

First, we document the choice of the reaction volume size. As a first criterion, the reaction volume V should be large enough to include the charge distributions of the ionic states $A^+ n_1 l_1$ involved in the open or weakly closed fragmentation channels. The majority of the R-matrix calculations performed in recent years have dealt with energies lower than the lowest $A^+ m_0 p$

threshold (m_0= 2, 3, 4, 5, 6 for Be, Mg, Ca, Sr, Ba, and Ra, respectively) and $n_1 l_1 n_2 l_2$ states corresponding to an orbital momentum l_2 for the outer electron such as $l_2 \leqslant 4$. Calculations in the lighter elements Be and Mg have typically used $r_0 \sim 9$–12 a.u. Those for the heavier elements Ca to Ra have used $r_0 \sim 15$–22 a.u. owing to the smaller binding energies of the ion (Greene and Aymar, 1991). A calculation of the Ca photoabsorption spectrum from the $4p$ threshold up to nearly the $6s$ threshold (Kim and Greene, 1988) and recent calculations of several autoionizing Rydberg series of Ba below the $7p$ threshold (Luc-Koenig and Aymar, 1992; Aymar *et al.*, 1994; Luc-Koenig, Aymar, and Lecomte, 1994; Luc-Koenig, Lecomte, and Aymar, 1994; Aymar and Luc-Koenig, 1995; Luc-Koenig *et al.*, 1995; van Leeuwen *et al.*, 1995, 1996) use larger r_0 values in the range of 30–50 a.u. The largest box sizes used in calculations of this type are around $r_0 \sim 100$–120 a.u.; they were used in the investigations of Ba near the $8s$ threshold, of Sr near the $6f, 6g, 6h$ thresholds (Wood and Greene, 1994) and also in the study of H^- and Li^- up to the $n=6$ thresholds (Pan *et al.*, 1994).

It is worth noting that the size of the reaction volume does not depend solely on the extent of the ionic levels that must be enclosed in the reaction volume. It is also governed by the value of the orbital momentum l_2 corresponding to the Rydberg or continuum electron. For calculations that neglect multipole interactions beyond the reaction volume V, a larger box size r_0 helps to describe these interactions accurately within V. These multipole effects play an especially important role in determining the small quantum defects for large l_2 values. Thus, for example, g-wave quantum defects are better described in Mg using $r_0=20$ a.u. than using 12 a.u. (Lindsay, Dai, *et al.*, 1992). In Sr also, a better description of the $4dng$ levels was found using $r_0=35$ a.u. instead of $r_0=20$ a.u. (Goutis *et al.*, 1992). Recently, from the observation of $7sni$ Rydberg series of Ba (Camus, Mahon, and Pruvost, 1993), it has been shown that a very good description of the measured quantum defects for $7sni$ Rydberg series is attained using $r_0 \sim 50$–60 a.u., while poor results are obtained using $r_0=30$ a.u. (Aymar *et al.*, 1994). The highest partial waves included in such calculations are up to $l_2 \sim 10$ in the Ba calculation of Wood and Greene (1994). These authors performed R-matrix calculations in jK coupling with an R-matrix box of 100 a.u.

Recently, Wood and Greene (1994) extended the eigenchannel R-matrix approach to include effects of long-range multipole interactions beyond the R-matrix reaction volume. More precisely, the Ψ_β eigensolutions and their derivatives have been propagated from r_0 to a larger radius r_0' by solving the close-coupling equations without exchange for $r \geqslant r_0$. Higher l_2 values can be studied without increasing the size of the reaction volume. l_2 values up to $l_2=12$ have been investigated in Sr, by propagating the solutions from $r_0=100$ a.u. up to $r_0' \sim 250$ a.u. Similarly, Pan *et al.* (1994) successfully analyzed highly doubly excited states converging onto the nearly degenerate thresholds $n=6$ in H^- and Li^-.

TABLE II. Closed-type basis set of $nlml'$ functions used for the $^1P^o$ symmetry of Ca.

$nsmp$	$4 \leqslant n \leqslant 8$	$4 \leqslant m \leqslant 9$	$+9s4p$
$npmd$	$4 \leqslant n \leqslant 8$	$3 \leqslant m \leqslant 8$	$+9p3d$
$ndmf$	$3 \geqslant n \leqslant 7$	$4 \leqslant m \leqslant 8$	$+3d9f$

Our aim now is to give details on the choice of the variational basis sets and to show that this choice is determined by the accuracy desired in the description of the physical observables. We concentrate on two simple examples.

The first example concerns an investigation of the Ca $^1P^o$ spectrum, which was studied by Greene and Kim (1987) over a range of energy from far below the $4s$ ionization threshold up to the $4p$ threshold. An accurate description of the bound spectrum and of the photoabsorption spectrum was obtained using small-scale LS-coupled R-matrix calculations. The five open or weakly closed channels relevant to the autoionizing energy range below the $4p$ threshold were: $4snp$, $3dnp$, $3dnf$, $4pns$, and $4pnd$. The calculation used an R-matrix boundary of $r_0=18$ a.u., which easily encloses the charge distribution of the Ca^+ $4p$ state within the reaction volume. Table II lists the closed-type basis set, which consists of 88 $n_1 l_1 n_2 l_2$ functions. This set was complemented by 15 open-type basis functions associated with the open or weakly closed channels, which results in a total of 103 two-electron basis functions. For each open or weakly closed channel, three open-type basis functions were included and another five or six closed-type basis functions. A total of 28 closed-type basis functions were used for these MQDT fragmentation channels, while another 60 closed-type functions were used to describe the strongly closed channels converging onto the Ca^+ ns, np, nd, and nf thresholds lying higher than the Ca^+ $4p$ threshold. At energies below the $4s$ threshold, the $3dnf$, $4pns$, and $4pnd$ channels are strongly closed, meaning that the energy is still below the first states in those channels. Accordingly, the R-matrix basis set used in this energy range did not contain any open-type functions for these channels. However, the same set of closed-type basis functions was used, which results in 94 two-electron basis functions.

The size of the basis set to be used strongly depends on the degree of convergence desired. Tests showed that the qualitative shape of the photoabsorption spectrum of Ca between the $4s$ and $3d$ thresholds could be obtained using only thirteen (three in the open channel and two in the weakly closed channels) basis functions (instead of 103) and $r_0=12$ a.u. (instead of 18 a.u.). However, the quality of the variational wave functions, as judged by the agreement between length and velocity results, is greatly improved by including a large set of strongly closed channels. Unfortunately, there is no general criterion for choosing the basis set before doing a calculation, whereas, after having done a calculation with a large basis, it is possible to eliminate basis func-

TABLE III. Closed-type basis set of $nlml$ functions used for the $^1S^e$ symmetry in Sr and Ba.

For $0 \leq l \leq 5$	$n_l \leq n \leq n_l+7$	$n_l+1 \leq m \leq n_l+7$
For $l=6$	$n_l \leq n \leq n_l+5$	$n_l+1 \leq m \leq n_l+5$
With	$l=0,1$	$n_s=n_p=m_0$
	$l=2$	$n_d=m_0-1$
	$l \geq 3$	$n_l=l+1$

tions y_k whose contributions are clearly negligible from inspection of the eigenvectors $C_{k\beta}$ corresponding to the different eigenvalues b_β in Eq. (3.7) or Eqs. (3.47) and (3.49).

The second example corresponds to the even-parity $J=0$ spectra of Sr and Ba investigated below the m_0p threshold. LS-coupled R-matrix calculations were combined with the jj-LS frame transformation (Sec. II.E). The Sr R-matrix calculations (Kompitsas *et al.*, 1991) for the $^1S^e$ and $^3P^e$ symmetries used a box size of $r_0=20$ a.u. The $^1S^e$ calculation included three open or weakly closed channels: m_0sns, $(m_0-1)dnd$, and m_0pnp. Table III lists the configurations included in the closed-type basis set. It consists of 237 $n_1l_1n_2l_2$ configurations with $l_2 \leq 6$. The additional 15 open-type basis functions associated with the open and weakly closed channels give a total of 246 two-electron basis functions. Among them, only 33 are associated with the open or weakly closed channels (eight closed-type functions and three open-type functions per channel).

To achieve convergence for the energy of the strongly correlated Ca $4p^2\ ^1S_0$ (Aymar and Telmini, 1991; Assimopoulos *et al.*, 1994), Sr $5p^2\ ^1S_0$ (Kompitsas *et al.*, 1991), and Ba $6p^2\ ^1S_0$ levels (Greene and Theodosiou, 1990; Greene and Aymar, 1991; Wood *et al.*, 1993), it was found essential to include a large number of closed-type $n_1l_1n_2l_2$ functions involving large orbital momenta $l_1, l_2 \geq 3$. This large number of functions represents high doubly-excited-type configurations that would frequently be neglected (Bartschat and Greene, 1993) but play an unexpectedly large role for these resonances unusually sensitive to the chosen model.

More generally, the LS-coupled R-matrix calculations performed at relatively low energies below the m_0p threshold typically use 100 to 400 basis functions to describe two to five open and weakly closed fragmentation channels. When the R matrix is set up in jj coupling, the number of basis functions is larger, typically by about a factor of three (or four), accounting for the three (or four) different LS symmetries generally involved in a single J symmetry. The most recent calculations performed in jj coupling at higher energies (Aymar *et al.*, 1994; Luc-Koenig, Aymar, and Lecomte, 1994; Luc-Koenig, Lecomte, and Aymar, 1994; Aymar and Luc-Koenig, 1995; Luc-Koenig *et al.*, 1995; van Leeuwen *et al.*, 1995, 1996) involve 30 to 50 fragmentation channels which are described by 1000 to 2500 basis functions. Some convergence-test calculations involve up to 5000 basis functions. The convergence of the variational calculation with respect to the basis-set size is dramatically slowed down if a value of r_0 is used that is larger than necessary. Indeed, the number of basis functions probably increases in proportion to $r_0{}^2$. As a rule of thumb, it is our experience that for $r_0 \leq 15$ a.u., good convergence is achieved using only six closed-type basis functions per channel. This number should be increased to eight for $r_0 \sim 20$ a.u. and to 15–18 for $r_0 \sim 50$ a.u.

The choice of open channels to be included in the calculation is easy because, for given symmetry and energy range, there exists a finite set of open channels. R-matrix calculations of autoionizing levels located below the $A^+\ (m_0+1)p$ threshold explicitly introduced all relevant open channels. In contrast, the number of closed channels is infinite. The choice of which weakly closed and strongly closed channels to include in the R-matrix calculation is not unique. In particular, it depends on which short-range reaction matrix $\underline{K}(E)$ or $\underline{K}^0(E)$ is used in the MQDT calculations. R-matrix calculations performed to determine a $\underline{K}(E)$ matrix should treat the channel $i=\{n_1l_1l_2\}$ as strongly closed when the photoelectron energy is smaller than $-1/2l_2^2$. This restriction can be bypassed by using a $\underline{K}^0$ matrix. However, as shown below, the use of a $\underline{K}^0$ matrix complicates the calculations.

Although no fully general rule has been found to choose the channels to be treated as weakly closed or strongly closed, from our experimentation we recommend:

(1) The use of matrices $\underline{K}$ rather than matrices $\underline{K}^0$. For a given energy range, the matrix $\underline{K}$ refers to fragmentation channels i in which the photoelectron energy is larger than $-1/2l_2^2$. This leads to treatment of a specific channel $i=\{n_1l_1l_2\}$ as strongly closed when the photoelectron energy is smaller than $-1/2l_2^2$. Thus, MQDT calculations over a large energy range require the determination of several $\underline{K}$ matrices involving different sets of fragmentation channels. It is also crucial to introduce a large number of strongly closed channels to get converged results. MQDT calculations with a fixed number of fragmentations channels could be conducted over a large energy range with a single $\underline{K}^0$ matrix that is able to treat all fragmentation channels throughout the energy range independently of how the photoelectron energy compares to $-1/2l_2^2$. Such treatment does not affect the results, but it complicates the calculations by increasing the number of fragmentation channels. Furthermore, in the low-energy range this causes avoided crossings and strong energy dependences of the μ_α and also near degeneracies among some of the μ_α.

(2) Inclusion of all weakly closed channels relevant to the studied energy range and symmetry. Failure to include all weakly closed channels can distort the final results, especially when the neglected channels interact strongly with weakly closed channels included in the calculation. This can induce rapid increase by one unit of some eigenquantum defects μ_α, in particular when the lowest resonances in the weakly closed channel treated as strongly closed lie in the studied energy range. This may also cause adverse effects on the results. In particular, the resonances in the omitted channels will lie much too high in energy unless these resonances fit inside the

R-matrix reaction volume (Kim and Greene, 1988; Lecomte *et al.*, 1994, 1995). However, our experience has shown that treating weakly closed channels that do not interact significantly with the channels under study as strongly closed makes no differences in many cases. Closed channels $n_1 l_1 l_2$ with relatively high l_2 values can often be treated as strongly closed. For example, results on $4fnf$ levels obtained by treating the $4fnh$ channels as strongly closed (Luc-Koenig, Aymar, and Lecomte, 1994) agree perfectly with those obtained by treating the $4fnh$ channels as weakly closed (van Leeuwen *et al.*, 1995).

(3) Caution when using a large reaction volume. Difficulties related to the exponential growth of closed-channel Coulomb solutions (for which asymptotic boundary conditions have been postponed) are amplified. Moreover, it was found that when the lowest resonances belonging to a weakly closed channel fit inside the R-matrix box then this channel becomes uncoupled from the others and its eigenquantum defect μ_α decreases rapidly with energy (Kim and Greene, 1988; Lecomte *et al.*, 1995). An adaptation of the eigenchannel method developed recently to circumvent the difficulties occurring at the bottom end of Rydberg series, where MQDT parameters acquire the strongest energy dependence, is presented in Sec. III.H below.

H. Alternative streamlined solutions of the generalized eigensystem

An adaptation of the streamlined eigenchannel method was recently developed to circumvent the difficulties encountered in describing doubly excited states of alkaline earths that are located at the bottom end of Rydberg series. The method developed for studying $6d^2$ and $7p^2$ autoionizing levels of Ba (Lecomte *et al.*, 1994) reduces to identifying some levels enclosed in the reaction volume with bound states and treating their interactions with the open continua. The method is close in spirit to the Fano's (1961) configuration-interaction method, which dealt with the same situation.

First, consider the treatment of the $6d^2$ levels, which are located above the $6s$, $5d$, and $6p$ thresholds, and which do not interact with Rydberg series converging to thresholds higher than $6p$. Instead of viewing the $6d^2$ levels as the lowest members of Rydberg series converging to $6d_j$ thresholds and treating their interaction with the open channels using standard MQDT techniques, a reaction volume ($r_0 \sim 40$–50 a.u.) is chosen to be large enough to enclose the $6d^2$ levels. The $6dnd$ channels are treated as strongly closed channels in the energy range enclosing the $6d^2$ resonances. The eigenchannel R-matrix method is employed to construct a matrix $\underline{R}$ restricted to open channels from which a scattering matrix $\underline{S}$ referring to open channels only is deduced [Eqs. (2.34) and (2.43)].

As in the standard streamlined eigenchannel R-matrix method, the two-electron basis functions are partitioned into two distinct sets. However, in contrast with this former approach (Sec. III.E), the partition does not depend on the type (open or closed) of the basis functions but on the nature of the channels they describe:

(i) Open channels: each of the N_0 open channels converging to the $6s$, $5d$, or $6p$ ionization limits is described not only by some open-type functions but also by several closed-type functions. The corresponding set of two-electron functions is denoted $\{\bar{o}\}$.

(ii) Strongly closed channels: a great number of basis functions describes strongly closed channels converging onto thresholds located higher than the $6p$ threshold; among them there are the $6dnd$ channels. The corresponding basis functions, constructed from closed-type functions only, form the set denoted $\{\bar{c}\}$.

Two key points follow from the new partition:

(1) As in the streamlined eigenchannel R-matrix method, the eigensystem [Eq. (3.7)] is transformed by partitioning the matrices $\underline{\Gamma}$, $\underline{\Lambda}$, and $\underline{O}$ into submatrices referring to the subsets $\{\bar{o}\}$ and $\{\bar{c}\}$ and then transformed again into a representation in which the closed portion of the Hamiltonian $\underline{H}_{\bar{c}\bar{c}}$ is diagonalized using an orthogonal eigenvector matrix $\underline{W}$. Among the eigenstates of $\underline{H}_{\bar{c}\bar{c}}$, those corresponding to the lowest eigenvalues can be identified with physical low-lying doubly excited states such as $6d^2$, $7p^2$, $7s5g, \ldots$ enclosed within the reaction volume. Corresponding states (denoted as Φ_r) are grouped in a first set denoted $\{r\}$. A second set $\{p\}$ groups the remaining eigenstates, which cannot be identified with physical states; these eigenstates describe polarization effects. The division of the set $\{\bar{c}\}$ into the sets $\{r\}$ and $\{p\}$, which depends on the studied energy range, is somewhat arbitrary, but the final results are completely independent of this division.

With this new partition, some submatrices that do not have zero values in the standard streamlined eigenchannel R-matrix formulation now vanish. More precisely, one has

$$\underline{L}_{\bar{o}\bar{c}}=0, \quad \underline{O}_{\bar{o}\bar{c}}=0, \quad \text{and} \quad \underline{O}_{\bar{c}\bar{o}}=0. \tag{3.51a}$$

Moreover, $\underline{\Gamma}_{oc}$ [Eqs. (3.9) and (3.51a)] reduces to

$$\underline{\Gamma}_{\bar{o}\bar{c}}=-2\underline{H}_{\bar{o}\bar{c}}. \tag{3.51b}$$

As detailed by Lecomte *et al.* (1994), the generalized eigensystem can be transformed into the form

$$\underline{\Gamma}'\vec{x}_{\bar{o}}\equiv[\underline{\Gamma}'_{\bar{o}\bar{o}}-\underline{\Gamma}'_{\bar{o}r}\tfrac{1}{2}(E-E_r)^{-1}\underline{\Gamma}'_{r\bar{o}}]\vec{x}_{\bar{o}}=\underline{\Lambda}_{\bar{o}\bar{o}}\vec{x}_{\bar{o}}b, \tag{3.52a}$$

$$\vec{x}_r=-\tfrac{1}{2}(E-E_r)^{-1}\underline{\Gamma}'_{r\bar{o}}\vec{x}_{\bar{o}}, \tag{3.52b}$$

where the matrix $\vec{x}_r$ represents the amplitudes of the function Φ_r, associated with the eigenvalues E_r, in the N_o eigensolutions Ψ_β. In Eq. (3.52a), the matrix

$$\underline{\Gamma}'_{\bar{o}\bar{o}}=\underline{\Gamma}_{\bar{o}\bar{o}}-\underline{\Gamma}_{\bar{o}\bar{c}}\underline{W}_{\bar{c}p}\tfrac{1}{2}(E-E_p)^{-1}\underline{W}^t_{p\bar{c}}\underline{\Gamma}_{\bar{c}\bar{o}} \tag{3.53a}$$

includes the contribution of the eigenstates of $\underline{H}_{\bar{c}\bar{c}}$ describing polarization effects. The matrix

$$\underline{\Gamma}'_{\bar{o}r}=\underline{\Gamma}_{\bar{o}\bar{c}}\underline{W}_{\bar{c}r} \tag{3.53b}$$

couples the physical eigenstates Φ_r to the set $\{\bar{o}\}$ describing the open channels.

(2) A second key point of the new partition and of the subsequent transformation of Eq. (3.7) into Eq. (3.52) is that, from Eqs. (3.9) and (3.51b), the matrix $\underline{\Gamma}'_{r\bar{o}}$ is such that each of its elements is proportional to the matrix element of $1/r_{12}$ between a particular state Φ_r and a particular function of the set $\{\bar{o}\}$ that describes continua.

As detailed by Lecomte *et al.* (1994), the new partition permits an easy identification of doubly excited states within the R-matrix box. Moreover, the construction of the matrix $\underline{R}$ associated with the solutions of the eigensystem [Eq. (3.52)] gives a scattering matrix $\underline{S}$ in a form well suited to resonance analysis. This matrix is expressed as the sum of a nonresonant part ($\underline{S}^{(0)}$) and a resonant part as

$$S_{ij}=S_{ij}^{(0)}-2i\pi\sum_{aa'\in\{r\}}T_{ia}^{t}\left(E-E_r-\underline{\Delta}_{rr}+\frac{i}{2}\underline{\gamma}_{rr}\right)^{-1}_{aa'}T_{a'j}. \tag{3.54}$$

The background matrix $\underline{S}^{(0)}$ varies very slowly with energy. This matrix describes the continua when the doubly excited levels Φ_r and the open channels are not coupled, i.e., when $\underline{\Gamma}'_{r\bar{o}}=0$; this matrix was obtained from a separate R-matrix calculation involving a basis excluding the doubly excited levels contained in the set $\{r\}$. In the resonant part, $\underline{\Delta}_{rr}$ and $\underline{\gamma}_{rr}$ are shift and width matrices, respectively, and the matrix $\underline{T}$ represents the $1/r_{12}$ interaction between the doubly excited states Φ_r (set $\{r\}$) included in the R-matrix box and the nonresonant continua.

We consider now the treatment of $7p^2$ levels or higher-lying nl^2 levels, such as $4f^2$ levels, that are mixed with neighboring levels pertaining to Rydberg series converging to high-lying thresholds. The approach developed to treat the $6d^2$ levels, where no weakly closed channel are introduced, is no longer valid to describe these levels. An extension of the approach discussed above allows the mixing between the $7p^2$ or $4f^2$ levels and the Rydberg series to be accounted for (Lecomte *et al.*, 1994, 1995). The $6d^2$, $7p^2$, and $4f^2$ levels are still assumed to be contained and identified within the reaction volume, i.e., the channels converging to the $6d$, $7p$, and $4f$ thresholds are still treated as strongly closed channels. However, some channels treated as strongly closed in the previous formulation are now treated as weakly closed in order to describe Rydberg levels that are not included in the reaction volume. The R-matrix calculation gives a short-range scattering matrix referring to open and closed channels. The resonances correspond either to the doubly excited states Φ_r enclosed within the reaction volume or to levels pertaining to the weakly closed channels. The two types of resonances can be analyzed simultaneously, as described by Lecomte *et al.* (1995).

IV. ALKALINE-EARTH ATOMS

This section describes the multichannel spectroscopy of a variety of different atoms and different symmetries. Our efforts concentrate on the alkaline-earth atoms ranging from beryllium to radium, i.e., on two-electron atoms for which the long-range potential experienced by a single escaping electron is Coulombic. Another class of two-electron systems will not be treated in detail but only succinctly mentioned in this review. It concerns two-electron systems for which the long-range electron-core potential differs from a pure attractive Coulomb field. This second class includes atomic helium, the hydrogen negative ion, and the alkali negative ions.

Our goals for this section are:

(1) To show, with examples, how complex spectra provide us with a window into the nature of channel interactions. Theoretical multichannel spectroscopy provides a powerful way of analyzing the global aspects of the short-range dynamics that are common to the entire energy-level and autoionizing pattern of a spectrum. We also develop practical graphical techniques for opening this dynamical window.

(2) To develop in detail one particularly powerful approach to the calculation of complex spectra. This approach marries the techniques of multichannel spectroscopy (or multichannel quantum-defect theory) to the eigenchannel R-matrix method. We refer to this general computational scheme as nearly *ab initio* multichannel spectroscopy; its strength is the capability to calculate the short-range scattering parameters relating to both open and closed channels. Practical considerations of the method will be stressed and its current limitations will be described.

(3) To develop a catalog of the types of spectra that can be observed. The catalog not only illustrates the great diversity of photoabsorption spectra, it also verifies the general applicability of the nearly *ab initio* approach to calculate many different observables over broad energy ranges. Section A deals with bound spectra. Sections B and C show how to extract information on the autoionizing resonances without reference to the excitation process. Section B is devoted to the energy-level structure of autoionizing spectra, and Sec. C concerns the autoionization widths and branching ratios. Sections D and E deal with two kinds of photoionization spectra corresponding to different excitation schemes starting from either a low-lying or a Rydberg level. Accurate results can be obtained, not only for the most common observables such as energy-level positions and total photoionization cross sections, but also for observables more sensitive to channel interactions and spin-orbit effects. Special attention will be given to anisotropic observables such as the photoelectron angular distributions.

(4) To demonstrate how multichannel spectroscopy permits the extraction of regularities and differences among the channel interactions for different atoms and symmetries. These are harder to extract from raw spectra for two reasons: (i) multichannel resonant spectra are so complicated in general that it is hard to extract anything simple from the spectrum of one atom to compare with that of another atom; (ii) complex spectra depend on other details, such as the ionic threshold ener-

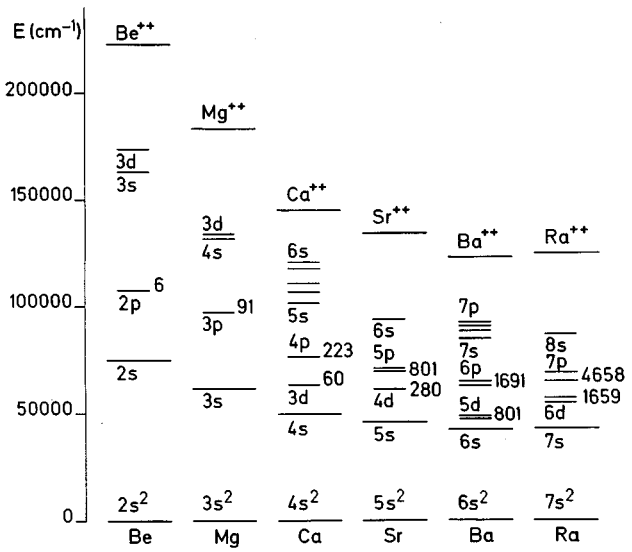

FIG. 8. Schematic energy diagram of the alkaline-earth atoms Be to Ra, displaying the lowest ionization limits with their fine-structure splittings (in cm^{-1}) and the double-ionization limits. For each atom, the energy is relative to the $m_0 s^2$ ground state.

gies, which can greatly modify one atom's spectral appearance from that of a comparable atom even if the channel-interaction parameters are identical.

(5) To assess the validity of assumptions made in semiempirical quantum-defect studies that fit MQDT parameters to reproduce experimental data. Results obtained by combining the R-matrix and MQDT methods are compared to those provided by semiempirical and other *ab initio* approaches. These comparisons show that the calculation of short-range scattering parameters by the eigenchannel R-matrix method greatly enhances the predictive power of multichannel spectroscopy. At the same time, we show that many semiempirical studies carried out prior to these nearly *ab initio* studies were able to unravel the spectra successfully.

Some readers may prefer to skim this section to get a flavor for the different types of spectra that are possible for multichannel systems. Most of the individual subsections in the following are self-contained to encourage this approach. At the same time, we have attempted to cover a substantial fraction of the work in this area in recent years, to permit use of this section as an encyclopedia of alkaline-earth spectra.

A. Discrete spectra

Figure 8 compares schematic energy diagrams of all of the alkaline-earth atoms. Over the energy range considered here, the electrons in the closed shells of the doubly charged ionic core cannot be excited. We treat only two-electron excitations in the range extending from the ground state, denoted as $m_0 s^2$ (Be, m_0 =2, Mg, m_0 =3; Ca, m_0 =4; Sr, m_0 =5; Ba, m_0 =6, Ra, m_0 =7), to the double ionization limit A^{++}. The positions of the lowest ionization limits and their fine-structure splittings are indicated on Fig. 8 for each atom.

The energy-level structure of the alkaline-earth atoms differs qualitatively from the spectrum of a one-electron atom or ion, with the alkaline earths exhibiting far greater complexity. In particular, Rydberg states of the outer valence electron attached to different states of the inner valence electron can perturb each other strongly, especially when states of the same symmetry become nearly degenerate in energy. The resulting channel interactions produce great visual complexity in the valence photoabsorption spectrum, even though only two electrons participate. A major difference between the "lighter" alkaline-earth atoms Be and Mg and the "heavier" alkaline earths Ca, Sr, Ba, and Ra is that the first excited state of Be^+ and Mg^+ is the $m_0 p$ state, whereas it is the $(m_0-1)d$ state for the heavier alkaline-earth ions. The lightest alkaline-earth atoms Be and Mg have comparatively few doubly excited perturbing levels in the bound-state spectrum below the first ionization threshold, whereas the perturbations are numerous in Ca, Sr, Ba, and Ra, even at such low energies. Accordingly, the following discussion of the bound Rydberg series perturbations focuses on the heavier alkaline-earth atoms.

Eigenchannel R-matrix calculations have been carried out both in LS and jj coupling schemes to analyze the perturbations of bound Rydberg series $m_0 snl$ by low-lying doubly excited levels located below the first $m_0 s$ ionization limit. Not surprisingly, these perturbations strongly affect the energy-level structure and other observables that are even more sensitive to channel mixing. Effects of perturbations on energy spectra and on other observables will be discussed in succession.

1. Energy spectra

Figure 9 compares the Lu-Fano plots of the odd-parity $J=1$ bound levels for all of the "heavier" alkaline-earth atoms: Ca, Sr, Ba, and Ra. On each Fig. 9(a) to 9(d), the solid curve shows the quantum defects calculated using the eigenchannel R-matrix method, while the points give the quantum defects of the experimental levels (Moore, 1949, 1952, 1958; Tomkins and Ercoli, 1967; Armstrong *et al.*, 1979, 1980). As explained in Sec. II.F, the theoretical quantum defects are shown as continuous curves, whereas the quantum defect of each experimental level is a discrete point. The continuity of the resulting plot improves our ability to visualize the full energy dependence of the quantum defects. The perturbation of the $m_0 snp\ ^1P$ Rydberg series of Ca [Fig. 9(a)] or Sr [Fig. 9(b)] by the $(m_0-1)dm_0 p\ ^1P$ doubly excited state was well described by a two-channel R-matrix calculation in LS coupling (Greene and Kim, 1987; Aymar *et al.*, 1987). Compared to Ca and Sr, the $J=1^o$ spectrum of Ba [Fig. 9(c)] displays much greater complexity. In Ba, it is no longer possible to neglect spin-orbit effects; these have been accounted for approximately in the calculation through the jj-LS frame transformation. A quantitative description of the $J=1^o$ bound spectrum of Ba

was achieved (Aymar, 1990) in an LS-coupled R-matrix calculation for the $^1P^o$, $^3P^o$, and $^3D^o$ symmetries. The treatment included three channels ($6snp$, $5dnp$, and $5dnf$) for the ^1P and ^3P symmetries and two channels ($5dnp$ and $5dnf$) for the ^3D symmetry. The LS-coupled reaction matrices were recoupled into a single jj-coupled matrix of dimension 8 for $J=1$. This problem involves three ionization limits ($6s$, $5d_{3/2}$,

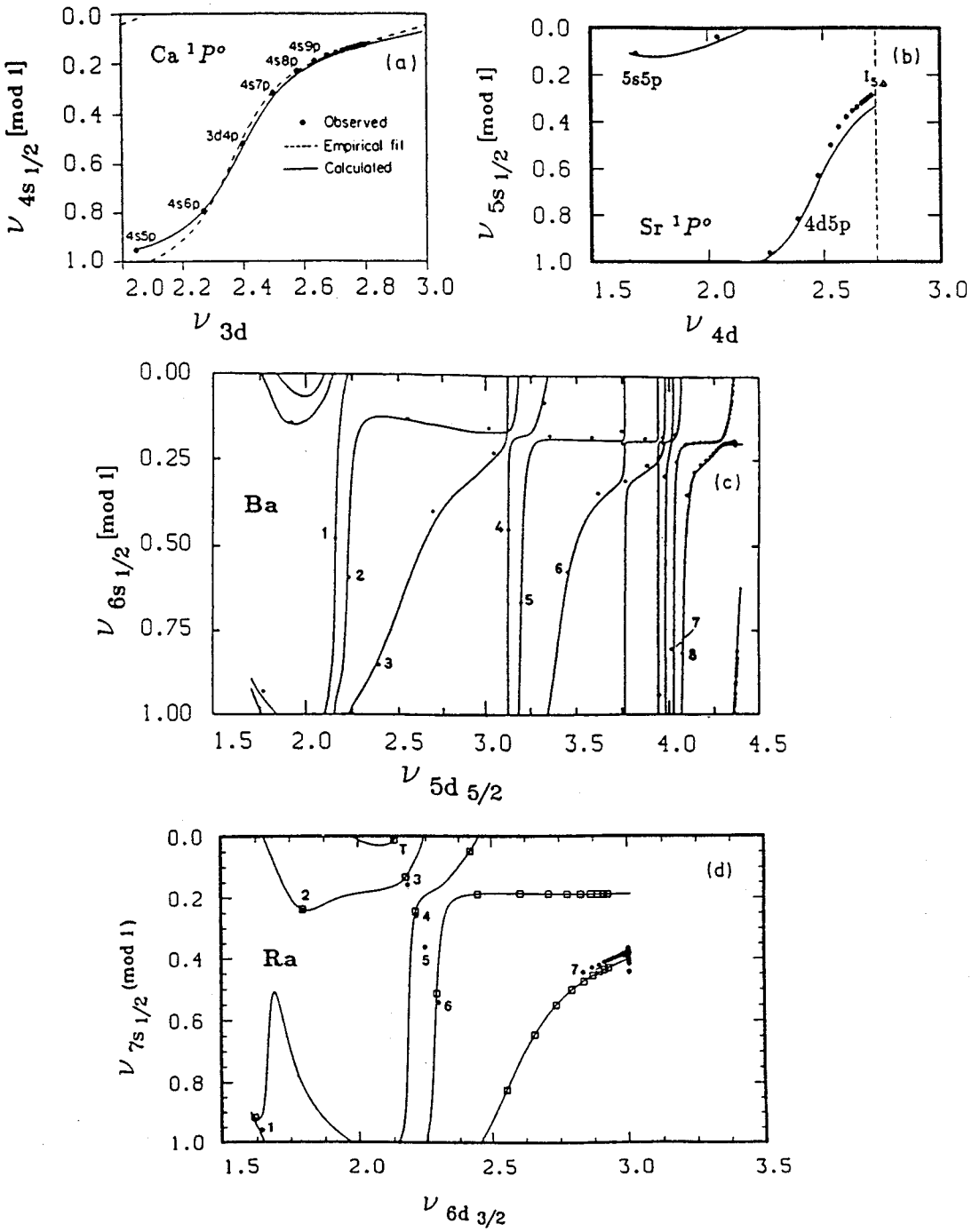

FIG. 9. Lu-Fano plots of the odd-parity $J=1$ bound levels of Ca to Ra, comparing experimental values, depicted by solid points, with eigenchannel R-matrix calculations (solid curves and open squares). (a),(b) Results on the m_0snp ^1P Rydberg series of (a) Ca and (b) Sr perturbed by the $(m_0-1)dm_0p$ ^1P level were obtained in LS coupling; the dashed curve for Ca is the empirical MQDT fit of Armstrong *et al.* (1979). (c) The LS-coupled R-matrix result for Ba combined with the jj-LS frame transformation; the levels (1) to (8) correspond to $5dnp$ perturbers of the $6snp$ $^1P_1$ and $^3P_1$ Rydberg series, the $5d6p$ $^1P_1$ being labeled by (3) and the $5d7p$ $^1P_1$ by (6); the $5d8p$ $^1P_1$ level is diluted into high-lying $6snp$ $^1P_1$ levels; the three $5d4f$ levels cause the rapid increases of the quantum defects for $3.75 \leqslant \nu_{5d_{5/2}} \leqslant 4$. (d) The jj-coupled R-matrix result for Ra for the $7snp$ $^1P_1$ and $^3P_1$ Rydberg series perturbed by the $6d7p$ $J=1$ levels [for assignment of the levels (1) to (7) see Greene and Aymar (1991)]. (From Aymar *et al.*, 1987; Greene and Kim, 1987; Aymar, 1990, and Greene and Aymar, 1991).

$5d_{5/2}$). For this reason Fig. 9(c) is the projection of a three-dimensional Lu-Fano plot onto the two-dimensional plane of $-\nu_{6s}$ (mod 1) versus $\nu_{5d_{5/2}}$. A characteristic feature of the energy diagram of Fig. 8 is the smaller gap between the $6s$ and $5d$ thresholds in Ba compared to the corresponding gaps between the $m_0 s$ and $(m_0-1)d$ thresholds in Ca, Sr, and even Ra. For this reason, in Ba, a large number (twelve) of doubly excited levels, which are the lower members of the $5dnp$ ($6 \leqslant n \leqslant 8$) and $5dnf$ ($n=4$) Rydberg series, perturb the $6snp$ $^1P_1$ and $^3P_1$ Rydberg series. Figure 9(d) shows that the Ra Lu-Fano plot, obtained using a 13-channel jj-coupled R-matrix calculation (Greene and Aymar, 1991) looks simpler than the Ba plot. In fact, only the three Ra $6d7p$ $J=1$ doubly excited levels are located below the $7s$ limit and thus perturb the $7snp$ $^1P_1$ and $^3P_1$ Rydberg series. The comparison of calculated (open squares) and observed (solid points) levels is satisfying for the lower- and higher-lying $7snp$ $^1P_1$ levels, whereas some discrepancies occur in the intermediate energy range. In particular, the theoretical level labeled by T cannot be associated with any experimental level. It remains unclear whether these discrepancies are due to some inaccuracy of the calculation, or to an experimental error or misclassification. As expected, poorer agreement is obtained between theory and experiment for the higher-lying $7snp$ $^1P_1$ levels using LS-coupled eigenchannel R-matrix calculations combined with the jj-LS frame transformation (see Greene and Aymar, 1991).

Perturbations of the $m_0 snp$ $J=1$ series have been analyzed previously for every alkaline-earth atom from Ca to Ra using empirical MQDT models fitted to experiment (Armstrong *et al.*, 1979, 1980). The dashed curve for Ca [Fig. 9(a)] is the MQDT least-squares fit of Armstrong *et al.* (1979). The nearly *ab initio* R-matrix calculations improve upon the description of the low-lying levels achieved in those empirical studies. This improvement derives from the correct description of the energy dependence of the short-range scattering parameters; in most semiempirical fits an oversimplified energy dependence has been assumed, in order to minimize the number of fitted parameters.

The Ca and Sr Lu-Fano plots are remarkably similar to each other, while Ba and Ra differ. Most of the differences between the lightest and heaviest atoms derive from two effects: from the different number of doubly excited levels located below the first ionization limit and from spin-orbit effects. The short-range scattering parameters exhibit strong similarities among all atoms from Ca to Ra. Below the $m_0 s$ threshold, the $J=1^o$ spectra are dominated by the mixing between the $m_0 snp$ ^1P and $(m_0-1)dnp$ ^1P channels, which is reflected by the large curvature of the Lu-Fano plots of Ca [Fig. 9(a)] and Sr [Fig. 9(b)]. Similar curvature is apparent for Ba [Fig. 9(c)] around $\nu_{5d_{3/2}} \sim 2.5$ ($5d6p$ ^1P perturber) and $\nu_{5d_{3/2}} \sim 3.5$ ($5d7p$ ^1P perturber), and for Ra [Fig. 9(d)] around $\nu_{6d_{3/2}} \sim 2.7$ ($6d7p$ ^1P perturber). These similarities are even more evident in Fig. 10, where the eigenquantum defects μ_α [Figs. 10(a), 10(c), 10(e), and 10(g)] and mixing angles θ [Figs. 10(b), 10(d), 10(f), and 10(h)] from R-matrix calculations (Aymar *et al.*, 1987; Greene and Kim, 1987; Aymar, 1990; Greene and Aymar, 1991) are displayed for the $m_0 snp$ ^1P and $(m_0-1)dnp$ ^1P channels of Ca to Ra versus the energy. The Ca and Sr results were obtained from a two-channel treatment, whereas those for Ba and Ra were derived from calculations involving a larger number of channels. The dashed curves in Figs. 10(e) and 10(f) for Ba show the empirical smooth scattering parameters fitted by Armstrong *et al.* (1979). The assumption that these parameters have a linear energy dependence, frequently made in empirical studies, is seen to be quantitatively valid only over a restricted energy range near the threshold; far below the $m_0 s$ threshold, the energy dependence becomes much more complicated (see also Fig. 7). Because R-matrix calculations carried out in the different atoms use different r_0 values and different numbers of interacting channels, a detailed comparison between the different curves (a), (c), (e), and (g) displaying the energy dependence of μ_1 and μ_2 is not very meaningful. However, let us note that the values of $\Delta_\mu = \mu_1 - \mu_2$ (mod 1) near the lowest threshold are comparable for each element: 0.36 (Ca), 0.36 (Sr), 0.25 (Ba), 0.33 (Ra).

Even more striking similarities are evident for the two-channel mixing angle θ [Figs. 10(b), 10(d), 10(f), 10(h)]. For all elements, θ evolves from zero at low energy to a maximum $\sim 0.20\pi$ around the $m_0 s$ threshold where the two channels are strongly mixed. Recalling Sec. II.F, note that the strongest possible mixing corresponds to $\theta = \pi/4$ and $\Delta_\mu = 0.5$. This near invariance of the strength of channel mixing was previously discussed by Armstrong *et al.* (1979, 1980) and by Wynne and Armstrong (1979). These authors showed that all $^1P^o$ bound-state data for Ca, Sr, and Ba can be compactly represented by using the two common parameters $\theta = 0.19\pi$ and $\Delta_\mu = 0.40$ and a third parameter $\bar{\mu} = \mu_1 - \Delta_\mu/2$ that is different for each atom. These empirical values obtained with a two-channel treatment agree well with the R-matrix predictions, although more poorly for Ba and Ra. These discrepancies for the heaviest alkaline-earth atoms primarily reflect the fact that more than two channels are actually involved in the dynamics.

One additional paper should be mentioned here. Armstrong *et al.* (1981) carried out *ab initio* calculations of short-range scattering parameters in alkaline earths using a local-density approximation for the exchange correlation potential. Their calculated two-channel interaction parameters for the $^1P^o$ series agree with the fitted parameters for Ca and Ba, while for Sr the agreement is poorer. That study also showed how the channel-interaction angle θ varies with energy.

We turn now to the even-parity $J=0$ spectra of Ca, Sr, and Ba. Calculated Lu-Fano plots displayed in Fig. 11 are compared with experimental levels (Moore, 1949, 1952, 1958; Armstrong *et al.*, 1977; Esherick, 1977; Aymar *et al.*, 1978; Sugar and Corliss, 1985). For Ca [Fig. 11(a)] and Sr [Fig. 11(b)], the curves (solid lines) were obtained with LS-coupled eigenchannel R-matrix calcu-

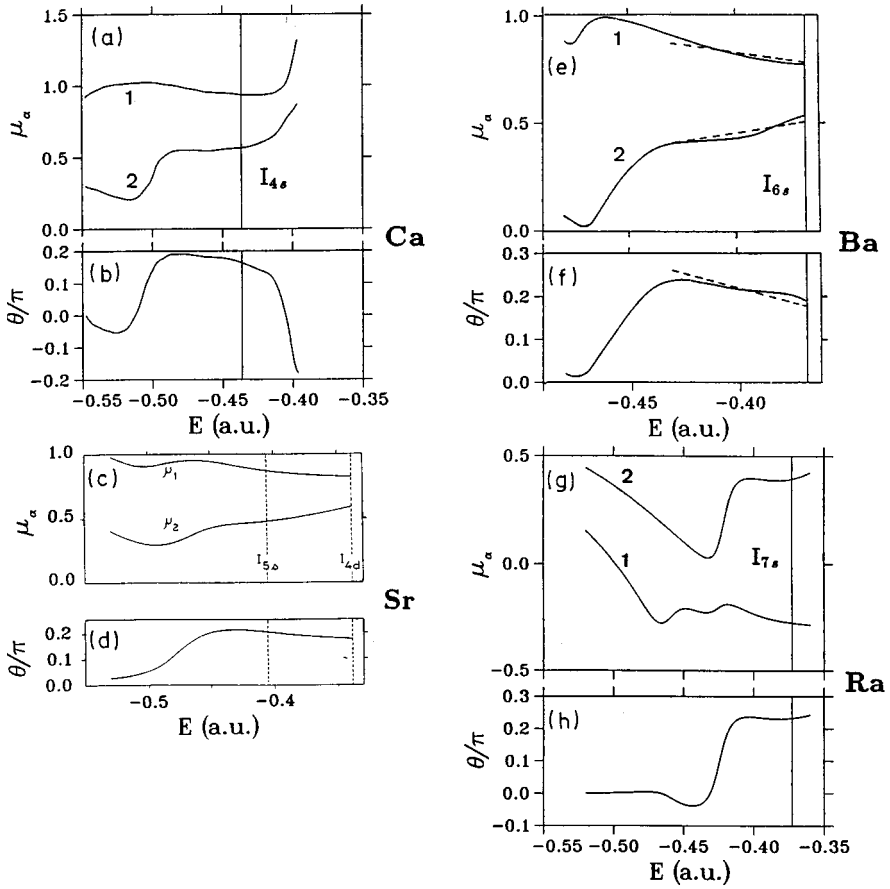

FIG. 10. Eigenquantum defects μ_α and mixing angle θ for the $m_0snp\ ^1P$ (1) and $(m_0-1)dnp\ ^1P$ (2) channels of Ca to Ra below the m_0s ionization limit, as functions of the energy E referred to the double-ionization limit. The curves (full lines) are derived from LS-coupled eigenchannel R-matrix calculations. The dashed lines for Ba correspond to the empirical MQDT fit of Armstrong *et al.* (1979). (From Aymar *et al.*, 1987; Greene and Kim, 1987; Aymar, 1990, and Greene and Aymar, 1991).

lations combined with the jj-LS frame transformation. Ca results are from Aymar and Telmini (1991); Sr results are derived from those of Aymar *et al.* (1987) and of Kompitsas *et al.* (1991). These R-matrix calculations involve the following five LS-coupled channels: [m_0sns, m_0pnp, and $(m_0-1)dnd\ ^1S$], [m_0pnp and $(m_0-1)dnd\ ^3P$]. The Ba Lu-Fano plot [Fig. 11(c)] was obtained from a five-channel jj-coupled eigenchannel R-matrix calculation (Greene and Aymar, 1991). The Lu-Fano plots of Ca [Fig. 11(a)] and Sr [Fig. 11(b)] extend across the first ionization limit, while the Ba plot [Fig. 11(c)] is restricted to the bound spectrum. The plots of Fig. 11 are projections of four-dimensional surfaces onto the $-\nu_{m_0s}$ (mod 1) versus $\nu_{(m_0-1)d_{3/2}}$ plane. The Ca and Sr Lu-Fano plots above the ionization limit display the physical "collision" eigenphase shifts obtained by diagonalization of the physical scattering matrix [Eq. (2.50)]. Each sharp rise of the phase shift is associated with an autoionizing resonance. The size of each avoided crossing between the branches of the Lu-Fano plots in Fig. 11 can be interpreted as reflecting the channel-interaction strength between either the m_0pnp ($^1S_0$, $^3P_0$) channels or else the $(m_0-1)dnd$ ($^1S_0$, $^3P_0$) channels and the $m_0sns\ ^1S_0$ Rydberg series (or $m_0s\epsilon s\ ^1S_0$ continuum). The $J=0^e$ spectra of Ca [Fig. 11(a)] and Sr [Fig. 11(b)], which are immediately seen to be similar, are strongly dominated by the mixing between singlet channels. In fact, in Ca the interaction between the singlet and triplet channels is almost negligible in the energy range of Fig. 11(a), which means that it is adequate to neglect their coupling altogether. This approximation is no longer valid for Ca at higher energies very close to the $3d_j$ spin-orbit-split thresholds, as will be documented in Sec. IV.B. Figure 11(b) shows that neglect of singlet-triplet mixing for this symmetry in Sr is only valid below the $5s$ threshold.

For the $^3P_0$ symmetry of Ca and Sr, two perturbers m_0p^2 (labeled by A) and $(m_0-1)d^2$ (labeled by B) are located below the m_0s threshold. Concerning the $^1S_0$ symmetry of Ca and Sr, R-matrix calculations have shown that the levels referred to as P_0 and P_0' involve comparable admixtures of the $(m_0-1)d^2$ and $m_0p^2\ ^1S$ configurations. Multiconfiguration Hartree-Fock calculations also demonstrated that the P_0 level is a strong mixture of those configurations (Froese Fischer and Hansen, 1981, 1985; Vaeck *et al.*, 1988). Recently Brage and Froese Fischer (1994a) have applied a nonvariational Spline-Galerkin method to reinvestigate a large number of $4snl$ Rydberg series of Ca. They used atomic wave functions in a close-coupling form, including pseudostates. Radial functions for the channel functions and for the pseudostates were taken from Ca^+ Hartree-Fock calculations, while a B-spline expansion was used to represent the radial functions of the outer electrons. Core-polarization effects were also incorporated. A very accurate description of $4sns\ ^1S_0$ Rydberg levels up to $n=23$ was achieved. They also found nearly equal weights for the $3dnd$ and $4pnp\ ^1S_0$ channels in the P_0

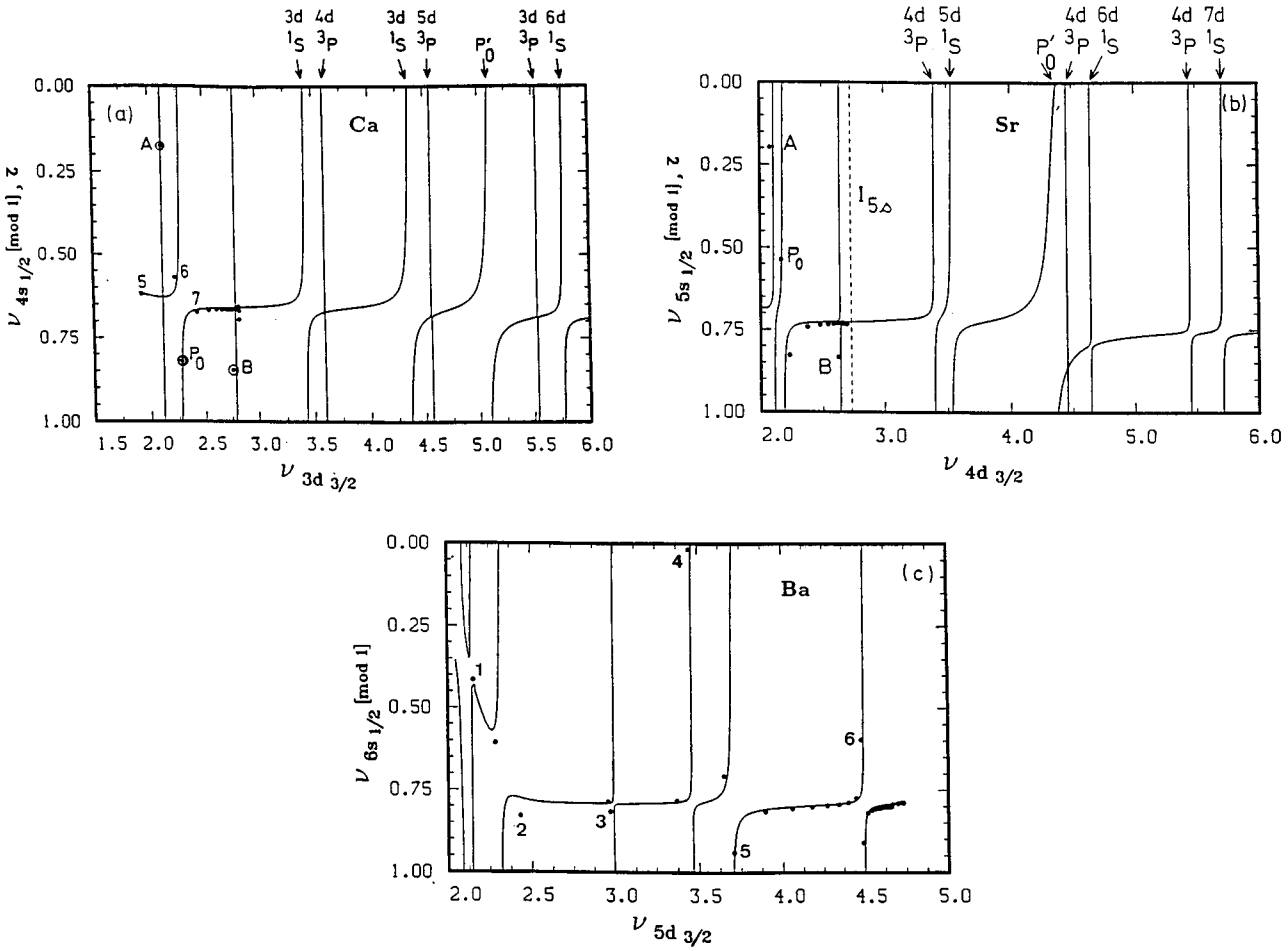

FIG. 11. Lu-Fano plots of the even-parity $J=0$ levels of Ca to Ba comparing experimental values depicted by solid points with eigenchannel R-matrix calculations (solid curves). (a),(b) For (a) Ca and (b) Sr the plots were obtained with LS-coupled eigenchannel R-matrix calculations combined with the jj-LS frame transformation. Below the first limit, (a) and (b) illustrate the perturbation of the $m_0sns\ ^1S_0$ Rydberg series by doubly excited levels: (A) $m_0p^2\ ^3P_0$, (B) $(m_0-1)d^2\ ^3P_0$, with P_0 and P_0' corresponding to admixtures of the $(m_0-1)d^2$ and $m_0p^2\ ^1S$ configurations. Above the first limit located at $\nu_{3d_{3/2}}=2.83$ in Ca and $\nu_{4d_{3/2}}=2.74$ in Sr, (a) and (b) display the eigenphase shifts, the vertical arrows, at the top of the figures, indicating the positions of autoionizing resonances. (c) The Ba result obtained with jj-coupled eigenchannel R-matrix calculation displays the perturbation of the $6sns\ ^1S_0$ Rydberg series by doubly excited levels: (1) $5d^2\ ^3P$, (2) $5d^2\ ^1S$, (3) $6p^2\ ^3P$, (4) $5d6d\ ^3P$, (5) $5d6d\ ^1S$, (6) $5d7d\ ^3P$. [The Ca figure is from Aymar and Telmini (1991) and the Ba figure from Greene and Aymar (1991).]

level. For levels such as these, which exhibit such strong electron correlations, classifications based on independent-electron quantum numbers should not be taken too seriously. With this qualification in mind, the trends of the $(m_0-1)dnd$ autoionizing series for Ca and Sr investigated with the R-matrix method (see Sec. IV.B below) suggest that the labels given in the earlier literature (Moore, 1949, 1952) should be reversed. This leads to the identification of P_0 as the $(m_0-1)d^2$ level and P_0' as the m_0p^2 level. As discussed below in Sec. IV.B, the upper level P_0' shows up as an autoionization feature, which was observed in the $J=0^e$ autoionizing spectra of Ca (Bolovinos *et al.*, 1992) and Sr (Kompitsas *et al.*, 1991). In both Ca and Sr, the position and width of that $m_0p^2\ ^1S_0$ (P_0') resonance agree well with R-matrix results (Aymar and Telmini, 1991; Kompitsas *et al.*, 1991). Below the m_0s threshold, the calculations accurately reproduce the perturbations of the m_0sns $^1S_0$ Rydberg series by the P_0 doubly excited state. A similar description of the $4sns\ ^1S_0$ perturbed Rydberg series of Ca was obtained by Osani *et al.* (1991), using a Wigner-Eisenbud-type formulation of the R-matrix method.

Figure 11(c) shows that more $J=0^e$ doubly excited states appear below the first ionization limit in Ba (namely six) than in either Ca and Sr (three), much like the situation discussed for the $J=1^o$ spectrum. In addition to the $5d^2\ ^3P_0$, $5d^2\ ^1S_0$, and $6p^2\ ^3P_0$ doubly excited levels, homologous to the three perturbers appearing in Ca and Sr, there are three other $5dnd$ doubly excited levels. The $5d^2\ ^1S_0$ level (labeled by 2) lies below the $6s$ threshold, while other R-matrix calculations show that the $6p^2\ ^1S_0$ level of Ba is a broad autoionizing resonance, although we postpone discussion of this point. The admixture of the $(m_0-1)d^2$ and $m_0p^2\ ^1S_0$ configurations were found to be much smaller than in Ca

and Sr; so, for instance, the weight of $5dnd$ channels for the $5d^2\ ^1S_0$ is ~75%. Except in the lowest energy range, the R-matrix calculation correctly reproduces the perturbation of the $6sns\ ^1S_0$ Rydberg series by doubly excited levels.

Figure 12 displays Lu-Fano plots of the even-parity $J=2$ bound levels of Ca, Sr, and Ba. On each Fig. 12(a)–12(c), the quantum defects of experimental levels (Moore, 1949, 1952, 1958; Armstrong *et al.*, 1977; Esherick, 1977; Aymar *et al.*, 1978; Sugar and Corliss, 1985) are depicted by points, which can be compared with quantum defects calculated in eigenchannel R-matrix calculations (solid curves). Results from LS-coupled R-matrix calculations for the $^1D^e$ levels of Ca (Aymar and Telmini, 1991) and of Sr (Aymar *et al.*, 1987) are displayed in Figs. 12(a) and 12(b). The calculations included four interacting MQDT channels: m_0snd, $(m_0-1)dnd$, $(m_0-1)dns$, and m_0pnp. The low-lying P_2 state perturbs the $m_0snd\ ^1D$ series, while the sharp rises of the quantum defects near the ionization limit reflect perturbations by the $(m_0-1)d(m_0+1)s$ and P_2' doubly excited states, where $m_0 = 3$, 4, and 5 for Ca, Sr, and Ba, respectively. As for the $J=0^e$ case, similar results were obtained by Osani *et al.* (1991). These results also agree with multiconfiguration Hartree-Fock predictions (Froese Fischer and Hansen, 1981, 1985; Vaeck *et al.*, 1988) and with the recent Spline-Galerkin calculation of Brage and Froese Fischer (1994a, 1994b). The P_2 and P_2' levels involve a strong admixture of the $(m_0-1)d^2$ and $m_0p^2\ ^1D$ configurations. Also, following the case for $J=0^e$, the labels previously given in the literature (Moore, 1949, 1952) should be reversed. Specifically we recommend identifying P_2 as the $(m_0-1)d^2$ level and P_2' as the m_0p^2 level. In both Ca and Sr, the $(m_0-1)d(m_0+1)s$ perturber is spread out over many m_0snd Rydberg levels. In Sr, the resonance associated with the $5p^2$ level was observed (Esherick, 1977) just above the threshold. In Ca, the $4p^2$ (P_2') level is predicted (Aymar and Telmini, 1991) to be centered almost exactly on the $4s$ ionization limit. The character of this perturber is so diluted among the high $4snd$ Rydberg levels that it does not make sense to identify any individual quantum state as this P_2' level.

The barium $J=2^e$ states display greater complexity. Figure 12(c) shows the perturbations of the $6snd\ ^1D_2$ and $^3D_2$ Rydberg series by 16 doubly excited levels associated with the $5dns$, $5dnd$, and $6p^2$ configurations. These theoretical results were based on an 11-channel jj-coupled R-matrix calculation (Greene and Aymar, 1991) that included the channels $6s_{1/2}nd_{3/2}$, $6s_{1/2}nd_{5/2}$, $5d_{3/2}ns_{1/2}$, $5d_{3/2}nd_{3/2}$, $5d_{3/2}nd_{5/2}$, $5d_{5/2}ns_{1/2}$, $5d_{5/2}nd_{3/2}$, $5d_{5/2}nd_{5/2}$, $6p_{1/2}np_{3/2}$, $6p_{3/2}np_{1/2}$, and $6p_{3/2}np_{3/2}$. Except for some discrepancies, theory is in clear agreement with the experimental quantum defects, accounting for the great complexity of the Ba spectral pattern. In contrast with Ca and Sr, the Ba $5d^2$ (labeled by 1) and $6p^2\ ^1D_2$ (labeled by 2) levels are both bound and, as in the $^1D_2$ case, only weakly admixed together.

Returning to the $J=0^e,2^e$ spectra, the jj-coupled R-matrix results for Ba presented in Figs. 11 and 12 have been compared (Greene and Aymar, 1991) with LS-coupled R-matrix calculations followed by a jj-LS

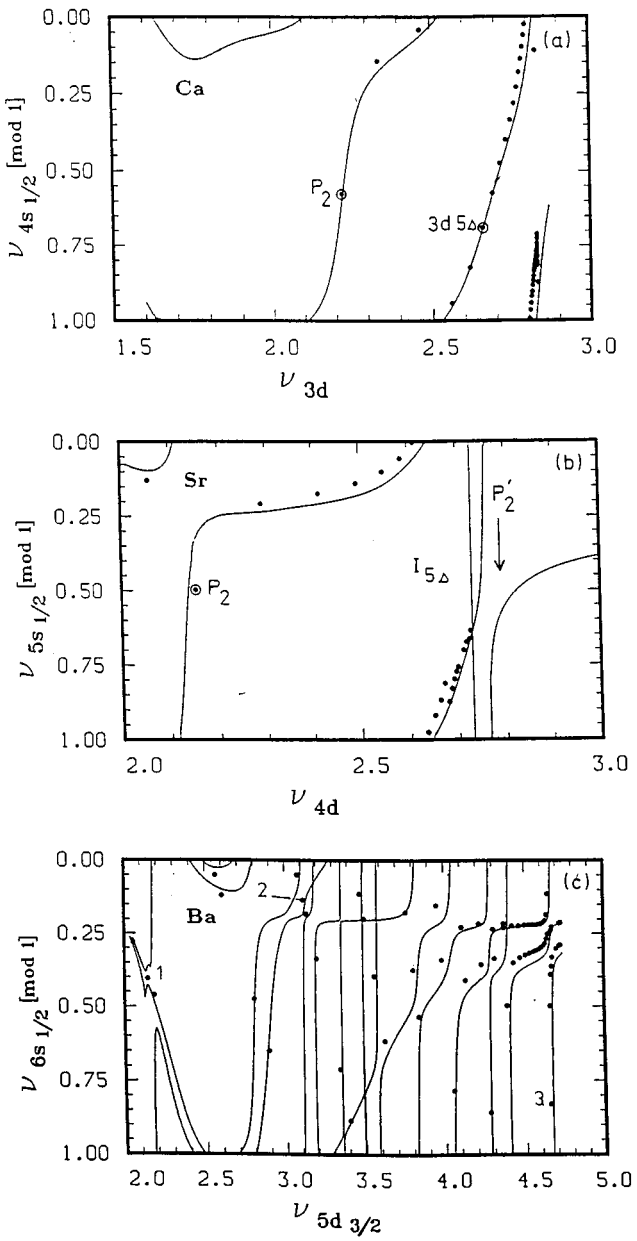

FIG. 12. Lu-Fano plots of the even-parity ^1D bound levels of Ca and Sr and $J=2^e$ bound levels of Ba comparing experimental values, depicted by solid points, with eigenchannel R-matrix calculations (solid curves). (a),(b) LS-coupled R-matrix results for (a) Ca and (b) Sr display the perturbation of the $m_0snd\ ^1D$ series by the P_2 and P_2' levels which correspond to admixture of the $(m_0-1)d^2$ and $m_0p^2\ ^1D$ configurations and by the $(m_0-1)d(m_0+1)s\ ^1D$ level. (c) The jj-coupled R-matrix result for the $6snd\ ^1D_2$ and $^3D_2$ Rydberg series of Ba perturbed by $5dnl$ and $6p^2\ J=2$ levels; in particular: (1) $5d^2\ ^1D_2$, (2) $6p^2\ ^1D_2$, and (3) $5d7d\ ^1D_2$. [The Ca figure is from Aymar and Telmini (1991) and the Ba figure from Greene and Aymar (1991).]

frame transformation. As explained above in Sec. II.F, use of the frame transformation near the bottom end of a Rydberg series requires some caution. Because the $J=0^e,2^e$ spectra involve the low-lying $6p^2$ levels, the K matrices deduced from LS-coupled R-matrix calculations were used to conduct separate MQDT test calculations, using either experimental j-dependent $6p_{1/2,3/2}$ threshold energies or theoretical spin-orbit-averaged $6p$ threshold energies. The jj-LS calculation required the use of theoretical threshold energy in order to give a correct description of the whole $J=2^e$ spectrum, in contrast with the $J=0^e$, whose spectrum is much less sensitive to the threshold energies utilized. This extreme sensitivity to threshold energies is an undesirable consequence of carrying out a frame transformation using quantum defects that vary rapidly with energy; it reflects a limitation of current implementations of the frame-transformation calculations. For both the $J=0^e$ and $J=2^e$ cases, neglect of the Ba^+ $6p$ ionic-core fine structure adversely affects the accuracy of the frame-transformation calculation compared to the jj-calculation, but only for the $6p^2$ levels.

Empirical MQDT analyses of the $J=0^e,2^e$ spectra were previously carried out in Ca (Armstrong *et al.*, 1977; Wynne and Armstrong, 1979), Sr (Esherick, 1977; Wynne and Armstrong, 1979), and Ba (Aymar *et al.*, 1978; Aymar and Robaux, 1979) with the purpose of interpreting newly observed data. There, the experimental levels were exactly on the fitted Lu-Fano curves, whereas some deviations are visible on Figs. 11 and 12. However, there are two improvements of these R-matrix studies over the empirical fits. First, the lowest levels, lying in the energy range in which smooth scattering parameters acquire a strong energy dependence, are for the most part correctly described, whereas empirical studies generally disregarded them. The second, more striking, improvement concerns the assignment of levels. As previously pointed out by Wynne and Armstrong (1979) and by Froese Fischer and Hansen (1981), the empirical MQDT method developed to take into account the effects of periodic perturbation fails to identify isolated perturbers such as the P_0 and P_2 levels occurring in Ca and Sr. Previous empirical MQDT fits of the $J=0^e,2^e$ spectra of Ca and Sr (Armstrong *et al.*, 1977; Esherick, 1977; Wynne and Armstrong, 1979) made some hypotheses for the perturber identifications and entirely neglected the m_0p^2-$(m_0-1)d^2$ interaction. The R-matrix approach bypasses these difficulties encountered in Ca and Sr. A detailed comparison between R-matrix and fitted short-range scattering parameters obtained in Ca was given by Aymar and Telmini (1991).

The $J=2^e$ Ba spectrum is better suited to empirical MQDT studies than are Ca and Sr because each $5dnl$ series supports several bound levels, while the $6p^2$ perturbers are still considered as "isolated" perturbers. The identifications deduced from MQDT fits (Aymar *et al.*, 1978; Aymar and Robaux, 1979) were completely confirmed for the $J=0^e$ spectrum, while the $6p^2$ perturbers and some neighboring levels were misclassified in the $J=2^e$ case. Greene and Aymar (1991) discussed these misclassifications.

Spectral regularities along the $^1S_0^e$ and $^1D_2^e$ series of Ca, Sr, and Ba were also previously analyzed by Wynne and Armstrong (1979). In contrast with the $^1P_1^o$ case, neither for the $^1D_2^e$, nor for the $^1S_0^e$ spectra was it possible to fit the level positions for all atoms using a common set of short-range scattering parameters. In particular, the parameters fitted to Ca and Sr completely failed to reproduce the Ba data. R-matrix calculations confirm these conclusions obtained empirically. All even-parity spectra are dominated by a strong mixing between the singlet m_0pnp and $(m_0-1)dnd$ channels, but the evolution of this mixing with energy is different for each atom. The differences in the dynamics of electron correlations in odd- and even-parity bound singlet spectra is probably related to the presence, in the latter spectra, of the strongly correlated singlet m_0p^2 and $(m_0-1)d^2$ levels involving two electrons in the same orbit.

2. Observables other than energies

A good description of an energy spectrum is certainly necessary, but not sufficient, to confirm that channel interactions have been treated accurately. Other observables test the accuracy of the wave functions more sensitively.

The hyperfine structure of perturbed Rydberg levels, for instance, is quite sensitive to state mixing (for references see Aymar, 1984a, 1984b). Hyperfine structure observed in high-lying $6snd\ ^{1,3}D_2$ Rydberg levels of Ba, perturbed by the $5d7d\ ^1D_2$ level [labeled by 3 in Fig. 12(c)] has been analyzed in terms of Rydberg singlet-triplet mixing. Just below the $6s$ threshold, the zero-order wave function (associated with the Hamiltonian without hyperfine effects) of each $J=2^e$ level can be written to a good approximation as

$$\Psi^{(n)}=\alpha_n|6snd\ ^1D_2\rangle+\beta_n|6snd\ ^3D_2\rangle+\gamma_n|5d7d\ ^1D_2\rangle, \tag{4.1}$$

where the α_n, β_n, and γ_n expansion coefficients can be related to the closed-channel coefficients $Z_i^{(n)}$ [see Eq. (2.64)] in the wave function of each level n. (Note that β_n in this context should not be confused with the angular distribution asymmetry parameter, nor with the closed-channel quantum-defect-theory phase parameter of Sec. II.)

As explained by Eliel and Hogervorst (1983), Rinneberg and Neukammer (1982, 1983), and by Aymar (1984a, 1984b), the hyperfine energies can be calculated as a function of the α_n, β_n, and γ_n mixing coefficients. Using the γ_n coefficients inferred from semiempirical MQDT analysis of energy levels or from measurements of lifetime, isotope shifts and Landé factors, Eliel and Hogervorst (1983) and Rinneberg and Neukammer (1982, 1983) extracted the α_n and β_n coefficients by fitting the calculated energies to their experimental results. Figure 13 presents the evolution of the coefficient β_n as a function of the principal quantum number n, for levels

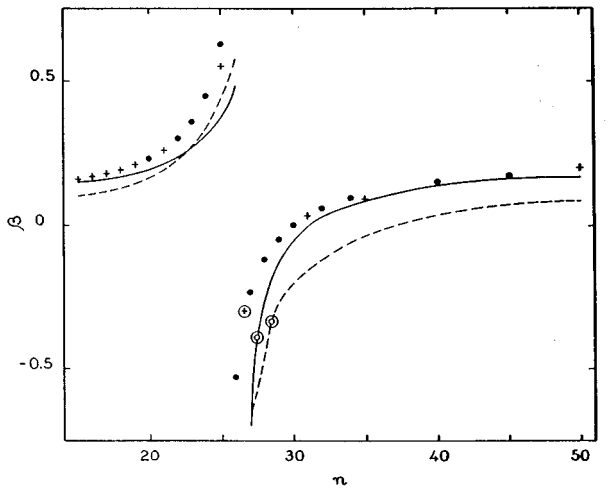

FIG. 13. Rydberg singlet-triplet mixing coefficients β [Eq. (4.1)] for the high-lying $6snd\ ^1D_2$ levels of Ba as functions of the principal quantum n in the energy range perturbed by the $5d7d\ ^1D_2$ level. The jj-LS (dashed line) and jj (full line) results are compared with values deduced from hyperfine-structure measurements: ● Eliel and Hogervorst (1983), + Rinneberg and Neukammer (1982, 1983). For the $5d7d\ ^1D_2$ level, the mixing coefficient (circled +) obtained by Rinneberg and Neukammer (1982, 1983) is compared with the theoretical predictions, depicted by concentric open circles. (From Greene and Aymar, 1991.)

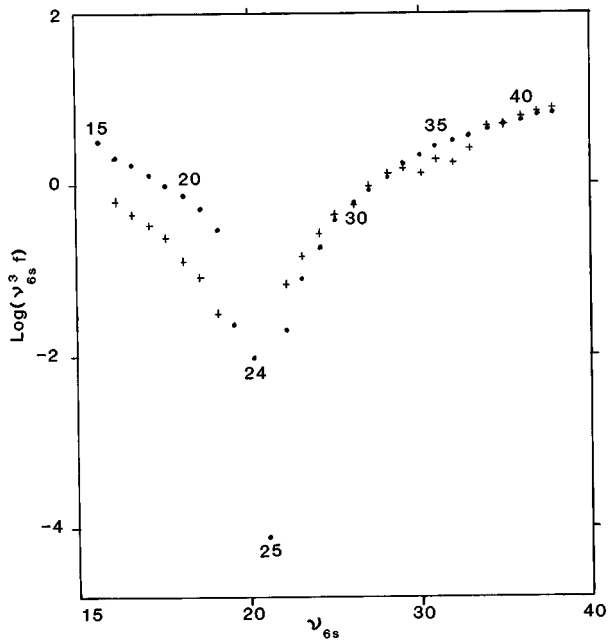

FIG. 14. Oscillator strengths of the $6s^2\ ^1S_0 \rightarrow 6snp\ ^1P_1$ transitions of Ba. The $\log_{10}(\nu_{6s}^3 f)$ values are plotted as functions of the effective quantum number ν_{6s} relative to the $6s$ ionization limit. The experimental results (+) of Connerade *et al.* (1988) are compared with the velocity results (●) obtained by combining LS-coupled R-matrix calculations with the jj-LS frame transformation. The $6snp\ ^1P_1$ levels are labeled by their principal quantum number n. (From Aymar, 1990.)

identified as singlets (i.e., those levels with $\alpha_n^2 \geqslant \beta_n^2$). The dot and plus symbols marked are derived from hyperfine structure measurements of Eliel and Hogervorst (1983), and from those of Rinneberg and Neukammer (1982, 1983), respectively. The dashed and solid curves depict β_n values obtained with 11-channel LS- and jj-coupled R-matrix calculations (Greene and Aymar, 1991). (Note that the jj-coupled R-matrix calculation corresponds to the calculation giving the Lu-Fano plot of Fig. 12(c).) The theoretical positions of the $5d7d\ ^1D_2$ level (circled open circle) are somewhat higher than the experimental position, which causes both theoretical curves to be shifted slightly toward high-n values. However, it is clear that the experimental behavior is better reproduced by the jj-coupled R-matrix results than by the jj-LS and frame-transformation calculation.

An interesting and little-probed energy regime occurs for the very high-lying m_0snl Rydberg levels of odd alkaline-earth isotopes, when the hyperfine splitting of the inner m_0s electron becomes comparable to the energy separation ($\approx 1/n^3$ a.u.) between adjacent Rydberg levels. In this energy range, the spectrum is truly multichannel in character, and the hyperfine interaction affects the Rydberg-electron motion nonperturbatively. Even though the nature of the threshold splitting is different from the fine-structure-split thresholds discussed in Sec. II.E, the MQDT description can be immediately generalized to treat this case. This extension of the frame-transformation method to treat hyperfine structure has been carried out by Sun, Lu, and co-workers (Sun and Lu, 1988; Sun, 1989; Sun *et al.*, 1989). The Sr $5sns$ and $5snd$ hyperfine structures observed by Beigang *et al.* (1983) and by Beigang (1985) for states with $n \gg 100$ have been successfully analyzed with the help of semiempirical MQDT models based on this hyperfine frame-transformation method (Sun and Lu, 1988; Sun *et al.*, 1989).

We return now to the $J=1^o$ spectrum of Ba, in the energy range close to the lowest ionization threshold where the $5d8p\ ^1P_1$ doubly excited level is diluted into high-lying $6snp$ Rydberg levels [$\nu_{5d_{3/2}} \geqslant 4.1$ on Fig. 9(c)]. In this range, the oscillator strengths [Eq. (2.66)] observed for the $6s^2\ ^1S_0 \rightarrow 6snp\ ^1P_1$ transitions (Parkinson *et al.*, 1976; Connerade *et al.*, 1988) deviate dramatically from the simple ν_{6s}^{-3} law expected for an unperturbed series. The modulation of $\log_{10}(\nu_{6s}^3 f)$ near the $5d8p\ ^1P_1$ perturber arises from the redistribution of the perturbing level's intensity among the high-lying $6snp\ ^1P_1$ levels as well as into the adjacent continuum, with a maximum close to the $6s$ threshold. Figure 14 compares the experimental data (crosses) obtained by Connerade *et al.* (1988) with results (dots) obtained by combining LS-coupled R-matrix calculations with the jj-LS frame transformation (Aymar, 1990). Theory reproduces the intensity minimum near $n \sim 24{,}25$ as well as the oscillator strengths of high-lying levels, but it overestimates the oscillator strengths for the lowest levels considered here. The modulation of Rydberg-level oscillator strengths near an isolated perturber is reasonably well described by the standard Fano line-shape formula (Fano, 1961), even though this formula was derived for one discrete

state interacting with a continuum, because the Rydberg levels are so closely spaced that they resemble a continuum (Connerade, 1992).

A combined theoretical and experimental investigation of several oscillator strengths connecting discrete levels of Sr was carried out by Werij *et al.* (1992). This project showed that a reliable description of many transitions can be achieved using LS-coupled eigenchannel R-matrix and quantum-defect calculations. Not surprisingly, theory describes the stronger transitions more effectively than the weaker ones, since the weak transitions tend to have competing contributions of opposite sign in the configuration-interaction expansion. In the independent-electron model, no single electron transition from the ground state can give an absorption oscillator strength larger than 1. For the main resonance transition of Sr, namely $5s^2\,{}^1S \rightarrow 5s5p\,{}^1P^o$, the absorption oscillator strength is approximately $f \approx 1.9$, which implies that both valence electrons participate strongly in the transition. For most of the singlet transitions, the calculated oscillator strengths (Werij *et al.*, 1992) agree reasonably well with multiconfiguration Hartree-Fock calculations of Vaeck *et al.* (1988). No similarly exhaustive multiconfiguration Hartree-Fock study is available for the triplet manifold for comparison with the R-matrix values.

B. Energy positions of autoionizing levels

It can be difficult to fully interpret a spectrum of autoionizing states from study of the experimental or theoretical photoionization cross section alone. Complexities associated with autoionizing levels can remain hidden, and frequently even the resonance positions cannot be extracted. Moreover, interferences between the discrete and continuum excitation amplitudes often result in asymmetric Beutler-Fano profiles (Fano, 1961), which further complicates the pattern of autoionization and its relation to the true "resonance energies." In some cases, resonances fail to appear in a particular cross section because they have vanishing transition strengths. Another difficulty that plagues the analysis of complex multichannel systems is the overlapping nature of the resonance pattern. It is crucial for theoretical multichannel spectroscopy to develop the ability to extract resonance positions, widths, and classifications that are independent of the excitation process.

In Sec. II.F, it was mentioned that a Lu-Fano plot can be extended into the energy range above an ionization threshold to gain useful information about autoionizing resonances; examples of this are shown in the right-hand portions of Figs. 11(a) and 11(b). Each rise of one phase shift $\delta = \pi\mu$ by one cycle implies the existence of one resonant state. As usual, the magnitude of the gap at an avoided crossing indicates the strength of interactions between closed and open channels, which determines the resonance widths. However, the quantitative determination of the positions and widths of autoionizing resonances from such a plot is possible only in relatively simple cases involving a small number of channels (see, for example, Giusti-Suzor and Fano, 1984).

For more complicated situations involving several interacting open and closed channels (see Sec. II.D.3), the resonance energies and classifications can be obtained by using MQDT techniques for treating bound-state spectra, starting from an effective reaction matrix $\underline{K}_{\rm eff}$ whose open-channel components have been "eliminated" in some manner. For example, this matrix may correspond to the real part of the κ-matrix introduced in Eq. (2.73). In this way resonances have been analyzed in Ca, Sr, and Ba (Kompitsas *et al.*, 1990, 1991; Aymar and Telmini, 1991; Gounand *et al.*, 1991; Luc-Koenig and Aymar, 1991, 1992; Goutis *et al.*, 1992; Assimopoulos *et al.*, 1994; Aymar *et al.*, 1994; Luc-Koenig, Aymar, and Lecomte, 1994; Luc-Koenig, Bolovinos, *et al.*, 1994; Luc-Koenig, Lecomte, and Aymar, 1994). The effective reaction matrix $\underline{K}_{\rm eff}$ restricted to the subspace of closed channels immediately permits a determination of the resonance positions and of the corresponding channel decompositions $Z_i^{(n)}$ [see Eq. (2.64)]. These coefficients determine the dominant closed channel i to which a resonance belongs. The interactions among closed channels can also be analyzed graphically using Lu-Fano plots. This entire procedure based on the construction of an effective reaction matrix is (generally) adequate to locate the position of a resonance with an error comparable to its autoionization width. Another method for extracting resonance properties based on the time-delay (or density-of-states) matrix gives in addition the autoionization widths; this method will be described in Sec. IV.C below.

The procedure of the preceding paragraph has been applied to interpret autoionizing Rydberg series of Ca, Sr, and Ba converging to the ionic fine-structure levels $(m_0-1)d_{3/2}$ and $(m_0-1)d_{5/2}$. The analysis provides information about the perturbers of these series that correspond to the lower-lying members of Rydberg series converging to the $m_0 p_{1/2,3/2}$ thresholds. For illustration, we concentrate on the even-parity autoionizing $J=0^e$ levels.

Figure 15 displays Ca Lu-Fano plots obtained with two effective matrices $\underline{K}_{\rm eff}$ deduced from two separate LS-coupled eigenchannel R-matrix calculations carried out for the ${}^1S^e$ and ${}^3P^e$ symmetries (Aymar and Telmini, 1991). The reaction matrix $\underline{K}^{3P}$ has no continuum channel in this energy range; it can thus be used directly to analyze the resonances since when the ${}^1S^e$-${}^3P^e$ mixing is disregarded, all states are bound. For the ${}^1S^e$ symmetry, a closed-channel matrix $\underline{K}^{1S}_{\rm eff}$ was first deduced from the complete reaction matrix $\underline{K}^{1S}$ connecting the open channel $4s\epsilon s$ and the two closed channels $3dnd$ and $4pnp$. The predicted resonance energies are plotted in the $-\nu_{3d}$ (mod 1) versus ν_{4p} plane, the effective quantum numbers ν_{3d} and ν_{4p} having been calculated using spin-orbit-averaged ionization limits. The $4pnp$ perturbers of the $3dnd$ Rydberg series are easy to identify. Each perturbing level causes a sharp rise of $-\nu_{3d}$ for the relevant branch of the Lu-Fano curve. The

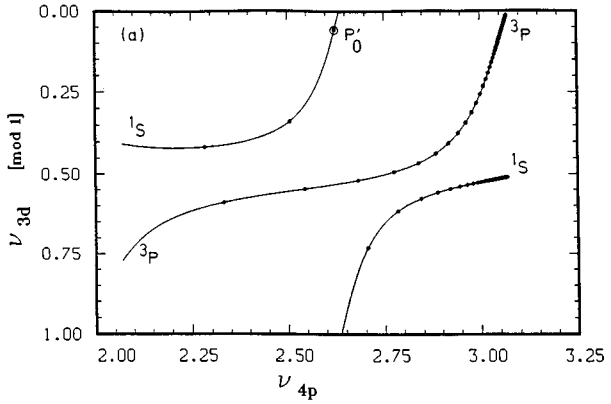

FIG. 15. Lu-Fano plot of the energy positions of even-parity autoionizing levels of Ca between the $4s$ and $3d$ ionization limits. The solid lines and points were obtained from two separate LS-coupled eigenchannel R-matrix calculations carried out for the $^1S^e$ and $^3P^e$ symmetries. The quantities ν_{3d} and ν_{4p} are the effective quantum numbers relative to the spin-orbit-averaged Ca^+ $3d$ and $4p$ ionization limits. The $3dnd$ ^1S Rydberg series is perturbed by the P'_0 level, which corresponds to an admixture of the $4p^2$ and $3d^2$ ^1S configurations. The rapid increase of $-\nu_{3d}$ near $\nu_{4p}\sim 3$ reflects the perturbation of the $3dnd$ ^3P Rydberg series by the $4p5p$ ^3P level, which is diluted among high-lying $3dnd$ ^3P Rydberg levels. (From Aymar and Telmini, 1991.)

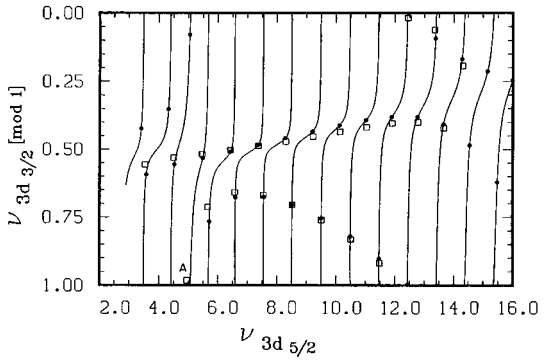

FIG. 16. Lu-Fano plot of the energy positions of even-parity $J=0$ autoionizing levels of Ca between the $4s$ and $3d_{3/2}$ ionization limits. The experimental data of Bolovinos *et al.* (1992) (open squares) are compared with the results of Aymar and Telmini (1991) (solid points and curves) obtained with LS-coupled eigenchannel R-matrix calculations combined with the jj-LS frame transformation. The open square labeled A depicts the $4p^2$ $^1S_0$ perturber of the $3d_{3/2}nd_{3/2}$ and $3d_{5/2}nd_{5/2}$ series.

discussion of Fig. 11(a) in Sec. IV.A.1 considered the classification of the P'_0 state, which is a strong admixture of the $3d^2$ and $4p^2$ singlet configurations but is somewhat better identified as the $4p^2$ ^1S state. This identification follows in part from the fact that P'_0 lies on a nearly vertical branch of the ^1S Lu-Fano plot. The rapid increase of $-\nu_{3d}$ along the ^3P branch, just below the $3d$ threshold at $\nu_{4p}\sim 3$, reflects a perturbation of the $3dnd$ ^3P series by a $4p5p$ state that is centered almost right on the $3d$ threshold. The character of this $4p5p$ ^3P perturber is entirely diluted among the high-lying members of the $3dnd$ ^3P series. A similar procedure has been used to identify the $J=2^e$ $4pnp$ levels that perturb the $3dnd$ and $3dns$ series.

Initial survey calculations in LS coupling were followed by more complete jj-LS frame-transformation treatments of the $J=0^e,2^e$ spectra that incorporated fine-structure effects (Aymar and Telmini, 1991). When fine structure is included, the energies of the $4pnp$ perturbers remain close to the predictions of the LS-coupled calculations. Close to the $3d_{3/2}$ threshold, however, the high-lying $3dns,nd$ levels are strongly affected, especially the $3dnd$ $J=0$ levels. Recently, R-matrix predictions for the Ca $J=0^e,2^e$ spectra have been confirmed by the experiment of Bolovinos *et al.* (1992). These authors reported the first observation of the broad $4p^2$ $^1S_0$ (P'_0) autoionizing resonance, whose width is around 80 cm^{-1}. Figure 16 shows that the Lu-Fano plot of experimental (open squares) low-lying $3dnd$ $J=0$ levels and of the $4p^2$ $^1S_0$ level (labeled by A) agrees with the R-matrix predictions (solid line and points) of Aymar and Telmini (1991). The energy levels are now plotted in the $-\nu_{3d_{3/2}}$(mod 1) versus $\nu_{3d_{5/2}}$ plane which makes $4pnp$ perturbers more difficult to discern. This shows the interest of carrying out preliminary calculations in LS coupling. The MQDT treatment involves four closed fragmentation channels: $3d_{3/2}nd_{3/2}$, $3d_{5/2}nd_{5/2}$, $4p_{1/2}np_{1/2}$, and $4p_{3/2}np_{3/2}$. Neither Fig. 16 nor the complete Lu-Fano plot of $J=0^e$ levels of Ca located between the $4s$ and $3d_{3/2}$ limits ($2\leqslant\nu_{3d_{5/2}}\leqslant 42$), show the nearly horizontal line that typically represents an "unperturbed" $3d_{3/2}nd_{3/2}$ Rydberg series. In fact, the periodicity in $\nu_{3d_{5/2}}$, expected for the two-channel problem involving the two $3dnd$ series, is absent over the whole energy range. The periodicity is destroyed by the $4p^2$ $^1S_0$ (P'_0) perturber and by the $4p5p$ $^3P_0$ level close to the $3d_{3/2}$ threshold [see Fig. 16]. Accordingly, most of the predicted energy levels cannot be clearly attributed either to $3d_{3/2}nd_{3/2}$ or to $3d_{5/2}nd_{5/2}$ series. Moreover, in Ca various even-parity $3dnl$ levels with $0\leqslant J\leqslant 3$, which have been recorded using a two-step laser experiment, were successfully accounted by jj-coupled eigenchannel R-matrix calculations (Assimopoulos *et al.*, 1994; Luc-Koenig, Bolovinos, *et al.*, 1994).

The valence-electron spectrum of atomic strontium appears in most regions to be very similar to the calcium spectrum. Figure 17 displays a case in which some differences can be seen, namely for the even-parity $J=0$ autoionizing levels of Sr located below the $4d_{3/2}$ threshold, i.e., in the energy range analogous to that considered for Ca in Fig. 16. For Sr, in contrast with Ca, the experiment and the R-matrix calculations were conducted hand in hand (Kompitsas *et al.*, 1991). MQDT analysis of an effective closed-channel reaction matrix $\underline{K}_{\rm eff}$ helped greatly to interpret and identify the autoionizing resonances recorded in the even-parity spectra of Sr, for $J=0^e$ (Kompitsas *et al.*, 1991) and also for $J=1^e$ and $J=2^e$ (Goutis *et al.*, 1992). The experimental $J=0^e$ data in Fig. 17 (solid points) again agree with the

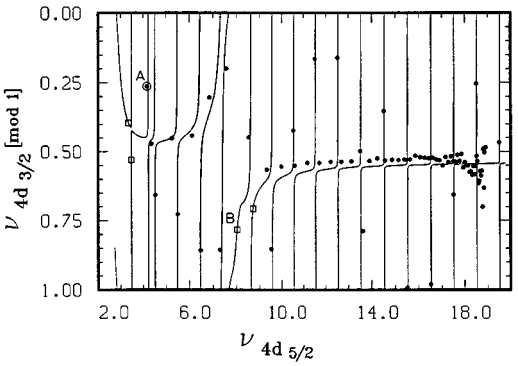

FIG. 17. Lu-Fano plot of the energy positions of the $J=0$ even-parity autoionizing levels of Sr between the $5s$ and $4d_{3/2}$ ionization limits. The experimental data (solid points) are compared with the results (solid curves) obtained with LS-coupled eigenchannel R-matrix calculations combined with the jj-LS frame transformation. The open squares correspond to unobserved levels. Concerning the perturbers of the $4d_{3/2}nd_{3/2}$ and $4d_{5/2}nd_{5/2}$ Rydberg series, the point A depicts the experimental data for the $5p^2\ ^1S_0$ level and B the prediction for the $5p6p\ ^3P_0$ level. (From Kompitsas *et al.*, 1991.)

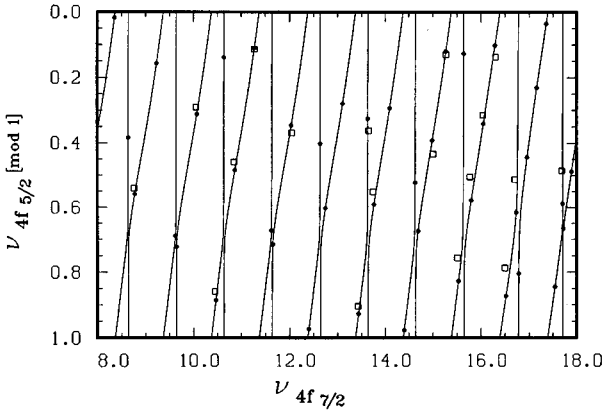

FIG. 18. Lu-Fano plot of the energy positions of the $4fnf$ $J=6$ autoionizing levels of Ba, comparing the experimental data (open squares) of de Graaff *et al.* (1992) with LS-coupled R-matrix calculations combined with the jj-LS frame transformation (solid curves and points). (From Luc-Koenig and Aymar, 1992.)

LS-coupled R-matrix calculations used in conjunction with the jj-LS frame transformation (Kompitsas *et al.*, 1991). In the energy range close to the $4d_{3/2}$ threshold ($\nu_{4d_{5/2}} \geqslant 10$), the autoionizing structures correspond to a $4d_{3/2}nd_{3/2}$ Rydberg series perturbed periodically by the $4d_{5/2}nd_{5/2}$ levels. A two-channel ($4d_{3/2}nd_{3/2}$, $4d_{5/2}nd_{5/2}$) MQDT model that would be appropriate for a description of the high-lying $J=0^e$ levels obviously fails to reproduce the data observed in the lower energy range. At lower energies, members of the $4dnd$ series are affected by the presence of the $5p^2\ ^1S_0$ and $5p6p\ ^3P_0$ perturbing levels, marked respectively as (A) and (B) in Fig. 17. The former level, denoted P_0' in Sec. III.A.1, corresponds to a broad autoionizing profile (with a width of 230 cm^{-1}) that was observed experimentally using two-photon laser excitation from the $5s^2$ ground state (Kompitsas *et al.*, 1991). The latter $^3P_0$ level has not yet been observed. However, its effect on the positions of neighboring $4dnd\ J=0$ levels is quite visible in Fig. 17. This level also affects the oscillator strengths of the $4d5p\ ^1P_1 \rightarrow 4dnd\ J=0$ transitions. The perturbations of $4dnl$ autoionizing Rydberg series by several $5p6p$ levels show still greater complexity for the $J=1^e$ and $J=2^e$ symmetries and also display good agreement between theory and experiment (Goutis *et al.*, 1992).

Figures 16 and 17 contrast the behavior of the $(m_0-1)dnd\ J=0^e$ series for Ca and Sr. For both atoms, these series are affected by the $m_0p^2\ ^1S_0$ perturber located among low-lying $(m_0-1)dnd$ levels. The $(m_0-1)dnd$ series of Ca and Sr are also affected by the $m_0p(m_0+1)p\ ^3P_0$ perturber. The evident differences between Ca (Fig. 16) and Sr (Fig. 17) result from the fact the $4p5p\ ^3P_0$ level of Ca is diluted into $3dnd$ high-lying Rydberg levels, whereas the $5p6p\ ^3P_0$ perturber is well localized in Sr. The low-lying Ba $5dnd\ J=0$ levels interact with the $6p^2\ ^1S_0$ perturber (Aymar *et al.*, 1982; Aymar *et al.*, 1983; Greene and Aymar, 1991), whereas the Ba $6p7p\ ^3P_0$ level is located above the $5d$ threshold (Camus *et al.*, 1983). Because of the differences in the location of the $m_0p^2\ ^1S_0$ and $m_0p(m_0+1)p\ ^3P_0$ levels, channel mixing near the $(m_0-1)d_{3/2}$ threshold differs considerably in Ca, Sr, and Ba.

Strong mixing, similar to that observed in the Ca $J=0^e$ spectrum, has been found in the $4fnf$ series of Ba. The strongly coupled Rydberg series are the $4f_{5/2}nf_{7/2}$ and $4f_{7/2}nf_{5/5}$ with $J=4$, 5, or 6, which converge to two different fine-structure levels (Luc-Koenig and Aymar, 1992; Luc-Koenig, Aymar, and Lecomte, 1994). Figure 18 displays the Lu-Fano plot of energy positions for the high-lying $4fnf\ J=6$ autoionizing levels of Ba. The frame-transformation result (solid curves and points) of Luc-Koenig and Aymar (1992) is compared to the experimental data (open squares) of de Graaff *et al.* (1992). This experiment probed the $4fnf$ series using a two-step laser-excitation scheme starting from the $5d^2$ metastable levels and using the $5dnf$ autoionizing resonances as intermediate levels. The theoretical energies in Fig. 18 agree well with the experimental data. For each level, the theoretical energy lies within the width of the recorded resonance.

To reproduce the energy positions of high-lying $4fnf$ $J=6$ levels, R-matrix calculations were conducted for the $^1I^e$ symmetry and for the $^3L^e$ symmetries with $L=5$, 6, and 7. The frame transformation gave a jj-coupled reaction matrix describing the coupling of 33 channels converging to the $6s$, $5d_j$, $6p_j$, $7s$, $6d_j$, and $4f_j$ thresholds. From this full reaction matrix, a smaller effective reaction matrix $\underline{K}_{\rm eff}$ was formed involving only the three $4fnf$ closed channels. This permitted a simplified analysis of the $4fnf\ J=6$ levels located between the $6d_{5/2}$ and $4f_{5/2}$ limits.

The slant lines on Fig. 18 correspond to the series $4f_{5/2}nf_{7/2}$ and $4f_{7/2}nf_{5/2}$, which interact strongly, whereas the vertical lines are associated with the nearly unper-

turbed $4f_{7/2}nf_{7/2}$ series. The behavior of the strongly mixed $4f_{5/2}nf_{7/2}$ and $4f_{7/2}nf_{5/2}$ $J=6$ series can be analyzed using a two-channel model involving the eigenchannels $4fnf\ ^1I$ and ^3I. The rotation angle that characterizes the orthogonal $U_{i\alpha}$ matrix in this two-channel model is approximately equal to $\theta_{12}\sim\pi/4$ and the slant branches of the Lu-Fano plot reflect the fact that the difference $|\Delta_\mu|=|\mu_1-\mu_2|$ of the eigenquantum defects amounts to 0.5, i.e., has the maximum value. This makes it impossible to classify the levels as belonging to any one series. Moreover, the channel mixing is highly energy dependent, with significant changes in mixing coefficients frequently found even in two successive levels. In the higher-energy range close to the $4f_{5/2}$ threshold, the $4f_{7/2}nf_{5/2}$ $J=6$ levels are completely diluted among the $4f_{5/2}nf_{7/2}$ states. Similarly strong mixing was found between the $4f_{5/2}nf_{7/2}$ and $4f_{7/2}nf_{5/2}$ $J=4$ or $J=5$ series; this was again related to a difference between the eigenquantum defects for the two channels $4fnf\ ^{1,3}L_{J=L}$ close to 0.5 (Luc-Koenig, Aymar, and Lecomte, 1994). For each final-state symmetry in the range J=4–6, the large value of $|\Delta_\mu|$ arises from the exchange electrostatic interaction and is typical of the $nln'l$ channel mixing. Strong mixing between the Ca $3dnd\ ^1L_{J=L}$ and $^3L_{J=L}$ $J=3$ channels was also observed and exhibited in the corresponding Lu-Fano plot (Luc-Koenig, Bolovinos, *et al.*, 1994).

In contrast, for the Ca $J=0^e$ symmetry (Fig. 16), where the coupling of $3dnd$ is also maximum, it is the $3dnd$-$4pnp$ mixing that indirectly (but strongly) couples the eigenchannels $3dnd\ ^1S$ and ^3P, even though they are not directly coupled by the electrostatic interaction. In this case, the channel mixing angle is also $\theta_{12}\sim\pi/4$, but $|\Delta_\mu|$ amounts to only 0.21. This translates [Eq. (2.82)] into a 40% probability that the Rydberg electron will scatter from one fine-structure channel to another when it collides with the Ca^+ $3d$ ionic core.

Returning to the $4fnf$ levels of Ba, we note that the resonance energy positions calculated by Luc-Koenig and Aymar (1992) agreed well with experimental data of de Graaff *et al.* (1992). This agreement provided some of the first evidence that the R-matrix and MQDT techniques are capable of handling excited autoionizing levels of Ba lying above the $6p$ threshold. As discussed below in Sec. IV.D.2, another calculation in a similar energy range had been carried out previously by Kim and Greene (1988) concerning the Ca photoabsorption spectrum up to the $6s$ threshold, but no experimental data are yet available to check those Ca predictions. The good agreement between theory and experiment for the energy positions of the Ba $4fnf$ levels with $J=6$, $J=4$, and $J=5$ is somewhat surprising for such a complex case. As in some of the lower-energy spectra already discussed, the spectrum is dominated by strong electron correlations and strong spin-orbit effects; this higher-energy range involves a much larger number of interacting channels; in addition the centrifugal barrier, sensitively controls the nature of the Ba f orbitals.

More recently, eigenchannel R-matrix studies were performed on several autoionizing Rydberg series of Ba in the energy range between the $6p$ and $7p$ thresholds (Aymar *et al.*, 1994; Lecomte *et al.*, 1994, 1995; Luc-Koenig, Aymar, and Lecomte, 1994; Luc-Koenig, Lecomte, and Aymar, 1994; van Leeuwen *et al.*, 1995, 1996). These studies were motivated primarily by recent experiments, and will be discussed later in Secs. IV.C, IV.D, and IV.E. Nevertheless, we point out here that the construction of an effective reaction matrix $\underline{K}_{\rm eff}$ has greatly helped in analyzing the perturbations of the $6dng$ $J=6$ series by several $4fnf$ and $4fnh$ levels (Aymar *et al.*, 1994). This analysis also helped to identify the 14 doubly excited levels that cause localized perturbations of the $7sng\ ^{1,3}G_4$ Rydberg series (Luc-Koenig, Lecomte, and Aymar, 1994).

We conclude from the two preceding sections on energy-level positions that Lu-Fano plots permit a unified and intuitive picture of the channel-mixing patterns. They convey the interaction strength in a simple manner that brings out aspects of the short-range dynamics common to the global level pattern of an atom. The R-matrix method in turn can be used to predict channel-mixing parameters, giving reliable energies and classifications even for very complicated perturbed Rydberg series. In addition, the R-matrix method bypasses difficulties encountered in empirical MQDT analyses of spectra such as the large number of undetermined channel-interaction parameters and the strong energy dependence of the smooth scattering parameters that is frequently caused by isolated perturbers. Furthermore, by constructing an effective reaction matrix restricted to closed channels, one can extend MQDT bound-state techniques to the energy range of autoionizing levels. We caution, however, against using single-channel quantum defects for the classification of such perturbed spectra, as is frequently done. This procedure can result in qualitatively incorrect classifications.

Other familiar methods have been widely used to calculate singly excited and low-lying doubly excited levels for all of the alkaline-earth atoms. These include the multiconfiguration Hartree-Fock studies of singlet bound spectra of Ca and Sr (Froese Fischer and Hansen, 1981, 1985; Vaeck *et al.*, 1988), the Spline-Galerkin calculations of Brage and Froese Fischer (1994a, 1994b) and the Wigner-Eisenbud-type R-matrix calculations of Osani *et al.* (1989a, 1989b, 1991) in Be, Mg, and Ca. The multiconfiguration Dirac-Fock method was employed to calculate energy levels of Ba (Rose *et al.*, 1978; Kotochigova and Tupizin, 1987). In contrast to these *ab initio* calculations just mentioned, numerous calculations have used model potentials to describe the interaction between core and valence electrons. Energy levels of Be and Mg were calculated using a frozen-core approximation in connection with the close-coupling method (Norcross and Seaton, 1976; Mendoza, 1981), or with configuration-interaction techniques (Laughlin and Victor, 1973). Ba was investigated using a model-potential approach including relativistic effects (Hafner and Schwartz, 1978). The calculations just discussed were restricted to low-lying levels. The resulting energy values have usually agreed poorly with experiment, es-

pecially in Ba. A configuration-interaction procedure developed by Chang (1986), which included higher Rydberg states, has been applied to calculate the positions and widths of $3pns,nd\ ^1P^o$ autoionizing states of Mg. However, the applicability of this approach to the highly perturbed and overlapping Rydberg series of the heavier alkaline earths remains to be demonstrated. To date, Chang's method has never been used to treat systems having more than one open channel per symmetry.

Calculations of the energy positions of higher-lying doubly excited levels of alkaline earths are relatively scarce. Three configuration-interaction calculations (Kim and Greene, 1988; Aymar, 1989; Morita and Suzuki, 1990) should be mentioned. These calculations, conducted in LS coupling, used a model-potential description of the core-valence interaction. The first study determined the $n_1sn_1p\ ^1P$ Wannier ridge states (Wannier, 1953) of Ca up to the $11s11p$ state (Kim and Greene, 1988). Energy positions of high-lying $n_1sn_1p\ ^1P$ states were obtained by diagonalization of the two-electron Hamiltonian using a set of closed-type two-electron functions that vanish at the boundary r_0= 120 a.u. The two-electron basis functions were of the same type as those used in streamlined eigenchannel R-matrix calculations to construct the Hamiltonian $\underline{H}_{cc}$ introduced in Sec. III.E. The use of a finite range basis helped to describe the mixing of ridge states with Rydberg states and continua. The n_1sn_1p states were identified in the eigenvalue spectrum by inspecting the eigenvectors. The same procedure was used (Aymar, 1989) to calculate the $n_1s^2\ ^1S$ Wannier ridge states of alkaline-earth atoms from Be through Ba. For each element, the energy positions of the $n_1s^2\ ^1S$ states were predicted up to the $(m_0+6)s^2$ state. A slightly smaller boundary radius r_0= 100 a.u. was used, the sphere of radius r_0 being found to be large enough to enclose the charge distribution of the $A^+\ (m_0+7)s$ ionic state whatever the element A. Finally, Morita and Suzuki (1990) performed a large-scale configuration-interaction calculation of doubly excited $n_1sn_2s\ ^1S$ states of Ca to interpret their laser spectroscopy observations. This work departs from those performed by Kim and Greene (1988) or Aymar (1989) in that Morita and Suzuki (1990) used two-electron basis functions which have zero amplitude at $r\rightarrow\infty$ rather than at finite r_0. The diagonalization of the two-electron Hamiltonian yielded the energy positions of $n_1sn_2s\ ^1S$ doubly excited states with $6\leqslant n_1\leqslant 10$ and $n_1\leqslant n_2\leqslant 20$. The theoretical energies agreed well with observed energies, deviations between theory and experiment being generally smaller than 2×10^{-4} a.u. Among all the observed states, only two states were tentatively ascribed to states having $n_1 = n_2$, with n_1= 9 and 10, respectively. The energy positions for the n_1s^2 states agreed well with those predicted by Aymar (1989).

The results obtained by Kim and Greene (1988), Aymar (1989), and Morita and Suzuki (1990) for the Wannier ridge states were analyzed in terms of two-electron Rydberg formulas. By viewing the pair of electrons as a single entity attached to the grand-parent ion, different formulas have been proposed to describe the (core) $n_1l_1n_1l_2$ states as members of a two-electron Rydberg series converging to the double-ionization limit (see Read, 1990, and references therein). The total energy of these states was expressed in terms of a screening parameter and of a quantum-defect parameter. The two-electron Rydberg formula proposed by Read (1977) is

$$E=-\frac{(Z-\sigma')^2}{(n_1-\delta_{n_1l_1}+\mu')^2}, \tag{4.2}$$

where Z is the charge of the core (here $Z=2$), $\delta_{n_1l_1}$ is the quantum defect of the ionic series (core) n_1l_1, σ' is a screening constant, and the effective quantum defect μ' is a correction to $\delta_{n_1l_1}$ accounting for the change of the penetration of the n_1l_1 electron into the core caused by the presence of the added n_1l_2 electron. An equivalent formula was derived by Rau (1983, 1984):

$$E=-\frac{4(Z-1/4-\sigma)^2}{(n_1+3/2-\mu)^2}. \tag{4.3}$$

Algebraically, the expressions (4.2) and (4.3) are essentially the same with parameters linearly related as follows:

$$\sigma=\sigma'/2+Z/2-1/4 \tag{4.4}$$

and

$$\mu=3/2+\delta_{n_1l_1}-\mu'. \tag{4.5}$$

Note that the μ' parameter of Eq. (4.2) is expected to be nearly core independent in contrast to the μ parameter involved in Eq. (4.3), which concerns the pair of electrons.

The applicability of the Rydberg formula to $n_1l_1n_1l_2$ states of alkaline earths was tested by Kim and Greene (1988), Aymar (1989), and Morita and Suzuki (1990) by plotting the predicted energy levels on an effective quantum-number scale, i.e., $\nu=(-2E)^{-1/2}$, as functions of n_1 or $n^*_{n_1l_1}=n_1-\delta_{n_1l_1}$. This plot should be a straight line with slope $[\sqrt{2}(Z-\sigma')]^{-1}$ or $[2\sqrt{2}(Z-1/4-\sigma)]^{-1}$. The energy levels calculated for ^1S (Aymar, 1989; Morita and Suzuki, 1990) and ^1P (Kim and Greene, 1988) Wannier states showed the expected linear dependence, demonstrating that these levels obey the two-electron Rydberg formula of Eqs. (4.2) or (4.3). An interesting result is that the slope obtained for ^1S Wannier states was almost the same for each element Be to Ba, showing only a slight increase of 3% when going from Be to Ba. Moreover, the slope for Ba is only 5% larger than that obtained for ^1S states of He (Rau, 1984).

The study of ^1S Wannier states allowed an interpretation of Ba and Ca experiments involving the high-lying doubly excited states $n_1l_1n_2l_2$ (l_1 and $l_2\leqslant 2$) with large n_1 values and $n_2>n_1$, i.e., on doubly excited states called "double-Rydberg" or "planetary" states (see Bloomfield *et al.*, 1984; Morita and Suzuki, 1990, and references therein). The observed levels were inter-

preted as members of Rydberg series converging to ionic A^+ $n_1 l_1$ states. These series are characterized by quantum defects $\bar{\delta}_{n_1 l_1}$, that are almost constant when $n_2 \gg n_1$. Moreover, the quantum defects increase linearly with n_1 with a slope of about 0.30–0.35 for all partial waves $(l_1 l_2)$ up through d waves. The independent-particle model predicts a linear dependence on n_1, but with a much smaller slope, in the range 0.20–0.25 (Aymar, 1989; Morita and Suzuki, 1990). Starting from the energy values calculated for the $n_1 s^2\ ^1S$ states it was possible to reproduce accurately the experimental results obtained for the quantum defects $\bar{\delta}_{n_1 s}$ of the $n_1 s n_2 s\ ^1S$ series of Ba (Bloomfield *et al.*, 1984) and Ca (Morita and Suzuki, 1990). Viewing the $n_1 s^2$ state, as the lowest member of the one-electron Rydberg series $n_1 s n_2 s\ ^1S$ converging to the A^+ $n_1 s$ state, and neglecting the variation of $\bar{\delta}_{n_1 s}$ with n_2, a linear relationship between $\bar{\delta}_{n_1 s}$ and $n^*_{n_1 s}$ (or equivalently n_1) was found (Aymar, 1989; Morita and Suzuki, 1990). The slope of the linear dependence, depending on the screening parameter σ', was about 0.31–0.35. The n_1 dependence of $\bar{\delta}_{n_1 s}$ was in much better agreement with experimental data than the independent-particle model prediction. This suggests that the correlation effects and the polarization distortion of the inner orbital induced by the presence of the outer electron are (not surprisingly) important for highly excited $n_1 s n_2 s$ states, even those with $n_2 \gg n_1$.

The two-electron Rydberg formulas of Eqs. (4.2) and (4.3) are known to successfully account for the position of Wannier states of He and H^-. It is also worth noting that generalized two-electron formulas capable of predicting the positions of the other dominant $^1P^o_1$ resonances $(n_2 \geqslant n_1)$ of He and H^- were obtained by combining the two-electron formula of Eq. (4.2) with the one-electron Rydberg formula (Sadeghpour and Greene, 1990; Domke *et al.*, 1991; Sadeghpour, 1991). These generalized two-electron energy formulas account, to a good approximation, for the observed energy positions of the dominant $_{n_2}(K=n_1-2,T=1)^+_{n_1}\ ^1P^o_1$ resonances (in Lin's notation, 1986) of He and H^-, with $n_2 \geqslant n_1$. At higher energies, however, different series begin to overlap, generating a rich spectrum dominated by multichannel perturbers. For $^1P^o$ symmetry, this new regime occurs above the $n_1 \approx 5$ threshold in He and above the $n_1 \approx 8$ threshold in H^-.

C. Autoionization widths and branching ratios

A wealth of data on doubly excited levels of alkaline earths has been obtained using multiphoton or multistep laser experiments. The excitation processes involved in these experiments are often so complicated that it is difficult to compute reliable theoretical photoionization spectra comparable with the observed spectra. In particular, as will be documented in Sec. IV.E below, numerous spectra have been investigated using multistep laser experiments based on the so-called isolated-core excitation technique (Cooke *et al.*, 1978). The theoretical description of the observed spectra depends on the correct description of final-state channel mixing and of the state from which the doubly excited levels are excited in the final step. The ability of theoretical multichannel spectroscopy to extract information (such as energy positions, widths, and classifications of autoionizing resonances) that is independent of the excitation process is particularly helpful in unraveling complex autoionizing spectra. The preceding section (Sec. IV.B) illustrated how the energy positions and identifications of the resonances can be obtained using the theoretical multichannel spectroscopy. The present section uses examples to document the development in Sec. II.D.3. Specifically, quantitative information on the widths and decay properties of autoionizing resonances emerges from a study of the density-of-states or time-delay matrices.

Our first example interprets the "anomalous" autoionization widths of states in the $7sng\ ^1G_4$ Rydberg series of Ba that were observed by Wang and Cooke (1993) using the isolated-core excitation method. The experiment found that the autoionization widths remain approximately constant instead of decreasing as ν_{7s}^{-3}. In addition, for $n \geqslant 15$, the quantum defects increase regularly. These anomalies reflect the perturbation of the series by localized perturbers. The even-parity $J=4$ levels located between 77 500 cm^{-1} (bottom end of the $7sng$ series, i.e., for $\nu_{7s}=l=4$) and the $7s$ threshold were studied using the jj-coupled eigenchannel R-matrix method (Luc-Koenig, Lecomte, and Aymar, 1994). The MQDT treatment used a short-range reaction matrix $\underline{K}^0$ (see Sec. II.D.3). The energy positions, identifications, and autoionization widths of $J=4^e$ levels were determined by analyzing the energy dependence of the analytic partial density of states introduced in Eq. (2.71). Fourteen doubly excited levels, low members of Rydberg series converging to the $6d$ and $4f$ thresholds, were predicted to lie in the studied energy range and to cause localized perturbations of the $7sng\ ^1G_4$ and $^3G_4$ Rydberg series. In addition, the $7sng$ series were affected by some $4fnp$ and $7pnf$ doubly excited levels that were diluted into several high-lying $7sng$ Rydberg levels. The calculated energy positions and widths of $7sng\ ^1G_4$ Rydberg levels agreed with the experimental data (Wang and Cooke, 1993). The anomalous behavior of the $7sng\ ^1G_4$ series for $n \geqslant 15$ (almost constant width and gradual increase of the quantum defect) reflects the perturbation by the $4f8p\ J=4$ levels and, in lesser extent, by the $7p5f\ J=4$ levels. Those resonances were predicted to be very broad and to lie around the $7s$ threshold. The $7sng\ ^3G_4$ series was predicted to be perturbed by the $4f5f\ ^3G_4$ level, which induces a narrowing of the $7sng\ ^3G_4$ widths around $n=17$.

Figure 19 shows how the characteristics of the resonances emerge from analysis of the energy dependence of the densities of states in closed channels. The three curves of Fig. 19 are associated with the $7sng$, $4fnf$, and $6dnd$ closed channels in the energy range corresponding to the low-energy end of the $7sng$ series. Each $ds^o_{n_1 l_1 l_2}(E)$ curve was obtained by summing the analytic

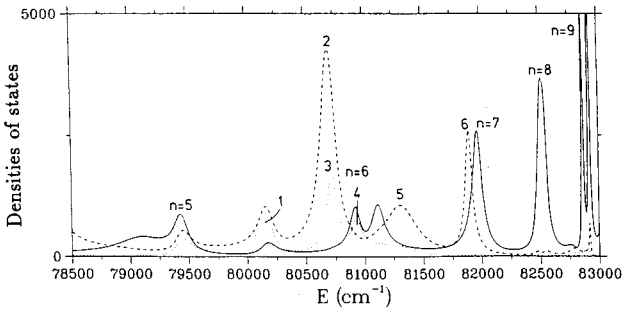

FIG. 19. Densities of states (in a.u.) for the even-parity $J=4$ states of Ba as functions of the energy relative to the Ba ground state: full line, ds^0_{7sg} density of states exhibiting $7sng$ resonances with $5\leqslant n\leqslant 9$; dashed line, ds^0_{4ff} density of states showing the $4f^2\ ^3H_4$ (2), $^1G_4$ (5), and $^3F_4$ (6) resonances; dotted line, ds^0_{6dd} density of states showing the $6d7d\ ^3G_4$ (1), $^3F_4$ (3), and $^1G_4$ (4) resonances. (From Luc-Koenig, Lecomte, and Aymar, 1994.)

partial densities of states [Eq. (2.71)] corresponding to jj-coupled fragmentation channels $i=\{n_1,l_1,j_1,l_2,j_2\}$ with the same quantum numbers n_1,l_1,l_2. The $ds^0_{7sg}(E)$ curve exhibits the $7sng$ $J=4$ resonances for $5\leqslant n\leqslant 9$. The extremely broad width for the $7s5g\ ^1G_4$ level at 79 100 cm^{-1} is ascribed to the strong coupling with the broad $4f7p$ (or $7p4f$) $^1G_4$ resonance. The $7s5g\ ^3G_4$ resonance appears at 79 450 cm^{-1}. The irregular evolution along the series of the fine-structure splitting between both $7sng\ ^{1,3}G_4$ levels derives from the perturbation of the series by numerous doubly excited levels. Three $4f^2$ resonances (numbers 2, 5, and 6) show up in the curve $ds^0_{4ff}(E)$ and the three peaks (1, 3, and 4) occurring in the $ds^0_{6dd}(E)$ profile are associated with $6d7d$ resonances.

It was shown, in Sec. IV.B above, that the eigenchannel R-matrix calculations of high-lying $4fnf$ levels ($n\geqslant 8$) with J=4–6 reproduce well the measurements of de Graaff *et al.* (1992). The calculations have been extended to the unobserved low-lying levels of the $4fnf$ series down to the $4f^2$ and $4f5f$ levels. Indeed, because of the strong mixing between the $4f_{5/2}nf_{7/2}$ and $4f_{7/2}nf_{5/2}$ Rydberg series, the quantum defect (mod 1) of high-lying $4fnf$ levels is strongly dependent on the levels. The unambiguous determination of the n value of $4fnf$ levels observed by de Graaff *et al.* (1992) requires that the series be followed down to their bottom end. The energy positions, identifications, and widths of $4f^2$ and $4fnf$ levels (up to $n=8$) were obtained, as for $7sng$ Rydberg levels, by analyzing the energy dependence of the total and partial analytical densities of states (Luc-Koenig, Aymar, and Lecomte, 1994). Eigenchannel R-matrix calculations were carried out using either the LS-coupled approach combined with the jj-LS frame transformation or the jj-coupled method. The $4f^2$ levels were found to be well separated from the other resonances. In contrast, many $4fnf$ levels ($5\leqslant n\leqslant 8$) were embedded into high-lying members of $7snl$ ($l=4,6$) and $6dnl$ ($l=2,4,6$) Rydberg series. Because of their coupling with Rydberg series, those $4fnf$ levels give rise to very intricated structures corresponding to complex resonance patterns (Giusti-Suzor and Lefebvre-Brion, 1984) with an apparent width related to the spectral range over which the Rydberg series is perturbed by the $4fnf$ interloper. A good recipe for determining the unperturbed width or apparent width of doubly excited levels embedded into Rydberg series is to treat the corresponding Rydberg series as open channels in the MQDT calculation and to analyze the energy dependence of the density of states associated with the doubly excited levels. Artificially opening a closed channel in the MQDT calculation removes all the perturbers associated with that channel. This procedure was used to predict the energy positions and apparent autoionization widths of $4fnf$ levels with J=4–6 and $5\leqslant n\leqslant 8$ and thus to determine the n values of high-lying $4fnf$ levels.

Recalling Sec. II.D.3, Smith's (1960) time-delay matrix [Eq. (2.69)] can be used to analyze resonances. The decay properties of some autodetaching Feshbach resonances of H^- were obtained by Sadeghpour *et al.* (1992) with an eigenchannel R-matrix calculation of the partial photodetachment cross sections, followed by an analysis of the eigenvectors of the time-delay matrix. The same procedure has also been used by Sadeghpour and Cavagnero (1993) to study the formation and decay of one prominent autoionizing resonance of He whose decay mode violates radial-correlation propensity rule satisfied by all other autoionizing resonances observed in He (for references, see Domke *et al.*, 1991).

The positions, autoionization widths, branching ratios, and identifications of the resonances can also be predicted using the alternative eigenchannel R-matrix approach described in Sec. III.H (Lecomte *et al.*, 1994). This method is adapted to the analysis of the lowest levels of Rydberg series described by doubly excited wave functions Φ_r completely included within the R-matrix reaction volume; moreover, the doubly excited levels are assumed not to interact with other Rydberg series. Lecomte *et al.* (1994) introduced a density-of-states matrix

$$\underline{Q}^p=2\pi\underline{x}_r^{\dagger}\underline{x}_r, \tag{4.6}$$

expressed in terms of the matrix $\underline{x}_r$ of Eq. (3.52b) whose element x_{ai} gives the amplitude of the doubly excited state Φ_a in the ith eigensolution of the transformed eigensystem [Eq. (3.52a)] satisfying the outgoing-wave normalization condition.

The resonant structures showing up in the autoionizing spectra can be analyzed from the energy dependence of $\mathrm{Tr}(\underline{Q}^p)$, which defines a density of states $ds(E)$. This total density of states can be decomposed in partial densities of states

$$ds_a(E)=2\pi\sum_i x_{ai}x_{ai}^*, \tag{4.7}$$

related to a single doubly excited states Φ_a.

Lecomte *et al.* (1994) have shown that, under the assumption of negligible energy dependence of the non-

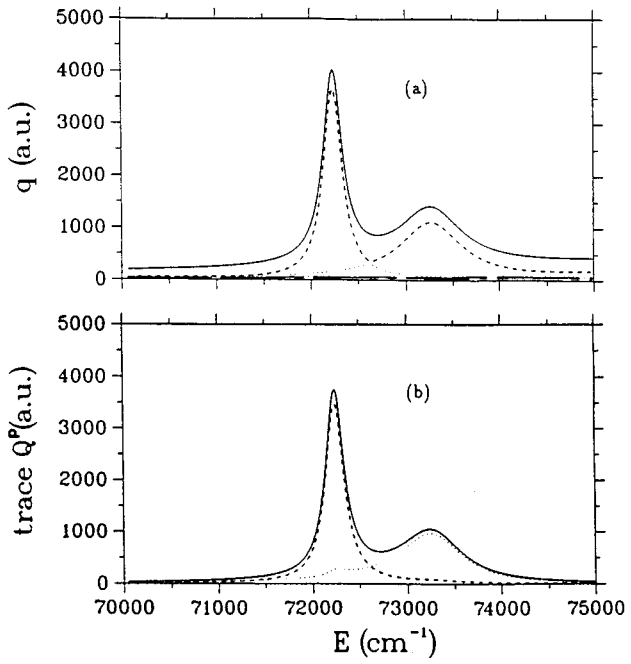

FIG. 20. The Ba $6d^2\ ^3F_4$ and $^1G_4$ resonances: (a) sum of eigenvalues q of the time-delay matrix $\underline{Q}$ identical to Tr$\underline{Q}$ (full line) and individual eigenvalues q (18 other lines)—note that the curves associated with 16 eigenvalues are almost superimposed with the horizontal axis $q=0$; (b) trace of the density matrix $\underline{Q}^p$ [Eq. (4.6)] (full line) and partial densities of states calculated with Eq. (4.7) for the $^3F_4$ (dashed line) and $^1G_4$ (dotted line) level. Energies are relative to the Ba ground state. (From Lecomte *et al.*, 1994.)

resonant scattering matrix $\underline{S}^{(0)}$, and thus of the coupling matrix $\underline{T}$ [Eq. (3.54)], the density-of-states matrix $\underline{Q}^p$ is identical to the time-delay matrix $\underline{Q}^{\rm phys}$ of Smith (1960) defined by Eq. (2.69). (Let us emphasize that, inasmuch as the R-matrix calculation is restricted to open channels, the time-delay matrix $\underline{Q}^{\rm phys}$ is identical to the short-range time-delay matrix $\underline{Q}$.) This allows one to ascribe unambiguously each resonance appearing in the evolution of Tr$(\underline{Q}^p)$ with energy to a particular doubly excited state Φ_a, and thus to identify every resonance.

The $6d^2$ J=0–4 resonances of Ba, located above the $6p$ threshold, were analyzed in this way, choosing a R-matrix reaction volume (r_0= 40 a.u.) large enough to contain the $6d^2$ levels. The doubly excited levels within the R-matrix box were identified as eigenstates of the closed part $\underline{H}_{cc}$ of the two-electron Hamiltonian (see Secs. III.E and III.H). Calculations were carried out in LS and jj couplings. For a given symmetry, the R matrix was restricted to open channels converging onto the $6s$, $5d$, and $6p$ thresholds. Figure 20 displays jj-coupled results for the $6d^2\ ^3F_4$ and $^1G_4$ resonances, which interact with 18 continua. Figure 20(a) shows the energy dependence of the trace of the time-delay matrix $\underline{Q}$ and of its eigenvalues q. Among the 18 eigenvalues, only two have non-negligible value. The two peaks visible on the full line near 72 200 cm^{-1} and 73 300 cm^{-1} are associated with the $6d^2\ ^3F_4$ and $^1G_4$ resonances, which are well isolated from the other resonances. Their separation in energy being larger than their widths, they can be viewed as "quasi-isolated" resonances. The energies of the resonances correspond to the maxima of the Tr$(\underline{Q})$ profile and the widths can be deduced from the full widths at half maximum of this profile.

Figure 20(b) shows the results obtained with the density matrix $\underline{Q}^p$ of Eq. (4.6). More precisely, it displays the energy dependence of the partial density of states $ds_a(E)$ defined in Eq. (4.7) for each individual $^3F_4$ (dashed curve) and $^1G_4$ (dotted curve) levels denoted 1 and 2, respectively. Although the dotted curve corresponding to the $^1G_4$ peak has a maximum also at the position of the prominent $^3F_4$ resonance, this secondary peak has a very small amplitude; this shows that the two resonances are almost uncoupled. The full curve corresponds to the sum $ds_1(E)+ds_2(E)$ of the individual contributions of these two $6d^2$ $J=4$ levels to the trace of the matrix $\underline{Q}^p$ defined by Eq. (4.6). The curve associated with the full line of Fig. 20(b) differs only slightly from the curve of Fig. 20(a) corresponding to the trace of the matrix $\underline{Q}$. Part of the differences results from the approximations (energy independence of the nonresonant continua and of the matrix $\underline{T}$) underlying the identity $\underline{Q}=\underline{Q}^p$. However, the differences primarily derive from the fact that the contributions to $\underline{Q}^p$ due to doubly excited states other than the $6d^2$ levels are neglected. The largest difference ($\sim$20%) occurring at the $^1G_4$ resonance peak was related to the neglect of the $7p4f\ ^1G_4$ level whose resonance is extremely diffuse and contributes to the time-delay matrix in a very wide energy range (see Luc-Koenig, Lecomte, and Aymar, 1994).

One major advantage of the resonance analysis in terms of the partial densities of states rather than with the time-delay matrix is the possibility of obtaining quantitative information on each individual resonance (including their identification) involved in complex structures corresponding to overlapping resonances. Figure 21 shows a complicated situation involving the two overlapping $6d^2\ ^3P_0$ and $^1S_0$ resonances and the close-lying $7s8s\ ^1S_0$ doubly excited level. Figure 21(a) shows the energy profiles of the trace and eigenvalues of the $\underline{Q}$ matrix calculated for $J=0^e$. In the higher-energy range, only one eigenvalue has a nonzero value, indicating that the $7s8s\ ^1S_0$ level corresponds to an isolated resonance. In contrast, in the lower energy range, two eigenvalues have non-negligible values and their profiles do not correspond to Lorentzian profiles, which means that the $6d^2\ ^1S_0$ and $^3P_0$ resonances are interacting. The positions and widths of each individual resonance cannot be extracted from such curves. These characteristics can be obtained by analyzing the energy dependence of the partial density of states [Eq. (4.7)] for each resonance. The jj-coupled results obtained for the $6d^2\ ^3P_0$ (dashed curve) and $^1S_0$ (dotted curve) resonances are shown on Fig. 21(b). The total density of state (full line) obtained by adding the contributions of each level is identical to that obtained from the time-delay matrix $\underline{Q}$, which means that the nonresonant continua and the matrix $\underline{T}$ are energy independent [Eq. (3.54)]. In con-

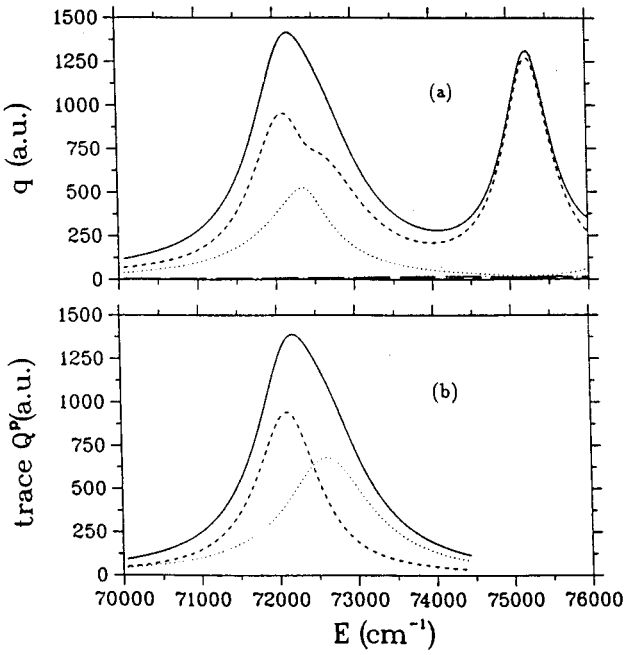

FIG. 21. The Ba $6d^2\ J=0$ and $7s8s\ ^1S_0$ resonances: (a) sum of eigenvalues q of the time-delay matrix $\underline{Q}$ identical to Tr$\underline{Q}$ (full line) and individual trace (full line) and individual eigenvalues q (5 other lines)—note that the curves associated with three eigenvalues are almost superimposed with the horizontal axis $q=0$; (b) trace of the density matrix $\underline{Q}^p$ [Eq. (4.6)] (full line) and partial densities of states calculated with Eq. (4.7) for the $6d^2\ ^3P_0$ (dashed line) and $^1S_0$ (dotted line) levels. Energies are relative to the Ba ground state. (From Lecomte *et al.*, 1994.)

trast, differences between the curves associated with the individual contributions [Fig. 21(b)] and the energy profiles of the eigenvalues of the matrix $\underline{Q}$ [Fig. 21(a)] are more marked than for the $J=4$ case.

The probabilities for each $6d^2$ resonant state to decay into the different available continua, i.e., the autoionization branching ratios, were predicted by an LS-coupled R-matrix calculation of the eigenvector of $\underline{Q}$ associated with its largest eigenvalue (see Sec. II.D.3). This procedure, valid only for isolated resonances, could be applied because for each LS symmetry there is only one $6d^2$ resonance. Branching ratios calculated in this way are expected to be valid for all isolated and quasi-isolated $6d^2$ resonances, which are well described in LS coupling.

The eigenchannel R-matrix calculations of the $6d^2$ (Lecomte *et al.*, 1994), $5d5g$ (Luc-Koenig *et al.*, 1995), and $4f7h$ (van Leeuwen *et al.*, 1995) levels as well as those of $6dng,ni$ (Aymar *et al.*, 1994), $7sng$ (Luc-Koenig, Lecomte, and Aymar, 1994), $4fnf$ (Luc-Koenig, Aymar, and Lecomte, 1994), and $4fng$ (van Leeuwen *et al.*, 1996) Rydberg series accounted for all the relevant continua $n_1l_1j_1\epsilon l_2j_2$ ($l_2\leqslant 8$) built on Ba^+ $6s$, $5d$, $6p$, ... The continua to which each level or series preferentially decays were identified using three different procedures centered around three different calculated quantities: the partial photoionization cross sections, the eigenvectors of the time-delay matrix, or phase-shifted MQDT parameters. The branching ratios were found to depend strongly on the specific level or series studied. There is no general rule that dictates which multipole term will predominate in autoionization caused by the Coulomb interaction. In many cases, resonances autoionize with large probability into channels associated with the lowest ($6s$ and $5d$) thresholds; this result is at variance with the statement (often found in the literature) that resonances autoionize preferentially into channels attached to the energetically closest ion core. R-matrix calculations that omit some channels built on low-lying thresholds must be viewed with caution, as they can give unreliable resonance widths and profiles.

Relatively few calculations of autoionization widths in the alkaline earths exist using theoretical approaches other than the eigenchannel R-matrix method. One is the configuration-interaction calculation of the positions and widths of $3pns,nd\ ^1P$ resonances of Mg (Chang, 1986). Bhalla *et al.* (1990) and Hahn and Nasser (1993) calculated the positions and widths of several doubly excited states of Ba using the multiconfiguration Hartree-Fock method. Theoretical quantum defects and widths calculated for $n_1sn_2s\ ^1S$ and $n_1sn_2d\ ^1D$ Rydberg levels converging to high-lying Ba^+ n_1s ($n_1\sim$7–10) levels were compared with the experimental data obtained for these series by Bloomfield *et al.* (1984). The n_1 dependence of quantum defects calculated by Bhalla *et al.* (1990) agrees excellently with experimental results; the calculated widths, however, disagree strongly with the measured widths. The agreement between the results of Hahn and Nasser (1993) and the experiment is rather poor for both positions and widths.

Autoionizing widths for some doubly excited levels of Ba with a large orbital momentum l_2 for the outer electron were calculated by Jones and Gallagher (1988), Poirier (1988, 1994), and Wang *et al.* (1991) assuming a single-configuration model for describing the doubly excited levels. Those authors used a Ba^+ orbital for the inner electron. Hydrogenic wave functions were used by Jones and Gallagher (1988) and Poirier (1988; 1994) for the outer electron, while Wang *et al.* (1991) used for the f wave involved in $6pnf$ levels wave functions that were calculated in the field of the Ba^{++} core screened by the inner electron. These calculations reproduce the experimental data well for $6pnf$ levels (Wang *et al.*, 1991) and $6pnl_2$ levels with $l_2\geqslant 4$ (Jones and Gallagher, 1988). Calculations show that the dominant decay path for $6pnl_2$ levels with $l_2\geqslant 4$ corresponds to dipole-allowed autoionization and accurately reproduce the observed rapid decrease of autoionization rates with l_2 for these levels.

The narrow autoionization widths of various Ba $5d5g$ levels located below the $5d_{3/2}$ threshold were measured accurately by van Leeuwen *et al.* (1994). Figure 22 shows an example of the $5d_{5/2}5g[K]$ levels, where the single-configuration model fails to reproduce the experimental widths. These jK-coupled levels, with nonoverlapping valence electrons, decay through the quadrupole interaction into the $6s\epsilon l$ continua. The single-

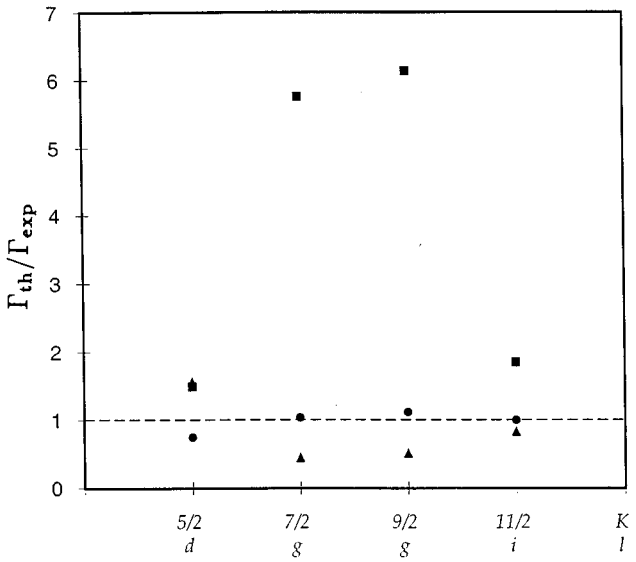

FIG. 22. Autoionization widths of $5d_{5/2}5g$ levels of Ba. The widths calculated by Luc-Koenig *et al.* (1995) using different approximations (Γ_{th}) are compared with the experimental values (Γ_{exp}) of van Leeuwen *et al.* (1994): full squares, single-configuration model; full triangles, *jj*-coupled eigenchannel *R*-matrix calculation accounting for the direct polarization of the inner electron by the outer electron; full circles, *jj*-coupled eigenchannel *R*-matrix calculation accounting for the direct polarization of the inner electron by the outer electron and for the dielectronic polarization term of Eq. (3.34). The ratios $\Gamma_{th}/\Gamma_{expt}$ obtained for the *jK*-coupled $5d_{5/2}5g[K]$ levels are plotted as functions of K. The l value of the $6s\epsilon l$ continuum toward which each $5d_{5/2}5g[K]$ level autoionizes is indicated below the K values.

configuration model gives autoionization widths systematically larger than the experimental data (full squares in Fig. 22). A detailed investigation of the $5d5g$ autoionization mechanisms was performed using the *jj*-coupled eigenchannel *R*-matrix approach (Luc-Koenig *et al.*, 1995). The autoionization widths were derived from the linewidths of the resonant peaks occurring in the calculated cross section and density-of-states profiles and from phase-shifted MQDT parameters. Widths calculated using those two different procedures agree. Two polarization effects were found to significantly influence the autoionization dynamics of the $5d5g$ states. The first effect was the direct polarization of the inner valence electron by the outer valence electron. This is a dipolar coupling between the $5dng$ and the $6pnl$ channels and, to a lesser extent, between the $5dng$ channels and the $4fnl$ channels, followed by autoionization through the $6pnl$ and $4fnl$ channels. This effect was accounted for in the calculations by including a large number of strongly closed channels (the same type included routinely in eigenchannel *R*-matrix calculations). This direct polarization effect significantly narrowed the $5d5g$ levels with $K \geqslant 7/2$, their widths becoming 1.5 to 3 times smaller than the experimental values (full triangles in Fig. 22). The second significant effect that played a critical role in the $5d5g$ autoionization process arose from the interaction of each valence electron with the electric dipole moment induced in the Ba^{++} core by the other valence electron. This dielectronic polarization correction [Eq. (3.34)] had the same angular dependence as the dipolar interaction but had an opposite effect; this correction partly canceled the polarization of the inner electron directly produced by the outer electron. The widths calculated with both polarization effects included (full circles in Fig. 22) agreed well with the experiment. This study was the first one to show that the dielectronic polarization correction can have a significant influence on the autoionization widths of neutral atoms. Its crucial role in negative ions was previously demonstrated by Thumm and Norcross (1991, 1992) who investigated the Cs^- negative ion using a fully relativistic Wigner-Eisenbud-type *R*-matrix calculation.

D. Photoionization from ground and low-lying states

1. Ground-state photoionization in lighter alkaline earths Be and Mg

Various theoretical approaches have been widely used to investigate ground-state photoionization of Be and Mg including double electron excitations. Among them, there are the configuration-interaction technique (Bates and Altick, 1973), the close-coupling method (Dubau and Wells, 1973; Mendoza and Zeippen, 1987), the multiconfiguration Tamm-Dancoff approximation (Radejovic and Johnson, 1985), the complex-basis-function technique (Rescigno, 1985), the L^2 technique (Moccia and Spizzo, 1989; Chang and Tang, 1992), the multiconfiguration Hartree-Fock method (Froese Fischer and Saha, 1987), many-body perturbation theory (Altun, 1989), the random-phase approximation (Chi *et al.*, 1991; Chi and Huang, 1994), the hyperspherical close-coupling method (Greene, 1981; Zhou and Lin, 1995), the Wigner-Eisenbud-type *R*-matrix method (Tully *et al.*, 1990), and the eigenchannel *R*-matrix method (O'Mahony and Greene, 1985). This last study was the first to demonstrate the ability of the eigenchannel *R*-matrix method to handle doubly excited levels of alkaline earths.

It is beyond the scope of this review to compare the results obtained with all these different methods. We compare only some unpublished eigenchannel *R*-matrix results with certain recent predictions and available experimental data. O'Mahony and Greene (1985) carried out an *LS*-coupled three-channel treatment (m_0snp, m_0pns, and m_0pnd) of the $^1P^o$ spectra of Be and Mg below the m_0p threshold. Because these early calculations used small sets of two-electron functions and a relatively crude unoptimized Hartree-Slater potential, we performed new *LS*-coupled eigenchannel *R*-matrix calculations of the photoabsorption spectra of Be and Mg improving both aspects. The differences between old and new results concern mainly the absolute values of cross sections, but not the shapes and positions of m_0pns and m_0pnd ^1P resonances. The new Be velocity result [Fig. 23(a)] is to be compared with recent theoretical predictions of Chi *et al.* (1991) [Fig. 23(b)]. These authors used the multiconfiguration relativistic

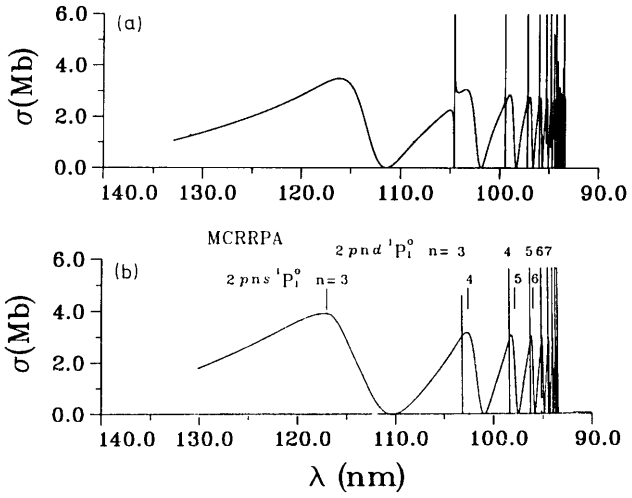

FIG. 23. Photoabsorption spectrum of Be below the $2p$ threshold as a function of the photon wavelength. (a) The LS-coupled eigenchannel R-matrix result; (b) the MCRRPA prediction of Chi *et al.* (1991). [Figure 23(b) is from Chi *et al.* (1991), courtesy of K. T. Cheng.]

random-phase approximation theory (MCRRPA), which is a generalization of the relativistic random-phase approximation including a multiconfiguration wave function for the ground state. Both R-matrix and MCRRPA calculations give a similar description of the broad $2pns\ ^1P^o$ series, and of the narrow $2pnd\ ^1P^o$ series, which appear owing to the $2p^2$-$2s^2$ mixing in the ground-state wave function. The positions of resonances as well as the cross sections at the $2pns$ peaks, agree well. Slight differences are visible in the wavelength range of the $2p3d$ and $2p4s$ resonances, where the R-matrix calculation predicts a stronger interaction between the $2pns$ and $2pnd$ channels than the MCRRPA calculation. However, the one available experiment is not precise enough to determine which calculation is better (Mehlman-Ballofet and Esteva, 1969).

Figure 24 compares the new R-matrix result for the Mg photoabsorption spectrum [Fig. 24(a)] with previous theoretical and experimental results [Fig. 24(b)]. Only velocity results are shown on [Fig. 24(a)], as the length and velocity results for the cross section agree to within better than 2%. In Fig. 24(b), the solid line corresponds to the prediction of Altun (1989), who used the many-body perturbation theory; the dot-dashed and dashed curves show the experimental results of Ditchburn and Marr (1953) and of Preses *et al.* (1984), respectively. The relative measurements of Preses *et al.* (1984) were normalized to the many-body perturbation theory results at the first resonance $3p4s\ ^1P$. Like the homologous Be resonances, the Mg $3pns$ resonances are broad and the $3pnd$ narrow. The energy range (7.6–10.6 eV) close to the $3s$ ionization threshold is very difficult to calculate accurately owing to the appearance of a Cooper minimum in the $3s \rightarrow \epsilon p$ transition. In Be, this Cooper minimum had occurred in the discrete spectrum. Various theories (Altun, 1989; Chang and Tang, 1992;

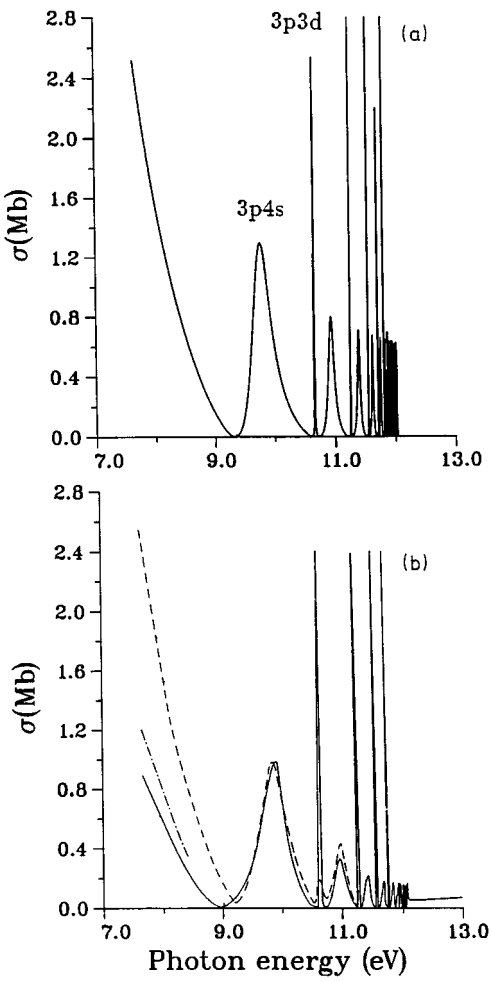

FIG. 24. Photoabsorption spectrum of Mg below the $3p$ threshold. (a) The LS-coupled eigenchannel R-matrix result; (b) the many-body perturbation theory prediction of Altun (1989) (full line), with experimental results of Ditchburn and Marr (1953) (dot-dashed line) and of Preses *et al.* (1984) (dashed line). The zero of the cross section near 9.0 eV arises from a Cooper minimum in the $3s \rightarrow 3p$ transition. [Figure 24(b) is from Altun (1989), courtesy of Z. Altun.]

Chi and Huang, 1994) predicted quite different cross section values at the threshold and for the lowest $3p4s$ resonance. The experimental threshold value of 2.39 ± 0.72 Mb (Yih *et al.*, 1989) agrees with this new R-matrix result of 2.5 Mb and with the calculation of Chang and Tang (1992), who obtained $\sim$ 2.4 Mb. These authors employed a simple configuration-interaction approach using a finite L^2-basis set constructed using B-splines and frozen-core Hartree-Fock orbitals.

A key result of the eigenchannel R-matrix and hyperspherical-coordinate studies of O'Mahony and Greene (1985) and of Greene (1981) is that near the $m_0 s$ threshold the wave functions of Be and Mg states are analogous to the wave functions describing the $2snp \pm 2pns$ states of He and H^- (Cooper *et al.*, 1963). They demonstrated that the $m_0 pns\ ^1P$ autoionizing resonances of Be and Mg could be described by wave functions that admix the $m_0 s\epsilon p$ open channel and the

m_0pns closed channel with equal amplitude. This "equipartition" of the wave function into the so-called plus and minus eigenmodes is reflected by the large width of m_0pns ^1P resonances of Be and Mg, visible in Figs. 23 and 24. In fact, these resonances are so broad that these doubly excited states decay after only half of a "Bohr-type orbit" is completed. This equipartition, and the strong similarities between the $^1P^o$ spectra of Be and Mg, are reflected in the short-range scattering parameters obtained in a two-channel treatment of the m_0snp and m_0pns channels. As visible on Figs. 1 and 6 of O'Mahony and Greene (1985), in Be and Mg the mixing angle goes to zero at an energy far below the m_0s threshold and increases to approximately $\pi/4$ at higher energies where the two m_0snp and m_0pns channels are essentially equally mixed. The variation of the mixing angle between the m_0snp and m_0pns channels as function of the energy for Be and Mg shows striking similarity with the variation of the mixing angle between the m_0snp and $(m_0-1)dnp$ ^1P channels of Ca, Sr, Ba, and Ra below the m_0s threshold displayed in Fig. 10. There also, the mixing is reminiscent of the so-called plus and minus states of H^- and He, in that the two corresponding ^1P eigenmodes of heavy alkaline earths Ca to Ra apparently have similarly strong coupling implied by the structure $(m_o-1)dnp \pm m_osnp$.

2. Ground-state photoionization in heavier alkaline earths Ca to Ra

The heavier alkaline-earth atoms have been experimentally investigated far more extensively than have Be and Mg. A wealth of experimental data on the $m_0s^2 \rightarrow J=1^o$ photoionization spectra of Ca, Sr, and Ba in the region below the m_0p threshold has been reported during the last three decades. Earlier spectra were obtained in photoabsorption using light from conventional sources or synchrotron radiation (Garton and Codling, 1960, 1968; Garton and Tomkins, 1969b; Brown *et al.*, 1973, 1983; Hudson *et al.*, 1969, 1970; Garton *et al.*., 1974; Brown and Ginter, 1978, 1980; Connerade *et al.*, 1980). Spectral structures were detected with photographic plates or photoelectric detectors. Recently the quality of the spectra has improved, especially in the spectral resolution, through the use of improved detection techniques (Griesmann *et al.*, 1988, 1992, 1994; Griesmann, 1990; Abutaleb, de Graaff, Ubachs, Hogervorst, and Aymar, 1991; Connerade and Farooqi, 1991; Farooqi *et al.*, 1991, 1992). Many eigenchannel R-matrix calculations have treated photoabsorption spectra of the heavy alkaline-earth atoms below the m_op threshold. Earlier calculations carried out for the $^1P^o$ spectra of Ca (Greene and Kim, 1987) and Sr (Aymar, 1987) treated these atoms in LS coupling and included five LS-coupled fragmentation channels: m_0snp, $(m_0-1)dnp$, $(m_0-1)dnf$, m_0pns, and m_0pnd. Then, more elaborated calculations including spin-orbit effects, either with the jj-LS frame transformation or directly in the variational calculation were performed for Ca (Kim and Greene, 1987; Ueda *et al.*, 1990; Farooqi *et al.*, 1991), Sr (Aymar *et al.*, 1987; Greene and Aymar, 1991; Farooqi *et al.*, 1992), Ba (Aymar, 1990; Abutaleb, de Graaff, Ubachs, Hogervorst, and Aymar, 1991; Greene and Aymar, 1991) and Ra (Greene and Aymar, 1991). When combined with the frame transformation, the LS-coupled R-matrix calculations determine three LS-coupled reaction matrices $\underline{K}^{^1P}$, $\underline{K}^{^3P}$ and $\underline{K}^{^3D}$ of dimension 5, 5, and 3, respectively. Channels involved for the $^1P^o$ and $^3P^o$ are the same and for the $^3D^o$ symmetry the LS-coupled channels are: $(m_0-1)dnp$, $(m_0-1)dnf$, and m_0pnd. The $\underline{K}^{LS}$ matrices are recoupled into a single jj-coupled reaction matrix using the jj-LS frame transformation. The MQDT calculations performed with the jj-coupled reaction matrix obtained from R-matrix calculations in either LS or jj coupling include 13 jj-coupled fragmentation channels: $m_0snp_{1/2}$, $m_0snp_{3/2}$, $(m_0-1)d_{3/2}np_{1/2}$, $(m_0-1)d_{3/2}np_{3/2}$, $(m_0-1)d_{3/2}nf_{5/2}$, $(m_0-1)d_{5/2}np_{3/2}$, $(m_0-1)d_{5/2}nf_{5/2}$, $(m_0-1)d_{5/2}nf_{7/2}$, $m_0p_{1/2}ns_{1/2}$, $m_0p_{1/2}nd_{3/2}$, $m_0p_{3/2}ns_{1/2}$, $m_0p_{3/2}nd_{3/2}$, and $m_0p_{3/2}nd_{5/2}$.

A few theoretical studies of the photoabsorption spectra of Ca, Sr, or Ba were previously carried out using many-body perturbation theory (Altun *et al.*, 1983; Frye and Kelly, 1987) or the Wigner-Eisenbud-type R-matrix formulation (Scott *et al.*, 1983; Bartschat *et al.*, 1986). Here, we compare some eigenchannel R-matrix results with some of those previous calculations, but we focus mainly on the the comparison with experimental spectra. Most of the theoretical spectra presented in this paper correspond to total photoionization cross sections versus the photon energy or wavelength, without any convolution over the finite experimental resolution. Consequently, no meaningful comparison can be made between experiment and theory for the intensity of narrow peaks.

Figure 25 compares the theoretical spectrum obtained between the $4s$ and $3d$ thresholds of Ca using the jj-coupled R-matrix method with the experiment of Farooqi *et al.* (1991). The theoretical curve in Fig. 25(a) is the geometric mean of the length and velocity curves. The experimental spectrum [Fig. 25(b)] was obtained using a tunable coherent vacuum-ultraviolet four-wave mixing source and a thermoionic diode detection. Absolute cross sections were obtained by calibrating data with previous absolute measurements (Parkinson *et al.*, 1976; McIlrath and Sandeman, 1972). The absorption lines were assigned to $3dnp$ and $3dnf$ resonances, members of six series converging to the $3d_{3/2,5/2}$ thresholds, and perturbed by the $4p5s$ $^{1,3}P_1$ resonances (Brown *et al.*, 1973). The broadest resonances correspond to the $3dnp$ $^1P_1$ levels strongly coupled to the $4s\epsilon s$ $^1P_1$ continuum. The strong mixing between the m_osnp and $(m_o-1)dnp$ ^1P channels which dominates the bound spectra of all the heavy alkaline-earth atoms (see Sec. IV.A.1) manifests itself also above the m_os threshold. Overall, the agreement between theory and experiment is remarkably good. The eigenchannel R-matrix calculation closely reproduces the irregular variation of the widths and intensities along the $3dnp$

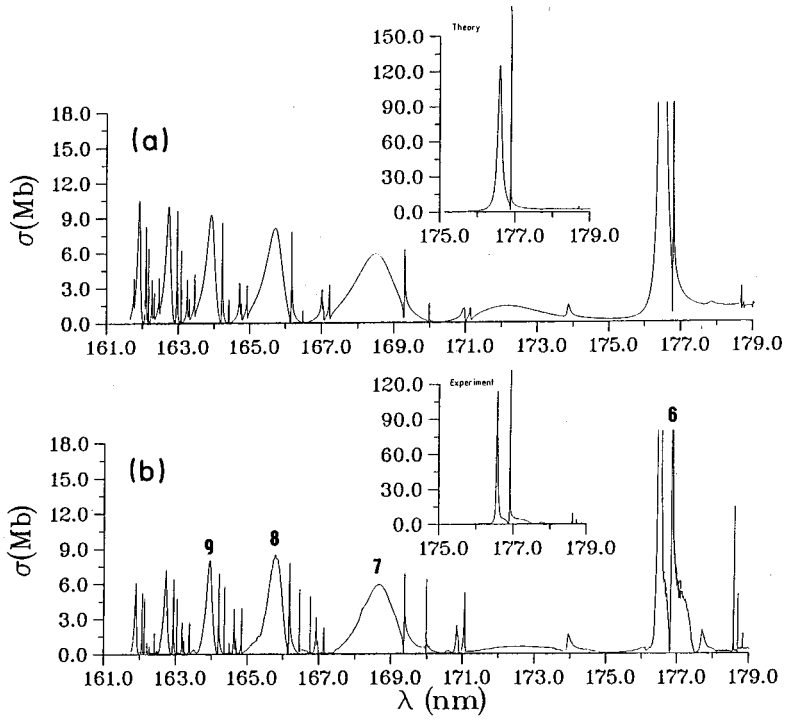

FIG. 25. Photoabsorption spectrum of Ca between the $4s$ and $3d_{3/2}$ thresholds. (a) The jj-coupled R-matrix result; (b) the experimental result (wavelength resolution ~0.02 nm). Some $3dnp\ ^1P_1$ resonances are labeled by their n values. (From Farooqi *et al.*, 1991.)

$^1P_1$ series. Some of the corresponding resonances are marked in Fig. 25(b) by their n values. The $3d6p\ ^1P_1$ resonance at $\lambda \sim 177$ nm is anomalously narrow and intense compared to the highest members of the series. The width irregularity was attributed to the influence of the $4p5s\ ^1P_1$ perturber located in between the $3dnp\ ^1P_1$ resonances with $n=6$ and 7 (Greene and Kim, 1987; Farooqi *et al.*, 1991; Connerade, 1992). More precisely, destructive interference results from cancellation between the two alternative autoionization paths $3dnp \rightarrow 4s\epsilon p$ and $3dnp \rightarrow 4pns \rightarrow 4s\epsilon p$ (Greene and Kim, 1987). Figure 25(a) includes weak features due to the spin-orbit interaction, though the earliest eigenchannel R-matrix calculation of Greene and Kim (1987) showed that an LS-coupled R-matrix treatment gives a good description of the ^1P resonances.

Two previous calculations were conducted in Ca in the same energy range, one using the many-body perturbation theory (Altun *et al.*, 1983) and one using the Wigner-Eisenbud-type R-matrix formulation (Scott *et al.*, 1983). Both calculations, which treated Ca in LS coupling and thus dealt with the ^1P resonances only, showed distinctly poorer agreement between theory and experiment for the ^1P resonances. The departure of the R-matrix results of Scott *et al.* (1983) from experiment may derive from their use of an *ab initio* all-electron description of the Ca^{++}-e interaction as opposed to the semiempirical potential used in the eigenchannel R-matrix studies (Greene and Kim, 1987; Farooqi *et al.*, 1991).

Many-body perturbation theory was also used by Frye and Kelly (1987) to calculate the photoabsorption of Sr in the analogous energy range, i.e., below the $4d$ threshold. As in Ca, spin-orbit effects were neglected and the description of the $4dnp$ and $4dnf\ ^1P$ resonances is, not surprisingly, poorer than that obtained with eigenchannel R-matrix calculations where fine-structure effects are included with the jj-LS frame transformation (Aymar, 1987).

Figure 26 compares the photoabsorption spectrum of Ca and Sr between the $(m_0-1)d_{5/2}$ and $m_0p_{3/2}$ thresholds. For Ca, the measurements of Griesmann *et al.* (1988) in Fig. 26(a), are compared with the frame-transformation results of Kim and Greene (1987), shown in Fig. 26(b). For Sr, the measurement of Griesmann (1990) [Fig. 26(c)] is compared with the jj-coupled eigenchannel R-matrix results of Greene and Aymar (1991) [Fig. 26(d)]. Measurements of Griesmann *et al.* (1988, 1994) and of Griesmann (1990) were obtained using synchrotron radiation and a linear thermoionic diode detector. In Ca [Fig. 26(a)], as for Fig. 25, absolute calibration was achieved using previous absolute measurements. In Sr, the experimental data have been normalized to achieve agreement with the R-matrix result at the $4d6p\ ^1P_1$ resonance which dominates the photoionization spectrum between the $5s$ and $4d_{3/2}$ thresholds (see Greene and Aymar, 1991).

In both Ca and Sr, the calculations reproduce the shapes of the observed m_0pns and $m_0pnd\ J=1$ resonances. In Ca, agreement between experiment and eigenchannel calculations remains superior to that of calculations performed by Scott *et al.* (1983) or by Altun *et al.* (1983).

Concerning the measured cross sections, calibrated as described above, the Ca $4pns$ peaks are slightly too weak compared to R-matrix results, while the Sr $5pns$ resonances are too intense. Recently, Griesmann *et al.* (1994) have calibrated their data (Griesmann,

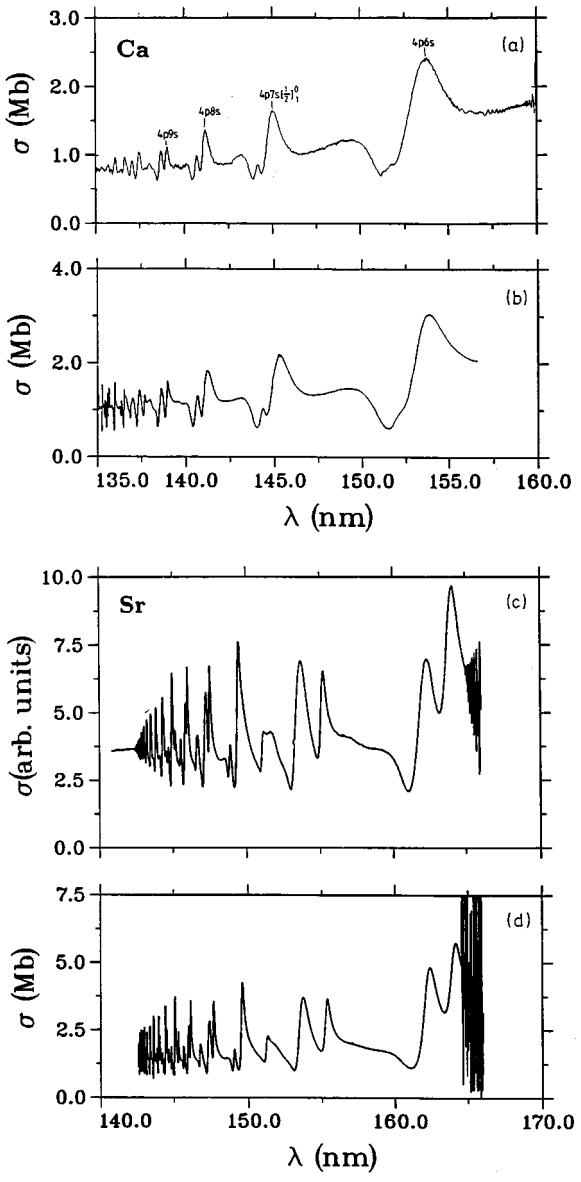

FIG. 26. Photoabsorption spectra of Ca and Sr between the $(m_0-1)d_{5/2}$ and $m_0p_{3/2}$ thresholds. (a) Ca measurement of Griesmann *et al.* (1988) (wavelength resolution $\sim$ 0.05 nm); (b) Ca frame-transformation result of Kim and Greene (1987). (c) Sr measurement of Griesmann (1990) (wavelength resolution $\sim$ 0.05 nm); (d) Sr jj-coupled eigenchannel R-matrix result of Greene and Aymar (1991). [Figures for Ca are from Griesmann *et al.* (1988) and those for Sr are from Greene and Aymar (1991).]

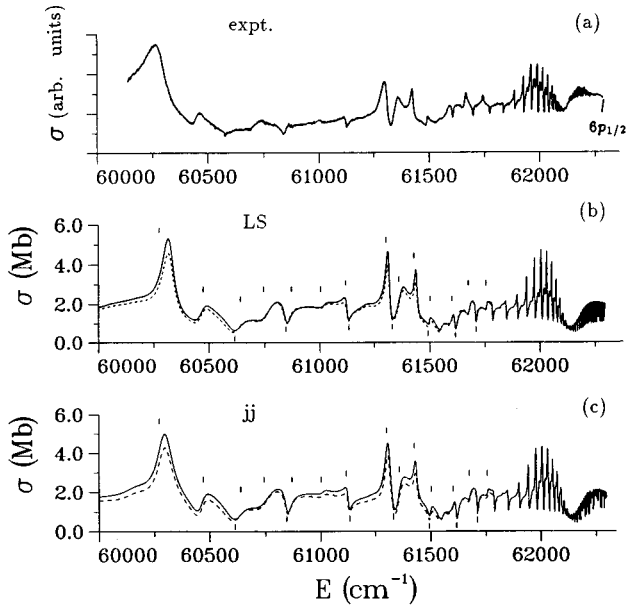

FIG. 27. Photoabsorption spectrum of Ba in the energy range from 60 000 cm^{-1} up to the $6p_{1/2}$ threshold: (a) relative measurement of Brown and Ginter (1978) (energy uncertainty $\sim$ 0.11 cm^{-1}) that was normalized to give the overall best agreement with the R-matrix results; (b) jj-LS velocity (full line) and length results (dashed line); (c) jj velocity (full line) and length results (dashed line). The vertical bars in (b) and (c) indicate the position of the observed absorption peaks and minima. (From Greene and Aymar, 1991.)

1990) with the cross section determined by Alexa *et al.* (1983) at the 5s threshold. In the energy range between the $4d_{5/2}$ and $5p_{3/2}$ thresholds, the magnitude of these normalized cross sections agree well with the R-matrix cross sections. However, the experimental cross section of the very strong $4d6p\ ^1P_1$ resonance is smaller than the R-matrix result. Therefore, the normalization of the data of Griesmann *et al.* (1988, 1994) in Ca and Sr is somewhat questionable and further absolute measurements are desirable. If the experimental normalization is in fact correct, this discrepancy may suggest that the energy dependence of calculated dipole matrix element needs to be described more accurately in sensitive cases such as these.

In both Ca and Sr, the m_0pnd resonances are very broad owing to their strong coupling with the $(m_0-1)d\epsilon f$ continua and are hardly recognizable as individual structures, whereas the members of the m_0pns series can be clearly identified. Correlation effects are very similar in Ca and Sr and major differences between Ca and Sr primarily reflect the increasing role of the spin-orbit interaction in Sr. Indeed, an LS-coupled R-matrix calculation correctly describes the main features of the Ca photoabsorption spectrum (Greene and Kim, 1987), but not of Sr. Due to the weakness of the spin-orbit interaction in Ca, the relative amplitude of the two m_0pns peaks corresponding to the same n value differs strongly in Ca [Figs. 26(a) and 26(b)]. That is, the Ca $^3P_1$ resonances to the left of the intense peaks in Fig. 26(a) are very weak. The stronger spin-orbit interaction in Sr [Figs. 26(c) and 26(d)] causes the corresponding resonances to have roughly the same intensity.

Figure 27 compares the high-resolution experimental Ba result of Brown and Ginter (1978), just below the $6p_{1/2}$ threshold, shown in Fig. 27(a), with the eigenchannel R-matrix results (Greene and Aymar, 1991). Figure 27(b) shows the spectrum obtained with R-matrix calculations in LS coupling combined with the jj-LS frame transformation. Figure 27(c) displays the jj-coupled

R-matrix result. The results obtained by both eigenchannel R-matrix approaches are almost identical and they reproduce the experimental spectrum accurately. In particular, the periodic enhancement of the cross sections due to low-lying $6p_{3/2}nl$ levels mixed with $6p_{1/2}n'l$ Rydberg levels is well described. Figures 27(b) and 27(c) display both velocity and length results (shown as solid and dashed lines) which are very close, giving some confidence in the convergence of the variational calculations.

One important point is that, even in Ba, R-matrix calculations including the spin-orbit terms within the reaction volume and those including these terms perturbatively through the jj-LS frame transformation give almost identical results. This is true in the energy range close to the $6p$ threshold but also in the whole energy range from the $6s$ threshold up to the $6p_{3/2}$ threshold (see Greene and Aymar, 1991). Thus, although no detailed comparison between photoabsorption spectra calculated with either the fully jj-coupled R-matrix method or using the jj-LS frame transformation was done for Ca and Sr, the conclusions obtained in Ba are expected to hold for the lightest elements Ca and Sr.

R-matrix calculations were also carried out in the heaviest alkaline-earth atom Ra (Greene and Aymar, 1991). Because no experimental spectrum is available in the autoionizing energy range of Ra we do not reproduce here the predicted photoionization spectra. We only briefly summarize the conclusions obtained previously. As in Ba, spectra predicted with LS-coupled R-matrix calculations combined with the jj-LS frame transformation were compared to those obtained with the jj-coupled R-matrix method. In Ra, not surprisingly, significant differences between the autoionizing pattern predicted by the two approaches occur. The differences are much more marked in the low-energy range between the $7s$ and $6d_{3/2}$ thresholds than in the higher-energy range between the $6d_{5/2}$ and $7p_{3/2}$ thresholds.

Figure 28 compares the photoabsorption spectra for all the heavier alkaline earths from Ca to Ra between the $m_0p_{1/2}$ and $m_0p_{3/2}$ thresholds. Results in Ca (Kim and Greene, 1987) [Fig. 28(a)], Sr (Aymar, 1987) [Fig. 28(b)], and Ba (Aymar, 1990) [Fig. 28(c)] were obtained with LS-coupled R-matrix calculations combined with the jj-LS frame transformation, while those for Ra (Greene and Aymar, 1991) [Fig. 28(d)] were obtained with the jj-coupled R-matrix method. In Ca [Fig. 28(a)], the theoretical result (thin line) is compared with the experimental result of Brown and Ginter (1980) (thick line). The quasiperiodic autoionizing structures formed by asymmetrical absorption profiles are very similar in all alkaline-earth atoms from Ca to Ra. This great similarity throughout the heaviest alkaline-earth atoms reflects the systematic near invariance of the electronic channel mixings. Here, the strongest channel mixing corresponds to the m_opnd-$(m_o-1)d\epsilon f$ mixing for $^1P_1$ channels.

The absolute squares of the off-diagonal elements $|S_{ij}|^2$ of the short-range scattering matrix defined by Eq. (2.43) provide an index of the mixing between channels

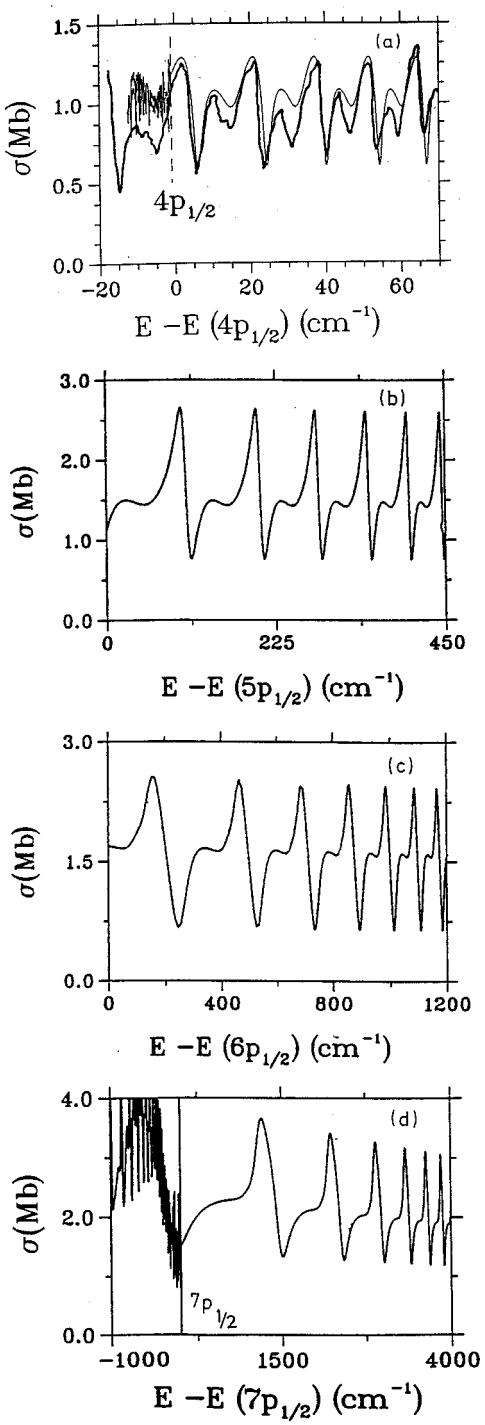

FIG. 28. Photoabsorption spectra of Ca to Ra between the $m_0p_{1/2}$ and $m_0p_{3/2}$ thresholds as functions of the energy relative to the $m_0p_{1/2}$ threshold. Results in Ca (a), Sr (b), and Ba (c) were obtained with LS-coupled R-matrix calculations combined with the jj-LS frame transformation, while those in Ra (d) correspond to the jj-coupled R-matrix result. In Ca, the theoretical result (thin line) is compared with the experimental result of Brown and Ginter (1980) (thick line). (From Aymar, 1987, 1990; Kim and Greene, 1987; and Greene and Aymar, 1991.)

i and j. Selected $|S_{ij}|^2$ elements obtained for Ca $^1P^o$ (Greene and Kim, 1987) with LS-coupled eigenchannel R-matrix calculations are shown in Fig. 29 as functions

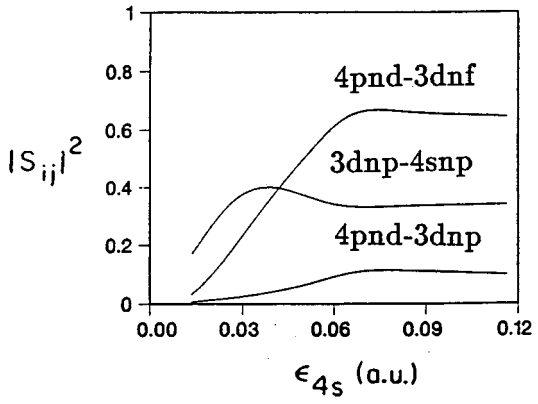

FIG. 29. Short-range scattering matrix elements for the $^1P^o$ symmetry of Ca. Absolute squares of selected matrix elements obtained with LS-coupled eigenchannel R-matrix calculation are shown as functions of the photoelectron energy between the $4s$ and $4p$ thresholds. (From Greene and Kim, 1987.)

of the photoelectron energy between the $4s$ and $4p$ thresholds. The very large widths of $4pnd\ ^1P$ levels, visible in Figs. 26 and 28(a), reflect the extremely strong mixing between the $4pnd$ and $3dnf$ channels. Such a m_0pnd-$(m_0-1)dnf$ channel mixing is shared by all the heavier alkaline earths, as visible on Fig. 28. Kim and Greene (1988) showed that this exceptionally strong channel mixing continues to dominate the photoabsorption spectrum of Ca at higher energies. The marginally weaker, but nevertheless strong $3dnp$-$4snp$ mixing generates the broad autoionization widths of $3dnp\ ^1P$ resonances of Ca for $n \neq 6$ (see Fig. 25). In this case also, the pair of channels $3dnp$-$4snp$ remains strongly coupled at high energy. The $(m_0-1)dnp$-m_0snp mixing is weaker in Sr, Ba, and Ra than it is in Ca, at least below the m_0p threshold, but it is still far from negligible.

A final example of photoabsorption spectra in the alkaline earths considers the energy range well above the m_0p threshold, where almost no experimental data are available to date. Figure 30 shows the Ca photoabsorption spectra predicted by Kim and Greene (1988) from the $4p$ threshold up to nearly the $6s$ threshold. Calculations were carried out with the LS-coupled eigenchannel R-matrix method. On Figs. 30(a) and 30(c), the upper curve is the velocity result and the lower one the length result. This study was the first one performed with the eigenchannel R-matrix method at an energy higher than the m_0p threshold. For this reason this study shed new light on fundamental aspects of R-matrix and MQDT technologies. The investigated energy range included the $5s$, $4d$, $5p$, $4f$, and $5d$ thresholds; the number of open and weakly closed channels (up to sixteen) included in the calculation depended on the energy range under study. The reaction volume radius was 31 a.u. The resonances pertaining to the $5snp$, $4dnp$, $4dnf$, $5pns$, $5pnd$, $4fnd$, $4fng$, and $6snp$ series, as well as the lowest resonances associated with the $5dnp$ and $5dnf$ series, were identified. The $5s5p$ and $6s6p\ ^1P$ autoionizing states, which involve two electrons with the same degree of excitation, are the analog of the so-called plus states that dominate the photoabsorption

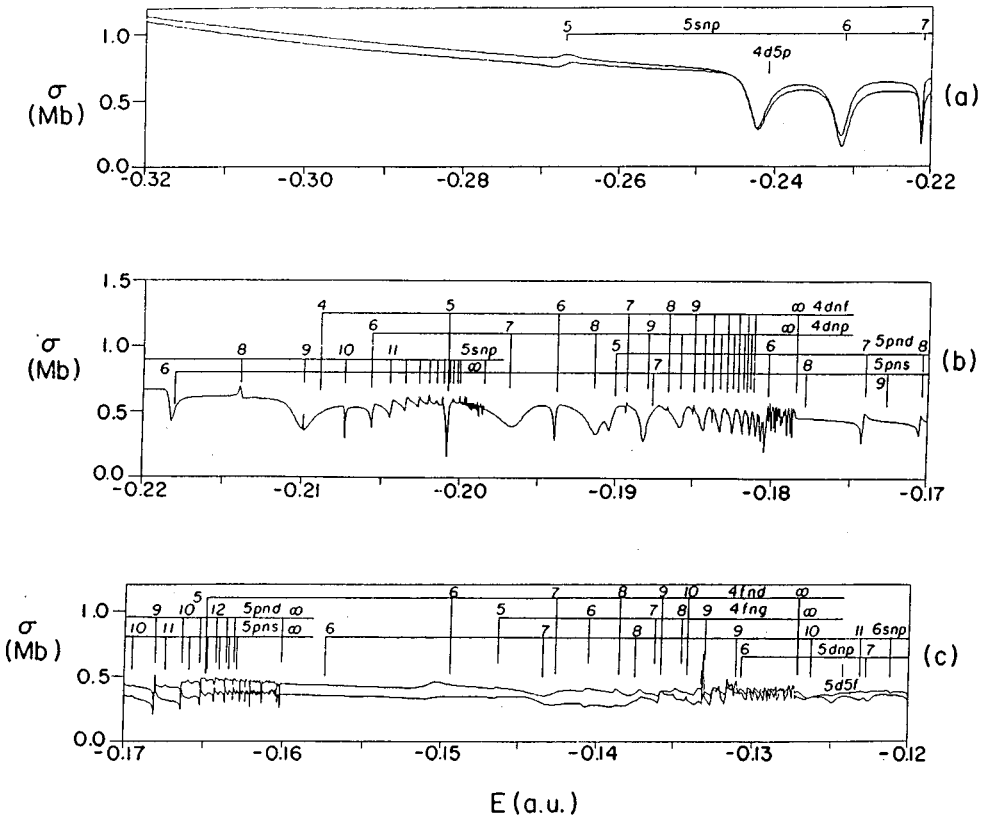

FIG. 30. Photoabsorption spectra of Ca predicted below the $6s$ ionization limit with LS-coupled eigenchannel R-matrix calculations: (a) energy for E between -0.32 a.u. and -0.22 a.u.; (b) for E between -0.22 a.u. and -0.17 a.u.; (c) for E between -0.17 a.u. and -0.12 a.u.. The upper curve is the velocity result and the lower one the length result. Energies in a.u. are referred to the double-ionization limit. (From Kim and Greene, 1988.)

spectrum of He (Cooper *et al.*, 1963). In contrast [Figs. 30(a) or 30(c)], the $5s5p$ and $6s6p$ resonances are surprisingly weak.

For ground-state photoionization, only total cross sections were measured experimentally. However, some other observables more sensitive to channel mixing and spin-orbit effects were predicted using the eigenchannel R-matrix method. In particular, Kim and Greene (1987) calculated for ground-state photoionization of Ca, in addition to the total cross section, the partial cross sections, the angular distributions of emitted electrons, and the alignment of the Ca^+ fragments. The energy range considered in that work was from the $4s$ threshold up to the $4p_{3/2}$ threshold. Not surprisingly, the weak spin-orbit interaction, accounted for through the jj-LS frame transformation, was seen to affect the photoelectron asymmetry parameters and the alignment parameters much more strongly than the total cross section.

3. Photoionization from low-lying excited states

The earliest experimental investigations on autoionizing states of alkaline-earth atoms mainly dealt with the odd-parity $J=1$ levels, which can be observed in absorption from the ground state. Now, owing to the development of laser spectroscopy, a wealth of data has been obtained for odd- and even-parity autoionizing levels with various J values. This section concerns photoionization from low-lying excited levels only. Photoionization spectra investigated using multistep laser experiments based on the the so-called isolated-core excitation (ICE) technique (Cooke *et al.*, 1978) will be treated in Sec. IV.E. As explained in Sec. III.F , the procedure used to calculate photoionization spectra from low-lying states is identical to the procedure employed for calculating photoabsorption spectra. Photoionization cross sections are calculated using short-range dipole matrix elements, which only include contributions within the reaction volume. This volume must be chosen to be large enough to enclose the full initial-state wave function. The use of too large a boundary radius r_0 complicates the R-matrix calculation of final-state channel mixing. Calculations of photoionization spectra from low-lying states of alkaline earths performed to date have been restricted to $r_0 \leqslant 50$. a.u. They dealt with various photoionization spectra from excited states of Ca (Aymar and Telmini, 1991; Assimopoulos *et al.*, 1994; Luc-Koenig, Bolovinos, *et al.*, 1994), Sr (Kompitsas *et al.*, 1990, 1991; Goutis *et al.*, 1992), and Ba (Greene and Theodosiou, 1990; Gounand *et al.*, 1991; Luc-Koenig and Aymar, 1991; Armstrong, Wood, and Greene, 1993; Bartschat and Greene, 1993; Telmini *et al.*, 1993; Wood *et al.*, 1993; Carré *et al.*, 1994; Aymar and Luc-Koenig, 1995; Lecomte *et al.*, 1995; Luc-Koenig *et al.*, 1995; Lagadec *et al.*, 1996). For illustration, we concentrate on photoionization from low-lying excited states of Ba. Results on total photoionization cross sections and on other observables will be discussed.

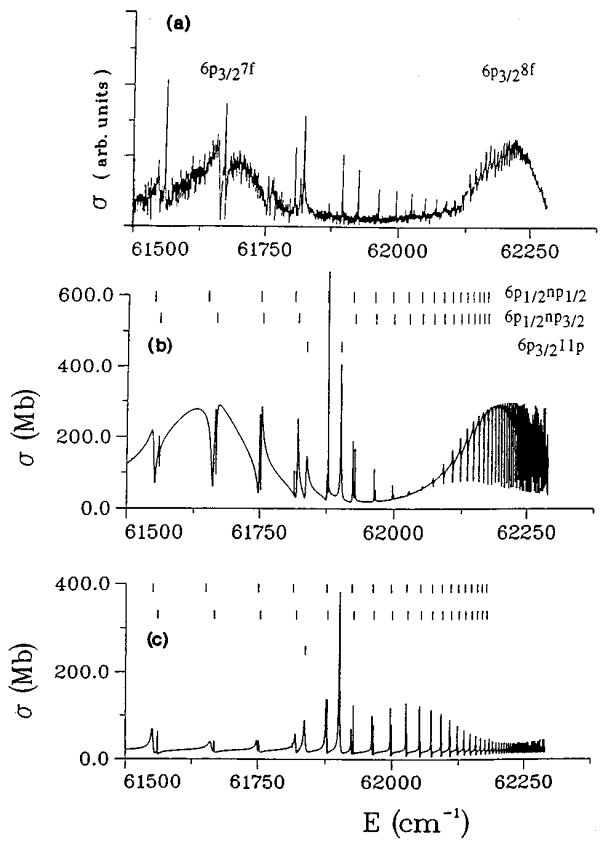

FIG. 31. Photoionization spectra for the $6pnp$, nf $J=1$ levels of Ba below the $6p_{1/2}$ threshold: (a) experimental spectrum recorded by de Graaff *et al.* (1990) from the $5d6p\ ^3P_0$ excited state; (b), (c) theoretical spectra obtained with LS-coupled eigenchannel R-matrix calculations and the jj-LS frame transformation corresponding to the $5d6p\ ^3P_0$ and $6s6p\ ^3P_0$ initial states, respectively. The vertical bars in (b) and (c) indicate the positions of the $6pnp$ $J=1$ resonances calculated from an effective short-range reaction matrix referring to the $6pnp$ closed channels (see Sec. IV.B). Energies are relative to the Ba ground state. (From Luc-Koenig and Aymar, 1991.)

a. Total photoionization cross sections

Figure 31 deals with the $6pnp$ and $6pnf$ $J=1$ levels of Ba, below the $6p_{1/2}$ threshold. The excitation spectrum recorded by de Graaff *et al.* (1990) from the $5d6p\ ^3P_0$ excited state [Fig. 31(a)] is compared with the theoretical spectrum [Fig. 31(b)] obtained with the frame-transformation treatment (Luc-Koenig and Aymar, 1991). The calculated spectrum reproduces the energy positions, widths, and shapes of the observed autoionizing resonances. The very narrow resonances corresponding to the Rydberg series $6p_{1/2}np_{1/2}$ and $6p_{1/2}np_{3/2}$ and to the $6p_{3/2}11p_{1/2}$ and $6p_{3/2}11p_{3/2}$ $J=1$ levels are superimposed on broad structures, the $6p_{3/2}nf$ $J=1$ resonances with $n=7$ and 8. The calculation reproduces accurately the large differences between the widths of $6pnp$ and $6pnf$ resonances. The extremely large widths of $6p_{3/2}nf$ $J=1$ levels reflect the very strong coupling of $6pnf$ channels with $5d\epsilon g$ continua. All Ba $6pnf$ states have similar anomalously large autoionization rates, with decay times of approximately half of the Bohr orbit period.

The autoionizing pattern depends on the initial state from which the resonances are excited. Figure 31(c) displays the calculated excitation spectrum of $6pnp,nf$ $J=1$ levels from the $6s6p\ ^3P_0$ initial level. The calculated cross sections differ greatly for the two initial states. The $6pnf$ resonances have vanishing cross sections in excitation from the $6s6p\ ^3P_0$ initial level. Indeed, the direct $6s6p \rightarrow 6pnf$ excitation is not allowed, in contrast to the $5d6p \rightarrow 6pnf$ excitation.

Similar dependence of the profiles of autoionizing lines on the choice of intermediate states used in the excitation process has been observed by Keller *et al.* (1991). Several $5dnd$ autoionizing resonances of Ba were observed in a multiphoton resonant ionization experiment involving either the $6snp\ ^1P_1$ or the $5dnp\ ^1P_1$ level as intermediate level. The shape of the observed $5dnd$ resonances was seen to drastically change with the intermediate state from which they were excited.

A major test case for theoretical and experimental methods has proven to be the photoionization of the excited Ba $6s6p\ ^1P_1$ level. A large number of experimental (Burkhardt *et al.*, 1988; Kallenbach *et al.*, 1988; He *et al.*, 1991, 1995; Keller *et al.*, 1991; Willke and Kock, 1991, 1993; Lange, Eichmann, and Sandner, 1991) and theoretical (Bartschat and McLaughlin, 1990; Greene and Theodosiou, 1990; Bartschat *et al.*, 1991; Greene and Aymar, 1991; Bartschat and Greene, 1993; Wood *et al.*, 1993) papers have been devoted to this excited-state photoionization process.

Figure 32 compares the *jj*-coupled eigenchannel *R*-matrix results of Wood *et al.* (1993) (lower curves) with the experiment of Lange, Eichmann, and Sandner (1991) (upper curves) in the wavelength region between 417 nm ($6s$ threshold) and 355 nm. Only relative photoionization cross sections were measured and in Fig. 32, the experimental cross sections were normalized by optimizing the agreement between theory and experiment in the region of the broad resonances near 372 nm. In addition, the theoretical spectra have been convolved with the experimental resolution of 0.2 cm^{-1}. Two pulsed lasers were used in the experiment. The first laser was used to excite the $6s6p\ ^1P_1$ level and the second laser photoionized this level. Both lasers were linearly polarized with the polarization vectors being either parallel [Fig. 32(a)] or perpendicular [Fig. 32(b)]. In the parallel case, the allowed final states were $J_f=0,2$, $M_{J_f}=0$, while in the perpendicular case they were $J_f=1,2$, $|M_{J_f}|=1$. Breakdown of these selection rules can lead in excited-state photoionization spectra to unexpected resonances that do not belong to the final-state symmetries selected by a given experiment. A central point of the treatment of Wood *et al.* (1993) was the inclusion of hyperfine effects in the odd isotopes of neutral barium to explain the presence of unexpected features in the photoionization spectra recorded by Lange, Eichmann, and Sandner (1991). Wood *et al.* (1993) have shown that the resonances marked by the arrows in Figs. 32(a) and 32(b) are only present in the calculations

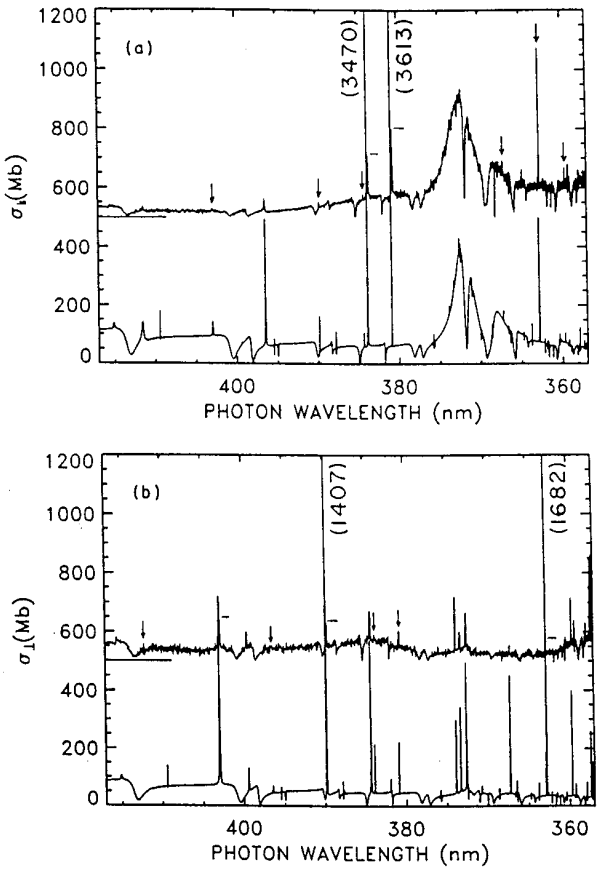

FIG. 32. Photoionization cross section of Ba $6s6p\ ^1P_1$ laser-excited level as a function of wavelength of the photoionizing laser: (a) for parallel polarization of the two lasers and (b) for perpendicular polarization of the two lasers. The baseline of the normalized experimental cross section (upper curves) has been set to 500 Mb. Experimental resonances, which are overlapped with theory, are labeled with horizontal bars. The *jj*-coupled *R*-matrix cross sections include the effect of hyperfine depolarization of the $6s6p\ ^1P_1$ level. Numbers in parentheses are peak intensities of theoretical cross sections. The resonances marked with the arrows are forbidden by electronic selection rules and are only present in the calculation when hyperfine effects are taken into account. (From Wood *et al.* 1993.)

when hyperfine effects are taken into account. "Electronically forbidden" resonances with $J_f=1$ arise in Fig. 32(a), while those with $J_f=0$ arise in Fig. 32(b). As shown by Wood *et al.* (1993), the cross section for photoionization of a $J_e=1$ state from a $J_0=0$ ground state in which both exciting and photoionizing lasers are linearly polarized has the general form

$$\begin{aligned}\sigma(J_0\rightarrow J_e\rightarrow J_f)=&\sigma^{(\mathrm{iso})}(1\rightarrow 0)[1+2g_{\mathrm{av}}^{(2)}P_2(\cos\theta)]\\&+\sigma^{(\mathrm{iso})}(1\rightarrow 1)[1-g_{\mathrm{av}}^{(2)}P_2(\cos\theta)]\\&+\sigma^{(\mathrm{iso})}(1\rightarrow 2)[1+\tfrac{1}{5}g_{\mathrm{av}}^{(2)}P_2(\cos\theta)].\end{aligned}\tag{4.8}$$

In Eq. (4.8), the factor $g_{\mathrm{av}}^{(2)}$ represents averages over

time and over the relative isotopic abundances of natural Ba of an expression for the time dependence of the effects of the quadrupolar hyperfine interaction on the J_e excited state. It is a reasonable approximation to assume that complete depolarization of the excited state occurs for the Ba isotope with $I=3/2$; in this limit one has $g_{\rm av}^{(2)}=0.864$. In Eq. (4.8), θ is the angle between the linear polarization vectors and P_2 is a Legendre polynomial. The "isotropic" cross section $\sigma^{(\rm iso)}(J_e \rightarrow J_f)$ is the total photoionization cross section for the transition $J_e \rightarrow J_f$ that would be calculated if the excited levels were randomly oriented, i.e., with equal population in all magnetic sublevels M_{J_e}. The calculation successfully reproduces the experimental data, including the forbidden resonances. The positions and widths of the resonances are generally very well reproduced, while some persistent discrepancies in the peak intensities and the resonance line shapes are still not resolved. As described elsewhere (Aymar *et al.*, 1982, 1983; Camus *et al.*, 1983; Greene and Aymar, 1991) the resonances are ascribed to $5dns, nd$ levels and to the $6p^2\ ^1S_0$ level which forms with neighboring $5dnd\ J=0$ levels a complex resonance near 372 nm. The eigenchannel R-matrix calculations (Greene and Theodosiou, 1990; Greene and Aymar, 1991; Wood *et al.*, 1993) confirmed the identifications deduced from empirical multichannel quantum-defect theory, in particular that of the $6p^2\ ^1S_0$ (Aymar *et al.*, 1982), which has been the subject of some controversy. Note finally that the isotropic eigenchannel R-matrix cross section $[\sigma^{(\rm iso)}(1\rightarrow 0)+\sigma^{(\rm iso)}(1\rightarrow 1)+\sigma^{(\rm iso)}(1\rightarrow 2)]$ at the 6s threshold (417 mm) agrees reasonably well with the absolute measurements of He *et al.* (1991) and of Willke and Kock (1993).

Apparent effects of the hyperfine interaction on excited-state photoionization cross sections were also found by Armstrong, Wood, and Greene (1993). Those authors studied photoionization of the $5d6p\ ^3D_1$ level both experimentally and theoretically. There also, experimental spectra were compared with jj-coupled eigenchannel R-matrix calculations and incorporation of hyperfine effects was found to be necessary for a complete description of the measured cross sections. The importance of hyperfine interaction in resonant three-photon ionization of Ba via excited levels was also appreciated by Mullins, Chien, Hunter III, Keller, and Berry (1985) and by Hunter *et al.* (1986); hyperfine-interaction effects were incorporated in the theoretical description in these papers.

Isotropic photoionization cross sections of the Ba $6s6p\ ^1P_1$ level were also calculated using the Wigner-Eisenbud-type R-matrix formulation (Bartschat and McLaughlin, 1990; Bartschat *et al.*, 1991). One-electron spin-orbit, mass-correction, and Darwin terms of the Breit-Pauli Hamiltonian were included in the variational calculation. The calculation of Bartschat and co-workers showed distinctly poorer agreement with the experimental spectra (He *et al.*, 1991, 1995; Lange, Eichmann, and Sandner, 1991; Willke and Kock, 1991, 1993) than the eigenchannel R-matrix results. The most striking discrepancy concerned the $6p^2\ ^1S_0$ resonance, which failed to appear in the spectrum calculated by Bartschat *et al.* (1991). This discrepancy between the eigenchannel and Wigner-Eisenbud-type R-matrix calculations was resolved by Bartschat and Greene (1993), who performed a set of test calculations with both R-matrix approaches. To make the comparison meaningful, all test calculations used the same empirical core potential of Eq. (3.26) and incorporated relativistic effects through the spin-orbit interaction operator only. These calculations showed that the photoionization cross section near the $6p^2\ ^1S_0$ resonance cannot be obtained by a standard close-coupling expansion involving only physical bound states; instead, the correct description of short-range correlation effects and of the relaxation of the $6p$ orbital requires the inclusion of doubly excited configurations of the continuum-continuum type. It should be noted that the eigenchannel R-matrix calculations routinely include doubly excited configurations confined within the R-matrix box and among them those of continuum-continuum type. In other words, short-range correlation and polarization effects are accounted for by using strongly closed channels described by two-electron basis functions constructed from closed-type orbitals. Convergence of the $6p^2\ ^1S_0$ resonance using a purely ionic basis set in the eigenchannel R-matrix calculation requires 324 closed-type basis functions. One reason for this surprisingly slow convergence for the Ba $6p^2\ ^1S_0$ resonance, and also for the $7p^2\ ^1S_0$ (Lecomte *et al.*, 1994), Ca $4p^2\ ^1S_0$ (Aymar and Telmini, 1991; Assimopoulos *et al.*, 1994), and Sr $5p^2\ ^1S_0$ (Kompitsas *et al.*, 1991) resonances is that these levels exhibit strong angular electron correlations. More precisely, all these levels were found to correspond to a strong admixture of the $m_0' p^2$ and $(m_0'-1)d^2\ ^1S_0$ configurations ($m_0'=m_0$ or m_0+1). Similarly strong electron correlations were found for the analogous $^1D_2$ resonances and for higher-lying $n_1 s n_1 s\ ^1S$ Wannier ridge states of alkaline earths (Aymar, 1989).

The work of Bartschat and Greene (1993) also indicated the need for caution regarding the apparent convergence of the close-coupling results in calculations performed with a limited number of short-range correlation functions. Recently, Mende *et al.* (1995) encountered the same difficulties in describing with Wigner-Eisenbud-type R-matrix calculation the Sr $5p^2\ ^1D_2$ resonance observed in the photoionization cross section of the Sr $5s5p\ ^1P_1^o$ excited level. To achieve reasonable agreement between theory and experiment, they simulated in a semiempirical way the short-range correlation and relaxation effects that are not fully described by the standard close-coupling expansion.

Various photoionization spectra from low-lying excited levels of Ba calculated with the eigenchannel R-matrix approach in either LS coupling (plus frame transformation) or jj coupling have been compared (see, for example, Greene and Aymar, 1991; Telmini *et al.*, 1993). Spectra are generally very similar except in some cases in which the low-lying level is not well described in LS coupling. Rather different results were found for the

excitation spectra of $6p_{1/2}nf\ J=1$–3 series of Ba excited from the $5d6p\ ^3F_2$ level in the energy range where the $6p_{3/2}8f\ J$=1–3 levels are located. These levels were not excited in the experimental spectrum recorded by Abutaleb, de Graaff, Ubachs, and Hogervorst (1991), nor in the theoretical spectrum calculated in jj coupling, while they are visible in the spectrum obtained in LS coupling (see Fig. 7 of Telmini *et al.*, 1993). Recall that the frame-transformation treatment incorporates fine-structure effects in the final states only but assumes that the initial level is well described in LS coupling. The $5d6p\ ^3F_2$ level (LS weight of $\sim$80%) corresponds to the pure jj-coupled $5d_{3/2}6p_{1/2}\ J=2$ level (97%). This explains why the LS calculations poorly describe photoionization from this level. Ground states of alkaline earths as well as the Ba $5d6p\ ^3P_0$ level involved in the photoionization process considered in Fig. 31 are well described in LS coupling. However, this is not the case for various excited states of Sr and mainly of Ba. Thus, a prerequisite of any calculation of photoionization spectrum in LS coupling (and frame transformation) must be to check whether the initial state is correctly described in that coupling. This reflects a limitation of the frame-transformation calculations.

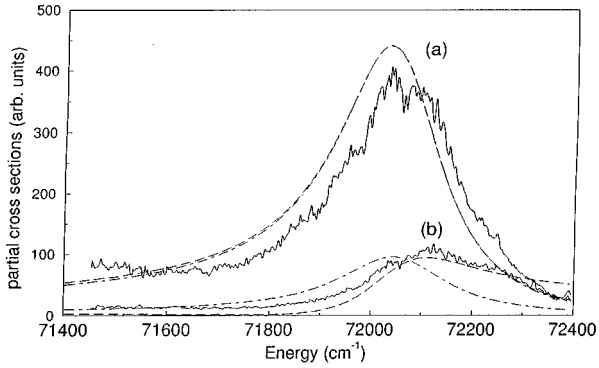

FIG. 33. Measured and calculated partial photoionization cross sections of the Ba $5d7p\ ^3D_1$ state as functions of the energy relative to the Ba ground state: (a) in unresolved $6s$, $5d_{3/2,5/2}\epsilon l$ continua and (b) in unresolved $6p_{1/2,3/2}\epsilon l$ continua. The experimental spectra (full curves) are compared with the calculated spectra (long-dashed curves). Cross sections calculated by disregarding the excitation of the $4f7p\ ^3F_2$ state are also shown (dot-dashed curves). Only the calculated and measured partial cross sections corresponding to electrons ejected into the $6s$, $5d_{3/2,5/2}\epsilon l$ continua (a) were adjusted. (From Lecomte *et al.*, 1995).

b. Partial photoionization cross sections and photoelectron angular distributions

Even-parity doubly excited levels of Ba have recently been investigated in a two-step laser experiment that covered a large energy range from the $6p_{3/2}$ threshold to (nearly) the $7s$ threshold. Excitation of the Ba ground state via $5d7p\ ^3P_1$ and $^3D_1$ levels produced photoelectrons that were analyzed in two groups of energy-resolved continua $6s$, $5d_{3/2,5/2}\epsilon l$ ("fast" electrons) and $6p_{1/2,3/2}\epsilon l$ ("slow" electrons). Laser beams were polarized and several combinations of the laser polarizations were used. The experimental partial cross sections were compared with results obtained with the alternative eigenchannel R-matrix formulation (Lecomte *et al.*, 1994) described in Sec. III.H. The R-matrix calculations were carried out in jj coupling using an R-matrix box of radius r_0=50 a.u. Both experiment and calculations were carried out in this study (Lecomte *et al.*, 1995). Figure 33 compares the experimental and theoretical partial photoionization cross sections in the 71 400–72 400 cm^{-1} energy range. The electron yields were recorded via the $5d7p\ ^3D_1$ level, with both lasers having the same circular (σ^+) polarization. Only $J=2$ final states were populated. All 17 $J=2$ open channels were included in the R-matrix calculation; no additional closed channels were introduced, except within the reaction volume through "closed-type" basis functions. The resonances resulted from the coupling between the open channels and the $6d^2$ doubly excited states that fit completely within the reaction volume. The positions and widths of $6d^2$ states were predicted by Lecomte *et al.* (1994). Experimental and theoretical spectra were in good agreement. Only the calculated and measured "fast" electron yields [Fig. 33, curves (a)] were adjusted, showing that the branching ratio of the experimental partial cross sections was reproduced by the calculation. The peak in Fig. 33 [curves (a) and (b)] is ascribed to the $6d^2\ ^3F_2$ state; the $6d^2\ ^3P_2$ state, predicted to lie in the same energy range, is more weakly excited (the corresponding dipole moments are in a ratio of $\sim$ 3). The higher-lying $4f7p\ ^3F_2$ state at 78 760 cm^{-1} was found to have a strong influence on the profiles. This is evident in the theoretical slow electron yield [Fig. 33, curves (b)], where the energy position and profile (long-dashed curve) are strongly modified when the direct excitation of the $4fnp$ channel is disregarded (dot-dashed curve). The $4f7p\ ^3F_2$ resonance, strongly excited from the intermediate level, has a very large autoionization width (Γ= 1600 cm^{-1}). Its coupling with the continua is large enough to induce a strong mixing with the $6d^2\ ^3F_2$ state. The energy difference between the maxima of both experimental cross sections was found to result from interference effects between the direct excitation of the $6d^2\ ^3F_2$ state and the indirect excitation via the $4f7p\ ^3F_2$ state. The fact that the calculated spectrum [Fig. 33, curves (b)] was more asymmetric than the experimental spectrum may indicate that the calculation overestimated the excitation of the $4f7p\ ^3F_2$ state. The eigenchannel R-matrix calculations were also able to successfully account for observations in the higher-energy range from 76 000 to 84 000 cm^{-1} (Lecomte *et al.*, 1995). There, resonances correspond either to doubly excited states, such as the $7p^2\ ^3P_2$ level, enclosed within the reaction volume, or to Rydberg states such as $7snd$, which are associated with closed channels. The procedures developed by Lecomte *et al.* (1994) were extended to handle such situations involving doubly excited levels confined within the reaction volume that interact with levels pertaining to Rydberg series. Special

attention has been given to the identification of each individual resonance in complex autoionizing structures. All resonances were found to exhibit strong electron correlations.

We mention here some experiments on angular distributions of photoelectrons obtained by resonance-enhanced multiphoton ionization through excited levels of alkaline earths. A review of experimental and theoretical studies carried out up to 1987 was given by Smith and Leuchs (1987). Resonant multiphoton ionization via various intermediate levels of Ca, Sr, and Ba has been used to study configuration mixing in these intermediate levels (Matthias *et al.*, 1983; Leuchs and Smith, 1985; Mullins, Chien, Hunter III, Jordan, and Berry, 1985; Mullins, Chien, Hunter III, Keller, and Berry, 1985; Mullins, Hunter III, Keller, and Berry, 1985; Hunter III *et al.*, 1986; Keller *et al.*, 1991). The angular distributions of photoelectrons ejected into channels attached to different ion cores were measured.

The photoelectron angular distributions observed by Mullins and co-workers and by Hunter III *et al.* (1986) were fitted to an appropriate parametric expression accounting for hyperfine interaction occurring from the coherent excitation of hyperfine states. These hyperfine effects are strong in some cases (Mullins, Chien, Hunter III, Keller, and Berry, 1985; Hunter III *et al.*, 1986).

Data obtained by Matthias *et al.* (1983) and Leuchs and Smith (1985) via $6snd\ ^{1,3}D_2$ and $6sns\ ^1S_0$ Rydberg levels, respectively, which interact with certain $5d7d$ doubly excited states, have been successfully interpreted by parametrizing the angular distributions in terms of ionization amplitudes and closed-channel coefficients previously obtained with semiempirical MQDT models. From the data they obtained in Ba via low-lying levels, Hunter III *et al.* (1986) suggested that semiempirical MQDT analysis of the $J=2^e$ and $J=0^e$ bound spectra (Aymar *et al.*, 1978; Aymar and Robaux, 1979) mislabeled some levels. Recent R-matrix calculations (Greene and Aymar, 1991) confirm the original labels given in Moore's table (1958) to $J=2^e$ levels, and thus do not support the reassignment obtained by semiempirical multichannel quantum-defect theory. In contrast, R-matrix calculations support the $6s8s\ ^1S_0$ label (Aymar *et al.*, 1978) given to the level at 34 731 cm^{-1} ($6p^2\ ^1S_0$ in Moore's table), in contradiction with the suggestion of Hunter III *et al.* (1986). As was detailed in the previous subsection, several experimental and theoretical studies have demonstrated that the $6p^2\ ^1S_0$ level corresponds to a broad autoionizing resonance around 44 800 cm^{-1}.

The various experiments quoted just above deal with ionization into a structureless continuum, i.e., with final-state energies far from any autoionization resonance. In contrast, the two-photon experiment of Keller *et al.* (1991), via the $5d6p$ or $6s6p\ ^1P_1$ level, measured the angular distributions of photoelectrons across $5dnd$ autoionizing resonances. Like the profiles of the autoionizing resonances, the angular distributions were found to drastically change with the intermediate level used in the excitation process.

We discuss below, in Sec. IV.E, several experiments in alkaline earths in which the angular distributions of photoelectrons were measured using multistep laser excitation based on the isolated-core excitation scheme; in the last step, the autoionizing levels were excited from a Rydberg level. Several experiments were performed over a large energy range across autoionizing resonances. In contrast, angular distributions of photoelectrons obtained by multistep ionization through low-lying excited levels were measured at fixed energy or over a restricted energy range.

An indirect determination of the angular distributions of photoelectrons ejected from Ba $6pns$, $nd\ J=1$ autoionizing levels into $6s\epsilon p$ and $5d_{3/2,5/2}\epsilon p$, f continua was recently reported by Lagadec *et al.* (1996). Measurements covered a 1000 cm^{-1} energy range. Autoionizing levels were populated from the Ba ground state using the three-step laser excitation scheme $6s^2 \rightarrow 6s6p\,^1P_1 \rightarrow 6p^2\ ^3P_0 \rightarrow 6pns$, $ndJ=1$. Linearly polarized laser beams were used. The variation of the asymmetry parameters characterizing the differential partial cross sections corresponding to electrons ejected into continua attached to the $6s$ or $5d_{3/2,5/2}$ ion cores were determined by measuring, for different combinations of the orientations of the laser polarization vectors, the differential partial cross sections for a fixed solid angle of photoelectron ejection. The experimental measurements were successfully accounted for by eigenchannel jj-coupled R-matrix calculations (Lagadec *et al.*, 1996).

E. Photoionization from Rydberg states

An impressive number of experimental investigations on autoionizing states of the alkaline earths Mg to Ba has been carried out using multistep laser experiments based on the isolated-core excitation (ICE) experimental technique. Earlier investigations focused first on Sr (Cooke *et al.*, 1978; Xu *et al.*, 1986, 1987; Zhu *et al.*, 1987) and Ba (Gounand *et al.*, 1983; Bloomfield *et al.* , 1984; Tran *et al.*, 1984; Kachru *et al.*, 1985; Bente and Hogervorst, 1990; Hieronymus *et al.*, 1990; Jones *et al.*, 1991a, 1991b; Lange, Aymar, *et al.*, 1991; de Graaff *et al.*, 1992, and references therein), then on Ca (Lange *et al.*, 1989; Morita and Suzuki, 1990), and more recently on Mg (Dai *et al.*, 1990; Schinn *et al.*, 1991; Lindsay, Cai, *et al.*, 1992; Lindsay, Dai, *et al.*, 1992). Finally, notice that an increasing number of laser experiments being performed in the alkaline earths now focus on doubly excited states with both electrons in a highly excited orbit, or on states with high angular momentum l_2 for the outer electron, or on states having both qualities (Camus *et al.*, 1989, 1992; Eichmann *et al.*, 1989, 1992; Jones and Gallagher, 1990; Roussel *et al.*, 1990; Jones *et al.*, 1991a; Camus, Cohen, *et al.*, 1993; Camus, Mahon, and Pruvost, 1993; Wang and Cooke, 1993; van Leeuwen *et al.*, 1995, 1996; Seng *et al.*, 1995, and references therein). For more details, the reader is referred to the book that Gallagher (1994) wrote recently on Rydberg atoms.

At the present time, the eigenchannel R-matrix technologies have not been extended to handle very high-lying levels. The highest levels at which experimental data have been compared with R-matrix calculations are located near the $6f$ threshold of Sr, the $8s$ threshold of Ba (Wood and Greene, 1994), and the $n=6$ thresholds in H^- and Li^- (Pan *et al.*, 1994).

In the ICE experiments performed on autoionizing states, multistep laser excitation reaches a particular bound (or long-lived autoionizing) Rydberg level. Then, starting from this Rydberg level, autoionizing resonances are reached by "isolated-core excitation" of the inner valence electron, the Rydberg electron being kept outside as a spectator. In the ICE approximation, the dipole operator acts only on the core electron because the outer electron spends too little time near the nucleus to absorb a visible or ultraviolet photon. In such an excitation process, only particular autoionizing levels are excited and the direct continuum excitation is usually negligible. Experiments using one- and two-photon excitation of the core electron were performed but we will consider mainly processes involving one-photon transitions, which can be compared with eigenchannel R-matrix results more easily.

When the outer electron is at distances larger than r_0, the wave function of the Rydberg initial level to be photoionized can be written as

$$\psi_0=\hat{\vec{r}}\Phi_0(\omega)W(\nu_0,l_0,r)\nu_0^{-3/2}, \tag{4.9}$$

where $\Phi_0(\omega)$ is the initial-state channel function, ν_0 is the effective quantum number, and l_0 the orbital momentum of the outer electron. In Eq. (4.9), $W(\nu_0,l_0,r)$ is the energy-normalized Coulomb function—introduced in Eq. (2.53)—that decays exponentially at infinity. Such an approximation for the initial wave function neglects exchange and all correlation effects for the initial state. The initial state is generally assumed to be described in a particular LS, jj, or jK coupling scheme. Calculation of photoionization cross sections [Eqs. (2.59) and (2.60)] requires the determination of dipole matrix elements $\underline{d}^{(-)}$ [Eq. (2.58)] connecting the initial-state wave function [Eq. (4.9)] to the N_0 energy-normalized physical solutions $\Psi_{i'}^{(-)}$ defined in Eq. (2.55), which obey incoming-wave boundary conditions (N_0 is the number of open channels).

Because the isolated-core approximation relies on negligible continuum excitation one has

$$d_{i'}^{(-)}=\langle\psi_0|D|\Psi_{i'}\rangle=\sum_{i\in c} d_i Z_{ii'}, \tag{4.10}$$

with the component d_i of the dipole matrix element associated with the closed channel i, characterized by the effective quantum number ν_i and the orbital momentum l_i for the outer electron, given by

$$d_i=\nu_0^{-3/2}\langle\Phi_0|D|\Phi_i\rangle\langle W_0(\nu_0,l_0,r)|W_i(\nu_i,l_i,r)\rangle \quad i\in c. \tag{4.11}$$

In Eq. (4.11) the one-photon transition moment implicitly contains all the angular coefficients related to the decoupling of the individual angular momenta and spins from the total angular momentum, as well as those related to the initial-state coupling. It also incorporates angular factors related to the polarizations of the lasers involved in the multistep laser excitation process.

As shown by Bhatti *et al.* (1981), for Coulomb functions normalized per unit energy range, the overlap integral can be approximately expressed as

$$\langle W_0(\nu_0,l_0,r)|W_i(\nu_i,l_i,r)\rangle = 2\frac{\sin\pi(\nu_i-\nu_0)}{\pi(\nu_i^2-\nu_0^2)}\nu_0^2\nu_i^2\delta(l_0,l_i). \tag{4.12}$$

The Kronecker delta function defines a subset i_0 of closed channels with $l_i=l_0$ that are directly accessible in the isolated-core excitation.

Experimental ICE results have been obtained not only for excitation spectra and for the positions and widths of levels, but also for the branching ratios and angular distributions of the ejected electrons. These latter observables are known to be highly sensitive to interseries interactions and to provide a much more stringent test of theory.

1. Excitation spectra

In both ordinary photoabsorption spectra and ICE spectra, a large part of the energy dependence of the photoionization cross sections is contained in the $Z_{ii'}(E)$ closed-channel coefficients [Eq. (2.54b)] involved in the closed part of the physical solutions of Eq. (2.55). However, there are two main differences between the ICE spectra and ordinary photoabsorption spectra. First, in the ICE spectra, only certain closed channels are excited and thus these spectra, do not display Beutler-Fano (Fano, 1961) profiles such as those occurring in the photoabsorption spectra, where structures are complicated by interferences between the discrete-channel and continuum-channel excitation. The second difference comes from the fact that a large part of the energy dependence of the ICE profiles is contained in the overlap integral of Eq. (4.12). The squared overlap integral is maximum for $\nu_i=\nu_0$, is zero for $\nu_i=\nu_0+p$, where p is a nonzero integer, and has subsidiary maxima for $\nu_i=\nu_0+p+1/2$.

The marked differences between isolated-core excitation and ground-state photoionization spectra are illustrated in Fig. 34. Figures 34(a) and 34(b) show part of the photoabsorption spectrum of Sr, where the $5pns$, $5pnd$ $J=1$ autoionizing levels are excited from the $5s^2$ ground state. Figures 34(c) to 34(f) display ICE spectra where, in the final transition, the $5pns$ $J=1$ levels are excited from a particular $5sns$ $^1S_0$ Rydberg level. The energy range involved in either Figs. 34(c) and 34(d) or Figs. 34(e) and 34(f) corresponds to a small part of the energy range covered by Figs. 34(a) and 34(b), around the $5p_{3/2}14s$ peak, denoted (*) in Fig. 34(b). Theoretical spectra [Figs. 34(b), 34(c), or 34(e)] obtained with LS-coupled R-matrix calculations combined with the

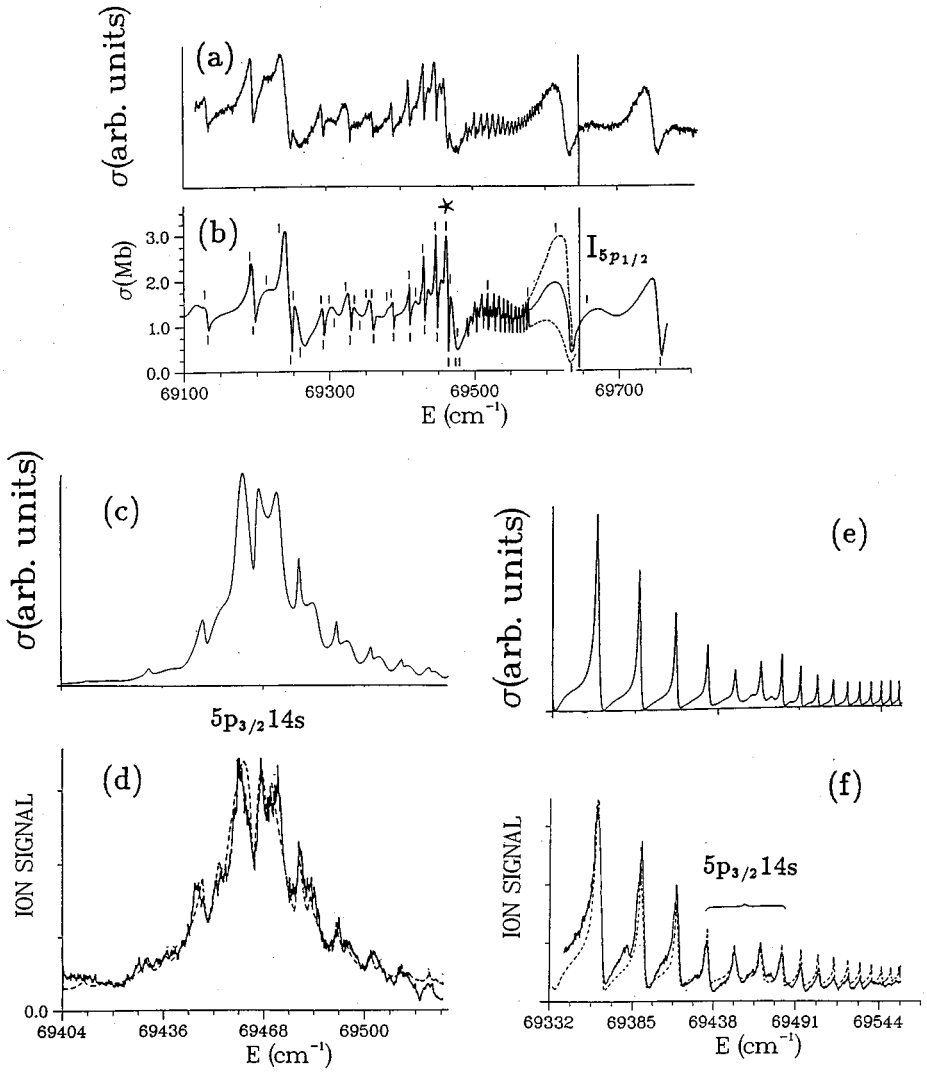

FIG. 34. Photoionization spectra for the odd-parity $5pns$, nd $J=1$ levels of Sr near the $5p_{1/2}$ threshold. Photoabsorption spectra from the $5s^2$ ground state [(a) and (b)] are compared with isolated-core excitation spectra from $5sns\ ^1S_0$ Rydberg states [(c to f)]. Experimental data are compared with results obtained with LS-coupled R-matrix calculations combined with the jj-LS frame transformation. (a) The photoabsorption spectrum recorded by Brown *et al.* (1983); (b) the R-matrix result; the vertical bars indicate the position of the observed absorption peaks and minima and the $5p_{3/2}14s$ level is denoted by an asterisk (*). The experimental ICE $5s14s \rightarrow 5p_{3/2}14s$ spectrum recorded by Xu *et al.* (1986) in the vicinity of the $5s \rightarrow 5p_{3/2}$ ionic transition (d) is compared with the R-matrix result (c). The shake-up satellite spectrum of the ICE $5s20s \rightarrow 5p_{1/2}20s$ transition recorded by Xu *et al.* (1986) far from the $5s \rightarrow 5p_{1/2}$ ionic transition (f) is compared with the R-matrix result (e). The dashed curves in (d) and (f) are the MQDT empirical fits of Xu *et al.* (1986). [Figures 34(a) and 34(b) are from Aymar (1987) while Figs. 34(c) to 34(f) are from Aymar and Lecomte (1989).]

jj-LS frame transformation are compared with corresponding experimental spectra [Figs. 34(a), 34(d), or 34(f)].

As we have already described various photoabsorption spectra in detail, we comment only briefly on Figs. 34(a) and 34(b). The photoabsorption spectrum calculated by Aymar (1987) [Fig. 34(b)] reproduces extremely complex structures occurring in the the spectrum recorded by Brown *et al.* (1983) [Fig. 34(a)]. The sharp structures correspond to the $5p_{1/2}ns$ and $5p_{3/2}n's$ resonances. The $5pnd$ resonances are too broad to be identifiable.

Using the experimental ICE technique, Xu *et al.* (1986) and Zhu *et al.* (1987) reported a complete set of measurements for the $5p_{1/2}ns$ and $5p_{3/2}ns$ $J=1$ autoionizing levels of Sr. These levels were investigated using three-step laser excitation via the $5s5p\ ^1P_1$ and $5sns\ ^1S_0$ Rydberg levels with $n \geqslant 10$. Experimental data on isolated or structured resonances concern the excitation spectra as well as the energy and angular distributions of ejected electrons. The isolated resonances have approximately Lorentzian profiles because of the negligible continuum excitation. We consider here only the excitation spectra of the more complex structured resonances whose features reflect the interactions between the $5p_{1/2}ns,nd$ and $5p_{3/2}ns,nd$ series. Two different types of spectrum reflecting the interseries interactions are

shown in Figs. 34(c) and 34(d) and in Figs. 34(e) and 34(f).

We first comment on Figs. 34(c) and 34(d), which compare theoretical and experimental results for the $5s14s \rightarrow 5p_{3/2}14s$ spectrum. Figure 34(d) shows the spectrum recorded by Xu *et al.* (1986), who obtained their results by tuning the wavelength of the last step excitation laser in the vicinity of the $5s \rightarrow 5p_{3/2}$ ionic line. The frame-transformation result [Fig. 34(c)] obtained by Aymar and Lecomte (1989) closely reproduced the recorded spectrum, in particular the central features involving three strongly interacting levels $5p_{3/2}14s$, $5p_{1/2}28s$, and $5p_{1/2}27d$. The shape of the spectrum is controlled mainly by the energy variation of the $Z_{ii'}(E)$ coefficients, because the spectrum is within the central lobe of the overlap integral. The spectrum exhibits complex structures associated with the mixing of the $5p_{3/2}14s$ level and the nearby $5p_{1/2}ns$ and $5p_{1/2}nd$ levels. Although only one d_{i_0} dipole matrix element associated with the $5p_{3/2}ns$ channel has a non-negligible amplitude, the $5p_{1/2}ns$ and $5p_{1/2}nd$ resonances appear in the spectrum because of their coupling with the $5p_{3/2}14s$ level. The positions and shapes of the $5p_{1/2}ns$ and $5p_{1/2}nd$ resonances agree with the results of the experiment, while the relative magnitudes of these secondary peaks are slightly underestimated by the calculation. The R-matrix calculation reproduces the experimental observations, as did the MQDT simulation performed by Xu *et al.* (1986) using a simplified semiempirical six-channel MQDT model based on the phase-shifted MQDT formalism developed by Cooke and Cromer (1985) [dashed curve on Fig. 34(d)]. The broad $5p_{1/2}nd$ resonances are described distinctly better by the R-matrix calculation.

Figures 34(e) and 34(f) correspond to another kind of ICE spectrum in which the autoionizing levels were excited by tuning the wavelength of the excitation laser far from any ionic transition. More precisely, the spectrum of Fig. 34(f), recorded by Xu *et al.* (1986) from the $5s20s\ ^1S_0$ level, was obtained by scanning the wavelength of the third laser to the blue side of the $5s \rightarrow 5p_{1/2}$ ionic transition. This shake-up spectrum of the $5s20s \rightarrow 5p_{1/2}20s$ transition compares well with the frame transformation R-matrix results of Aymar and Lecomte (1989) [Fig. 34(e)]. The precise form of the satellite peaks depends now on the $Z_{ii'}(E)$ coefficients, on both d_{i_0} dipole moments associated with the $5p_{1/2}ns$ and $5p_{3/2}ns$ channels, and on the variation of the overlap integral. The minima between each $5p_{1/2}ns$ peak correspond to the zeros of the overlap integral, while the maxima correspond approximately to those of the $Z_{ii'}(E)$ coefficients. The strong asymmetry of the peaks results from the distortion due to the overlap integral, whose zeros are very close to the maxima of the $Z_{ii'}(E)$ coefficients. The irregular behavior near n=27–30 reflects the presence of the $5p_{3/2}14s$ perturber. The calculated cross section perfectly reproduces all the subtle features occurring in the recorded spectrum. The quality of the R-matrix calculation is comparable to that of the MQDT simulation performed by Xu *et al.* (1986) [dashed curve on Fig. 34(f)]. One last remark concerns the features on the left side of the ns peaks (particularly visible near E=69 383 cm^{-1}), which cannot be reproduced by the calculation since, as explained by Xu *et al.* (1986), they are due to the impurity of the initial $5s20s$ level, which contains a small amount of nearby $5snd$ levels.

Complex structures, such as those visible in Figs. 34(c) and 34(d), have been observed in several ICE spectra of Sr (Xu *et al.*, 1987) and Ba (see, for example, Gounand *et al.*, 1983, Bente and Hogervorst, 1990, and Hieronymus *et al.*, 1990). They correspond to $m_0p_{3/2}n'l$ states degenerate with $m_0p_{1/2}nl$ levels having large n values. Shake-up or shake-down spectra of a given transition, such those shown on Figs. 34(e) and 34(f), were also frequently recorded in Ba. A common procedure used in the ICE experimental method is to saturate the central peak using high laser power in order to observe many satellite peaks. In this way, it is possible to obtain the positions and widths of doubly excited states that, for experimental reasons, cannot be easily excited directly (see, for example, Tran *et al.*, 1984, and Bente and Hogervorst, 1990).

The excitation spectra discussed above dealt with low-lying autoionizing levels located around the m_0p_j thresholds. They involve $n_1l_1n_2l_2$ doubly excited states with a small value of the orbital momentum l_2 ($l_2 \leqslant 2$) of the outer electron. Approximating the initial and final wave functions as products of one-electron wave functions that span different regions of space neglects overlap and exchange between the two valence electrons. For low-l_2 levels, the nonoverlapping property occurs only when $n_2 \gg n_1$, and thus the wave-function extensions of the Rydberg initial levels are too large to be contained within a reaction volume of moderate size, and the explicit calculation of the dipole matrix elements becomes inefficient. In this regime, the ICE approximation determines the dipole matrix elements far more efficiently. Eigenchannel R-matrix calculations that used the ICE approximation were carried out by Aymar and Lecomte (1989), Lange, Aymar, *et al.* (1991), Dai *et al.* (1990), and by Schinn *et al.* (1991); these were used to interpret experimental ICE spectra.

Some spectra have been measured that deal with higher-lying autoionizing levels with larger values of the orbital momentum l_2. One example can be found in the excitation spectra of the Ba $4f5g\ J=3$ levels from $5d5g\ J=2$ levels observed by Jones *et al.* (1991a) in a three-step laser experiment based on an isolated-core excitation scheme. All three lasers were circularly polarized in the same sense, ensuring that the final states were $4f5g$ levels with $J=3$ only. The $4f5g$ levels are of particular interest because the orbital momentum of each electron is equal to its maximum allowable value in this energy range: $l_1=n_1-1$, $l_2=n_2-1$. The classical orbits of the two electrons would therefore be circular in the absence of interactions; in this sense, the observation of

Jones *et al.* (1991a) was the first one involving autoionizing levels for which both electrons are ''in circular orbits.''

Photoionization cross sections from the jK-coupled $5d_{5/2}5g[5/2]$ and $5d_{3/2}5g[5/2]$ $J=2$ levels were calculated using the jj-coupled eigenchannel R-matrix method (Aymar and Luc-Koenig, 1995). For the first time, excitation spectra calculated using the ICE approximation were successfully reproduced by a separate calculation of dipole matrix elements restricted to the interior of the R-matrix reaction volume; in this case its radius was r_0=50 a.u. The theoretical excitation spectra agreed with the $5d_j5g[5/2]$ $J=2 \rightarrow 4f_{j'}5g$ $J=3$ spectra observed by Jones *et al.* (1991a). The ICE approximation was found to adequately describe the excitation of the $4f5g$ levels. The validity of the ICE approximation relies mainly on the absence of spatial overlap between the inner- and outer-electron orbitals. The nonoverlapping property occurring for the $4f5g$ levels, which involve two electrons having almost the same degree of excitation, is peculiar to the double-circular states. Another key result of the theoretical study of the double-circular $4f5g$ $J=3$ levels (Aymar and Luc-Koenig, 1995) is the large influence of electron correlations on the properties of these levels. Despite the negligible spatial overlap between the wave functions of the two valence electrons, correlation effects have been shown to affect the widths and excitation cross sections of the $4f5g$ levels very strongly. The low autoionization rates observed for the $4f5g$ levels cannot be reproduced by neglecting the mixing of $4f5g$ levels with several Rydberg series, most importantly the $6dnh$ series. The excitation spectrum from the $5d_{5/2}5g$ [5/2] level exhibits, in addition to the peaks associated with the four $4f5g$ $J=3$ levels, structures that were assigned to $6d8h$ levels. These levels are not directly excited in the ICE process but appear in the excitation spectrum owing to their mixing with the $4f5g$ levels.

More recently, experimental excitation spectra of higher-lying $4fng$ J=1–3 levels of Ba, recorded in a three-step ICE experiment, were successfully accounted for by eigenchannel R-matrix calculations (van Leeuwen *et al.*, 1996).

Another example, depicted in Fig. 35, deals with the $4f_{5/2}7h$ J'=4–6 levels of Ba that lie in the energy range between the $6d_{3/2}$ and $6d_{5/2}$ thresholds. These levels were excited from the jK-coupled $5d_{3/2}7h[11/2]$ J=5 level in a resonant two-step ICE experiment with pulsed lasers of van Leeuwen *et al.* (1995). The excitation spectrum of Fig. 35(a) was recorded by detecting Ba^{++} ions produced by photoionization of the Ba^+ $6d_{3/2}$ ion. The experimental spectrum was compared with the partial photoionization cross sections of the $5d_{3/2}7h[11/2]$ J=5 $\rightarrow 4f_{5/2}7h$ J' processes (summed over J'=4, 5, and 6) corresponding to electron ejection into the $6d_{3/2}\epsilon l'$ continua only [Fig. 35(b)]. The theoretical spectrum in Fig. 35(b) obtained with jj-coupled R-matrix calculations has been convolved with an instrumental linewidth of 0.2 cm^{-1} (van Leeuwen *et al.*, 1995).

The $4f_{5/2}7h$ levels interact with $6d_{5/2}ni$ levels and cause a complex interference pattern. All resonances fall within the central lobe of the overlap integral of Eq. (4.12), which peaks at the position of the $5d_{3/2} \rightarrow 4f_{5/2}$ ionic transition [see Fig. 35(a)]. The $4f_{5/2}7h$ J'=4–6 states correspond to the broad central features in Figs. 35(a) and 35(b). The narrow resonances were identified as members of $6d_{5/2}ni$ Rydberg series converging to the $6d_{5/2}$ ionization limit. These resonances, which are not directly accessible in the ICE process, appear because of their mixing with the $4f7h$ levels. The $6d_{5/2}ni$ levels on the low-energy side of the broad $4f_{5/2}7h$ J'=4–6 resonances are characterized by negative values of the lineshape parameter q (Fano, 1961) and those on the right side by positive values of q. The widths of $6d_{5/2}ni$ levels were found to vary strongly with n. The $6d_{5/2}23i$ level, located below the $6d_{3/2}$ ionization limit, as well as the $6d_{5/2}24i$ level, are extremely narrow. The predicted widths for these levels are respectively 0.08 and 0.15 cm^{-1}, which are below the instrumental linewidth of 0.2 cm^{-1}. This spectrum is complex, as it includes final states with three different values of J', each of which requires the correct description of interactions among a large number of channels (up to 47). In view of this complexity, the agreement between the experimental and theoretical spectra in Fig. 35 is excellent. The R-matrix approach successfully reproduces the complicated interference pattern involving q reversal and line-narrowing effects in the $6d_{5/2}ni$ series interacting with the $4f_{5/2}7h$ levels.

It was found that the final-state angular momentum $J'=5$ dominates in the complex interference pattern. Above the Ba^+ $6d_{3/2}$ threshold, the $J'=5$ spectrum involves 20 closed channels interacting with 24 open channels. Examination of the phase-shifted MQDT parameters deduced from R-matrix calculations (see Sec. II.D.3) have shown that, to a good approximation, the 44-channel $J'=5$ problem can be reduced to a three-channel problem. In fact, the $4f_{5/2}7h[11/2]$ level is mainly coupled to the $6d_{5/2}ni[11/2]$ Rydberg series and both the $4f7h$ level and the $6dni$ Rydberg levels decay mainly into the same $6d_{3/2}\epsilon i[11/2]$ continuum. A three-channel MQDT treatment of the $J'=5$ spectrum has been performed (van Leeuwen *et al.*, 1995) using a set of five phase-shifted MQDT parameters, whose values were fixed at the values obtained from the complete treatment. The three-channel MQDT model clearly showed that the interfence pattern does not result from interferences in the excitation process but from interferences in the spectral density of autoionizing states. The dramatic changes of the widths and the q reversal along the $6d_{5/2}ni$ autoionizing Rydberg series result from interference between direct autoionization and indirect autoionization via the $4f_{5/2}7h$ broad interloper of the Rydberg series.

Eigenchannel R-matrix calculations were conducted by Wood and Greene (1994) in Ba and Sr, in an energy range higher than the m_0p threshold, which was probed by the experiments of Camus, Cohen, *et al.* (1993) and of Eichmann *et al.* (1992). We discuss here the results

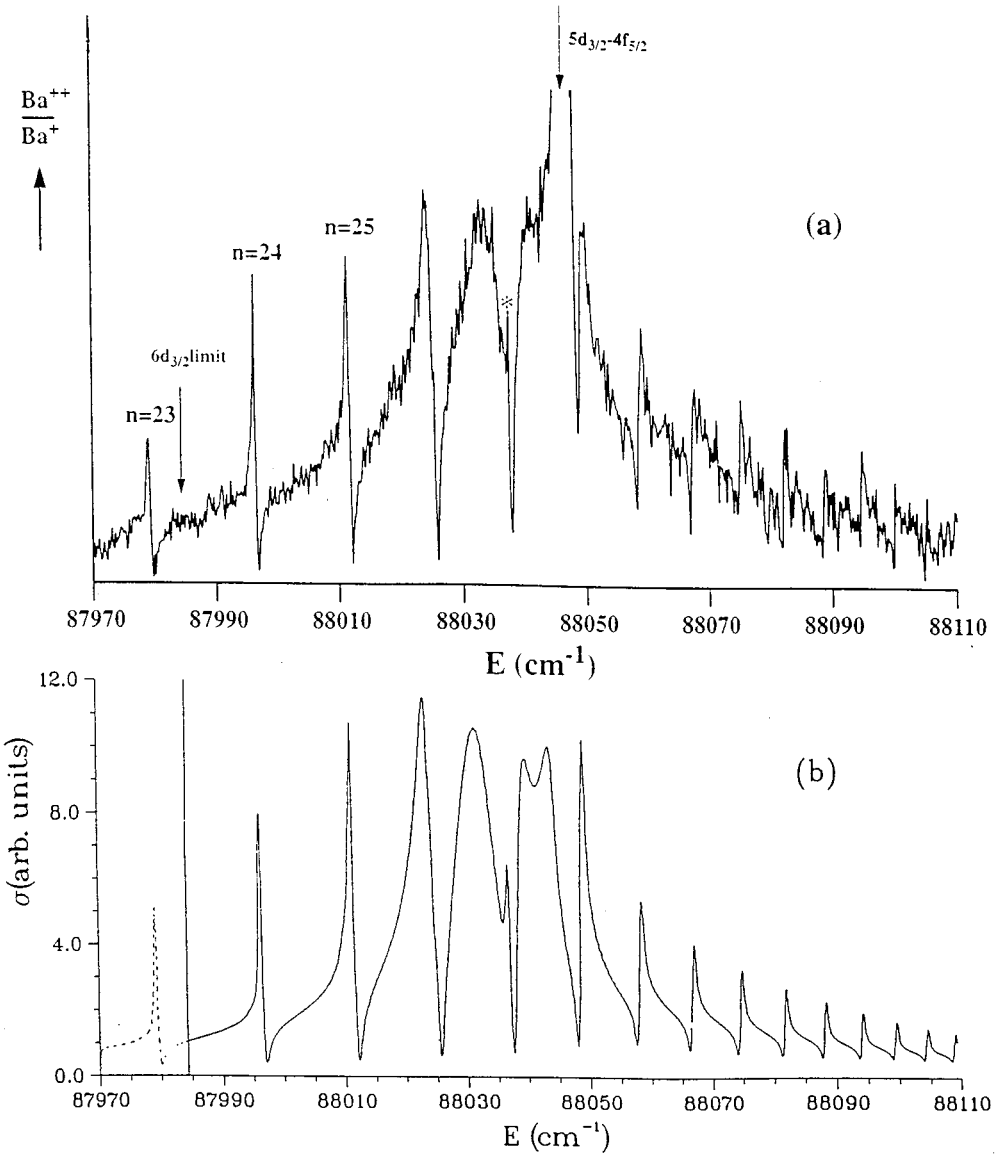

FIG. 35. Isolated-core excitation spectra $5d_{3/2}7h[11/2]\ J=5 \rightarrow 4f_{5/2}7h\ J'=4-6$ of Ba as functions of the energy relative to the Ba ground state: (a) experimental spectrum: the Ba^{++} signal is divided by the Ba^{+} signal; the narrow resonances were identified as $6d_{5/2}ni$ levels. The $6d_{5/2}27i\ J'=4$ level at 88 037 cm^{-1} is denoted by an asterisk (*). (b) Theoretical spectrum calculated with the *jj*-coupled eigenchannel *R*-matrix method. (From van Leeuwen *et al.*, 1995.)

obtained in Ba near the 8*s* threshold. Asymmetric $8snl$ levels were excited from $6snl$ levels that were populated by a Stark-switching technique (Cooke *et al.*, 1978). Photoionization cross sections have been measured using a two-photon isolated-core excitation (Camus, Cohen, *et al.*, 1993). Figure 36 compares the relative experimental and theoretical photoionization cross sections for the $6snl$ initial state with $n=14$ and $l=6$ over an energy range of $\sim$ 300 cm^{-1}, i.e., from $\nu_{8s}=16$ to $\nu_{8s}=12$. Eigenchannel *R*-matrix calculations were performed in *jK* coupling with a reaction volume radius of 100 a.u. Calculations included open channels converging to the $7s$, $6d_j$, $4f_j$, and $7p_j$ thresholds only and closed channels converging to the $5f_j$, $8s$, $7d_j$, $8p_j$, and $5g_j$ thresholds. Because the experimental ICE process corresponds to the absorption of two photons, it is no longer possible to express easily the transition amplitudes in terms of the analytical form [Eq. (4.12)] of the overlap integral of the outer-electron wave functions. Thus, Wood and Greene (1994) calculated approximate two-photon transition amplitudes. The resonances in Fig. 36 are due to the $5f_{5/2}nl$ levels ($5f_{5/2}$ threshold at -0.01061 a.u.) overlapping with the $5f_{7/2}nl'$ levels ($5f_{7/2}$ threshold at -0.0105 a.u.). Given the extreme complexity of the experiment, the calculation accounts for the measurement of Camus, Cohen, *et al.* (1993) reasonably well, except for the intensities of the $5f_jnl'$ resonances. A possible explanation for the discrepancy concerning the intensities of the $5f_jnl'$ resonances is that the approximations underlying the calculation of the dipole 2moments were overly simplified. A second possible reason for the discrepancy is the pres-

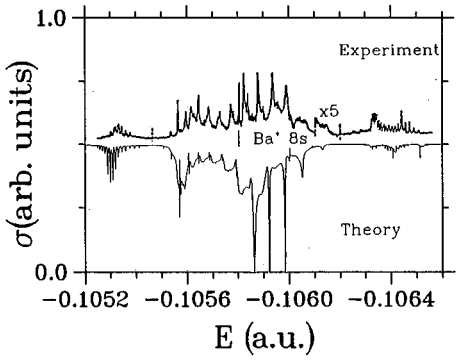

FIG. 36. Relative photoionization cross sections for the two-photon excitation spectrum of Ba from the $6snl$ initial state with $n=14$ and $l=6$ as functions of the energy relative to the double-ionization limit. The experimental spectrum (top) recorded by Camus, Cohen, *et al.* (1993) is compared with the jK-coupled eigenchannel R-matrix result of Wood and Greene (1994) shown as a mirror image (bottom). The position of the Ba^+ ionic line is indicated for reference. (From Wood and Greene, 1994.)

ence of perturbers in the energy range of Fig. 36. Wood and Greene (1994) found that $5g_jnd$ and $7d_jng$ perturbers lie in the that energy range. Moreover, they found that the $7d_jnl''$ channels play a crucial role in determining the intensities of the $5f_jnl'$ resonances. A slight error in the position of the $7d_jnl''$ perturbers could be responsible for the too large intensities of the calculated $5f_jnl'$ resonances.

The intensities of $5f_jnl'$ resonances are surprisingly large in view of the fact that the direct mixing of $8snl$ channels with the $5f_jnl'$ channels requires a change of three units of angular momentum. Wood and Greene (1994) analyzed the mechanism responsible for the interaction between the $8snl=6$ and the $5f_jnl'$ channels by calculating the short-range scattering matrix elements $|S_{ij}|^2$ connecting the $8snl=6$ channel to the $5f_jnl'$ channels. The largest coupling was found for the $5f_{7/2}nl'=7$ channel. However, this scattering probability is dramatically reduced when the $7d_jnl''$ channels are considered as open in the MQDT treatment, i.e. when all perturbers associated with these channels are removed (see Sec. IV.C). This provides strong evidence that the interaction between $8snl=6$ and the $5f_jnl'$ channels is being mediated through an interaction with the $7d_jnl''$ channels.

Camus, Cohen *et al.* (1993) speculated that the interaction between the $8snl$ and the $5f_jnl'$ channels could be due to a direct octopole coupling. This suggestion was not supported by the calculations of Wood and Greene (1994), who repeated both calculations of the short-range scattering matrix elements by omitting all multipoles higher than $k=2$ in the expansion of the $1/r_{12}$ interaction. The calculations gave results very close to those obtained from the calculations including all multipoles.

2. Branching ratios and angular distributions of electrons ejected from autoionizing levels

Several experimental investigations on angular distributions of electrons ejected from odd-parity doubly excited states $m_0pns\ J=1$ have been carried out in Mg (Lindsay, Cai, *et al.*, 1992), Ca (Lange *et al.*, 1989), Sr (Zhu *et al.*, 1987), and Ba (Hieronymus *et al.*, 1990; Lange, Aymar, *et al.*, 1991, and references therein). In addition, angular distributions of electrons ejected from the more complex $3pnd$ states of Mg have been also measured (Lindsay, Cai, *et al.*, 1992). In all these studies, the autoionizing Rydberg states were reached using three-step laser excitations via the $m_0sm_0p\ ^1P_1$ and a Rydberg level $m_0sns\ ^1S_0$ or $m_0snd\ ^1D_2$. The three lasers were linearly polarized in the same direction.

We first address the simplest case in which the third laser excites the $m_0pns\ J=1$ states from a spherically symmetric $m_0sns\ ^1S_0$ bound Rydberg state. The differential cross section for photoionization to a given ionic state i can be expressed (Yang, 1948) as

$$\frac{d\sigma_i}{d\Omega}(\theta)=\frac{\sigma_i}{4\pi}[1+\beta_i P_2(\cos\theta)], \tag{4.13}$$

where σ_i is the partial cross section in channel i integrated over Ω, θ the angle between the third laser polarization and the momentum of the electron ejected in the solid angle $d\Omega$, and $P_2(\cos\theta)$ is the second-order Legendre polynomial. The asymmetry parameter β_i characterizes the angular distribution of electrons ejected in channel i. In Mg, electrons are ejected into continua built on the $3s$ core while in Ca, Sr, and Ba, the electrons can be ejected into continua built on cores m_0s, $(m_0-1)d_{3/2}$, $(m_0-1)d_{5/2}$, and even $m_0p_{1/2}$ for levels located above the $m_0p_{1/2}$ limit. The measured observables that were compared to calculations include the β_i parameters, and in Ca, Sr, and Ba the branching ratios $r_i=\sigma_i/\Sigma\sigma_i$ that determine the relative probabilities of autoionization to the various ionic-core states.

The general angular properties of photoelectron angular distributions have been worked out by Dill and Fano (1972), by Fano and Dill (1972), and by Dill (1973) using the concept of angular momentum transfer. The angular distribution of the ejected electrons is expressed as a sum of incoherent contributions corresponding to different magnitudes of the angular momentum j_t transferred between the unobserved photofragments

$$\vec{j}_t=\vec{j}_i+\vec{s}-\vec{J}_0, \tag{4.14}$$

where $\vec{j}_i$ is the total angular momentum of the residual ion core, $\vec{J}_0$ the total orbital momentum of initial state, and $\vec{s}$ the spin of the ejected electron. There are parity-favored and parity-unfavored transfers. The differential partial cross section [Eq. (4.13)], or equivalently the β_i parameters, can be expressed in terms of reduced dipole matrix elements $d_{j_{is}J}=\langle J_0||D||[(j_is)j_{is},l]J^-\rangle$, where the minus sign indicates that the final state is normalized according to the incoming-wave boundary condition [see Eq. (2.55)]. The final total angular momentum is $\vec{J}=\vec{j}_{is}+\vec{l}$ and $\vec{l}$ is the orbital momentum of the ejected electron. As was mentioned in Sec. II.E, matrix elements are easier to evaluate in j_ij_{is} coupling (denoted by J_cJ_{cs} in Sec. II.E) than in jj coupling, and the short-

range reaction matrices $\underline{K}^J$ in the $j_i j_{is}$ coupling can be obtained from the LS- or jj-coupled matrices $\underline{K}$ through simple angular recoupling transformation.

Details on the computation of the β_i parameters are given elsewhere (Zhu *et al.*, 1987; Aymar and Lecomte, 1989; Hieronymus *et al.*, 1990; Lindsay, Cai, *et al.*, 1992; Lindsay, Dai, *et al.*, 1992) and are not reported here. We restrict our present comments to the β_s parameter corresponding to autoionization into a $m_0 s$ core in photoionization from a $m_0 s n s\ ^1S_0$ level. There, the angular momentum transfer is simply the total spin of the valence electron pair which is either 0 (parity favored) or 1 (parity unfavored), the final state being identical to a $m_0 s \epsilon p\ ^1P_1$ or $^3P_1$ state. The β_s parameter may have a value between -1 and 2. Deviation of β_s from 2 can reflect the strength of the parity-unfavored term, which originates in the spin-orbit interaction or final-state correlation effects.

Some results on the energy dependence of the asymmetry and branching-ratio parameters have been obtained in the heavier alkaline earths. Figure 37 compares the experimental energy dependence of cross sections, asymmetry parameters and branching ratios obtained in Ca and Ba with the eigenchannel R-matrix results. Data on the $4p_{3/2}14s$ level of Ca [Figs. 37(a)–37(d)] were obtained by Lange *et al.* (1989) starting from the $4s14s\ ^1S_0$ Rydberg level and scanning the third laser in the vicinity of the $4s \rightarrow 4p_{3/2}$ ionic resonance line. Data on the $6p_{3/2}20s$ state of Ba [Figs. 37(e)–37(k)] were obtained by Lange, Aymar, *et al.* (1991) in a similar way. The Ca $4p_{3/2}14s$ level is located below the $4p_{1/2}$ threshold. It is almost degenerate with the $4p_{1/2}16s$—denoted as s_3 on the top of Fig. 37(a). The positions of the neighboring $4p_{1/2}14d$ and $4p_{1/2}15d$ are denoted by d_2 and d_3, respectively. In contrast, the Ba $6p_{3/2}20s$ level is above the $6p_{1/2}$ threshold. Ba data are plotted as functions of the effective quantum number $\nu_{6p_{3/2}}$ associated with the $6p_{3/2}$ limit. The Ba $6p_{3/2}20s$ level ($\nu_{6p_{3/2}} \sim 15.7$) lies in between the $6p_{3/2}18d$ and $6p_{3/2}19d$ levels, which are around $\nu_{6p_{3/2}} \sim 15.3$ and $\nu_{6p_{3/2}} \sim 16.3$, respectively. The branching-ratio and asymmetry parameters corresponding to decay into $A^+\ m_0 s$ are denoted r_s and β_s; those corresponding to decay into the unresolved $A^+\ (m_0-1)d_{3/2}$ and $(m_0-1)d_{5/2}$, r_d and β_d. In Ba, autoionization into the $6p_{1/2}$ core is characterized by r_p and β_p. On each figure, 37(a)–37(k), the experimental data (dots) are compared with the results obtained with the LS-coupled eigenchannel R matrix combined with the jj-LS frame transformation (full lines). In Ca, theoretical values were computed using the short-range reaction matrix $\underline{K}$ determined by Kim and Greene (1987). In Ba, experiment and calculations were conducted simultaneously (Lange, Aymar, *et al.*, 1991). The positions, widths, and shapes of the resonances in Ca [Fig. 37(a)] and Ba [Fig. 37(e)] are nicely reproduced by the calculations (note that the heights of experimental resonance profiles are the only adjustable parameters in the comparison between theory and experiment). The Ca $4p_{3/2}14s$ profile is slightly asymmetric because this level interacts with nearby $4p_{1/2}ns,nd$ levels. The Ba $6p_{3/2}20s$ level has an approximately Lorentzian line profile, as is typical for the isolated resonances observed using the ICE experimental method. The calculations also closely reproduce the energy variations of the various branching-ratio parameters [Figs. 37(b) and 37(i)–37(k)], in particular the localized variations on either side of the Ba $6p_{3/2}20s$ resonance, which occur in the vicinity of the neighboring $6p_{3/2}nd$ ($n=18,19$) levels. In Ba and mainly in Ca, a large fraction of autoionizing electrons populate the $(m_0-1)d_{3/2,5/2}$ ionic levels. In Ca, this results in a population inversion of the Ca^+ ion produced by photoionization.

We turn now to the angular distribution parameters [Figs. 37(c), 37(d), and 37(f)–37(h)]. In Ba, the calculation perfectly reproduces the plateau value of $\beta_s \sim 1.8$ around the $6p_{3/2}20s$ resonance where departure from $\beta_s=2$ is due mainly to spin-orbit effects. Marked dips occur in the β_s spectra of Ba (on either side of the resonance) and Ca (at the resonance center). These dips located at the positions of the Ba $6p_{3/2}nd$ ($n=18,19$) perturbers and of the Ca $4p_{1/2}16s$ perturber reflect final-state channel mixing. These dips are not perfectly described by the theory. The general structure of the pronounced energy variation of β_d in Ba is well described by theory, but poorer agreement between theory and experiment is obtained for β_d in Ca and for β_p in Ba.

Finally, it is interesting to note that the electron branching ratios and angular distributions of various $6p_{1/2}ns$ and $6p_{3/2}ns$ levels of Ba investigated by Lange, Aymar, *et al.* (1991) were also calculated using the K matrix obtained with the jj-coupled R-matrix method. Although results are not always completely identical to those provided by the LS-coupled R-matrix method (and frame transformation), the overall agreement with experiment of Lange, Aymar, *et al.* (1991) is of the same quality.

A second example deals with $6pns\ J=1$ levels of Ba located just below the $6p_{1/2}$ threshold in the energy range in which the $6p_{3/2}12s$ level is degenerate with high-lying $6p_{1/2}ns,nd$ levels with $n \geq 22$. These levels were investigated by Hieronymus *et al.* (1990), starting from the $6s12s\ ^1S_0$ level and inducing the core transition $6s \rightarrow 6p_{3/2}$. Data concern the ion yields as well as the electron branching ratios and angular distributions as functions of the energy of the laser driving the core transition. Experimental data on electron angular distributions are compared with R-matrix results in Fig. 38. Experimental and theoretical asymmetry parameters are plotted as functions of the effective quantum number $\nu_{6p_{1/2}}$ associated with the $6p_{1/2}$ limit. The broad ($\Gamma \sim 85\ cm^{-1}$) $6p_{3/2}12s$ resonance is centered at $\sim 62\ 150\ cm^{-1}$, i.e., at $\nu_{6p_{1/2}} \sim 27.5$. Figures 38(a), 38(c), and 38(e) show the experimental results that were analyzed by Hieronymus *et al.* (1990) using semiempirical MQDT models, whose results are shown on Figs. 38(b), 38(d), and 38(f). Three different seven-channel MQDT models

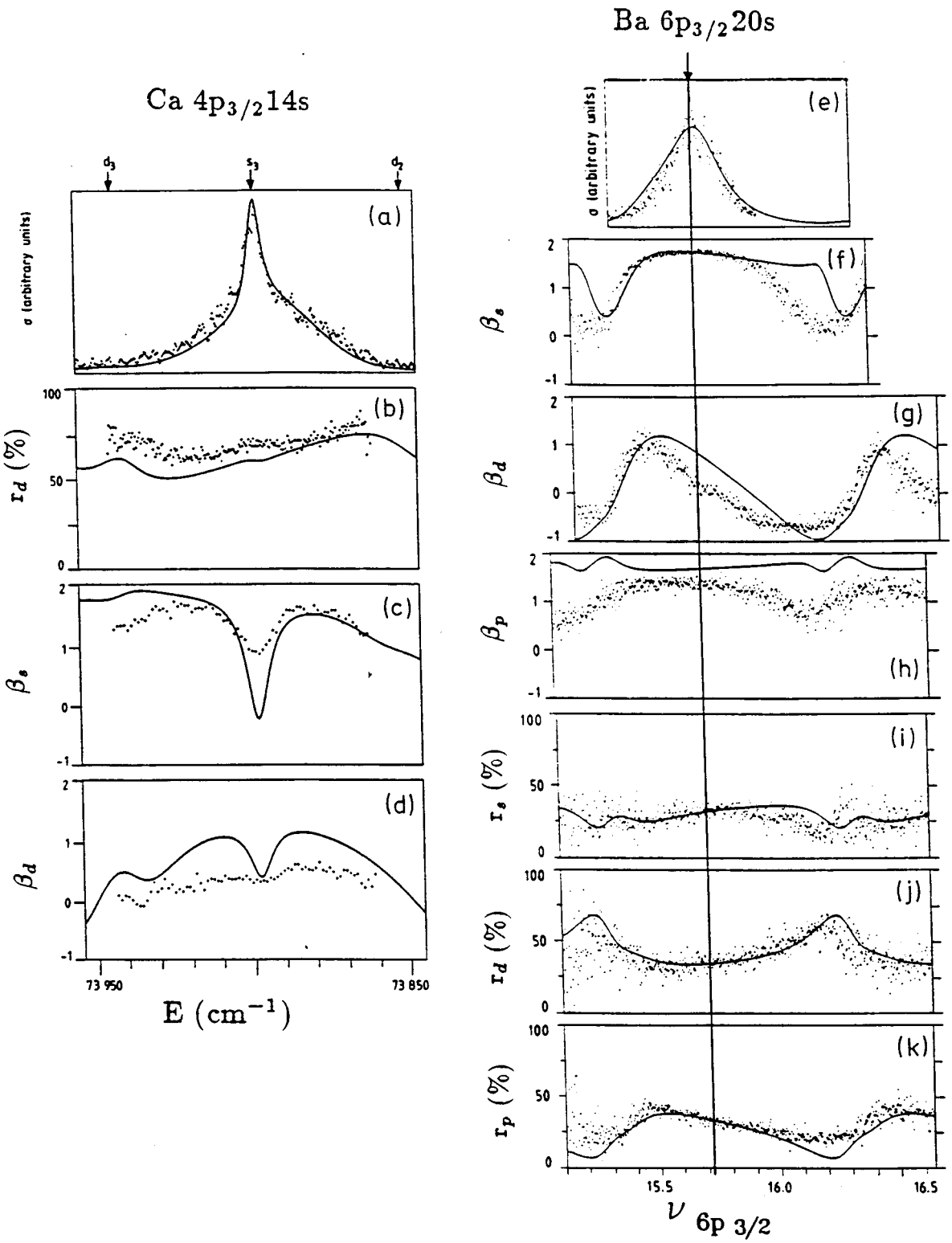

FIG. 37. Electron branching ratios and angular distributions of Ca $4pns$ and Ba $6pns$ autoionizing Rydberg states. The experimental data (solid points) for the $4p_{3/2}14s$ $J=1$ resonance of Ca [(a) to (d)] excited from the $4s14s$ $^1S_0$ Rydberg level and for the $6p_{3/2}20s$ $J=1$ resonance of Ba [(e) to (k)] excited from the $6s20s$ $^1S_0$ Rydberg level are compared with results (solid lines) obtained with LS-coupled R-matrix calculations combined with the jj-LS frame transformation. Data in Ca are plotted as functions of the energy relative to the Ca ground state and those for Ba as functions of the effective quantum number $\nu_{6p_{3/2}}$ associated with the $6p_{3/2}$ limit. The Ca $4p_{3/2}14s$ $J=1$ level located below the $4p_{3/2}$ threshold can autoionize to the $m_0s\epsilon l$ and $(m_0-1)d\epsilon l$ continua (denoted s and d, respectively), whereas in Ba the $6p_{3/2}20s$ $J=1$ level autoionizes in addition to the $m_0p_{1/2}\epsilon l$ continua (denoted p). The curves show: (a) and (e), resonance profiles; (b) and (i)–(k), branching ratios; (c), (d) and (f)–(h), asymmetry parameters β. [Ca figures are from Lange *et al.* (1989), courtesy of W. Sandner and Ba figures are from Lange, Aymar, *et al.* (1991).]

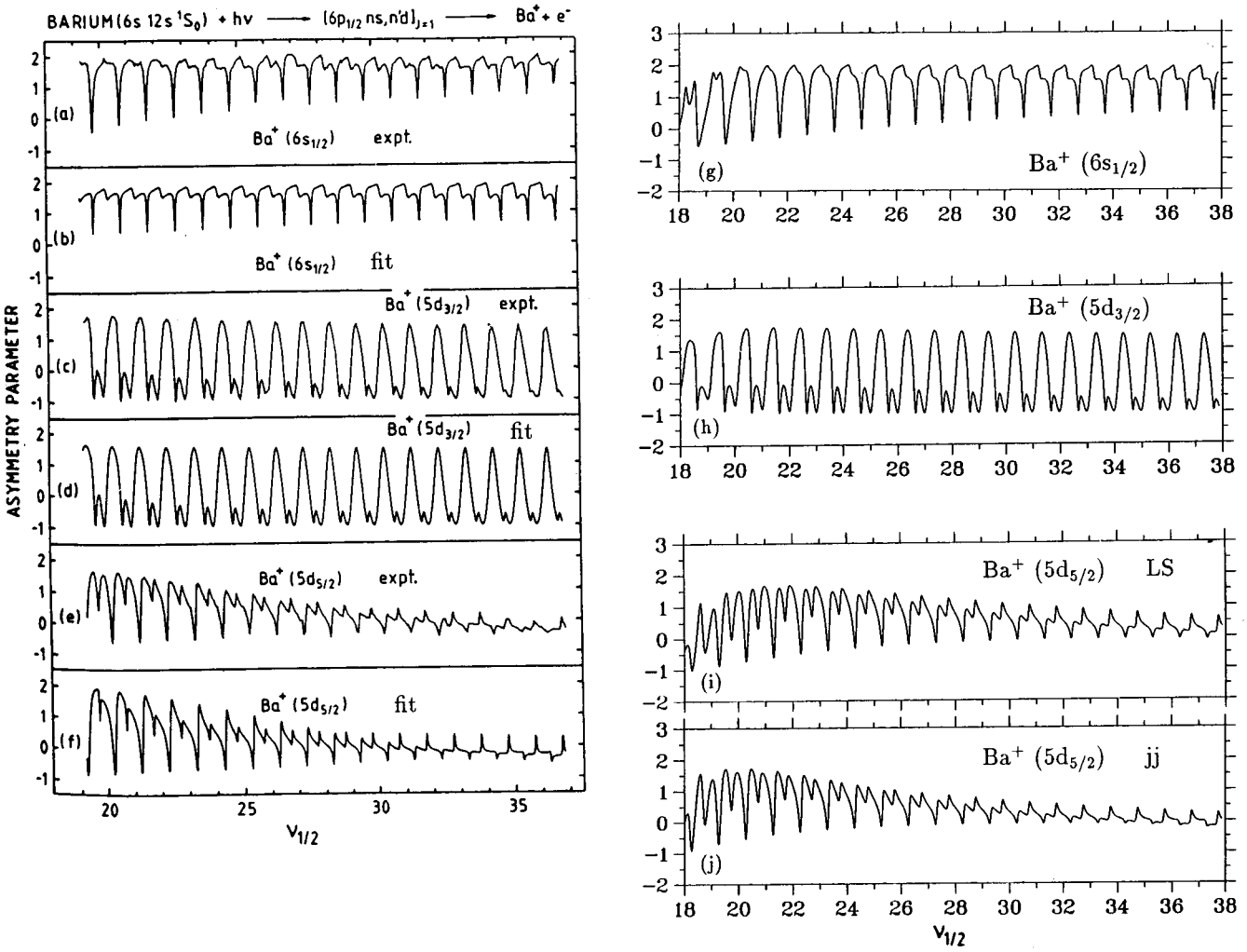

FIG. 38. Angular distributions of Ba $6p_{1/2}ns$, nd J=1 levels degenerate with the $6p_{3/2}12s$ level and excited from the $6s12s\ ^1S_0$ level by driving the $6s \rightarrow 6p_{3/2}$ core transition. Data are plotted as functions of the effective quantum number $\nu_{6p_{1/2}}$ associated with the $6p_{1/2}$ limit. Experimental results of Hieronymus *et al.* (1990) for the asymmetry parameters β_s, $\beta_{d_{3/2}}$, and $\beta_{d_{5/2}}$, associated with the final $6s$, $5d_{3/2}$, and $5d_{5/2}$ ionic states are shown (a), (c), and (e), respectively. The curves (b), (d), and (f) show the results of the MQDT simulations carried out by the same authors. At the right, (g)–(j) show the R-matrix results: (g) LS result for β_s; (h) jj-LS result for $\beta_{d_{3/2}}$; (i) jj-LS result for $\beta_{d_{5/2}}$; (j) jj result for $\beta_{d_{5/2}}$. [Figs. 38(a) to 38(f) are from Hieronymus *et al.* (1990), courtesy of H. Hieronymus.]

(one for each final ionic state) were adjusted by Hieronymus *et al.* (1990) on the ion-yield and asymmetry parameters. Figures 38(g)–38(i) show the eigenchannel R-matrix results.

We first comment briefly on the experimental results analyzed in greater detail by Hieronymus *et al.* (1990). The variations of the asymmetry parameters β_s, $\beta_{d_{3/2}}$, and $\beta_{d_{5/2}}$ associated with the $6s$, $5d_{3/2}$, and $5d_{5/2}$ final ionic states show pronounced modulations, almost periodic in $\nu_{6p_{1/2}}$, the effective quantum number associated with the $6p_{1/2}$ limit. As explained by Hieronymus *et al.* (1990), the positions of the resonances are strongly correlated with the positions of the $6p_{1/2}ns,nd$ Rydberg levels, which are not excited directly but only through their coupling with the $6p_{3/2}12s$ resonance. However the data are not strictly periodic in $\nu_{6p_{1/2}}$, changes in the various shapes occurring with increasing energy. These changes, particularly visible in Fig. 38(e), are due to the $6p_{3/2}10d$ (at $\nu_{6p_{1/2}} \sim 18$) and $6p_{3/2}11d$ (above the $6p_{1/2}$ limit) levels located on both sides of the $6p_{3/2}12s$ resonance.

We turn now to the description of eigenchannel R-matrix results obtained from two different short-range reaction matrices of dimension 13. The first one, obtained by combining LS-coupled R-matrix calculations with the jj-LS frame transformation, is the one that successfully reproduced the photoabsorption spectrum (Aymar, 1990) and the ICE data of Lange, Aymar, *et al.* (1991). The second matrix $\underline{K}$ was obtained with the jj-coupled R-matrix method. Both K matrices give almost identical results for β_s and $\beta_{d_{3/2}}$ and, for the sake of clarity, only LS results are shown in Figs. 38(g) and

38(h). In contrast, significant differences exist for $\beta_{d_{5/2}}$ between the frame-transformation and jj results shown on Figs. 38(i) and 38(j), respectively. The calculations correctly give the periodic modulations as well as the changes with increasing energy observed experimentally for the asymmetry parameters β_s and $\beta_{d_{3/2}}$. Comparison of Figs. 38(i) and 38(j) with Fig. 38(e) clearly shows that the marked decrease of the resonance amplitudes observed for $\beta_{d_{5/2}}$ is better reproduced by the fully jj-coupled R-matrix calculation. In addition, the $\beta_{d_{5/2}}$ spectrum is described slightly better by this R-matrix calculation than by the MQDT simulation of Hieronymus *et al.* (1990), whereas the fitted and calculated results are very close for β_s and $\beta_{d_{3/2}}$.

Although not shown here, the R-matrix calculations also trace out the modulations observed in the branching ratios r_s, $r_{d_{3/2}}$ and $r_{d_{5/2}}$; here no significant differences between the LS results (and frame transformation) and the jj results are found. The detailed shapes of the resonances showing up in the total ion yield are also very well reproduced by the two different R-matrix calculations, while some discrepancies exist for the relative heights of the successive peaks. Interestingly, this shows that resonance profiles (usually considered to be less sensitive to channel mixing than angular distributions) can in some cases give a more sensitive test of theory. This conclusion was also reached by Lange, Aymar, *et al.* (1991).

In Mg, the angular distributions of ejected electrons from autoionizing $3pns$ $J=1$ levels of Mg were measured by Lindsay, Cai, *et al.* (1992) as functions of the energy of the third laser, which drives the isolated-core excitation $3sns \rightarrow 3pns$. The experimental β_s spectrum (full line) obtained for the $3s14s \rightarrow 3p14s$ excitation is compared with the R-matrix calculation (dotted line) in Fig. 39. The spectrum covers an energy range of $\sim$ 800 cm^{-1} centered on the Mg^+ ion transitions $3s \rightarrow 3p_{1/2}$ and $3s \rightarrow 3p_{3/2}$ marked by vertical bars at the top of the figure. The calculations were carried out using a seven-channel reaction matrix determined by Greene (1990b) with LS-coupled R-matrix calculations combined with the jj-LS frame transformation. The LS-coupled channels were: $(3snp,\ 3pns,\ 3pnd)\ ^1P_1$, $(3snp,\ 3pns,\ 3pnd)\ ^3P_1$, and $3pnd\ ^3D_1$. The same K-matrix was also successfully employed to reproduce the line shapes of $3pnd$ $J=1$ autoionizing levels (Schinn *et al.*, 1991). Figure 39 shows how the calculations reproduce the experimental data almost perfectly. The only discrepancies that cannot be accounted for by experimental errors occur very close to the Mg^+ resonance lines.

Examination of Fig. 39 reveals that $\beta \sim 2$, except for dips, with minima up to $\beta \sim -1$. A broad dip appears between the ionic lines and narrower dips are located at the positions of the $3p_{1/2,3/2}ns,nd$ autoionizing levels. The $\beta \sim 2$ value corresponds to the excitation of a pure $3pns\ ^1P_1$ channel, which corresponds to a coherent superposition of $3p_{1/2}ns$ and $3p_{3/2}ns$ channels, followed by direct scattering into the $3s\epsilon p\ ^1P_1$ continuum. The $\beta=2$ value is observed far from the Mg^+ resonance lines and away from the $3pns,nd$ resonances. Indeed, far from the Mg^+ lines, both $3p_{1/2}ns$ and $3p_{3/2}ns$ channels are excited and starting from a $3sns\ ^1S_0$ level it is reasonable, in Mg where spin-orbit effects are very weak, to assume that a $3pns\ ^1P_1$ level is populated and decays immediately. Departures from $\beta \sim 2$ occur at the positions of the $3pns,nd$ resonances that are not excited directly. Similar dips are exhibited by the the $\beta_{m_0 s}$ spectra in Ca and Ba (see Figs. 37 and 38), but the dips are deeper in Mg than in Ca and Ba. Departures from $\beta \sim 2$ between the ionic lines are caused by large differences between the $3p_{1/2}ns$ and $3p_{3/2}ns$ excitation amplitudes in that energy range.

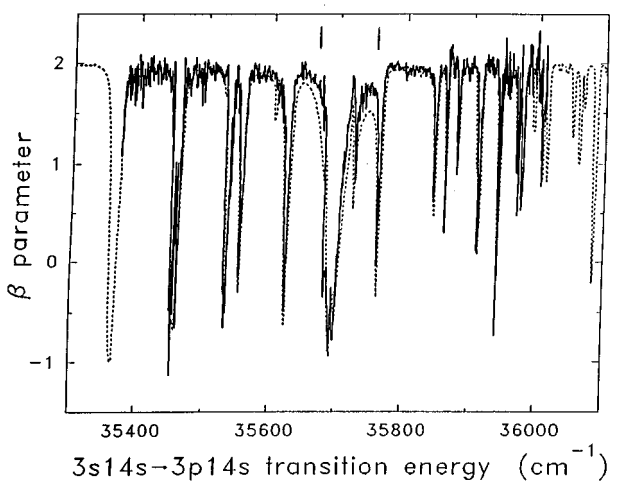

FIG. 39. Angular distributions of ejected electrons from the autoionizing $3p14s$ $J=1$ state of Mg. The experimental results for the asymmetry parameter β for the transition $3s14s \rightarrow 3p14s$ (full line), as functions of the photon energy, are compared with results (dotted line) obtained with LS-coupled R-matrix calculations combined with the jj-LS frame transformation. The vertical bars at the top indicate the positions of the $3s \rightarrow 3p_{1/2}$ and $3s \rightarrow 3p_{3/2}$ ionic transitions. (From Lindsay, Cai, *et al.*, 1992, courtesy of T. F. Gallagher.)

A far more complicated type of angular distributions arises when electrons are ejected from the autoionizing $3p12d$ $J=1$ and $J=3$ levels of Mg, which is the situation treated in Fig. 40. These levels were reached using a three-step excitation scheme via the $3s12d\ ^1D_2$ level (Lindsay, Dai, *et al.*, 1992). The three lasers were linearly polarized in the same direction, which ensured that only $J=1$ and $J=3$ levels were excited, and which also preserved cylindrical symmetry of the resulting angular distribution. The differential photoionization cross section for electrons ejected from an aligned $3snd\ ^1D_2$ Rydberg level has the form:

$$\frac{d\sigma}{d\Omega}(\theta)=\frac{\sigma}{4\pi}[1+\beta P_2(\cos\theta)+\gamma P_4(\cos\theta) + \epsilon P_6(\cos\theta)], \tag{4.15}$$

where σ is the total cross section integrated over the solid angle Ω, θ the angle between the third laser polarization and the direction of the ejected electron, and

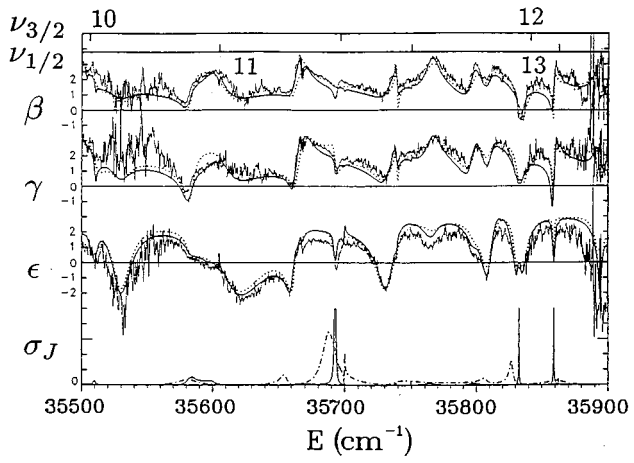

FIG. 40. Angular distributions of electrons ejected from the autoionizing $3p12d$ $J=1$ and $J=3$ levels of Mg. The three experimental angular parameters β, γ, and ϵ, as functions of the photon energy (jagged lines), are compared with two R-matrix calculations (full and dotted lines)—see the text. The horizontal lines indicate the zeros, σ_J is the relative photoionization cross section (in arbitrary units) contributed by the $J=1$ (solid line) and $J=3$ (dot-dashed curve) final states. The top of the figure shows the effective quantum number scales relative to the $3p_{1/2}$ and $3p_{3/2}$ thresholds in unit steps. (From Lindsay, Dai, *et al.*, 1992, courtesy of T. F. Gallagher.)

$P_k(\cos\theta)$ is the kth Legendre polynomial. The three angular parameters β, γ, and ϵ as functions of the energy constitute the experimental data that were measured and compared to R-matrix calculations. The experimental β, γ, and ϵ parameters obtained over a range of 400 cm^{-1} centered on the peaks of the $3s12d \rightarrow 3p12d$ transition correspond to the jagged solid line, and the theoretical results obtained with two different calculations are shown as smooth solid and dotted lines, respectively.

Two different R-matrix determinations of the LS-coupled reaction matrices $\underline{K}^{J=1}$ and $\underline{K}^{J=3}$ were carried out by Greene (1990b). The first set, successfully used to interpret the excitation spectra of $3pnd$ $J=1$ and $J=3$ states of Mg (Dai *et al.*, 1990; Schinn *et al.*, 1991) was obtained using a reaction volume of radius $r_0=12$ a.u. The $3png$ $J=3$ channels were ignored and only five LS-coupled channels were introduced: $(3snf, 3pnd)$ $^1F_3$, $(3snf, 3pnd)$ $^3F_3$, and $3pnd$ $^3D_3$. Corresponding results are shown on Fig. 40 as dotted lines. The second treatment, whose results are marked by solid lines, used a larger radius $r_0=20$ a.u. and included in addition the $3png$ $^1F_3$, $^3F_3$, and $^3G_3$ channels. Both calculations included fine-structure effects through the jj-LS frame transformation. Figure 40 shows that the angular distribution parameter spectra are complex and vary irregularly with energy. They appear drastically different from the β spectra for the $3pns$ states (Fig. 39). This is not surprising because the $3pnd$ states are more complex and two angular momenta $J=1$ and $J=3$ are excited. In contrast with the situation for the $3pns$ β parameter, there is no obvious correlation between the fluctuations of the β, γ, and ϵ parameters and the positions of the $3pns,nd$ $J=1$ and $J=3$ resonances. The results obtained with the two different calculations are almost the same and, in light of the experimental uncertainties, it is clear that theory agrees well with the experiment. Among the matrix elements involved in the calculation of the β and γ parameters, those corresponding to pure $J=1$ and $J=3$ terms can be distinguished from those associated with mixed-J terms. It was found that the structures of the β and γ spectra were essentially formed by the mixed-J terms and also that the $3pnd$ resonances autoionized preferentially into the $3s\epsilon f$ continua, favoring the ejection of the photoelectrons along the polarization axis.

We conclude from this section on observables recorded with the ICE experimental method that the eigenchannel R-matrix method, when combined with multichannel quantum-defect theory, provides a powerful tool for theoretical multichannel spectroscopy. This method can describe many subtle features of the excitation spectra, branching ratios and angular distributions of the emitted electrons. In all the cases studied, agreement ranging from excellent to satisfactory was achieved between high-precision experiments and theory. To our knowledge, no other theoretical method has been used to calculate such observables in alkaline earths to date. Of course, various sets of short-range scattering parameters were fitted to agree with particular sets of experimental data, in semiempirical MQDT analyses. For example, Hieronymus *et al.* (1990) fitted six different models to the data they obtained for $6pns$ $J=1$ levels of Ba, below or above the $6p_{1/2}$ ionization limit. However, as Aymar and Lecomte (1989) analyzed in detail for a specific example in Sr, the fitted parameters differ considerably from those calculated with the eigenchannel R-matrix method. This implies that in some complicated multichannel systems such semiempirical fits do not represent the short-range interactions alone, but rather represent an aggregate influence of all forces that are not considered explicitly.

V. OPEN-SHELL ATOMS

The eigenchannel R-matrix approach in combination with multichannel quantum-defect theory has been successfully applied to the calculation of photoionization and bound-state properties of several open p-subshell atoms and of two open d-subshell atoms, scandium and titanium. The first eigenchannel R-matrix study carried out in an atom with more than two valence electrons concerned Al, which has three electrons in the n=3 shell (O'Mahony, 1985), followed by Si, which has four valence electrons in the same shell (Greene and Kim, 1988). This calculation was the first application of the streamlined eigenchannel R-matrix approach to describe atomic systems with more than two valence electrons. The efficiency of the streamlined eigenchannel R-matrix approach (Greene and Kim, 1988) led to the adoption of this reformulation in almost all subsequent eigenchannel R-matrix calculations. Calculations have since been carried out for the halogen atoms (F to I)

(Robicheaux and Greene, 1992, 1993a), for the carbon-group atoms (C to Sn) (Robicheaux and Greene, 1993b), and more recently for the oxygen-group atoms (O to Te) (Chen and Robicheaux, 1994). Another theoretical study of this type by Miecznik *et al.* (1995) treated Al ground-state photoionization. These series of calculations were motivated largely by a desire to extract similarities and contrasts in the Rydberg-channel dynamics of chemically similar elements, and by a desire to isolate and categorize the most important physical effects. They also test the accuracy of the theoretical description of complex atoms that can be achieved through small-scale calculations.

The exploration of channel-interaction dynamics in complex open-shell atoms (Armstrong and Robicheaux, 1993; Robicheaux and Greene, 1993c, 1993d) began in earnest with calculations for scandium, the simplest transition-metal atom. A second complex atom with an open d subshell was studied subsequently, in calculations performed for titanium (Miecznik and Greene, 1996). Results for atoms with an open p subshell and for atoms with an open d subshell are summarized below.

A. Atoms with an open p subshell

1. Aluminum

We begin by describing a calculation carried out by O'Mahony (1985) in Al. The even-parity ^2D symmetry of Al involves the $3s^2nd$ Rydberg series perturbed by the $3s3p^2$ configuration, as was discerned from an early semiempirical MQDT analysis carried out by Lin (1974). O'Mahony's calculation provided a better understanding of the strong $3s^2nd$–$3s3p^2$ interaction. This mixing serves as a prototype for the $3s^23p^qnd$-$3s3p^{q+2}$ interaction, which is known to dominate the valence electron dynamics of third-row metalloide atoms and ions. This mixing was analyzed in parallel with the $3snd$-$3p^2$ mixing in Mg $^1D^e$. The $3s^2nd$-$3s3p^2$ channel mixing in Al $^2D^e$ and the $3snd-3p^2$ channel mixing in Mg $^1D^e$ near the lowest threshold were found to be very strong. In this regard, these systems are similar to the m_0snp-m_0pns $^1P^o$ mixing in Be and Mg, and to the m_0snp-$(m_0-1)dnp$ $^1P^o$ mixing in the heavier alkaline earths (see Sec. IV).

The early eigenchannel R-matrix calculation in Al (O'Mahony, 1985) was conducted in LS coupling. Moreover, it used a relatively crude unoptimized Hartree-Slater potential. In contrast, the most recent calculation of the photoionization spectrum of Al (Miecznik *et al.*, 1995) used the improved eigenchannel R-matrix techniques developed for open-shell atoms (see Sec. III.D). Moreover fine-structure effects were included through the jj-LS frame transformation. One major motivation of this study was to analyze the influence of spin-orbit effects on the photoionization spectrum of the $3s^23p\ ^2P^o$ ground state below the $3s3p\ ^1P^o$ ionization threshold. There are ten channels and three LS symmetries that can be excited by one photon from the ground state: $[(3s^2\ ^1S^e)ns\ ^2S^e]$, $[(3s^2\ ^1S^e)nd\ ^2D^e]$, $[(3s3p\ ^{3,1}P^o)np\ \ ^2S^e,\ \ ^2P^e,\ \ ^2D^e]$, $[(3s3p\ ^{3,1}P^o)nf\ ^2D^e]$. In LS coupling, the channels corresponding to different LS symmetries do not interact, since all non-Coulombic interactions, including fine-structure effects, are omitted from the Hamiltonian. The decay of $(3s3p\ ^{3,1}P^o)np\ ^2P^e$ resonances is forbidden below the $^3P^o$ threshold within this LS-coupling approximation. The spin-orbit interaction couples the channels mentioned above to each other and to a large number of other channels associated with five additional LS symmetries: $^4S^e$, $^4P^e$, $^4D^e$, and $^{2,4}F^e$. Eigenchannel R-matrix calculations were carried out using a box of 15 a.u. Configuration-interaction wave functions were determined for the three target states of Al^+, namely $3s^2\ ^1S^e$, $3s3p\ ^3P^o$, and $3s3p\ ^1P^o$. Basis functions used to describe all eight final LS symmetries were constructed by attaching s, p, d, f, and g orbitals to the components of the expansion of the ionic states. Additional correlation-type functions such as, for instance, $3s3p^2$ were also included. Length and velocity photoionization cross sections from the $3s^23p\ ^2P^o_{1/2,3/2}$ ground state were calculated by assuming a statistical mixture of the two initial J=1/2 and J=3/2 levels. Length and velocity results agreed to 1% accuracy typically, except at energies where they were small. Theoretical results were compared with the experimental measurements of Roig (1975) and with the Wigner-Eisenbud-type R-matrix calculation of Tayal and Burke (1987), which was conducted in LS coupling.

The cross section at the $3s^2$ threshold has an unusually large value that derives from the presence of the $3s3p^2\ ^2D^e$ level, which is diluted into the $3s^2nd\ ^2D^e$ bound states and the $3s^2\epsilon d\ ^2D^e$ continuum (Lin, 1974; O'Mahony, 1985; Komninos *et al.*, 1995). The calculated threshold value of 61 Mb agreed well with the experimental value of 65 $\pm$7 Mb (Roig, 1975) while Tayal and Burke (1987) found a slightly smaller value of 55 Mb. Aside from spin-orbit effects, the photoionization cross section below the $3s3p\ ^3P^o_2$ threshold agreed with the spectrum calculated by Tayal and Burke (1987). The lowest autoionizing resonance is the $3s3p^2\ ^2S^e$ level. The next broad resonances are members of the $(3s3p\ ^3P^o)np\ ^2D^e$ series, upon which sharp peaks are superimposed. These narrow peaks were ascribed to the LS-allowed $(3s3p\ ^3P^o)np\ ^2S^e$ and $(3s3p\ ^3P^o)nf\ ^2D^e$ series and to the LS-forbidden $(3s3p\ ^3P^o)np\ ^2P^e$ and $(3s3p\ ^3P^o)np\ ^4D^e$ series, which appear in the spectrum owing to their fine-structure-induced mixing with channels of the $^2D^e$ symmetry. Due to the occurrence of numerous sharp and overlapping resonances that converge to the closely spaced $3s3p\ ^3P^o_J$ thresholds, the spectrum including spin-orbit effects takes on a complicated appearance. Conspicuous spin-orbit effects arise just below the $3s3p\ ^3P^o_2$ threshold, including dramatic examples of enhancement or reduction of the resonance widths. For instance, the widths of the high-n LS-forbidden $(3s3p\ ^3P^o)np\ \ ^4D^e_{3/2,5/2}$ and $(3s3p\ ^3P^o)np\ ^2P^e_{1/2,3/2}$ resonances are larger or of the same order of magnitude as the widths of the

LS-allowed $(3s3p\ ^3P^o)np\ ^2S^e$ resonances. Indeed, since the widths for the $^2D^e$ series are about 10^3 times larger than for $^2S^e$, a very small admixture of $^2D^e$ character may cause the LS-forbidden states to autoionize faster than the $^2S^e$ states. Due to the n-dependence of the mixing between the $(3s3p\ ^3P^o)np\ ^2P^e_{3/2}$ and $(3s3p\ ^3P^o)np\ ^2D^e_{3/2}$ series, the widths exhibit an irregular evolution as a function of energy along various LS-forbidden series. The quantum defects of several Rydberg levels were found to agree with the available experimental data (Roig, 1975). In addition, Miecznik *et al.* (1995) analyzed the transition from LS to jj coupling for high-lying Rydberg levels below the $3s3p\ ^3P$ in the context of statistical distributions. While the spectrum exhibits a type of "chaotic" behavior according to these distributions, striking regularity remains in the pattern of energy levels and widths. One specific effect that is noteworthy is the periodic occurrence of very long-lived resonances.

Despite the strong influence of spin-orbit effects on the photoionization spectrum below and among the spin-orbit-split $3s3p\ ^3P^o_{0,1,2}$ thresholds, these effects remain almost negligible between the $3s3p\ ^3P^o_2$ and $3s3p\ ^1P^o_1$ thresholds since the $^1P^o_1$ threshold has no such splitting.

2. Halogens

Photoionization cross sections of the $m_0s^2m_0p^5\ ^2P^o$ ground state have been calculated in F (m_0=2), Cl (m_0=3), Br (m_0=4), and I (m_0=5) near the $m_0s^2m_0p^4$ thresholds (Robicheaux and Greene, 1992), and in Cl and Br near the higher-lying $m_0sm_0p^5$ thresholds (Robicheaux and Greene, 1993a). In the series of R-matrix calculations conducted for F through I, a reaction volume of radius $r_0=$ 9 a.u. was used. The same choice of basis functions was adopted for the different atoms, although the radial orbitals differed from one atom to another. The basis function sets were chosen to obtain converged results for I, which made necessary the inclusion of basis functions unnecessary for lighter halogens. The $m_0s^2m_0p^5\ ^2P^o$ ground state was described with ~300 basis functions. The target states in order of increasing energy were the $m_0s^2m_0p^4\ ^3P^e$, $^1D^e$, and $^1S^e$ ionic states. When combined with the jj-LS frame transformation, there were seven different final LS symmetries ($^2S^e$, $^{2,4}P^e$, $^{2,4}D^e$, $^{2,4}F^e$) and 15 final-state channels that entered the R-matrix calculations. These channels were constructed by attaching s and d waves to the three configuration-interaction target states. The basis set depended on the LS symmetry and the largest basis set size was ~700 for the $^2D^e$ symmetry. The jj-LS frame transformation in its simplest and most common form couples only closed channels converging to the same $^{2S_c+1}L_c$ threshold. (The index c refers to the ionic core.) For all atoms, except those with a single electron or hole in the target valence shell, the spin-orbit interaction not only splits the target states having the same L_c,S_c but different J_c, but also couples the states with the same J_c but different L_c,S_c. In the halogens the $m_0s^2m_0p^4\ ^3P^e_0$ state mixes with the $m_0s^2m_0p^4\ ^1S^e_0$ state, and the $m_0s^2m_0p^4\ ^3P^e_2$ state mixes with the $m_0s^2m_0p^4\ ^1D^e_2$ state. These mixings were accounted for by an intermediate-coupling frame transformation obtained empirically from the experimental ionization energies. It is worth noting that some states would not autoionize without this frame transformation. Note that this intermediate-coupling frame transformation has not been utilized in eigenchannel R-matrix calculations carried out for other open-shell atoms.

Figure 41 shows the photoionization cross sections for Cl, Br, and I between the $^3P^e$ and $^1D^e$ thresholds. The most striking feature of this figure is the remarkable similarity between Cl [Figs. 41(a), 41(b)], Br [Figs. 41(c), 41(d)], and I [Figs. 41(e), 41(f)]. The broad resonances are superposition of two broad autoionizing series, $(^1D^e)nd\ ^2P^e$ and $(^1D^e)nd\ ^2D^e$, while the sharp resonances are $(^1D^e)ns\ ^2D^e$ and $(^1D^e)nd\ ^2S^e$. Interestingly, $(^1D^e)nd\ ^2S^e$ resonances would not be able to autoionize in this theoretical description, except through the operation of the intermediate-coupling frame transformation. The photoionization cross section for F in the same energy range (not shown here) strongly differs from those displayed in Fig. 41 for the heavier halogens. In F, the $(^1D^e)nd$ resonances are sharper due to the lack of overlap between a d electron and the inner m_0p electron. Figure 41 shows that the calculated photoionization spectra reproduce most features in the experimental data (Berkowitz *et al.*, 1981; Ruščić and Berkowitz, 1983; Ruščić *et al.*, 1984b). The agreement was found to be the best in Cl. For Br, the broad $(^1D^e)nd\ ^2P^e$ and $(^1D^e)nd\ ^2D^e$ resonances were shifted slightly too high in energy, the error in the calculated quantum defects amounting to ~0.05. Similarly good agreement between theoretical and experimental (Ruščić *et al.*, 1984a) spectra was observed for F, although an error of ~0.01 in the quantum defect of the $(^1D^e)3s\ ^2S^e$ level caused a reversal in the order of the lowest autoionizing lines compared to the experiment. For the photoionization spectra between the $^1D^e$ and $^1S^e$ thresholds, experimental data exist only for Cl and I (Ruščić and Berkowitz, 1983; Berkowitz *et al.*, 1981). Good agreement between theory and experiment was found for Cl. The poorer agreement observed for I probably stems from the fact that the much larger spin-orbit splittings in I are too strong to be fully accounted for by frame-transformation procedures.

The photoionization cross sections of some halogen atoms have been calculated using different theoretical approaches. Each halogen atom from F through I was studied by Manson *et al.* (1979) using both the Hartree-Fock and the central-potential-model approximations. Cl was investigated by Starace and Armstrong (1976) using the random-phase approximation with exchange, by Fielder and Armstrong (1983) using the multiconfiguration Hartree-Fock method, by Shahabi *et al.* (1984) with an open-shell transition matrix method, by Lamoureux and Combet Farnoux (1979) with the Wigner-

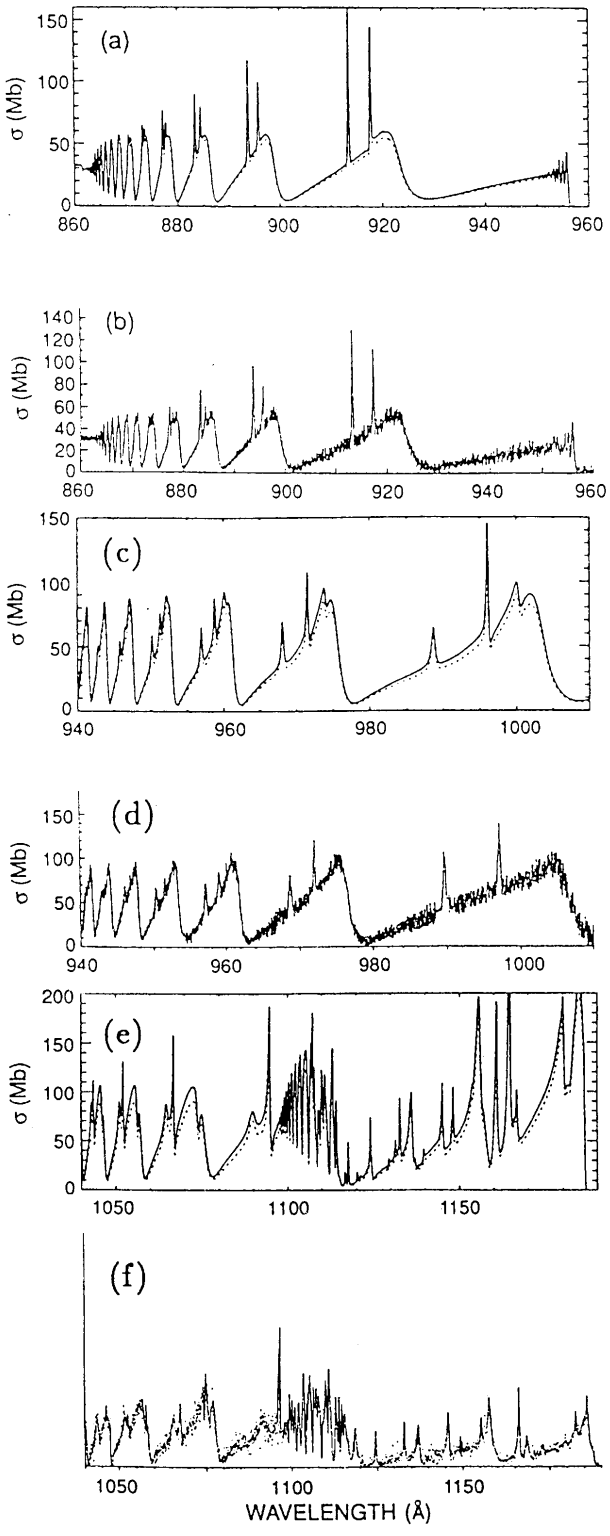

FIG. 41. Photoionization of the $m_0s^2m_0p^5\ ^2P^o_{3/2}$ ground state of halogens Cl to I between the $m_0s^2m_0p^4\ ^3P$ and ^1D thresholds. The calculated length (solid line) and velocity (dotted line) cross sections [(a), (c), and (e)] have been convolved with the experimental resolution of 0.28 Å. The theoretical results in Cl (a), Br (c), and I (e) are compared with the photoabsorption spectra (b), (d), and (f) recorded by Ruščić *et al.* (1983), Ruščić *et al.* (1984b), and Berkowitz *et al.* (1981), respectively. (From Robicheaux and Greene, 1992).

Eisenbud-type R-matrix method, and by Brown *et al.* (1980) using many-body perturbation theory. All these calculations were performed in strict LS coupling. Resonance structures were calculated only in the last two studies mentioned. In addition, I photoionization was calculated by Combet Farnoux and Ben Amar (1986) using a K-matrix method. The resonance structures obtained by Robicheaux and Greene (1992) compared well with those predicted by Brown *et al.* (1980), whereas only a moderate agreement with the predictions of Combet Farnoux and Ben Amar (1986) was found. Another point of comparison of the eigenchannel R-matrix results of Robicheaux and Greene (1992) with previous calculations is the magnitude of the total cross section at the $^1S^e$ threshold. In Cl, the theoretical value of 38±2 Mb is smaller than the experimental value of 43.6±3.5 Mb obtained by Samson *et al.* (1986). The threshold cross sections predicted for Cl by other methods range from 25 Mb to 60 Mb. Values obtained by the eigenchannel R-matrix calculations are smaller than the values obtained by Manson *et al.* (1979) except for F, where they agree. The threshold value of the I cross section obtained by Robicheaux and Greene (1992) was smaller than the value predicted by Combet Farnoux and Ben Amar (1986).

Robicheaux and Greene (1992) further analyzed the similarities among the halogens by comparing the short-range scattering parameters obtained for every halogen atom as functions of energy. The striking similarity between the heavier halogens that is apparent in Fig. 41, as well as the major differences from F, emerge clearly from this comparison. Moreover, this analysis of channel mixing helps to explain why all the ns resonances are narrow, while the nd resonances are very broad in all halogen atoms except F.

A second eigenchannel R-matrix study for the halogens determined partial and differential photoionization cross sections of Cl and Br near the higher-lying $m_0sm_0p^5\ ^{3,1}P^o$ thresholds (Robicheaux and Greene, 1993a). The eigenchannel R-matrix calculations were similar to those performed to calculate photoionization cross sections at lower energy. However, the $(m_0sm_0p^5\ \ ^3P^o,^1P^o)np$ channels were added in order to describe the $m_0sm_0p^5np$ autoionizing resonances. Observables calculated included partial photoionization cross sections and asymmetry parameters characterizing the energy and angular distributions of photoelectrons ejected, leaving the ionic core in the states $m_0s^2m_0p^4\ ^3P^e$, $^1S^e$, and $^1D^e$. Results calculated for Cl below the $3s3p^5\ ^3P^o$ threshold compared well with the experimental data obtained by van der Meulen, Krause, *et al.* (1992). The agreement deteriorated at energies near the $^1P^o$ threshold. Most features in the Br experimental partial cross sections below the $4s4p^5\ ^3P^o$ threshold (van der Meulen, Krause, and Lange, 1992) were also reproduced by the R-matrix calculation. The calculations accounted for singly excited state resonances only, but omitted doubly excited states such as the Cl $3s^23p^33d4p$ level. This omission appears to be respon-

sible for most of the discrepancies between the calculations and the experimental data.

Robicheaux and Greene (1993a) compared the values they obtained in Cl for partial cross sections and asymmetry parameters at a fixed energy far from resonances to the values derived by Shahabi *et al.* (1984) with an open-shell transition matrix method that neglected the resonance structures. Both sets of partial cross sections values agreed well with the experimental data of van der Meulen, Krause, *et al.* (1992), while Robicheaux and Greene's asymmetry parameters agreed better with the experimental results than did the values obtained by Shahabi *et al.* (1984). Robicheaux and Greene (1993a) also compared the resonance structures they obtained in Cl with those predicted by Brown *et al.* (1980) using many-body perturbation theory. Because these latter authors carried out their calculations in LS coupling, the comparison dealt only with LS results. Both sets of theoretical results agreed well below the $^3P^o$ threshold, while differences appeared near the $^1P^o$ threshold.

3. Carbon-group atoms

The carbon-group atoms are characterized by a $m_0s^2m_0p^2\ ^3P^e$ ground state with m_0=2 for C, m_0=3 for Si, m_0=4 for Ge, and m_0=5 for Sn. The first application of the streamlined eigenchannel R-matrix approach (Greene and Kim, 1988) dealt with the J=0 even-parity bound spectrum of Si, which involves the two $3s^23p_{1/2}np_{1/2}$ and $3s^23p_{3/2}np_{3/2}$ Rydberg series. It was found that LS-coupled R-matrix calculations combined with the jj-LS frame transformation accounted well for the experimental energy positions (Martin and Zalubas, 1983).

A series of small-scale calculations carried out by Robicheaux and Greene (1993b) in the carbon group considered the odd-parity bound Rydberg spectra with J=0–3 and the photoabsorption spectra. These LS-coupled eigenchannel R-matrix calculations followed by the frame transformation were focused on the region below and between the $m_0s^2m_0p\ ^2P^o_{1/2}$ and $^2P^o_{3/2}$ thresholds. The R-matrix volume radius was $r_0=15$ a.u. As for the halogens, the basis-function sets used to describe initial and final states were the same for the different atoms; the ground state, the final states, and the $m_0s^2m_0p\ ^2P^o$ target state were all computed using configuration interaction. The $m_0s^2m_0p^2\ ^3P^e$ ground state was described by ~150 basis functions. Study of the odd-parity spectra with J=0–3 required the R-matrix calculations to be performed for six different LS symmetries: $^{1,3}P^o$, $^{1,3}D^o$, $^{1,3}F^o$. The largest basis-set size was ~275 for $^{1,3}P^o$ symmetries. Basis functions for the final-state symmetries were constructed by attaching a s or d wave to the odd-parity $m_0s^2m_0p\ ^2P$ configuration-interaction target state. In addition to these close-coupling-type variational basis functions, correlation-type basis functions were introduced as well. Basis functions associated with strongly closed channels were constructed by attaching a p or f wave to the configuration-interaction even-parity target states $m_0sm_0p^2$, $m_0s^2m_0d$, and $m_0s^2(m_0+1)s$. These latter channels are relevant to the study of the odd-parity spectra with J=0–3 because the $(m_0s^2m_0p\ ^2P^o)ns$ and $(m_0s^2m_0p\ ^2P^o)nd$ Rydberg series converging to the two ionic thresholds $m_0s^2m_0p\ ^2P^o_{J_c}$ (J_c=1/2 and 3/2) are perturbed by $m_0sm_0p^3$ states.

Oscillator strengths for transitions from the $m_0s^2m_0p^2\ ^3P^e_0$ ground state to odd-parity bound levels with J=1 were calculated for all elements. For C, where previous experimental and theoretical values were available for some lines (Nussbaumer and Storey, 1984; Goldbach and Nollez, 1987; Goldbach *et al.*, 1989), theoretical results compared well with the data. Robicheaux and Greene (1993b) compared the photoabsorption spectra between the $m_0s^2m_0p\ ^2P^o_{J_c}$ thresholds for the different atoms (see their Fig. 8). The cross sections exhibited one $(m_0s^2m_0p\ ^2P^o_{3/2})ns$ autoionizing Rydberg series and two $(m_0s^2m_0p\ ^2P^o_{3/2})nd$ autoionizing series converging to the $^2P^o_{3/2}$ threshold. The s-wave resonances were sharper than the d-wave resonances except in C, where all resonances had small widths because, as in F, the d waves did not interact strongly with the core. The Sn and Ge autoionization spectra resembled each other while the Si and mainly the C, the spectra looked very different. The only experimental spectrum available for comparison was a densitometer trace constructed by Brown *et al.* (1977a) for Ge. The agreement between experiment and theory was very good for the positions of the resonances but somewhat poorer for the line shapes.

We consider now the results obtained for the energy-level positions of odd-parity bound Rydberg levels with J=0–3. Extensive experiments conducted on the carbon-group atoms were interpreted using approximate Lu-Fano plots drawn through experimental quantum defects, or through the use of semiempirical MQDT fits (Brown *et al.*, 1975; Feldman *et al.*, 1976; Brown *et al.*, 1977a, 1977b; Ginter *et al.*, 1986; Ginter and Ginter, 1986). The theoretical energy values provided by eigenchannel R-matrix calculations were compared with experimental data using Lu-Fano plots. Very good agreement was found for all symmetries in C and Si and in the J=0 symmetry of Ge and Sn. For $J=1-3$, the agreement between the experimental and theoretical results is poorer for Ge and Sn than was obtained for the lighter atoms. The main reason for the discrepancies is the strong energy dependence of several short-range scattering parameters due to the presence of the $m_0sm_0p^3$ states. In Ge and Sn, these states cause rapid energy dependence of the quantum defects in $^{1,3}P^o$ and $^{1,3}D^o$ symmetries, with the strongest effects occurring near threshold in the $^3D^o$ symmetry. This large energy dependence makes the application of the jj-LS frame transformation somewhat problematic. Indeed, depending upon whether the scattering parameters were referred to theoretical or experimental thresholds, noticeably different results were found. Importantly, the $m_0sm_0p^3$ states cause an energy dependence of the scattering parameters in all atoms. However, the carbon pa-

rameters are energy dependent only at low energy, while in Si, Ge, and Sn, the energy dependence is strong over a much larger range. Carbon and silicon have much smaller spin-orbit splittings than heavier carbon-group elements, whereby the *jj-LS* frame-transformation approximation remains valid in C and Si.

Note finally that the calculation of Robicheaux and Greene (1993b) provided the first nearly *ab initio* description of these spectra for the carbon-group atoms. The calculations described the energy dependence of dynamical scattering parameters better than semiempirical fits (Brown *et al.*, 1977a, 1977b; Ginter *et al.*, 1986; Ginter and Ginter, 1986). Indeed, the parameters introduced in the fits were, in most cases, assumed to be energy independent.

4. Chalcogens

Chen and Robicheaux (1994) calculated the photoionization cross sections of the $m_0s^2m_0p^4\ {}^3P_2^e$ ground states of O ($m_0=2$), S ($m_0=3$), Se ($m_0=4$), and Te ($m_0=5$) using *LS*-coupled eigenchannel *R*-matrix calculations combined with the *jj-LS* frame transformation. As was described in Sec. III.D, calculations were carried out with the Hamiltonian referring to the full atom [Eq. (3.41)]. The dipole polarizability of the core was accounted for in the Se and Te calculations only. The calculations were conducted using the Wigner-Eisenbud-type reformulation of the eigenchannel approach (Schneider, 1975; Robicheaux, 1991). Calculations were restricted to photoionization of the outermost m_0p subshell, the relevant target states in *LS* coupling being $m_0s^2m_op^3\ {}^4S^o$, ${}^2D^o$, and ${}^2P^o$, in order of increasing energy. In *LS* coupling, there are nine channels and three *LS* symmetries that can be excited by one photon from the ground state: $[({}^4S^o)ns\ {}^3S^o,\ nd\ {}^3D^o]$, $[({}^2D^o)nd\ {}^3S^o,\ nd\ {}^3P^o,\ ns,\ nd\ {}^3D^o]$, $[({}^2P^o)ns,\ nd\ {}^3P^o, nd\ {}^3D^o]$. When spin-orbit effects are neglected, channels corresponding to different *LS* symmetries do not interact; in particular the $({}^2D^o)nd\ {}^3P^o$ states are not coupled to any continuum, which means that the decay of $({}^2D^o)nd\ {}^3P^o$ resonances is forbidden in *LS* coupling below the ${}^2D^o$ threshold. The spin-orbit interaction can couple the channels mentioned above to each other and to a large number of other channels such as the $({}^4S^o)ns\ {}^5S^o$, $nd\ {}^5D^o$, and similar channels associated with ${}^2D^o$ and ${}^2P^o$ thresholds. Effects of the spin-orbit interaction were incorporated approximately, through the *jj-LS* frame transformation. A reaction volume of radius of 11 a.u. was used for O and one of 13 a.u for the heavier chalcogens. The rare-gas-core electrons were frozen and no correlation or excitation of the inner-core electrons was included. Configuration-interaction wave functions for the target states were determined variationally as a superposition of only five configurations: $m_0s^2m_0p^3$, $m_0s^2m_0pm_0d^2$, $m_0s^2m_0p^24f$, $m_0sm_0p^3m_0d$, and m_0p^5. For a given configuration, all possible intermediate angular couplings were introduced into the many-electron basis set. The same list of configurations was used for the different atoms. The differences between the atoms were the radial orbitals of all electronic states involved.

Photoionization cross sections were calculated at final-state energies between the ${}^4S^o$ and ${}^2D^o$ thresholds and between the ${}^2D^o$ and ${}^2P^o$ thresholds. Theoretical cross sections were convolved with the experimental width using a preconvolution technique (Robicheaux, 1993). Chen and Robicheaux (1994) focused on the heavier chalcogens S, Se, and Te, which have been studied far less than oxygen (for references see Seaton, 1987b). The spectrum of O differs from the spectra of the other chalcogens since it consists of sharp resonances only. As in C (Robicheaux and Greene, 1993b) and F (Robicheaux and Greene, 1992) in the second row, the absence of broad features in O is a consequence of the small overlap between the $2p$ and nd orbitals. We restrict our discussion to the heavier chalcogens, where correlations are stronger than in O.

The calculated photoionization cross section of S below the ${}^2D^o$ threshold reproduced the experimental spectrum of Gibson *et al.* (1986a). The positions and widths of the resonances pertaining to the four series attached to the ${}^2D^o$ threshold were well described. In particular, as observed, the *LS* forbidden $({}^2D^o)nd\ {}^3P^o$ appeared as very intense and narrow resonances. However, the calculation did not reproduce the relative intensities of those resonances perfectly. There are three $({}^2P^o)3d\ {}^3D^o$, ${}^3P^o$ and $({}^2P^o)5s\ {}^3P^o$ perturbers attached to the ${}^2P^o$ threshold which fall below the ${}^2D^o$ threshold; the description of those perturbing resonances was slightly poorer. Indeed, the error in energy of the perturber is ΔE (a.u.)$=\delta\mu/\nu^3$, which can be large when the effective quantum number ν in the perturbing channel is small. The intensities and shapes of nearby resonances are very sensitive to the exact position of the perturbers. The resonances associated with the cross section between the ${}^2D^o$ and ${}^2P^o$ thresholds are dominated by the $({}^2P^o)nd\ {}^3D^o$ and ${}^3P^o$ resonances, which are broad and overlapping. Agreement with experiment (Gibson *et al.*, 1986a) was quite satisfactory.

Photoionization cross sections of S have been calculated using different theoretical approaches (Mendoza and Zeippen, 1988; Tayal, 1988; Altun, 1992, and references therein). Tayal (1988) used the Wigner-Eisenbud-type *R*-matrix approach, Mendoza and Zeippen (1988) adopted the close-coupling approximation, while Altun (1992) implemented many-body perturbation theory. Because all of those calculations were performed in a strict *LS*-coupling approximation, they failed to show the *LS*-forbidden $({}^2P^o)nd\ {}^3P^o$ resonances below the ${}^2D^o$ threshold. Chen and Robicheaux (1994) compared their positions and classifications, for states in the autoionizing series converging to the ${}^2D^o$ and ${}^2P^o$ thresholds, to those of Gibson *et al.* (1986a) and of other calculations. Below the ${}^2D^o$ threshold, the calculations of Tayal (1988) and Altun (1992) gave global agreement with the experiment, but the errors in the quantum defects of some autoionizing levels were larger (up to 0.2) than those calculated with the eigenchannel *R*-matrix method (error within 0.02 for most resonances). The

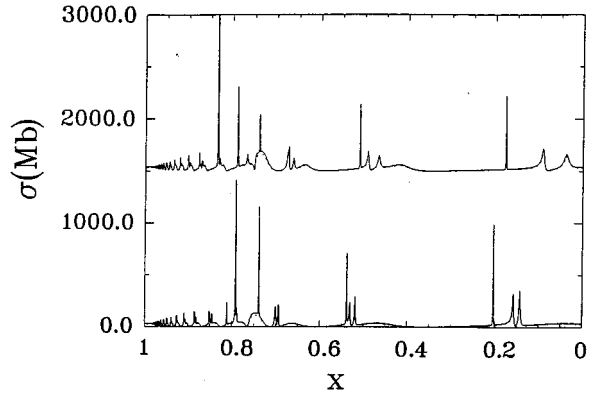

FIG. 42. Photoabsorption cross sections of S (lower) and Se (upper + 1500 Mb) between the $m_0s^2m_0p^3\ ^4S^o$ and $^2D^o$ thresholds. LS results are drawn vs a dimensionless quantity $\times=(\omega-E_{4S})/(E_{2D}-E_{4S})$. (From Chen and Robicheaux, 1994).

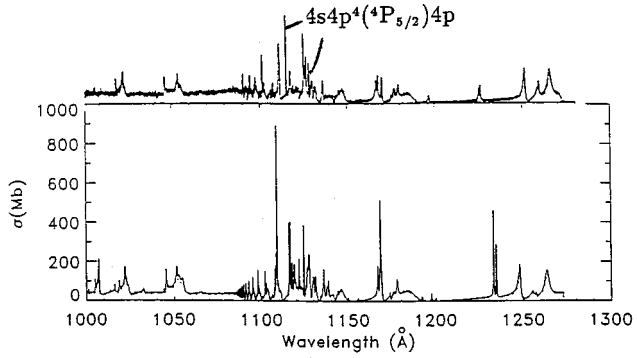

FIG. 43. The photoabsorption cross section of Se obtained by combining LS-coupled R-matrix calculations with the jj-LS frame transformation (lower curve) is compared with the experimental result (in arbitrary units) of Gibson *et al.* (1986b). The zero of the experimental curve corresponds to the horizontal line. The vertical scale of the theoretical curve has been adjusted to reproduce the experimental mean background. (From Chen and Robicheaux, 1994, courtesy of F. Robicheaux.)

eigenchannel R-matrix calculations also resolved a controversy existing in the literature on the assignment of the $(^2D^o)nd\ ^3S^o$ and $(^2D^o)ns\ ^3D^o$ resonances; the experimental classifications of those series should be interchanged. All previous calculations gave good agreement with experiment in the energy range between the $^2D^o$ and $^2P^o$ thresholds.

The origin of spectral features in S was analyzed in some detail by Chen and Robicheaux (1994). The origin of the broad and sharp features of the S spectrum as well as the differences of the quantum defects of the $(^2D^o)nd\ ^3S^o$, $(^2P^o)nd\ ^3P^o$, and $^3D^o$ series could be understood through an examination of the matrix elements that couple those channels. Chen and Robicheaux (1994) also studied the convergence of the wave-function expansion, and have shown the importance of polarization-type basis functions for the description of atomic dynamics. Moreover, they compared the results of their full electron (16) calculation with those they obtained using a model potential to account for the effects of closed shells and six valence electrons. Both calculations were conducted with the same configuration list. For all levels, the quantum defects of both calculations were found to differ by less than 0.01; negligible differences were also found for dipole moments. This showed that the Ne-like core could be well approximated with a local potential.

Figure 42 compares the photoionization cross sections of S and Se calculated in LS coupling. This figure clearly shows the similarities between the two atoms; it is obvious that the two atoms have nearly identical electrostatic interactions between the valence and Rydberg electrons. Figure 43 shows Se cross section calculated using the jj-LS frame transformation to incorporate fine-structure effects. The calculated results gave global, but not detailed, agreement with the experiment of Gibson *et al.* (1986b). As in S, most of the discrepancies are near the perturbers at $\sim$ 1120 Å attached to the $^2P^o$ threshold. In this energy range there are two peaks assigned by the experiment as $4s4p^4(^4P^e_{5/2})4p$ states. Chen and Robicheaux (1994) found that the $4s4p^5$ states should not be assigned to any of the experimental resonances. They ascribed the perturbers to the $(^2P^o)4d$ and $(^2P^o)6s\ ^3P^o$ states, which are analogous to the perturbers of the $(^2D^o)ns,nd$ series of S.

The quality of the Te calculation of Chen and Robicheaux (1994) has noticeably deteriorated, compared to Se. This might indicate some limitation of the frame-transformation treatment for including spin-orbit effects. Another possibility is that wave function exhibits poorer convergence. Although the resonances are more strongly mixed in Te than in Se, Chen and Robicheaux (1994) managed to identify some of them. As in the case of the Se $4s4p^5$ levels, they concluded that the $5s5p^5$ classification given in the experiment (Berkowitz *et al.*, 1981) to some of the peaks is inappropriate. No other theoretical calculation is available for comparison in either Se or Te.

B. Open d-subshell atoms

1. Scandium

An extensive study of the Sc atom was performed by Robicheaux and Greene (1993c, 1993d) and Armstrong and Robicheaux (1993) using the LS-coupled eigenchannel R-matrix method combined with the jj-LS frame transformation. The main purpose of these investigations was to test whether the eigenchannel R-matrix method could reproduce the extremely complicated spectra of a transition-metal atom. The good agreement between theory and experiment obtained for photoionization spectra from the Sc ground state $3d4s^2\ ^2D^e_{3/2,5/2}$ and from the Sc $3d^3\ ^2D^e_{3/2}$ excited state demonstrated, for the first time, that the eigenchannel R-matrix techniques could achieve the accuracy needed to describe the complex spectra of Sc. The studies per-

formed in Sc did not aim solely at the calculation of accurate spectra. They also probed the reasons for the success of the calculations, as well as the limitations, and they explored the underlying atomic dynamics of Sc.

The theoretical description of Sc is complicated by the large number of closely spaced thresholds. The first fourteen states of Sc^+ have even parity, with the configurations $3d4s$, $3d^2$, and $4s^2$. The first thirteen thresholds ($3d4s\ ^3D^e_1$, $3d4s\ ^3D^e_2$, $3d4s\ ^3D^e_3$, $3d4s\ ^1D^e_2$, $3d^2\ ^3F^e_2$, $3d^2\ ^3F^e_3$, $3d^2\ ^3F^e_4$, $3d^2\ ^1D^e_2$, $4s^2\ ^1S^e_0$, $3d^2\ ^3P^e_0$, $3d^2\ ^3P^e_1$, $3d^2\ ^3P^e_2$, $3d^2\ ^1G^e_4$, in order of increasing energy) have a spread of only 14 000 cm^{-1}, while the $3d^2\ ^1S^e_0$ threshold is at 25 955 cm^{-1} above the $3d4s\ ^3D^e_1$ ionic ground state. The small spread of even-parity thresholds is partly due to the near degeneracy of the $4s$ and $3d$ orbitals. The Rydberg series attached to the closely spaced thresholds interact with each other, producing complicated spectra. Almost every Rydberg series is perturbed and the calculated short-range scattering parameters need to be very accurate to place the perturbers in the correct position. As was emphasized above, the theoretical spectrum may bear no resemblance to the experimental spectrum if a perturber has even a small error in its quantum defect.

The eigenchannel R-matrix techniques used for the Sc calculations are similar to those employed for the open p-subshell systems. However, the complexity of Sc compared to open p-subshell atoms led Robicheaux and Greene (1993c) to carefully analyze the factors that affect the convergence of the calculation. Here we describe the most vital features of the method developed for Sc. The R-matrix volume radius was r_0=21 a.u. As in the open p-subshell atoms, the parameters α^i_l and r_c introduced in the one-electron Hamiltonian H_v of Eq. (3.38) were fitted to optimize agreement between the calculated energy levels of H_v and the experimental levels of Sc^{++}. However, in Sc, a large weight was put in the optimization on fitting the spin-orbit splitting of the Sc^{++} $3d$ levels, which ensured a better shape of the Sc^{++} nd orbitals.

As in previous work, the calculation began by the choice and construction of the target wave functions. Convergence tests showed that the lower odd-parity ionic states (from 26 000 cm^{-1} to 39 000 cm^{-1} above the Sc^+ ground state) play a large role in Sc dynamics. Indeed, perturbers such as $3d4p5s$ and $4s4p4d$ fall in the energy range close to the higher even-parity thresholds; it is crucial to obtain a reasonably good description of these perturbers in order to obtain quantum defects that are reasonably well converged. Moreover, the introduction of these odd-parity target states was found to be crucial in order to describe the polarizabilities of the low-lying even-parity states of Sc^+.

The variational basis functions were constructed with natural orbitals, as in the calculations for p-subshell atoms. In Sc, the natural orbitals were chosen to give the best overall convergence for the lowest even- and odd-parity ionic target states. The initial states, the final states, and the target states were computed using configuration-interaction methods. The basis functions used to construct the even-parity $3d4s^2\ ^2D^e_{3/2,5/2}$ and $3d^3\ ^2D^e_{3/2}$ initial states were obtained by attaching s-wave, d-wave, and g-wave orbitals to the even-parity target states and p-wave and f-wave orbitals onto the odd-parity target states. A large number of LS- and jj-coupled channels entered the calculations of photoionization cross sections from the ground-state fine-structure levels $3d4s^2\ ^2D^e_{3/2,5/2}$. Construction of the jj-coupled short-range reaction matrices for final J_f values ranging from J_f=1/2 to J_f=7/2 required LS-coupled eigenchannel R-matrix calculations to be carried out for eleven LS symmetries: $^{2,4}S^o$, $^{2,4}P^o$, $^{2,4}D^o$, $^{2,4}F^o$, $^{2,4}G^o$, and $^4H^o$. For a given final LS symmetry, between two and thirteen channels entered the calculation. For a given J_f, anywhere from 23 to 43 channels entered the calculation in the jj-coupled representation. Open and weakly closed channels were constructed by attaching p-wave and f-wave orbitals onto the even-parity target states. In addition to these channels, a large number of strongly closed channels were included in the calculations. They were constructed by attaching s-wave, d-wave, and g-wave orbitals to the odd-parity target states.

Two papers (Robicheaux and Greene, 1993c, 1993d) treated the photoabsorption spectrum out of the ground-state fine-structure levels $3d4s^2\ ^2D^e_{J_g}$ (J_g=3/2,5/2). This spectrum was studied experimentally by Garton *et al.* (1973). Robicheaux and Greene (1993c) calculated length and velocity cross sections for the six different $^2D^e_{J_g}\rightarrow J_f$ transitions: 3/2→1/2, 3/2→3/2, 3/2→5/2, 5/2→3/2, 5/2→5/2, and 5/2→7/2. Very good agreement was found between length and velocity results. Calculations covered the wavelength range from the lowest $3d4s\ ^3D^e_1$ threshold up to $3d^2\ ^1G^e_4$ threshold. The spectrophotographic plates of Garton *et al.* (1973) were compared with theoretical calculations performed for a statistical mixture of J_g=3/2 and J_g=5/2 ground-state fine-structure levels; this reflected the level of thermal excitation of the Sc vapor in the experiment.

Robicheaux and Greene (1993c) constructed simulated "theoretical plates" by translating photoabsorption intensity into a grayscale image. To mimic saturation effects, cross sections less than 3 Mb were displayed as white, while cross sections greater than 18 Mb were shown as black. All major experimental features were reproduced by the calculation. The numerous perturbing states complicated the appearance of the spectrum. Additional absorption lines associated with the substantial population in both of the ground-state fine-structure levels added further complexity as well.

Global aspects of the Sc dynamics were analyzed by Robicheaux and Greene (1993c), who studied the scattering probability matrix S_{ij} that characterizes the mixing strengths of different channels. The photoionization propensities provided additional insight: The photoabsorption spectrum was expected to display pairs of autoionizing lines with the ground-state splitting. For ex-

ample a $^2D^o$ state should appear in both $^2D^e_{5/2} \rightarrow {}^2D^o_{3/2}$ and $^2D^e_{5/2} \rightarrow {}^2D^o_{5/2}$. Although the lines tend to appear in both J_f symmetries that are possible, usually one line has much more oscillator strength. By analyzing the angular part of the reduced dipole matrix elements, Robicheaux and Greene (1993c) showed that the favored transitions were simply those for which $\Delta J = \Delta L$. This means, for example, that the cross section for $^2D^e_{5/2} \rightarrow {}^2D^o_{3/2}$ is fourteen times smaller than the $^2D^e_{5/2} \rightarrow {}^2D^o_{5/2}$ cross section.

The exploration of the dynamics of Sc on a large scale permitted a qualitative understanding of what determines the positions and shapes of various autoionizing lines and the origin of several marked features of the Sc spectrum. Robicheaux and Greene (1993c) successfully labeled the more prominent Rydberg series for excitation from the $3d4s^2\ ^2D^e_{3/2}$ ground state. However, a better understanding of Sc (and a more complete classification of the autoionizing lines) can be obtained only by studying the details on a fine scale. Robicheaux and Greene (1993d) classified the lines measured by Garton *et al.* (1973) and compared the calculated lines with theoretical spectra. The classification was performed in two steps. First, the experimental and theoretical lines were paired visually to give the best agreement between theoretical and experimental quantum defects and oscillator strengths. Then the classification was performed with the procedure described in Sec. IV.B, i.e., by throwing away all the open channels in the MQDT calculation that converts the problem to a search for bound levels. A crucial aspect of the classification was the derivation of an estimation of the level of acceptable error in the positions of the perturbers. Another key aspect was ascertaining from the scattering probability matrix how strongly a perturber interacted with various Rydberg series. The theoretical classification agreed for the most part with the experimental classification, but there were some discrepancies. While several lines could not be classified, owing to uncertainties in the calculation, Robicheaux and Greene (1993d) were able to complete the classification of numerous "partially classified" lines of Garton *et al.* (1973) and to classify most of their lines that had remained totally unclassified. All the lines could be classified in either the LS or jj coupling and the classification was presented in the coupling scheme for which the state was the purest.

The comparison of theoretical and experimental lines permitted an evaluation of the accuracy of the calculation. At energies far from perturbers, the errors in quantum defects were less than 0.03, the (typically smaller) quantum defects for the nf series being more accurate than those for the np series. Indeed, the f-wave channels hardly interact with other channels because the f-wave electrons do not penetrate into the complicated core region of Sc, while the p-wave channels display stronger interactions. The oscillator strengths are highly susceptible to cancellation effects and are expected to be less accurate than the quantum defects. In the vicinity of perturbing states, the quantum-defect errors are larger due to the relatively large errors in the positions of the low-n perturbers. The high accuracy achieved for the short-range scattering parameters was crucial for the classification. It probably would not have been possible to classify most of the lines if the calculated quantum-defect errors had been greater than ~ 0.06.

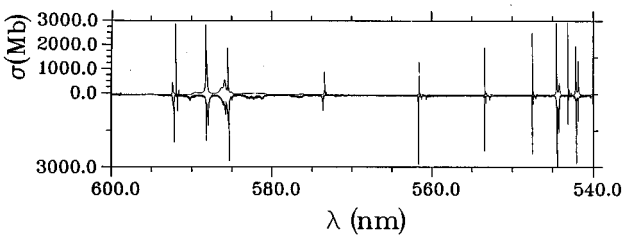

FIG. 44. Photoionization cross section of the Sc $3d^3\ ^2D^e_{3/2}$ excited level as a function of the wavelength of the photoionizing laser. The wavelength range goes from the $Sc^+\ 3d4s\ ^3D^e_1$ threshold at 600.8 nm to 540 nm, below the $3d4s\ ^1D^e_2$ threshold at 521.2 nm. The length theoretical cross section (unconvolved) is compared with the experimental ion signal, shown as a mirror image. (From Armstrong and Robicheaux, 1993, courtesy of F. Robicheaux.)

The fact that, in the experiment of Garton *et al.* (1973), the two lowest bound levels $3d4s^2\ ^2D^e_{3/2}$ and $3d4s^2\ ^2D^e_{5/2}$ were simultaneously photoionized introduced difficulty in the identification of all the experimental lines. To overcome this difficulty, and to test further the eigenchannel R-matrix method developed for Sc ground-state photoionization, a new measurement of the relative photoionization cross section for the excited Sc $3d^3\ ^2D^e_{3/2}$ level was carried out by Armstrong and Robicheaux (1993). An initial state having the same S_g, L_g, and parity as the ground state was used in order to probe the same final states as those observed by Garton *et al.* (1973). The relative measurement of photoionization cross section was performed by resonant two-step excitation via the $4s^24p\ ^2P^o_{1/2}$ and subsequent photoionization of the $3d^3\ ^2D^e_{3/2}$ level. The photoionization cross section was measured over the energy range from the $Sc^+\ 3d4s\ ^3D^e_1$ lowest threshold to just above the $3d^2\ ^3F^e_4$ threshold. The experimental spectrum was compared with a photoionization spectrum calculated using the same reaction matrices with $J_f = 1/2$–$5/2$ as those used to describe final states excited from the ground state. The only difference between these two calculations concerned the description of the initial state and thus the values of dipole matrix elements and transition frequencies. Figure 44 compares the unconvolved theoretical cross section and the measured Sc^+ ion signal in the wavelength range from the $3d4s\ ^3D^e_1$ threshold at 600.8 nm up to 540 nm, i.e., below the $3d4s\ ^1D^e_2$ ionization threshold at 521.2 nm. Most of the prominent sharp lines were ascribed by Armstrong and Robicheaux (1993) to $(3d4s\ ^1D^e_2)nf\ ^2P_{1/2}$, $(3d4s\ ^1D^e_2)nf\ ^2D_{3/2}$, and $(3d4s\ ^1D^e_2)nf\ ^2F_{5/2}$ Rydberg levels. In addition, in this wavelength range are the lowest members of the $(3d^2\ ^3F^e_{J_c})nf\ J_f$ Rydberg series corresponding to $n=5$ (588–585 nm) and to $n=6$ (545–542

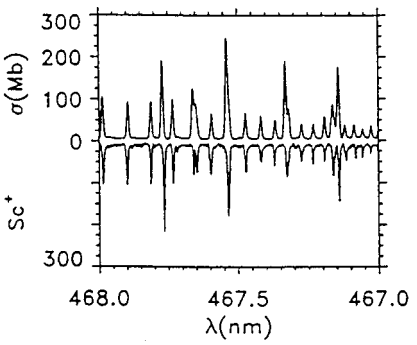

FIG. 45. Photoionization cross section of the Sc $3d^3\ ^2D^e_{3/2}$ excited level as a function of the wavelength of the photoionizing laser. The figure covers a small wavelength range below the $Sc^+\ 3d^2\ ^3F^e_2$ threshold at 466.2 nm, where the Rydberg series attached to the $3d^2\ ^3F^e_2$, $^3F^e_3$, and $^3F^e_4$ thresholds are interacting. The length theoretical cross section convolved with a Gaussian function of 0.4 cm^{-1} full width at half maximum is compared with the experimental ion signal, shown as a mirror image. (From Armstrong and Robicheaux, 1993, courtesy of F. Robicheaux.)

nm), as well as the $(3d^2\ ^3P^e)5p\ ^4P^o$ and $(3d^2\ ^3F^e_2)7p$ perturbing states near 582 nm. These perturbers are broader than the $(3d4s\ ^1D^e_2)nf$ resonances. The measured and calculated cross sections agreed quite well overall. It should be noted that the theoretical cross section was obtained from short-range scattering parameters and dipole matrix elements that were calculated before the experiment was completed. The most marked disagreement in resonance location between experiment and theory visible on Fig. 44 appears near $\lambda = 573.6$ nm. However, the corresponding $(3d4s\ ^1D^e_2)8f\ ^2F^o_{5/2}$ level has an error in its quantum defect of only ~ 0.01–0.02, relative to the experiment.

Similar good agreement was found at shorter wavelengths for the series converging to the $3d4s\ ^1D^e_2$ threshold. Above the $3d4s\ ^1D^e_2$ threshold, the positions of the resonances that belong to the various $(3d^2\ ^3F^e_{J_c})nf\ J_f$ interacting Rydberg series were also in very good agreement. The most pronounced disagreement was found for the $(3d^2\ ^1D^e_2)4f$ broad perturber, which corresponds to a low-n level, whose position is very sensitive to the accuracy of the calculation. In Fig. 44 the calculated spectrum was unconvolved. In a wavelength range involving high-n resonances, a better comparison between theory and experiment was achieved by convolution of the theoretical spectrum with the laser line width. Figure 45 shows a small portion of the cross section where the spectrum has been convolved with a Gaussian line profile of 0.4 cm^{-1}. This figure displays the interacting Rydberg series attached to the three $3d^2\ ^3F^e$ thresholds. The $(^3F^e_2)nf$ ($n \sim 44$ near the middle of the figure) series is perturbed by the $(^3F^e_3)\ nf$ states with n=27 to 30 and by the $(^3F^e_4)\ nf$ states with n=21 and 22. The positions and shapes of the peaks are accurately reproduced by the calculation.

Armstrong and Robicheaux (1993) also compared the photoionization cross sections from the $3d4s^2\ ^2D^e_{3/2}$ ground level and from the $3d^3\ ^2D^e_{3/2}$ excited level in the range from the lowest $3d4s\ ^3D^e_1$ threshold to just above the $3d^2\ ^3F^e$ thresholds. The photoionization cross section differs greatly for the two initial states. In particular, the cross section from the $3d^3\ ^2D^e_{3/2}$ state is dominated by f-wave resonances; this is expected owing to dominance of the one-electron dipole matrix element for the $3d \rightarrow nf$ excitation over the $3d \rightarrow np$ and $4s \rightarrow np$ excitations. Consequently, the cross section from the $3d^3\ ^2D^e_{3/2}$ level consists of mostly symmetric sharp lines except for some of the broad perturbers, while the cross section from the ground state displays many asymmetric Beutler-Fano profiles (Fano, 1961).

2. Titanium

The progress achieved by eigenchannel R-matrix calculations for Sc (Armstrong and Robicheaux, 1993; Robicheaux and Greene, 1993c, 1993d) led Miecznik and Greene (1996) to tackle the theoretical description of titanium, the second transition-metal atom, whose ground state is $3d^24s^2\ ^3F^e_2$. Photoabsorption and photoionization spectra were calculated from the four excited levels $3d^2(^3F^e)4s4p(^3P^o)\ ^3D^o_2$, $3d^2(^3F^e)4s4p(^3P^o)\ ^3G^o_{3,4}$, and $3d^3(^4F^e)4p\ ^5F^o_5$, whose cross sections were measured (Page and Gudeman, 1990; Sohl *et al.*, 1990). (Below, those initial levels will be referred to as the $3d^24s4p\ ^3D^o_2$, $3d^24s4p\ ^3G^o_{3,4}$, and $3d^34p\ ^5F^o_5$ levels.) The theoretical description of Ti, like Sc, is complicated by the large number of closely-spaced ionic target states. These cause irregularities in the pattern of interacting Rydberg series that converge to those target states as the principal quantum number increases. The first 15 LS-coupled states of Ti^+ have even parity and lie within 25 000 cm^{-1} above the Ti^+ ground state. All these states correspond to different LS terms of either the $3d^24s$, $3d^3$, or $3d4s^2$ configuration. Fine-structure effects were incorporated through the jj-LS frame transformation and the use of experimental (fine-structure-split) ionization thresholds. When fine-structure effects were taken into account, there were 34 even-parity ionization thresholds associated with the 14 LS-coupled target states relevant to the study, i.e., more than twice as many as in Sc^+. The lowest odd-parity $3d^24p$ thresholds lie above 25 000 cm^{-1}. Additional complications result from the presence of four electrons in the nearly degenerate $3d$ and $4s$ subshells. One major motivation of the Ti project was to investigate whether the eigenchannel R-matrix could overcome those additional difficulties and achieve an accuracy comparable to that found for Sc. Comparisons of the theoretical cross sections with the spectra measured by Sohl *et al.* (1990) and by Page and Gudeman (1990) were used to test the accuracy of the calculations. As discussed above in Sec. III.D, Miecznik and Greene (1996) adopted an all-electron (21) Hamiltonian to describe Ti^+, in order to account for the crucial complications of the Ti atom. They also developed a new method to generate radial

orbitals that incorporated the mutual screening and correlation of all electrons in the targets. In contrast with most of the earlier eigenchannel R-matrix calculations, radial orbitals were obtained in a multiconfiguration Hartree-Fock approximation (Froese Fischer, 1977) that directly generated natural orbitals for the target states.

Eigenchannel R-matrix calculations were performed in LS coupling using a box of radius $r_0=16$ a.u., which was large enough to enclose the charge distribution of the four odd-parity initial levels. Calculations were carried out for even-parity final states from -500 cm^{-1} to 8000 cm^{-1} relative to the first ionization threshold $3d^24s\ ^4F^e_{3/2}$. The four LS-coupled thresholds lying in this energy range are: $3d^24s\ ^4F^e$, $3d^3\ ^4F^e$, $3d^24s\ ^2F^e$, and $3d^24s\ ^2D^e$, in order of increasing energy. As for all open-shell atoms, the calculation began with the construction of target-state wave functions. As in Sc, the lower odd-parity ionic states were found to play a large role in Ti dynamics, primarily through their influence on the polarizabilities of low-lying even-parity levels of Ti^+. Target states were constructed from multiconfiguration Hartree-Fock orbitals that gave the fastest convergence for all even-parity Ti^+ states below 25 000 cm^{-1} and for some lowest-lying $3d^24p$ odd-parity Ti^+ states. The even- and odd-parity target states, the odd-parity initial states, and the even-parity final states were computed using configuration interaction. The $3d^24s(^2F^e)4p$ and the $3d^24s(^4F^e)4p$ configurations were found to contribute strongly to the wave functions of the $3d^24s4p\ ^3D^o$ and $3d^24s4p\ ^3G^o$ initial states. On the other hand, the $3d^24s4p$ components were negligible in the $3d^34p\ ^5F^o_5$ initial state.

Construction of the jj-coupled short-range reaction matrices for final J_f values ranging from $J_f=1$ to $J_f=6$ required LS-coupled eigenchannel R-matrix calculations to be carried out for 19 LS symmetries. Open and weakly closed channels for final even-parity symmetries were constructed by attaching s-wave and d-wave orbitals to the even-parity configuration-interaction target states. Besides these channels, a large number of strongly-closed channels were included in the calculations. They were constructed by attaching p-wave and f-wave orbitals onto the odd-parity configuration-interaction target states. Additional four-electron correlation functions were also included in the final-state wave-function expansions.

The photoabsorption and photoionization cross sections from the $3d^24s4p\ ^3D^o_2$, $3d^24s4p\ ^3G^o_3$, and $3d^24s4p\ ^3G^o_4$ levels were compared with the experiment of Sohl *et al.* (1990). This experiment probed the energies both above and below the first ionization threshold $3d^24s\ ^4F^e_{3/2}$ because of the presence of a weak external field that lowered the ionization barrier. The final states were in the energy range of the fine-structure-split $3d^24s\ ^4F^e_j$ and $3d^3\ ^4F^e_j$ thresholds. Highly-excited Rydberg levels with principal quantum numbers $n\geqslant 19$ converging onto the $3d^24s\ ^4F^e_j$ thresholds were recorded. Figure 46 compares the calculated spectrum for photoabsorption from the initial $3d^24s4p$ $^3G^o_4$ state with the experimental spectrum recorded by of Sohl *et al.* (1990). The theoretical cross section was preconvolved (Robicheaux, 1993) with the experimental resolution of 0.6 cm^{-1}. Figure 46 deals with the energy range just below the $3d^24s\ ^4F^e_{7/2}$ threshold, where the dominant Rydberg series are the $(3d^24s\ ^4F^e_{7/2})nd$ and $(3d^24s\ ^4F^e_{9/2})nd$ series. Good agreement between theory and experiment is apparent over the whole energy range. The differences between the measured and calculated quantum defects of the dominant $(3d^24s\ ^4F^e_{7/2})nd$ resonances are about 0.03. The theoretical cross section in Fig. 46 is a 15-channel calculation that includes closed channels converging to the $3d^24s\ ^4F^e_{J_c}$, $3d^3\ ^4F^e_{J_e}$, and $3d^24s\ ^2F^e_{J_c}$ thresholds. This cross section was compared with that obtained in a six-channel calculation that included only channels associated with the $3d^24s\ ^4F^e_{J_c}$ targets. The widths, line-shape parameters q (Fano, 1961) and strengths of the resonances were very different in the two calculations. Indeed, Miecznik and Greene (1996) found that a broad perturber at $\sim$55 259 cm^{-1}, ascribed to the $(3d^24s^2F^e)6d\ ^1H^e_5$ level, strongly modified the resonances over a very wide energy range, including the range displayed in Fig. 46.

Miecznik and Greene (1996) also compared the calculated photoionization cross section of the $3d^34p\ ^5F^o_5$ level with the experimental data of Page and Gudeman (1990), at energies below the $3d^3\ ^4F^e_{9/2}$ threshold. The

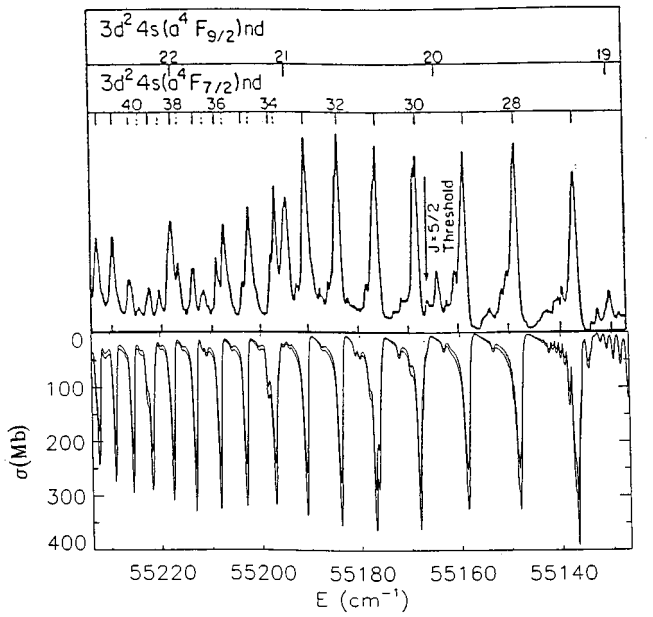

FIG. 46. Photoionization cross section of the Ti $3d^24s4p\ ^3G^o_4$ excited level as a function of the energy relative to the Ti ground level $3d^24s^2\ ^3F^e_2$. The experimental measurement of Sohl *et al.* (1990) (upper curve) is compared with the jj-LS result, shown as a mirror image; the theoretical cross section has been convolved with the experimental resolution of 0.6 cm^{-1}. The two theoretical lines are length and velocity results. (From Miecznik and Greene, 1996).

calculation reproduced the positions of the major experimental peaks, the $(3d^3\ ^4F^e_{9/2})nd$ resonances, but the agreement was poorer for intensities and widths.

The experimental excited-level cross sections of Sohl *et al.* (1990) and Page and Gudeman (1990) covered energies only slightly (1215 cm^{-1}) above the Ti^+ ground state. Miecznik and Greene (1996) predicted photoionization cross sections of the same excited levels at higher energies up to 8000 cm^{-1} above that lowest ionization threshold. This calculation extended nearly up to the energy of the fourth LS-coupled $3d^24s\ ^2D^e$ threshold at 8505 cm^{-1}. The dominant Rydberg series occurring in photoionization spectra of the four different initial levels were classified by Miecznik and Greene (1996). The similarities and differences among the spectra from different initial levels were interpreted using simple arguments based on the selection rules for the dipole operator and on the configuration-interaction expansions of the initial states. The photoionization cross sections of the $3d^24s4p\ ^3D^o_2$ and $3d^24s4p\ ^3G^o_{3,4}$ excited levels are dominated by the $(3d^24s\ ^4F^e)nl$ and $(3d^24s\ ^2F^e)nl$ resonances. The $(3d^3\ ^4F^e)nl$ resonances, which are very weakly excited from the $3d^24s4p\ ^3D^o_2$ and $3d^24s4p\ ^3G^o_{3,4}$ excited levels, dominate the photoionization cross sections of the $3d^34p\ ^5F^o_5$ level. The cross sections of the $3d^24s4p\ ^3D^o_2$ and $3d^24s4p\ ^3G^o_{3,4}$ excited levels exhibit similar features at most final-state energies. This results from the fact that all those initial states have the common configuration $3d^2(^3F)4s4p(^3P)$ and differ only in the LS-term value. Moreover, the comparable strength of the $(3d^24s\ ^4F^e)nd$ resonances and the $(3d^24s\ ^2F^e)nd$ resonances could be understood as resulting from the near equality of contributions from the $(3d^24s\ ^4F^e)4p$ and $(3d^24s\ ^2F^e)4p$ components in the initial-state configuration-interaction expansions. Miecznik and Greene (1996) found that below the fourth threshold, the autoionizing resonances converging to the four LS-coupled lowest-lying thresholds were not the only ones present. Other low-lying members ($n \leqslant 6$) of resonant Rydberg series attached to higher-lying thresholds were intense and had large widths. Additional short-range $3d^24p^2$ perturbers also arose. A major resonance peak in the cross section from the $3d^34p\ ^5F^o_5$ level, for instance, was ascribed to the $3d^2(^3P^e)4p^2(^3P^e)\ ^5D^e$ level. The presence of all those perturbers complicates the spectra tremendously at higher-energies, causing extremely complex interference patterns. Miecznik and Greene (1996) estimated the error in quantum defects for Rydberg levels to be at most 0.03, which translates as an error of $\sim$100–200 cm^{-1} for the low-n perturbers. Nevertheless, additional experimental tests of the predictions remain desirable.

The Sc and Ti results are prototype demonstrations that show the capabilities of LS-coupled eigenchannel R-matrix calculations combined with frame-transformation methods and multichannel quantum-defect theory. The fact that the complicated electron dynamics of Sc and Ti could be unraveled bodes well for future efforts in the other transition-metal elements, which are still more complicated. It is important to maintain or improve the level of accuracy, i.e., to limit the error in quantum defects to $\sim$ 0.03. Otherwise it will be difficult to obtain a sensible theoretical description for open-shell atoms with more d electrons. This will pose a difficult challenge for future calculations.

C. Concluding remarks

Theoretical multichannel spectroscopy can describe the complicated dynamics of open p-subshell atoms with $Z \leqslant 53$ near the lower ionizations thresholds. Calculations have traced out systematic trends in the Rydberg dynamics of chemically similar elements. The approach was also successful in unraveling the extremely complicated dynamics of the simplest transition metals Sc and Ti. The jj-LS frame-transformation treatment has been surprisingly successful at the description of a class of spin-orbit effects that are important at energies near fine-structure-split thresholds. In short, these results show that the eigenchannel R-matrix method can be used to obtain reliable photoionization spectra and classifications of the resonances even for extremely complicated spectra such as those of Sc and Ti. Despite its notable successes, the frame-transformation treatment does have some limitations, however. Examples visible from the calculations in open p-subshell atoms include the bound-level spectra of Ge and Sn (see Sec. V.A.3). The study of the halogen atoms showed the need for an intermediate-coupling frame transformation when the target states do not have definite values of the total orbital L and spin S angular momenta (see Sec. V.A.2). In addition, once the spin-orbit splittings of core levels exceed about 1 eV, as in the iodine calculations, a more satisfactory description of spin-orbit effects begins to become imperative. A ubiquitous phenomenon, which plagues theoretical multichannel spectroscopy of open-shell atoms and limits its ultimate capability to describe highly complex spectra, is the presence of numerous low-n perturbers located near the bottom end of Rydberg series converging to higher thresholds. An accurate description of these perturbing levels is needed because even a small error in quantum defect can eliminate all resemblance between the theoretical spectrum and experiment. As in alkaline earths, one way to improve upon the jj-LS frame-transformation approximation, and to achieve a better description of low-n perturbers, is to include the spin-orbit interaction within the reaction volume and to perform the variational calculations in jj coupling. The LS-coupled eigenchannel R-matrix calculations carried out for open-shell atoms were relatively modest and were carried out on desktop workstations. Calculations in jj coupling would probably be more appropriate for a high-speed supercomputer, especially for a transition-metal or lanthanide atom.

A number of calculations for open-shell atoms have been conducted with other theoretical approaches. The most widely used has been the Wigner-Eisenbud-type R-matrix approach that was developed by the Belfast group (Burke and Robb, 1975). For references, the

reader is referred to the comprehensive R-matrix compilation volume that was written recently by Burke and Berrington (1993). Most of the calculations have so far treated atoms and ions with atomic number below 20. In particular, we cite the extensive calculations of accurate radiation absorption and emission properties carried out in the framework of the worldwide "Opacity Project" of Seaton and co-workers (Seaton, 1987a; Berrington *et al.*, 1987, and subsequent papers referred to as "atomic data for opacity calculations"). In that framework, the R-matrix method provided the energies and wave functions of bound states, oscillator strengths, photoionization cross sections, and parameters for line broadening by electron impact. Calculations were obtained on a large scale for neutral atoms as heavy as neon, and for their isoelectronic sequences. Calculations for ions of cosmically abundant elements containing more than 10 electrons are planned. Some have already been carried out, such as the investigation by Le Dourneuf *et al.* (1993) of Fe^+ photoionization. Theoretical calculations of the "Opacity Project" are being used to obtain improved values for the opacity of stellar envelopes; these should be of interest across a range of problems in physics and astronomy (Zeippen, 1995).

Apparently, the number of theoretical photoionization calculations performed for the open d-subshell elements has been relatively small. In addition to the calculation of Fe^+ photoionization (Le Dourneuf *et al.*, 1993), electron impact ionization of Cr and electron impact excitation of Fe^+ have been investigated by Reid *et al.* (1992) and Pradhan and Berrington (1993), respectively. Moreover, photoionization of Zn and Hg were studied by Bartschat and co-workers (Bartschat and Scott, 1985a, 1985b; Bartschat, 1987). In these last two calculations mentioned, the $3d$ subshell in Zn or the $5d$ subshell in Hg is closed for the ground state only, but not in some target states included in the calculations.

The large number of channels has limited most Wigner-Eisenbud-type R-matrix calculations to a strictly nonrelativistic approximation, i.e., neglecting all fine-structure effects. However, Scott and Burke (1980) developed a Breit-Pauli R-matrix formulation and applied it to the study of electron impact excitation of Fe^+ (Pradhan and Berrington, 1993). Photoionization of Zn and Hg was also investigated with this approach (Bartschat and Scott, 1985a, 1985b; Bartschat, 1987).

VI. CONCLUSIONS AND PERSPECTIVES

Theory has developed a new capability in recent years: the capability to calculate and interpret atomic spectra of unprecedented complexity. The set of techniques used is termed multichannel spectroscopy. The term is intended to convey the notion that many of the tools of multichannel collision theory, such as the scattering matrix, remain applicable even in the presence of closed channels, provided the tools are suitably generalized.

Some of these tools were initially introduced from a phenomenological or semiempirical viewpoint, but theory has progressed to the point that key quantities such as R matrix or the S matrix can now be calculated from first principles. One technique that is particularly well suited to carry out such nearly *ab initio* calculations is the R-matrix method; it has been discussed at length in this review. While our examples have been drawn primarily from the eigenchannel version of R-matrix theory, this is a "detail" that remains largely a matter of preference. Indeed, the most important details are not whether the eigenchannel or Wigner-Eisenbud variants of R-matrix theory are used; these two variants have in fact been shown to be exactly equivalent if identical basis sets are used in both calculations. Other theoretical methods, such as the Schwinger variational principle (Schwinger, 1947) or the complex Kohn variational principle (Kohn, 1948) can also describe complicated spectra, in principle. Applications of these methods to multichannel Rydberg spectra can be expected to be relatively inefficient, however, if they are not extended to take advantage of scattering theory ideas in closed Rydberg channels; this is a huge simplification exploited by multichannel quantum-defect theory. Aside from the flexibility of the theoretical formulation adopted, the most important detail that controls the likely success of any given calculation is the choice of the type (and number) of variational basis functions, and on the actual physics included in the real or model Hamiltonian of the system.

Multichannel spectroscopy is a theoretical description that not only determines complex spectra, but which also obtains the amplitudes and phases for ejection of an electron (or other particle) into the various accessible channels that are open or weakly closed. The information contained in this set of intermediate quantities, namely the smooth short-range scattering parameters $\underline{S}$ and $\underline{d}$ used by multichannel quantum-defect theory, considerably enhances the predictive power of multichannel spectroscopy. Knowledge of the "short-range" scattering matrix implies a far more detailed understanding of the final-state dynamics than can be extracted from a single total or partial cross section spectrum.

Inclusion of the relativistic spin-orbit interaction at different levels of approximation enhances the capability of multichannel spectroscopy to describe high-lying Rydberg levels near fine-structure-split ionization thresholds. Impressive agreement between theory and experiment has been obtained for extremely complicated spectra, including the perturbed pattern of alkaline-earth atom autoionizing states at high energies within 0.02 a.u of the double-escape threshold. Even the complex autoionizing spectra of some transition-metal elements have been calculated to spectroscopically useful accuracy. In Sc and Ti, for instance, errors in the calculated scattering parameters were found to be small at energies far from perturbers: errors in the calculated quantum defects were typically less than ~ 0.03. Near a perturber, however, quantum-defect errors can be larger because the low value of the perturber principal quantum number n magnifies the error in the perturber binding energy according to $\Delta E \approx \Delta\mu/n^3$. This problem appears to be ubiquitous in the heavy open-shell atoms,

because the large density of ionization thresholds generates many perturbing levels in any given energy range.

Accurate results have been obtained for other observables besides energy-level positions and total photoionization cross sections. These include anisotropic observables more sensitive to electron correlations and spin-orbit effects, such as the angular distributions of electrons ejected from alkaline-earth atom autoionizing levels. Multichannel spectroscopy has capabilities that extend beyond the accurate reproduction of experimental spectra. It also permits classification of observed resonance structures and a detailed analysis of the mechanisms (such as the dominant channel couplings and autoionization pathways) that govern the Rydberg-electron dynamics. It also provides a powerful way to elucidate global trends and systematics in the electron correlations and channel interactions. Despite the inherent complexity of multichannel spectra, the underlying short-range dynamics of these spectra often exhibit remarkable simplicity, and are usually controlled by a small number of physical parameters. This review highlights the extent to which spectral regularities and channel-interaction invariances are revealed despite the seemingly intractable complexity of the cross sections. Numerous spectral regularities occur along the series of alkaline-earth atoms and along the series of chemically similar open p-shell atoms. Likewise, the complicated electron dynamics in scandium and titanium present visible similarities.

The numerous examples in this review have concentrated on the alkaline earths and on some open-shell atoms. These examples share one thing in common: an attractive Coulombic long-range potential is experienced in each channel by the lone escaping electron. The examples have also dealt with field-free photoionization spectra excited by one photon from the ground state or an excited state. To convey a glimpse of the generality of these methods, we turn now to a few applications of theoretical multichannel spectroscopy to a broader class of systems and processes. Some results obtained by other powerful approaches will also be mentioned. Possible extensions that are suggested by the success of some of these calculations are commented upon. We also draw attention to limitations of these methods.

We begin with systems for which the long-range electron-core interaction differs from an attractive Coulombic (plus centrifugal) potential; this category includes He, H^-, and other negative ions. In H^-, an escaping electron experiences a $1/r^2$ dipole potential at large r. This unusual dipolar character results from the permanent electric dipole moment that is established in the excited hydrogen fragment $H(n)$ by the electric field of the outer electron. This dipole moment is essentially "permanent" in this context rather than "induced," owing to the approximate degeneracy of the excited $H(n)$ thresholds. Moreover, the effective dipole interaction is attractive in some channels, which generates an infinite number of levels converging to the corresponding threshold. In other channels the dipole moment repels the outermost electron. In He, the long-range potential in each channel has a combined Coulomb and dipole character. For negative ions other than H^-, the escaping electron usually experiences a long-range polarization potential whose asymptotic form is $-\alpha/2r^4$, with α the atomic polarizability when the core is isotropic. For anisotropic core states a channel-dependent polarizability emerges that depends on both the scalar and tensor polarizabilities of the corresponding atomic states. Multichannel spectroscopy accounts for long-range multipole interactions beyond the reaction volume in H^-, He, and negative ions, either through the use of quantum-defect theory, generalized to account for the relevant long-range potential (Greene *et al.*, 1979, 1982; Watanabe and Greene, 1980), or else by direct integration of the close-coupling equations without exchange (Pan *et al.*, 1994).

The first eigenchannel R-matrix calculation for negative ions was carried out for the alkaline-earth negative ions (Kim and Greene, 1989). Three-electron LS-coupled eigenchannel R-matrix calculations were combined with a generalized one-channel quantum-defect treatment of long-range motion in a dipole polarization potential. The calculation of Kim and Greene (1989) concurred with the earlier prediction by Froese Fischer *et al.* (1987) that Ca^- has a stable negative-ion state $4s^24p$; both of these early calculations overestimated the Ca electron affinity by about a factor of 2, judging from recent experiments (see, for example, Walter and Peterson, 1992). It is not surprising that theory struggles to predict the Ca electron affinity accurately, since it is so small ($\approx$20 meV). The most successful theoretical calculation to date of the Ca^- binding energy is the semiempirical model-potential calculation of van der Hart *et al.* (1993), who include the dielectronic polarization term. After adjusting the "cutoff" radius to obtain an accurate ground-state energy of neutral calcium, van der Hart *et al.* (1993) then used the resulting dielectronic term in their calculation of Ca^- to obtain a binding energy that agreed well with experiment. Kim and Greene (1989) also predicted that the heavier alkaline-earth atoms Sr, Ba, and Ra would have stable negative ions, of similar $m_o s^2 m_0 p\ ^2P$ designation, whereas the corresponding Be^- and Mg^- states are unstable shape resonances. New experimental results for Ba^- show that most calculations overestimated the strength of binding by about a factor of 2 (Petrunin *et al.*, 1995).

This class of theoretical techniques was also extended to treat the photodetachment spectra of the alkali negative ions. Nonrelativistic close-coupling calculations by Moores and Norcross (1972, 1974) derived realistic results for photodetachment of Li^- and Na^- up to the energy of the first excited alkali energy level m_0p. For the heavier alkali negative ions, the experiments of Lineberger and co-workers (Patterson *et al.*, 1974; Slater *et al.*, 1978) showed prominent effects associated with the alkali m_0p fine-structure splitting, indicating the need for inclusion of spin-orbit effects into the theory. Lee (1975) developed a multichannel effective-range theory treatment that included fine-structure effects

through a frame transformation, along the lines of the earlier study of S^- photodetachment by Rau and Fano (1971). Lee's semiempirical fit was able to reproduce the measured (Patterson *et al.*, 1974) Cs^- photodetachment cross sections, and was influential because it was able to fit cross sections for other alkali negative ions. Moreover, the resulting fitted parameters permitted prediction of other quantities, such as partial detachment cross sections, which were confirmed by subsequent measurements. The formulation of Lee (1975) neglected the long-range potentials entirely. Taylor and Norcross (1986) calculated the smooth, short-range reaction matrix $\underline{K}^0$ that Lee (1975) had assumed to be energy independent across the 550 cm^{-1} fine-structure splitting of $Cs(6p)$, and discovered that $\underline{K}^0$ actually varied quite rapidly with energy. They showed, however, that the energy variation could be expressed as an energy-dependent long-range phase shift in each channel, which did not affect the total or partial cross sections. Watanabe and Greene (1980) used generalized quantum-defect theory to demonstrate that the strong energy dependence of $\underline{K}^0$ is caused by the huge polarizability ($\alpha \sim 10^3$ a.u.) of the $m_0 p$ excited state. Moreover, a different reaction matrix $\underline{K}^0_{\rm pol}$ could be defined that was nearly energy independent and better suited to the application of a fine-structure frame transformation.

Greene (1990a) combined a *jj*-coupled eigenchannel *R*-matrix calculation with the generalized MQDT treatment of electron escape in a polarization potential in the first nearly *ab initio* calculation able to reproduce the observed photodetachment spectra of the heavy alkali-metal negative ions. Resonant photodetachment spectra of Cs^-, Rb^-, and Fr^- were calculated near the lowest $m_0 s$ and $m_0 p$ thresholds, which are quite similar in all of these heavy alkali-metal negative ions. The calculation also predicted the existence of three Cs^- $6s6p\ ^3P^0_J$ states that are barely bound, in addition to the $6s^2$ ground state, in agreement with an earlier tentative conclusion reached by Froese Fischer and Chen (1989). A subsequent theoretical treatment of Cs^- bound states carried out by Thumm and Norcross (1991, 1992) disputed the stability of these Cs^- $6s6p\ ^3P^0_J$ levels. Thumm and Norcross calculated *e*-Cs scattering cross sections using a relativistic Wigner-Eisenbud-type *R*-matrix calculation based on the Dirac Hamiltonian, also using a model potential. Electron affinities of the Cs^- $6s^2\ ^1S^e_0$, $6s6p\ ^3P^o_J$, and $6p^2\ ^3P^e_J$ levels were calculated in two different ways: with and without the dielectronic term that represents an additional electron-core-electron interaction [Eqs. (3.34) and (3.40)]. Calculations carried out without the dielectronic term agreed with those of Greene (1990a), who omitted it from the model Hamiltonian. When the dielectronic term was included, however, the negative-ion spectrum was found to change dramatically: the $6s6p\ ^3P^o_J$ levels were shifted into the continuum, where they appeared as narrow shape resonances instead of as bound levels. These states are exceedingly close to threshold, so the question of whether they are bound states or resonances will probably not be resolved until they are investigated experimentally. For the present, though, the best calculation performed thus far is probably that of Thumm and Norcross (1991, 1992).

Sadeghpour and Cavagnero (1993) investigated the photoabsorption spectrum of He below the $n=3$ threshold with the *LS*-coupled eigenchannel *R*-matrix approach; the motion beyond the reaction volume utilized generalized quantum-defect theory (Greene *et al.*, 1982) for long-range potentials of Coulomb-plus-dipole form. Sadeghpour *et al.* (1992) combined an *LS*-coupled eigenchannel *R*-matrix calculation with a quantum-defect description of electron motion in a dipole field to predict the photodetachment spectrum of H^-, including resonant structures up to the $n=4$ hydrogenic threshold. Higher-lying doubly excited states of H^- up to the $n=6$ threshold were calculated by Pan *et al.* (1994), who adopted an *LS*-coupled eigenchannel *R*-matrix calculation. The reaction volume in this study extended out to $r_0=110$ a.u., but long-range coupling caused by the large core multipole moments required direct solution of the close-coupling equations in the outer region, instead of the economical (but approximate) quantum-defect method. This calculation accounted well for the experimental results of Harris *et al.* (1990). High-lying doubly excited states of Li^- were treated using the same procedures and found to be remarkably similar to the H^- resonance pattern, although some conspicuous differences were apparent.

This review has not explicitly discussed electron-ion and electron-atom scattering processes, although they have been studied extensively in Wigner-Eisenbud-type *R*-matrix calculations. Burke and Berrington (1993) published a survey of calculations carried out with the Belfast *R*-matrix packages. Relatively few calculations have been carried out using the eigenchannel *R*-matrix approach. One eigenchannel study was that of Pan (1991a, 1991b), who calculated electron collisions with Be^+, Mg^+, and Ca^+ ions at low energies. Pan developed a systematic and comprehensive analysis of the prominent and complicated series of double excitation of the collision complex. Pan's calculations also resolved a long-standing discrepancy between theory and experiment in the near-threshold excitation of the Be^+ resonance transition by electron impact.

More recently, Robicheaux *et al.* (1994) studied the controversial problem of *e*-H^- inelastic scattering above the triple-electron escape threshold. The main purpose of this investigation was to see whether H^{--} resonances (if they exist) could influence the scattering process. Experiment (Walton *et al.*, 1970, 1971; Peart and Dolder, 1973) and theory (Taylor and Thomas, 1972) had long ago presented evidence in support of this claim. To deal with this problem, it was necessary to extend the eigenchannel *R*-matrix method to describe approximately the effects of multiple-electron escape. The *R*-matrix calculation, conducted in parallel with a configuration-interaction study of the dependence of the $2s^2 2p\ ^2P$ resonance on the nuclear charge *Z*, led to a prediction that the previously observed (and calculated) H^{--} resonances could not exist. This prediction has since been

confirmed by a new experiment of Andersen *et al.* (1995), who observed no evidence for resonances in electron-scattering from the deuterium negative ion. (D^- is expected to behave the same as H^- in such electron scattering experiments.)

Following the lead of Robicheaux *et al.* (1994) in extending R-matrix methods to handle the double continuum $H+e+e$, Meyer and Greene (1994) calculated double photoionization of He by one-photon absorption in the energy range from the He^{++} double-escape threshold up to photon energies near 200 eV. The standard LS-coupled eigenchannel R-matrix method, applied previously to single photoionization only, was adapted to describe a class of two-electron escape processes. Although the boundary conditions imposed in the calculation appeared not to allow the possibility of direct electron escape into the double continuum, a realistic description of the He double-photoionization cross section, and of the ratio of double- and single-photoionization cross sections of He was obtained. The central idea was to distinguish among the closed-type orbitals used to represent the inner electron He^+ in a close-coupling expansion: those that had negative energies (relative to the double-escape threshold) were interpreted differently from those having positive energies. The He^+ eigenfunctions that had positive energies were viewed as representing a discretized continuum state of He, whereby all flux escaping in channels associated with a positive-energy inner electron was interpreted as contributing to double photoionization. All flux escaping in channels with a negative-energy inner electron was similarly associated with single photoionization. Pseudoresonances appeared in the double-photoionization cross section, owing to the artificial discretization of the He^+ continua. These artifacts of the finite-volume calculation were eliminated from the final spectrum by using two averaging techniques: (i) the weakly closed channels were treated as though they were open when the MQDT equations were solved to determine the photoionization cross section; (ii) the spectrum was calculated for a number of different values of the R-matrix box size r_0, and these results were averaged to determine the final spectrum that was compared with experiment. The basic ideas have been improved in a subsequent study by Meyer *et al.* (1995), through the introduction of a frame-transformation-type projection of the ''box eigenstates'' of the residual ion onto the true continuum states of the ion. Other methods have been proposed through the years to describe two-electron escape. One of these, the R-matrix theory for two active electrons proposed by Burke *et al.* (1987), might be able to describe two-electron continua and high-lying doubly excited states. An important step in its development was the Le Dourneuf *et al.* (1990) implementation of a two-dimensional R-matrix propagation procedure for an s-wave model (Temkin, 1962; Poet, 1978) of e-H scattering. Two formulations that have shown great promise are the convergent close-coupling approach of Bray and Stelbovics (1992, 1995) and the hyperspherical close-coupling approach developed by Kato and Watanabe (1995). Further theoretical effort is still needed, however, to overcome limitations of all these methods and to develop an efficient R-matrix method or other approach that can handle two escaping electrons.

Another source of extremely rich spectra that have been successfully described using theoretical multichannel spectroscopy is the system of a one- or two-electron atom in an external magnetic or electric field. The hydrogen atom in a magnetic field has attracted much attention. This and related systems have served as prototypes for the study of ''quantum chaos,'' i.e., the study of nonseparable quantum systems whose classical dynamics are chaotic. Nonseparability of the Schrödinger equation for hydrogen in a magnetic field becomes paramount near the zero-field ionization threshold. For states in that energy range, the cylindrically symmetric diamagnetic term (associated with the Lorentz force) achieves a strength comparable with the spherically symmetric Coulomb potential. In this situation, neither perturbative nor adiabatic treatments (Starace and Webster, 1979; Wang and Greene, 1989) can describe the extremely complicated diamagnetic spectra. However, the adiabatic treatment in cylindric coordinates by Wang and Greene (1989) correctly described some qualitative features of the quasi-Landau resonance spectra, such as the $\frac{3}{2}\omega_c$ spacing of resonances observed by Garton and Tomkins (1969a) and the existence of ''one-dimensional'' Rydberg states (Iu *et al.*, 1989) converging to the ω_c-spaced Landau ionization thresholds. Any convincing theoretical treatment must account for the strong interactions between these Rydberg series. As shown by Wintgen and Friedrich (1986, 1987) and by Wang and Greene (1991a), the quasi-Landau ''resonances'' can be viewed as broad perturbers embedded among densely packed high-Rydberg states that belong to series converging to lower-lying Landau thresholds; these quasi-Landau resonances interact with high-Rydberg states to form complex resonances. Moreover, destructive interferences occur periodically, resulting in the occurrence of resonances whose width nearly vanishes. Hydrogen photoionization in an astrophysical strong magnetic field was described by Greene (1983) and by Wang and Greene (1991b) using an eigenchannel R-matrix calculation augmented by a multichannel quantum-defect description of the asymptotic wave functions in cylindrical coordinates. The latter of these papers used a mixed-symmetry basis set that included spherical basis functions that could describe the important departures from cylindrical symmetry close to the nucleus. The R-matrix calculations carried out within a cylindrical R-matrix box determined the smooth short-range reaction matrix and dipole matrix elements that were then used to calculate the photoionization cross section on a fine energy mesh.

Wang and Greene (1991b) calculated photoionization spectra for superstrong magnetic fields $B \geqslant 10^3$ T. The calculation of MQDT parameters, needed to account for spectroscopic observations in magnetic fields relevant to terrestrial experiments ($B \sim 6$ T), is far more difficult because of the large number of interacting channels and

the large volume over which the Hamiltonian is nonseparable, a cylinder of radius $\approx 10^3$ a.u. and length $\approx 10^4$ a.u., for B=6 T. A variety of different methods have been developed to calculate the diamagnetic Rydberg spectra of atoms in a magnetic field of laboratory strength. Among them, the methods developed by Delande *et al.* (1991), O'Mahony and Mota-Furtado (1991), Watanabe and Komine (1991) or Halley *et al.* (1992, 1993), were used to interpret recent observations. Two of these calculations (O'Mahony and Mota-Furtado, 1991; Watanabe and Komine, 1991) determined a smooth short-range reaction matrix that characterizes the solutions in the cylindrical asymptotic region. This information was then used to calculate the photoionization cross section. Both of these approaches introduced a small spherical inner region where the Rydberg electron motion could be described by field-free MQDT parameters; they both solved the Schrödinger equation over a large region in spherical coordinates, and then made a spherical-to-cylindrical two-dimensional frame transformation at large distances. O'Mahony and Mota-Furtado (1991) connected the outer asymptotic region to the inner region using an R-matrix propagation scheme. Watanabe and Komine (1991) implemented the diabatic-by-sector method of Launay and Le Dourneuf (1982) to construct channel functions that were treated diabatically within each radial sector. Both methods achieved impressive agreement with the high-resolution spectra of Li in a magnetic field of 6 T (Iu *et al.*, 1989, 1991). Delande *et al.* (1991) calculated the photoionization cross section of hydrogen in a magnetic field by replacing $\vec{r} \rightarrow \vec{r} e^{i\theta}$, $\vec{p} \rightarrow \vec{p} e^{-i\theta}$ in the Hamiltonian and diagonalizing once and for all the complex rotated Hamiltonian $H(\theta)$ built on a large basis of roughly 10^5 Sturmian functions. Finally, Halley *et al.* (1992, 1993) combined the complex-coordinate method with a variant of the R-matrix method (Schneider, 1981) to interpret the high-resolution diamagnetic spectra of Li (Iu *et al.*, 1989, 1991) and of the heavier alkaline earths Sr and Ba (Lu *et al.*, 1978). This combination of the R-matrix and complex-coordinate methods was also successfully applied to interpret high-resolution diamagnetic spectra of He (Delande *et al.*, 1994) and Stark and diamagnetic spectra of Na (Seipp and Taylor, 1994). Furthermore, it remains the only method presently available to treat atoms in much more complex situations, such as in crossed electric and magnetic fields, where the asymptotic solution is not accurately known.

The complex-coordinate method (Ho, 1983) is emerging as one of the simpler alternatives that currently exist for calculations of the total photoabsorption spectrum, or of resonance positions and total decay widths. If a convenient basis set can be found for a problem with relatively few degrees of freedom, such as the Sturmian basis set for hydrogen in a magnetic field, it is relatively straightforward to form an enormous Hamiltonian matrix and solve for many of its eigenvalues and eigenvectors. Moreover, if the matrix turns out to be sparse, as is again true of the Sturmian basis set for hydrogen diamagnetism, the Lanczos algorithm (see Ericsson and Ruhe, 1980, and references therein) or its competitors can efficiently solve the eigenvalue problem even when the basis-set size grows to enormous dimensions. The main limitations of this method are: (i) It has been used almost exclusively for the calculation of *total* photoabsorption cross sections (see, for example, Berzinsh *et al.*, 1995). A limited number of attempts have been made to extract other observables, such as partial cross sections (Han and Reinhardt, 1995), but the ability of this method to compete with the techniques of multichannel spectroscopy for calculations of partial cross sections, angular distributions, and other observables has not yet been demonstrated. (ii) It is difficult to interpret the dynamics of the resulting wave functions, as the complex rotation of the coordinates modifies the continuum solutions in a nontrivial manner. It is possible that, as experience with this theoretical tool grows, the interpretive capabilities of this approach will improve. (iii) A final disadvantage of the complex coordinate method and its relatives is that they do not produce intermediate quantities, such as the smooth short-range scattering matrix of multichannel spectroscopy. As this review has shown, these tools can be decisive in the interpretation of the spectrum; they can readily predict any observables that it is possible to measure, and they can be utilized to predict the outcome of entirely new experiments, such as one with a new external field applied. The examples in the following paragraph describe this last capability. Nevertheless, when one is interested in a calculation of the total photoabsorption spectrum, say for comparison with an experimental measurement, the complex-coordinate approach is certainly one to consider, owing to its ease of implementation.

The problem of a nonrelativistic hydrogen atom in a static electric field can be solved exactly (Luc-Koenig and Bachelier, 1980a, 1980b) because the time-independent Schrödinger equation separates in parabolic coordinates. However, the Hamiltonian becomes nonseparable for a more complex atom in an electric field, since the potential of an electron departs from a pure Coulomb field within the core of a nonhydrogenic atom. The Stark spectra of autoionizing levels of nonhydrogenic atoms exhibit tremendous complexity and can be viewed as multichannel spectra (Harmin, 1984; Sakimoto, 1986). Extensive measurements and calculations of Ba autoionizing Stark spectra around the $5d_j$ ionization thresholds were reported recently (Armstrong *et al.*, 1993; Armstrong and Greene, 1994). The spectra were recorded by photoionization of the laser-excited Ba $5d6p\ ^3D_1$ level in the presence of an electric field. The theoretical description combined information from jj-coupled eigenchannel R-matrix calculations, performed for zero external field, with a Harmin-Fano-type field-dependent frame transformation (Harmin, 1984, and references therein). The calculations successfully reproduced the complex resonance patterns observed over broad spectral regions that included as many as six interacting Stark manifolds attached to the two different $5d_{3/2}$ and $5d_{5/2}$ ionization thresholds. The average widths of autoionizing Stark states were found

to scale approximately as ν^{-4}, ν being the relevant effective quantum number. However, large departures from this scaling law were observed for individual resonances, which could be important for the theoretical description of other processes in an electric field, such as dielectronic recombination (Jacobs and Davis, 1979; Nahar and Pradhan, 1992).

The statistics of resonance distributions in multichannel atomic and molecular spectra has been a subject of increasing interest in connection with ''quantum chaos'' studies. Statistical analyses of quantum-mechanical spectra have attempted to ascertain the extent to which the resonance positions and widths follow the predictions of random-matrix theory. Specifically, the statistical distributions of energy-level spacings (nearest-neighbor spacings) have been compared with the Wigner distribution, which applies when strong level repulsion results in few closely spaced levels. The resonance width distributions were compared with the Porter-Thomas distribution, whose form implies that small widths are by far the most probable (for references see Brody *et al.*, 1981, and Delande and Buchleitner, 1994). While portions of field-free autoionizing spectra were found to exhibit the Wigner and Porter-Thomas distributions of positions and widths (see, for example, Connerade *et al.*, 1990, and Miecznik *et al.*, 1995) there remain at the same time striking regularities and Rydberg periodicities in the pattern of resonance energies and decay widths. This work suggests that caution should be exercised before automatically interpreting ''classical chaos'' as reflecting ''quantal irregularity.'' Similar results were found for diamagnetic spectra: in the regions in which the classical dynamics is chaotic, the statistical properties of quantum spectra are accurately described by random-matrix theory (Grémaud *et al.*, 1993; Delande and Buchleitner, 1994); again, however, regular Rydberg progressions have been locally observed (Iu *et al.*, 1989, 1991) or predicted (Wang and Greene, 1991a, 1991b). In multichannel spectra, the distribution of nearest-neighbor spacings evolves from the Poisson to the Wigner distribution as the channel coupling increases (Draeger and Friedrich, 1991). Moreover, extremely narrow resonances typical of the Porter-Thomas distribution appear periodically in the vicinity of each broad interloper of Rydberg series, owing to destructive interferences between autoionization pathways associated with different closed channels (Wintgen and Friedrich, 1986, 1987; Wang and Greene, 1991a, 1991b). This implies that complex spectra (which may or may not reflect classical chaos) need not be totally irregular, random, and unpredictable, but can possess similar statistical properties. In fact, as discussed recently (Ivanov *et al.*, 1995; Zakrzewski *et al.*, 1995) for two-electron atoms and hydrogen in a magnetic field with classical chaotic dynamics, even close to an ionization threshold, there remain regions in the classical phase space where an approximate adiabatic separation of the motion along two coordinates exists that can induce deviations from random-matrix theory.

This review has primarily treated photoionization spectra associated with single-photon absorption from the ground state or from a laser-prepared excited state. One striking difference between the one-photon and multiphoton cross sections is the greater prominence of resonances in the latter process. In multiphoton ionization cross sections, Rydberg series of resonances can arise at each intermediate or final step of the process. Interest in the description of multiphoton processes in multielectron atoms continues to grow. Most theories have dealt with nonresonant processes and have calculated multiphoton ionization cross sections using perturbation theory at the lowest order. Fink and Zoller (1989) proposed a multichannel quantum-defect parametrization of perturbative two-photon ionization cross sections, in the presence of intermediate- and final-state resonances, suitable for use with *ab initio* calculations. Retaining the ideas of Fink and Zoller (1989), Robicheaux and Gao (1991, 1993) developed an efficient method for calculating perturbative two-photon ionization cross sections based on variations of the eigenchannel R-matrix method and multichannel quantum-defect theory. The method was applied to two-photon ionization of the Mg and Ca ground states. A relativistic time-dependent Dirac-Fock approach combined with multichannel quantum-defect theory was used by Fink and Johnson (1990) to calculate two-photon ionization cross sections of the rare gases. One of the first results obtained by the Belfast group with the Wigner-Eisenbud form of the R-matrix method concerned its applicability to the calculation of the infinite summations over intermediate states involved in dynamical dipole polarizabilities (Allison *et al.*, 1972). Later, Shorer (1980) and then Smith *et al.* (1992) extended the codes of the Belfast group to the calculation of two-photon excitation and ionization. Applications to Ne, Be, and C atoms were presented. A configuration-interaction formulation, suitably extended to incorporate field-induced effects, was used by Lambropoulos *et al.* (1988) to interpet experimental observations on multiphoton ionization in Sr. Configuration-interaction approaches using L^2 basis sets were used to calculate multiphoton ionization (detachment) cross sections in H^-, He, Be, and Mg (Moccia and Spizzo, 1989; Chang and Tang, 1992; Sánchez *et al.*, 1995, and references therein). The study of atomic systems interacting with intense laser fields has attracted considerable interest in recent years. Among the nonperturbative methods developed to treat multiphoton processes accounting for strong-field effects, the R-matrix-Floquet theory developed by Burke and coworkers (Burke *et al.*, 1991; Dörr *et al.*, 1992, 1993) looks very promising.

Photoionization spectra investigated with the eigenchannel R-matrix approach have been restricted to treatments of valence-shell photoionization. However, the subject of atomic inner-shell photoionization continues to be of great interest to both experimenters and theorists. For instance, inner-shell photoabsorption spectra of alkaline-earth elements exhibit various anomalies that reveal strong correlation and spin-orbit effects (Connerade *et al.*, 1990; Connerade and Sarpal,

1992). The great majority of eigenchannel R-matrix photoionization calculations used a frozen-core model potential to account for the effects of the closed shells. Theoretical investigation of inner-shell photoionization in alkaline-earth atoms would require an *ab initio* description of all electrons, as was used in eigenchannel R-matrix calculations of the chalcogen (Chen and Robicheaux, 1994) and Al (Miecznik *et al.*, 1995) outer-shell photoionization cross sections. Many successful calculations of photoionization spectra involving inner-shell excitation have been carried out using powerful methods such as the relativistic random-phase approximation, many-body perturbation theory, or the Wigner-Eisenbud-type R-matrix approach (for references see Starace, 1982; Kelly, 1987, and Burke and Berrington, 1993).

We address now the description of relativistic effects. As shown in Secs. IV and V, the jj-LS frame-transformation treatment was found to be very successful in describing numerous nonperturbative spin-orbit effects in some atoms as heavy as barium or as complicated as titanium. Despite the clear success of the approximate frame-transformation treatment, examples were found for two-electron systems in which the jj-coupled eigenchannel R-matrix calculations (which include explicit spin-orbit terms in the Hamiltonian) gave improved agreement with measurements. Although among the relativistic effects only the spin-orbit terms are included explicitly, we believe that numerous other relativistic effects, such as the mass-velocity and Darwin terms, are implicitly taken into account (at least approximately) through the use of a semiempirical one-electron model potential (Greene, 1990a; Greene and Aymar, 1991). The jj-coupled eigenchannel R-matrix approach has not yet been extended to treat open-shell atoms, though we anticipate that it should give improved results, for instance in heavy open p-shell atoms. The possibly surprising success of this non-Dirac description of relativistic valence-electron dynamics probably stems from the fact that photoabsorption (or photodetachment) mainly probes the details of the wave functions beyond $\sim$ 1 a.u. from the nucleus. Poorer theoretical results are anticipated for short-range observables such as hyperfine splittings. A more correct, but also much more complex, way to treat relativistic effects is to use the Dirac Hamiltonian. A relativistic version of the eigenchannel R-matrix method based on the Dirac Hamiltonian was formulated by Hamacher and Hinze (1991), but no application was reported. Wigner-Eisenbud-type R-matrix approaches based on the Dirac Hamiltonian have been developed by Chang (1975, 1977), Norrington and Grant (1981), and by Thumm and Norcross (1991, 1992). To our knowledge, these methods have been applied only to electron-scattering calculations. A relativistic R-matrix treatment would be useful in its own right, and to check the validity of the predictions obtained for Fr^- (Greene, 1990a) and Ra (Greene and Aymar, 1991). This would also be a natural tool for investigations of photoionization and electron-scattering processes involving multicharged positive ions. In this review, we have considered electric dipole transitions only; the study of magnetic and higher-order electric dipole transitions in heavy multicharged positive ions could also be profitably studied using a relativistic R-matrix description.

Despite the great amount of progress in multichannel-spectroscopy theory, improvements are still desirable in a number of directions: (i) To reach higher energies very close to thresholds for escape of two or more electrons, for instance, one must adopt a very large reaction volume. The convergence of calculations deteriorates rapidly as the size of the reaction volume grows, which renders intractable the type of basis-set-based variational calculations emphasized in this review. New concepts will be required to handle that regime, such as the promising hyperspherical close-coupling method (Tang *et al.*, 1992), which has obtained accurate results for helium. (ii) Titanium is the most complicated atomic system that has been studied using the eigenchannel R-matrix approach. More complicated spectra, such as those involving an open $4f$ (lanthanides), $5f$ (actinides), or $4d$ subshell, present a serious challenge for theory. The description of these elements remains a difficult undertaking for the future. (iii) The use of these techniques to treat molecular species, i.e., combining *ab initio* R-matrix calculations with multichannel quantum-defect theory, have been rare (Stephens and McKoy, 1992; Greene and Yoo, 1995) and still require substantial improvement in order to develop a scheme for calculations that is spectroscopically accurate. (iv) The development of improved methods for interpretation and visualization of the quantum dynamics of multichannel spectra remains a key task as well. Tremendous insight has been gained in some classes of few-body systems through the use of adiabatic hyperspherical methods (Fano and Rau, 1986; Lin, 1995) yet their extension to each new type of quantum-mechanical system still requires great effort.

ACKNOWLEDGMENTS

We would like to thank Jean-Marie Lecomte and Gregory Miecznik for their careful reading of parts of the manuscript and for their helpful comments. Some of the numerical calculations were carried out on the Cray 98 belonging to the ''Institut du Développement et des Ressources en Informatique Scientifique'' of the Centre National de la Recherche Scientifique and on the Cray YMPEL of the computer center ''Paris Sud Informatique.'' The laboratoire Aimé Cotton is associated with the Université Paris-Sud. This work was supported in part by the National Science Foundation.

REFERENCES

Abutaleb, M., R. J. de Graaff, W. Ubachs, and W. Hogervorst, 1991, Phys. Rev. A **44**, 4187.

Abutaleb, M., R. J. de Graaff, W. Ubachs, W. Hogervorst, and M. Aymar, 1991, J. Phys. B **24**, 3565.

Alexa, B., M. A. Baig, J.-P. Connerade, W. R. S. Garton, J. Hormes, and T. A. Savrakas, 1983, Nucl. Instrum. Methods **208**, 841.
Allison, D. C. S., P. G. Burke, and W. D. Robb, 1972, J. Phys. B **5**, 55.
Altun, Z., 1989, Phys. Rev. A **40**, 4968.
Altun, Z., 1992, J. Phys. B **25**, 2279.
Altun, Z., S. L. Carter, and H. P. Kelly, 1983, Phys. Rev. A **27**, 1943.
Andersen, L. H., D. Mathur, H. T. Schmidt, and L. Vejby-Christensen, 1995, Phys. Rev. Lett. **74**, 892.
Armstrong, D. J., and C. H. Greene, 1994, Phys. Rev. A **50**, 4956.
Armstrong, D. J., C. H. Greene, R. P. Wood, and J. Cooper, 1993, Phys. Rev. Lett. **70**, 2379.
Armstrong, D. J., and F. Robicheaux, 1993, Phys. Rev. A **48**, 4450.
Armstrong, D. J., R. P. Wood, and C. H. Greene, 1993, Phys. Rev. A **47**, 1981.
Armstrong, J. A., P. Esherick, and J. J. Wynne, 1977, Phys. Rev. A **15**, 180.
Armstrong, J. A., S. S. Jha, and K. C. Pandey, 1981, Phys. Rev. A **23**, 2761.
Armstrong, J. A., J. J. Wynne, and P. Esherick, 1979, J. Opt. Soc. Am. **69**, 211.
Armstrong, J. A., J. J. Wynne, and F. S. Tomkins, 1980, J. Phys. B **13**, L133.
Assimopoulos, S., A. Bolovinos, A. Jimoyiannis, P. Tsekeris, E. Luc-Koenig, and M. Aymar, 1994, J. Phys. B **27**, 2471.
Aymar, M., 1984a, Phys. Rep. **110**, 163.
Aymar, M., 1984b, J. Opt. Soc. Am. B **1**, 239.
Aymar, M., 1987, J. Phys. B **20**, 6507.
Aymar, M., 1989, J. Phys. B **22**, 2359.
Aymar, M., 1990, J. Phys. B **23**, 2697.
Aymar, M., P. Camus, M. Dieulin, and C. Morillon, 1978, Phys. Rev. A **18**, 2173.
Aymar, M., P. Camus, and A. El Himdy, 1982, J. Phys. B. **15**, L759.
Aymar, M., P. Camus, and A. El Himdy, 1983, Phys. Scr. **27**, 183.
Aymar, M., and J.-M. Lecomte, 1989, J. Phys. B **22**, 223.
Aymar, M., and E. Luc-Koenig, 1995, J. Phys. B **28**, 1211.
Aymar, M., E. Luc-Koenig, and J.-M. Lecomte, 1994, J. Phys. B **27**, 2425.
Aymar, M., E. Luc-Koenig, and S. Watanabe, 1987, J. Phys. B **20**, 4325.
Aymar, M., and O. Robaux, 1979, J. Phys. B **12**, 531.
Aymar, M., and M. Telmini, 1991, J. Phys. B **24**, 4935.
Bartschat, K., 1987, J. Phys. B **20**, 5023.
Bartschat, K., and C. H. Greene, 1993, J. Phys. B **26**, L109.
Bartschat, K., and B. M. McLaughlin, 1990, J. Phys. B **23**, L439.
Bartschat, K., B. M. McLaughlin, and R. A. Hoversten, 1991, J. Phys. B **24**, 3359.
Bartschat, K., M. R. H. Rudge, and P. Scott, 1986, J. Phys. B **19**, 2469.
Bartschat, K., and P. Scott, 1985a, J. Phys. B **18**, L191.
Bartschat, K., and P. Scott, 1985b, J. Phys. B **18**, 3725.
Bates, G. N., and P. L. Altick, 1973, J. Phys. B **6**, 653.
Beigang, R., 1985, Comments At. Mol. Phys. **16**, 117.
Beigang, R., W. Makat, A. Timmerman, and P. J. West, 1983, Phys. Rev. Lett. **51**, 771.
Bente, E. A. J. M., and W. Hogervorst, 1990, J. Phys. B **23**, 1403.
Berkowitz, J., C. H. Batson, and G. L. Goodman, 1981, Phys. Rev. A **24**, 149.
Berrington, K. A., P. G. Burke, K. Butler, M. J. Seaton, P. J. Storey, K. T. Taylor, and Yu Yan, 1987, J. Phys. B **20**, 6379.
Berrington, K. A., P. G. Burke, M. Le Dourneuf, W. D. Robb, K. T. Taylor, Vo Ky Lan, 1978, Comput. Phys. Commun. **14**, 367.
Berzinsh, U., G. Haeffler, D. Hanstorp, A. Klinkmüller, E. Lindroth, U. Ljungblad, and D. J. Pegg, 1995, Phys. Rev. Lett. **74**, 4795.
Bethe, H. A., 1949, Phys. Rev. **76**, 38.
Bhalla, C. P., K. R. Karim, and M. Wilson, 1990, Phys. Rev. A **41**, 1715.
Bhattii, S. A., C. L. Cromer, and W. E. Cooke, 1981, Phys. Rev. A **24**, 161.
Blatt, J. M., and D. J. Jackson, 1949, Phys. Rev. A **76**, 18.
Blatt, J. M., and V. F. Weisskopf, 1952, *Theoretical Nuclear Physics* (Wiley, New York).
Bloch, C., 1957, Nucl. Phys. **4**, 503.
Bloomfield, L. A., R. R. Freeman, W. E. Cooke, and J. Bokor, 1984, Phys. Rev. Lett. **53**, 2234.
Bohr, N., 1936, Nature **137**, 344.
Bolovinos, A., A. Jimoyiannis, S. Assimopoulos, and P. Tsekeris, 1992, J. Phys. B **25**, L533.
Born, M., and R. J. Oppenheimer, 1927, Ann. Phys. (USA) **84**, 457.
Brage, T., and C. Froese Fischer, 1994a, Phys. Scr. **49**, 651.
Brage, T., and C. Froese Fischer, 1994b, Phys. Rev. A **50**, 2937.
Bray, I. and A. T. Stelbovics, 1992, Phys. Rev. Lett. **69**, 53.
Bray, I., and A. T. Stelbovics, 1993, Phys. Rev. Lett. **70**, 746.
Bray, I. and A. T. Stelbovics, 1995, Adv. At. Mol. Phys. **35**.
Breit, G., 1959, in *Encyclopedia of Physics*, edited by S. Flügge, Handbuch der Physik **41**/1 (Springer, New York), p. 107.
Breit, G., and H. A. Bethe, 1954, Phys. Rev. **93**, 888.
Breit, G., and E. P. Wigner, 1936, Phys. Rev. **49**, 519.
Brody, T. A., J. Flores, J. B. French, P. A. Mello, A. Pandey, and S. S. M. Wong, 1981, Rev. Mod. Phys. **53**, 385.
Brown, E. R., S. L. Carter, and H. P. Kelly, 1980, Phys. Rev. A **21**, 1237.
Brown, C. M., and M. L. Ginter, 1978, J. Opt. Soc. Am. **68**, 817.
Brown, C. M., and M. L. Ginter, 1980, J. Opt. Soc. Am. **70**, 87.
Brown, C. M., M. S. Longmire, and M. L. Ginter, 1983, J. Opt. Soc. Am. **73**, 985.
Brown, C. M., S. G. Tilford, and M. L. Ginter, 1973, J. Opt. Soc. Am. **63**, 1454.
Brown, C. M., S. G. Tilford, and M. L. Ginter, 1975, J. Opt. Soc. Am. **65**, 385.
Brown, C. M., S. G. Tilford, and M. L. Ginter, 1977a, J. Opt. Soc. Am. **67**, 584.
Brown, C. M., S. G. Tilford, and M. L. Ginter, 1977b, J. Opt. Soc. Am. **67**, 607.
Brown, C. M., S. G. Tilford, and M. L. Ginter, 1977c, J. Opt. Soc. Am. **67**, 1240.
Brown, C. M., S. G. Tilford, R. Tousey, and M. L. Ginter, 1974, J. Opt. Soc. Am. **64**, 1665.
Brueckner, K. A., 1955, Phys. Rev. **97**, 1353.
Buckman, S. J., and C. W. Clark, 1994, Rev. Mod. Phys. **66**, 539.
Burke, P. G., and K. A. Berrington, 1993, *Atomic and Molecular Processes: An R-Matrix Approach* (IOP, Bristol).

Burke, P. G., J. W. Cooper, and S. Ormonde, 1969, Phys. Rev. **183**, 245.
Burke, P. G., P. Francken, and C. J. Joachain, 1991, J. Phys. B **24**, 761.
Burke, P. G., D. F. Gallaher, and S. Geltman, 1969, J. Phys. B **2**, 1142.
Burke, P. G., and D. D. McVicar, 1965, Proc. Phys. Soc. London **86**, 989.
Burke, P. G., C. Noble, and P. Scott, 1987, Proc. R. Soc. London A **410**, 289.
Burke, P. G., and W. D. Robb, 1975, Adv. At. Mol. Phys. **11**, 143.
Burke, P. G., and K. Smith, 1962, Rev. Mod. Phys. **34**, 458.
Burke, P. G., and K. T. Taylor, 1975, J. Phys. B **8**, 2620.
Burkhardt, C. E., J. L. Libbert, J. Xu, J. J. Leventhal, and J. D. Kelley, 1988, Phys. Rev. A **38**, 5949.
Buttle, P. J. A., 1967, Phys. Rev. **160**, 719.
Calogero, F., 1967, *Variable Phase Approach to Potential Scattering* (Academic, New York).
Camus, P., S. Cohen, L. Pruvost, and A. Bolovinos, 1993, Phys. Rev. A **48**, R9.
Camus, P., M. Dieulin, A. El Himdy, and M. Aymar, 1983, Phys. Scr. **27**, 125.
Camus, P., T. F. Gallagher, J.-M. Lecomte, P. Pillet, L. Pruvost, and J. Boulmer, 1989, Phys. Rev. Lett. **62**, 2365.
Camus, P., J.-M. Lecomte, C. Mahon, P. Pillet, and L. Pruvost, 1992, J. Phys. II (Paris) **2**, 715.
Camus, P., C. R. Mahon, and L. Pruvost, 1993, J. Phys. B **26**, 221.
Carlsten, J. L., and T. J. McIlrath, 1973, J. Phys. B **6**, L284.
Carré, B., P. Fournier, D. Porterat, H. Lagadec, F. Gounand, and M. Aymar, 1994, J. Phys. B **27**, 1027.
Chang, J. J., 1975, J. Phys. B **8**, 2327.
Chang, J. J., 1977, J. Phys. B **10**, 3335.
Chang, J. J., 1993, Phys. Rev. A **48**, 1769.
Chang, T. N., 1986, Phys. Rev. A **34**, 4550.
Chang, T. N., and X. Tang, 1992, Phys. Rev. A **46**, R2209.
Chatwin, R. A., 1970, Phys. Rev. C **2**, 1167.
Chen, C. T., and F. Robicheaux, 1994, Phys. Rev. A **50**, 3968.
Chi, H. C., and K.-N. Huang, 1994, Phys. Rev. A **50**, 392.
Chi, H. C., K.-N. Huang, and K. T. Cheng, 1991, Phys. Rev. A **43**, 2542.
Child, M. S., and Ch. Jungen, 1990, J. Chem. Phys. **93**, 7756.
Chisholm, C. D. H., and U. Öpik, 1964, Proc. Phys. Soc. London **83**, 541.
Combet Farnoux, F., and M. Ben Amar, 1986, J. Electron Spectrosc. Relat. Phenom. **41**, 67.
Condon, E. U., and G. H. Shortley, 1935, *The Theory of Atomic Spectra* (Cambridge University, Cambridge).
Connerade, J.-P., 1992, J. Phys. II (Paris) **2**, 757.
Connerade, J.-P., M. A. Baig, W. R. S. Garton, F.R.S., and G. H. Newsom, 1980, Proc. R. Soc. London A **371**, 295.
Connerade, J.-P., M. A. Baig, and M. Sweeney, 1990, J. Phys. B **23**, 713.
Connerade, J.-P., and S. M. Farooqi, 1991, J. Phys. B **24**, L331.
Connerade, J.-P., H. Ma, N. Shen, and T. A. Stavrakas, 1988, J. Phys. B **21**, L241.
Connerade, J.-P., and B. K. Sarpal, 1992, J. Phys. B **25**, 2245.
Cooke, W. E., and C. L. Cromer, 1985, Phys. Rev. A **32**, 2725.
Cooke, W. E., T. F. Gallagher, S. A. Edelstein, and R. M. Hill, 1978, Phys. Rev. Lett. **40**, 178.
Cooper, J. W., U. Fano, and F. Prats, 1963, Phys. Rev. Lett. **10**, 518.
Dai, C. J., G. W. Schinn, and T. F. Gallagher, 1990, Phys. Rev. A **42**, 223.
Dalgarno, A., 1962, Adv. Phys. **11**, 281.
Dalitz, R. H., F.R.S, and R. G. Moorhouse, 1970, Proc. R. Soc. London A **318**, 279.
Danos, M., and W. Greiner, 1966, Phys. Rev. **146**, 708.
de Graaff, R. J., W. Ubachs, and W. Hogervorst, 1992, Phys. Rev. A **45**, 166.
de Graaff, R. J., W. Ubachs, W. Hogervorst, and M. Abutaleb, 1990, Phys. Rev. A **42**, 5473.
Delande, D., A. Bommier, and J.-C. Gay, 1991, Phys. Rev. Lett. **66**, 141.
Delande, D., and A. Buchleitner, 1994, Adv. At. Mol. Phys. **34**, 85.
Delande, D., K. T. Taylor, M. H. Halley, T. van der Veldt, W. Wassen, and W. Hogervorst, 1994, J. Phys. B **27**, 2771.
Delves, L. M., 1958, Nucl. Phys. **8**, 358.
Dill, D., 1973, Phys. Rev. A **7**, 1976.
Dill, D., and U. Fano, 1972, Phys. Rev. Lett. **29**, 1203.
Ditchburn, R. W., and G. V. Marr, 1953, Proc. Phys. Soc. London **66**, 655.
Domke, M., C. Xue, A. Puschmann, T. Mandel, E. Hudson, D. A. Shirley, G. Kaindl, C. H. Greene, H. R. Sadeghpour, and H. Petersen, 1991, Phys. Rev. Lett. **66**, 1306.
Dörr, M., P. G. Burke, C. J. Joachain, C. J. Noble, J. Purvis, and M. Terao-Dunseath, 1993, J. Phys. B **26**, L275.
Dörr, M., M. Terao-Dunseath, J. Purvis, C. J. Noble, P. G. Burke, and C. J. Joachain, 1992, J. Phys. B **25**, 2809.
Draeger, M., and H. Friedrich, 1991, Phys. Rev. A **45**, 3346.
Du, M. L., and J. B. Delos, 1988a, Phys. Rev. A **38**, 1896.
Du M. L., and J. B. Delos, 1988b, Phys. Rev. A **38**, 1913.
Dubau, J., and J. Wells, 1973, J. Phys. B **6**, 1452.
Eichmann, U., P. Brockmann, V. Lange, and W. Sandner, 1989, J. Phys. B. **22**, L361.
Eichmann, U., V. Lange, and W. Sandner, 1992, Phys. Rev. Lett. **68**, 21.
Eliel, E. R., and W. Hogervorst, 1983, J. Phys. B **16**, 1881.
Ericsson, T., and A. Ruhe, 1980, Math. Comput. **35**, 1251.
Esherick, P., 1977, Phys. Rev. A **15**, 1920.
Fajans, K., and G. I. Joos, 1924, Z. Phys. **23**, 1.
Fano, U., 1935, Nuovo Cimento, **12**, 156.
Fano, U., 1961, Phys. Rev. **124**, 1866.
Fano, U., 1970, Phys. Rev. A **2**, 353.
Fano, U., 1975, J. Opt. Soc. Am. **65**, 979.
Fano, U., 1981, Phys. Rev. A **24**, 2402.
Fano, U., 1983, Rep. Prog. Phys. **46**, 97.
Fano, U., D. Dill, 1972, Phys. Rev. A **6**, 185.
Fano, U., and C. M. Lee, 1973, Phys. Rev. Lett. **31**, 1573.
Fano, U., and A. R. P. Rau, 1986, *Atomic Collisions and Spectra* (Academic, Orlando).
Farooqi, S. M., J.-P. Connerade, and M. Aymar, 1992, J. Phys. B **25**, L219.
Farooqi, S. M., J.-P. Connerade, C. H. Greene, J. Marangos, M. H. R. Hutchinson, and N. Shen, 1991, J. Phys. B **24**, L179.
Feldman, U., C. M. Brown, G. A. Doschek, C. E. Moore, and F. D. Rosenberg, 1976, J. Opt. Soc. Am. **66**, 583.
Fermi, E., 1934, Nuovo Cimento **11**, 157.
Fermi, E., and L. Marshall, 1947, Phys. Rev. **71**, 666.
Feshbach, H., 1958, Ann. Phys. (N.Y.) **5**, 357.
Feshbach, H., 1962, Ann. Phys. (N.Y.) **19**, 287.
Fielder, W. R., and L. Armstrong, Jr., 1983, Phys. Rev. A **28**, 218.
Fink, M. G. J., and W. R. Johnson, 1990, Phys. Rev. A **42**, 3801.

Fink, M. G. J., and P. Zoller, 1989, Phys. Rev. A **39**, 2933.
Friedrich, H., 1990, *Theoretical Atomic Physics* (Springer, New York).
Froese Fischer, C., 1977, *The Hartree-Fock Method for Atoms* (Wiley, New York).
Froese Fischer, C., 1991, Comput. Phys. Commun. **64**, 369.
Froese Fischer, C., and D. Chen, 1989, J. Mol. Struct. **199**, 61.
Froese Fischer, C., and J. E. Hansen, 1981, Phys. Rev. A **24**, 631.
Froese Fischer, C., and J. E. Hansen, 1985, J. Phys. B **18**, 4031.
Froese Fischer, C., J. B. Lagowski, and S. H. Vosko, 1987, Phys. Rev. Lett. **59**, 2263.
Froese Fischer, C., and H. P. Saha, 1987, Can. J. Phys. **65**, 772.
Frye, D., and H. P. Kelly, 1987, J. Phys. B **20**, L677.
Gallagher, T. F., 1994, *Rydberg Atoms*, Cambridge Monographs on Atomic, Molecular, and Chemical Physics 3, edited by A. Dalgarno, P. L. Knight, F. H. Read, and R. N. Zare (Cambridge University, New York).
Garton, W. R. S., and K. Codling, 1960, Proc. Phys. Soc. London **75**, 87.
Garton, W. R. S., and K. Codling, 1968, J. Phys. B **1**, 106.
Garton, W. R. S., F.R.S., and W. H. Parkinson, 1974, Proc. R. Soc. London A **341**, 45.
Garton, W. R. S., E. M. Reeves, F. S. Tomkins, and B. Ercoli, 1973, Proc. R. Soc. London A **333**, 1.
Garton, W. R. S., and F. S. Tomkins, 1969a, Astrophys. J. **158**, 839.
Garton, W. R. S., and F. S. Tomkins, 1969b, Astrophys. J. **158**, 1219.
Gauyacq, J. P., 1987, *Dynamics of Negative Ions* (World Scientific, Singapore).
Gerjuoy, E., A. R. P. Rau, and L. Spruch, 1983, Rev. Mod. Phys. **55**, 725.
Gibson, S. T., J. P. Greene, B. Ruščić, and J. Berkowitz, 1986a, J. Phys. B **19**, 2825.
Gibson, S. T., J. P. Greene, B. Ruščić, and J. Berkowitz, 1986b, J. Phys. B **19**, 2841.
Ginter, D. S., and M. L. Ginter, 1986, J. Chem. Phys. **85**, 6536.
Ginter, D. S., M. L. Ginter, and C. M. Brown, 1986, J. Chem. Phys. **85**, 6530.
Giusti-Suzor, A., and U. Fano, 1984, J. Phys. B **17**, 215.
Giusti-Suzor, A., and H. Lefebvre-Brion, 1984, Phys. Rev. A **30**, 3057.
Goforth, T. L., G. L. Snitchler, and D. K. Watson, 1987, Phys. Rev. A **35**, 904.
Goforth, T. L., and D. K. Watson, 1992, Phys. Rev. A **46**, 1239.
Goldbach, C., M. Martin, and G. Nollez, 1989, Astron. Astrophys. **221**, 155.
Goldbach, C., and G. Nollez, 1987, Astron. Astrophys. **181**, 203.
Goldberg, I. B., and R. H. Pratt, 1987, J. Math. Phys. **28**, 1351.
Gounand, F., B. Carré, P. R. Fournier, P. d'Oliveira, and M. Aymar, 1991, J. Phys. B **24**, 1309.
Gounand, F., T. F. Gallagher, W. Sandner, K. A. Safinya, and R. Kachru, 1983, Phys. Rev. A **27**, 1925.
Goutis, S., M. Aymar, M. Kompitsas, and P. Camus, 1992, J. Phys. B **25**, 3433.
Greene, C. H., 1980, Phys. Rev. A **22**, 149.
Greene, C. H., 1981, Phys. Rev. A **23**, 661.
Greene, C. H., 1983, Phys. Rev. A **28**, 2209.
Greene, C. H., 1985, Phys. Rev. A **32**, 1880.
Greene, C. H., 1988, in *Fundamental Processes of Atomic Dynamics*, edited by J. Briggs, H. Kleinpoppen, and H. Lutz (Plenum, New York), p. 105.
Greene, C. H., 1990a, Phys. Rev. A **42**, 1405.
Greene, C. H., 1990b, private communication.
Greene, C. H., and M. Aymar, 1991, Phys. Rev. A **44**, 1773.
Greene, C. H., U. Fano, and G. Strinati, 1979, Phys. Rev. A **19**, 1485.
Greene, C. H., and Ch. Jungen, 1985, Adv. At. Mol. Phys. **21**, 51.
Greene, C. H., and L. Kim, 1987, Phys. Rev. A **36**, 2706.
Greene, C. H., and L. Kim, 1988, Phys. Rev. A **38**, 5953.
Greene, C. H., A. R. P. Rau, and U. Fano, 1982, Phys. Rev. A **26**, 2441.
Greene, C. H., and C. E. Theodosiou, 1990, Phys. Rev. A **42**, 5773.
Greene, C. H., and B. Yoo, 1995, J. Phys. Chem. **99**, 1711.
Grémaud, B., D. Delande, and J.-C. Gay, 1993, Phys. Rev. Lett. **70**, 1615.
Griesmann, U., 1990, private communication.
Griesmann, U., B. Esser, and M. A. Baig, 1992, J. Phys. B **25**, 3475.
Griesmann, U., B. Esser, and J. Hormes, 1994, J. Phys. B **27**, 3939.
Griesmann, U., N. Shen, J.-P. Connerade, K. Sommer, and J. Hormes, 1988, J. Phys. B **21**, L83.
Gutzwiller, M. C., 1967, J. Math. Phys. **8**, 1979.
Hafner, P., and W. H. E. Schwartz, 1978, J. Phys. B **11**, 217.
Hahn, Y., and I. Nasser, 1993, Z. Phys. D **27**, 203.
Halley, M. H., D. Delande, and K. T. Taylor, 1992, J. Phys. B **25**, L525.
Halley, M. H., D. Delande, and K. T. Taylor, 1993, J. Phys. B **26**, 1775.
Ham, F. S., 1955, in *Solid State Physics*, edited by F. Seitz and D. Turnbull (Academic, New York), p. 127.
Hamacher, P., and J. Hinze, 1989, J. Phys. B **22**, 3397.
Hamacher, P., and J. Hinze, 1991, Phys. Rev. A **44**, 1705.
Hameed, S., 1972, J. Phys. B **5**, 746.
Han, S. and W. P. Reinhardt, 1995, J. Phys. B **28**, 3347.
Harmin, D. A., 1984, Phys. Rev. A **30**, 2413.
Harris, P. G., H. C. Bryant, A. H. Mohaghedi, R. S. Reeder, H. Sharifian, C. Y. Tang, H. Tootoonchi, J. B. Donahue, C. R. Quick, D. C. Risolve, W. W. Smith, and J. E. Stewart, 1990, Phys. Rev. Lett. **65**, 309.
He, L.-W., C. E. Burkhardt, M. Ciocca, J. J. Leventhal, and S. T. Manson, 1991, Phys. Rev. Lett. **67**, 2131.
He, L.-W., C. E. Burkhardt, M. Ciocca, J. J. Leventhal, H.-L. Zhou, and S. T. Manson, 1995, Phys. Rev. A **51**, 2085.
Heisenberg, W., 1943, Z. Phys. **120**, 673.
Hieronymus, M., K. Kohl, J. Neukammer, A. König, H. Rinneberg, and H. Spinger-Bolk, 1990, Phys. Rev. A **41**, 1477.
Ho, Y. K., 1983, Phys. Rep. **99**, 1.
Hudson, R. D., V. L. Carter, and P. A. Young, 1969, Phys. Rev. **180**, 77.
Hudson, R. D., V. L. Carter, and P. A. Young, 1970, Phys. Rev. A **2**, 643.
Humblet, J., and L. Rosenfeld, 1961, Nucl. Phys. **26**, 259.
Hunter III, J. E., J. S. Keller, and R. S. Berry, 1986, Phys. Rev. A **33**, 3138.
Iu, C., G. R. Welch, M. M. Kash, L. Hsu, and D. Kleppner, 1989, Phys. Rev. Lett. **63**, 1133.
Iu, C., G. R. Welch, M. M. Kash, D. Kleppner, D. Delande, and J.-C. Gay, 1991, Phys. Rev. Lett. **66**, 145.

Ivanov, M. Yu., D. Bitouk, K. Rzążewski, and S. Kotochigova, 1995, Phys. Rev. A **52**, 149.
Jacobs, V. L., and J. Davis, 1979, Phys. Rev. A **19**, 776.
Johnson, W. R., and K. T. Cheng, 1979, J. Phys. B **12**, 863.
Johnson, W. R., K. T. Cheng, K.-N. Huang, and M. Le Dourneuf, 1980, Phys. Rev. A **22**, 989.
Johnson, W. R., D. Kolb, and K.-N. Huang, 1983, At. Data Nucl. Data Tables **28**, 333.
Johnson, W. R., and C. D. Lin, 1979, Phys. Rev. A **20**, 964.
Jones, R. R., P. Fu, and T. F. Gallagher, 1991a, Phys. Rev. A **44**, 4260.
Jones, R. R., P. Fu, and T. F. Gallagher, 1991b, Phys. Rev. A **44**, 4265.
Jones, R. R., and T. F. Gallagher, 1988, Phys. Rev. A **38**, 2846.
Jones, R. R., and T. F. Gallagher, 1990, Phys. Rev. A **42**, 2655.
Jungen, Ch., 1984, Phys. Rev. Lett. **53**, 2394.
Jungen, Ch., 1988, in *Fundamental Processes of Atomic Dynamics*, edited by J. Briggs, H. Kleinpoppen, and H. Lutz (Plenum, New York), p. 79.
Jungen, Ch., and D. Dill, 1980, J. Chem. Phys. **73**, 3338.
Kachru, R., N. H. Tran, P. Pillet, and T. F. Gallagher, 1985, Phys. Rev. A **31**, 218.
Kallenbach, A., M. Kock, and G. Zierer, 1988, Phys. Rev. A **38**, 2356.
Kato, D., and S. Watanabe, 1995, Phys. Rev. Lett. **74**, 2443.
Keller, J. S., J. E. Hunter III, and R. S. Berry, 1991, Phys. Rev. A **43**, 2270.
Kelly, H. P., 1987, Phys. Scr. T **17**, 109.
Kim, L., and C. H. Greene, 1987, Phys. Rev. A **36**, 4272.
Kim, L., and C. H. Greene, 1988, Phys. Rev. A **38**, 2361.
Kim, L., and C. H. Greene, 1989, J. Phys. B **22**, L175.
Kohn, W., 1948, Phys. Rev. **74**, 1763.
Komninos, Y., G. Aspromallis, and C. A. Nicolaides, 1995, J. Phys. B **28**, 2049.
Kompitsas, M., S. Cohen, C. A. Nicolaides, O. Robaux, M. Aymar, and P. Camus, 1990, J. Phys. B **23**, 2247.
Kompitsas, M., S. Goutis, M. Aymar, and P. Camus, 1991, J. Phys. B **24**, 1557.
Kotochigova, S. A., and I. I. Tupizin, 1987, J. Phys. B **20**, 87.
Lagadec, H., B. Carré, D. Porterat, P. Fournier, and M. Aymar, 1996, J. Phys. B **29**, 471.
Lambropoulos, P., X. Tang, P. Agostini, G. Petite, and A. L'Huillier, 1988, Phys. Rev. A **38**, 6165.
Lamoureux, M., and F. Combet Farnoux, 1979, J. Phys. (Paris) **40**, 545.
Lane, A. M., 1986, J. Phys. B **19**, 253.
Lane, A. M., and D. Robson, 1966, Phys. Rev. **151**, 774.
Lane, A. M., and D. Robson, 1969, Phys. Rev. **178**, 1715.
Lane, A. M., and R. G. Thomas, 1958, Rev. Mod. Phys. **30**, 257.
Lange, V., M. Aymar, U. Eichmann, and W. Sandner, 1991, J. Phys. B **24**, 91.
Lange, V., U. Eichmann, and W. Sandner, 1989, J. Phys. B **22**, L245.
Lange, V., U. Eichmann, and W. Sandner, 1991, Phys. Rev. A **44**, 4737.
Langer, R. E., 1937, Phys. Rev. **51**, 669.
Laughlin, C., and G. A. Victor, 1973, in *Atomic Physics 3; Proceedings*, edited by S. J. Smith and G. K. Walters (Plenum, New York), p. 247.
Launay, J.-M., and M. Le Dourneuf, 1982, J. Phys. B **15**, L455.
Lecomte, J.-M., 1987, J. Phys. B **20**, 3645.
Lecomte, J.-M., 1993, private communication.
Lecomte, J.-M., B. Carré, M. Telmini, H. Lagadec, P. R. Fournier, D. Porterat, and M. Aymar, 1995, J. Phys. B **28**, L655.
Lecomte, J.-M., M. Telmini, M. Aymar, and E. Luc-Koenig, 1994, J. Phys. B **27**, 667.
Le Dourneuf, M., J.-M. Launay, and P. G. Burke, 1990, J. Phys. B **23**, L559.
Le Dourneuf, M., S. N. Nahar, and A. K. Pradhan, 1993, J. Phys. B **26**, L1.
Le Rouzo, H., and G. Raseev, 1984, Phys. Rev. A **29**, 1214.
Lee, C. M., 1974a, Phys. Rev. A **10**, 584.
Lee, C. M., 1974b, Phys. Rev. A **10**, 1598.
Lee, C. M., 1975, Phys. Rev. A **11**, 1692.
Lee, C. M., and W. R. Johnson, 1980, Phys. Rev. A **22**, 979.
Lee, C. M., and K. T. Lu, 1973, Phys. Rev. A **8**, 1241.
Leuchs, G., and S. J. Smith, 1985, Phys. Rev. A **31**, 2283.
Lin, C. D., 1974, Astrophys. J. **87**, 385.
Lin, C. D., 1986, Adv. At. Mol. Phys. **22**, 77.
Lin, C. D., 1995, Phys. Rep. **257**, 1.
Lindsay, M. D., L.-T. Cai, G. W. Schinn, C.-J. Dai, and T. F. Gallagher, 1992, Phys. Rev. A **45**, 231.
Lindsay, M. D., C.-J. Dai, L.-T. Cai, T. F. Gallagher, F. Robicheaux, and C. H. Greene, 1992, Phys. Rev. A **46**, 3789.
Löwdin, P. O., 1955, Phys. Rev. **97**, 1474.
Löwdin, P. O., and H. Shull, 1956, Phys. Rev. **101**, 1730.
Lu, K. T., 1971, Phys. Rev. A **4**, 579.
Lu, K. T., 1977, Proc. R. Soc. London A **353**, 431.
Lu, K. T., and U. Fano, 1970, Phys. Rev. A **2**, 81.
Lu, K. T., F. S. Tomkins, and W. R. S. Garton, 1978, Proc. R. Soc. London A **362**, 421.
Luc-Koenig, E., and M. Aymar, 1991, J. Phys. B **24**, 4323.
Luc-Koenig, E., and M. Aymar, 1992, J. Phys. II (Paris) **2**, 865.
Luc-Koenig, E., M. Aymar, and J.-M. Lecomte, 1994, J. Phys. B **27**, 2447.
Luc-Koenig, E., M. Aymar, R. van Leeuwen, W. Ubachs, W. Hogervorst, 1995, Phys. Rev. A **52**, 208.
Luc-Koenig, E., and A. Bachelier, 1980a, J. Phys. B **13**, 1740.
Luc-Koenig, E., and A. Bachelier, 1980b, J. Phys. B **13**, 1769.
Luc-Koenig, E., A. Bolovinos, M. Aymar, S. Assimopoulos, A. Jimoyiannis, and P. Tsekeris, 1994, Z. Phys. D **32**, 49.
Luc-Koenig, E., J.-M. Lecomte, and M. Aymar, 1994, J. Phys. B **27**, 699.
Madden, R. P., and K. Codling, 1965, Astrophys. J. **141**, 364.
Mahan, G. D., 1981, *Many-Particle Physics* (Plenum, New York).
Mahaux, C., and H. A. Weidenmüller, 1968, Phys. Rev. **170**, 847.
Manson, S. T., A. Msezane, A. F. Starace, and S. Shahabi, 1979, Phys. Rev. A **20**, 1005.
Martin, W. C., and R. Zalubas, 1983, J. Phys. Chem. Ref. Data **12**, 323.
Matthias, E., P. Zoller, D. S. Elliot, N. D. Piltch, S. J. Smith, and G. Leuchs, 1983, Phys. Rev. Lett. **50**, 1914.
McCurdy, C. W., B. I. Schneider, and T. R. Rescigno, 1987, Phys. Rev. A **36**, 2061.
McIlrath, T. J., and R. J. Sandeman, 1972, J. Phys. B **5**, L217.
Mehlman-Ballofet, G., and J.-M. Esteva, 1969, Astrophys. J. **157**, 945.
Mende, W., K. Bartschat, and M. Kock, 1995, J. Phys. B **28**, 2385.
Mendoza, C. J., 1981, J. Phys. B **14**, 397.
Mendoza, C. J., and C. J. Zeippen, 1987, Astron. Astrophys. **179**, 346.

Mendoza, C. J., and C. J. Zeippen, 1988, J. Phys. B **21**, 259.
Messiah, A., 1958, *Quantum Mechanics* (Wiley, New York).
Meyer, K. W., and C. H. Greene, 1994, Phys. Rev. A **50**, R3573.
Meyer, K. W., C. H. Greene, and I. Bray, 1995, Phys. Rev. A **52**, 1334.
Miecznik, G., and C. H. Greene, 1996, J. Opt. Soc. Am. B **13**, 244.
Miecznik, G., C. H. Greene, and F. Robicheaux, 1995, Phys. Rev. A **51**, 513.
Mies, F. H., and P. S. Julienne, 1984, J. Chem. Phys. **80**, 2526.
Miller, W. H., 1988, Comments At. Mol. Phys. **22**, 115.
Milne, W. E., 1930, Phys. Rev. **35**, 863.
Mo, T., and W. F. Hornyak, 1969, Phys. Rev. **187**, 1220.
Moccia, R., and P. Spizzo, 1989, Phys. Rev. A **39**, 3855.
Moore, C. E., 1949, *Atomic Energy Levels as Derived from the Analysis of Optical Spectra I*, National Bureau of Standards Circular 467 (U.S. Dept. of Commerce, National Bureau of Standards, Washington, D. C.).
Moore, C. E., 1952, *Atomic Energy Levels as Derived from the Analysis of Optical Spectra II*, National Bureau of Standards Circular 467 (U.S. Dept. of Commerce, National Bureau of Standards, Washington, D. C.).
Moore, C. E., 1958, *Atomic Energy Levels as Derived from the Analysis of Optical Spectra III*, National Bureau of Standards Circular 467 (U.S. Dept. of Commerce, National Bureau of Standards, Washington, D. C.).
Moores, D. L., and D. W. Norcross, 1972, J. Phys. B **5**, 1482.
Moores, D. L., and D. W. Norcross, 1974, Phys. Rev. A **10**, 1646.
Morita, N., and T. Suzuki, 1990, Phys. Rev. A **41**, 2370.
Mullins, O. C., R.-l. Chien, J. E. Hunter III, D. K. Jordan, and R. S. Berry, 1985, Phys. Rev. A **31**, 3059.
Mullins, O. C., R.-l. Chien, J. E. Hunter III, J. S. Keller, and R. S. Berry, 1985, Phys. Rev. A **31**, 321.
Mullins, O. C., J. E. Hunter III, J. S. Keller, and R. S. Berry, 1985, Phys. Rev. Lett. **54**, 410.
Nahar, S. N., and A. K. Pradhan, 1992, Phys. Rev. Lett. **68**, 1488.
Nesbet, R. K., 1980, *Variational Methods in Electron-Atom Scattering Theory* (Plenum, New York).
Newsom, G. H., 1966, Proc. Phys. Soc. London **87**, 975.
Noble, C. J., M. Dörr, and P. G. Burke, 1993, J. Phys. B **26**, 2983.
Norcross, D. W., and M. J. Seaton, 1976, J. Phys. B **9**, 2983.
Norrington, P. H., and I. P. Grant, 1981, J. Phys. B **14**, L261.
Nussbaumer, H., and P. J. Storey, 1984, Astron. Astrophys. **140**, 383.
O'Mahony, P. F., 1985, Phys. Rev. A **32**, 908.
O'Mahony, P. F., and C. H. Greene, 1985, Phys. Rev. A **31**, 250.
O'Mahony, P. F., and F. Mota-Furtado, 1991, Phys. Rev. Lett. **67**, 2283.
O,'Mahony, P. F., and S. Watanabe, 1985, J. Phys. B **18**, L239.
Osani, Y., T. Noro, and F. Sasaki, 1989a, J. Phys. B **22**, 3615.
Osani, Y., T. Noro, and F. Sasaki, 1989b, J. Phys. B **22**, 3631.
Osani, Y., T. Noro, and F. Sasaki, 1991, J. Phys. B **24**, 2641.
Page, R. H., and C. S. Gudeman, 1990, J. Opt. Soc. Am. B **7**, 1761.
Pan, X., 1991a, Phys. Rev. Lett. **66**, 2972.
Pan, X., 1991b, Phys. Rev. A **44**, 7269.
Pan, C., A. F. Starace, and C. H. Greene, 1994, J. Phys. B **27**, L137.
Parkinson, W. H., E. M. Reeves, and F. S. Tomkins, 1976, J. Phys. B **9**, 157.
Patterson, T. A., H. Hotop, A. Kasdan, D. W. Norcross, and W. C. Lineberger, 1974, Phys. Rev. Lett. **32**, 189.
Peart, B., and K. Dolder, 1973, J. Phys. B **6**, 1497.
Petrunin, V. V., J. D. Voldstad, P. Balling, P. Kristensen, T. Andersen, and H. K. Haugen, 1995, Phys. Rev. Lett. **75**, 1911.
Poet, R., 1978, J. Phys. B **11**, 3081.
Poirier, M., 1988, Phys. Rev. A **38**, 3484.
Poirier, M., 1994, Phys. Rev. A **50**, 1335.
Post, B. H., W. Wassen, and W. Hogervorst, 1986, J. Phys. B **19**, 511.
Pradhan, A. K., and K. A. Berrington, 1993, J. Phys. B **26**, 157.
Preses, M., C. E. Burkhardt, W. P. Garver, and J. J. Leventhal, 1984, Phys. Rev. A **29**, 985.
Radojevic, V., and W. R. Johnson, 1985, Phys. Rev. A **31**, 2291.
Raoult, M., and Ch. Jungen, 1981, J. Chem. Phys. **74**, 3388.
Raseev, G., and H. Le Rouzo, 1983, Phys. Rev. A **27**, 268.
Rau, A. R. P., 1983, J. Phys. B **16**, L699.
Rau, A. R. P., 1984, Pramana J. Phys. **23**, 297.
Rau, A. R. P., 1988, Phys. Rev. A **38**, 2255.
Rau, A. R. P., and U. Fano, 1971, Phys. Rev. A **4**, 1751.
Read, F. H., 1977, J. Phys. B **10**, 449.
Read, F. H., 1990, J. Phys. B **23**, 951.
Reid, R. H. G, K. Bartschat, and P. G. Burke, 1992, J. Phys. B **25**, 3175.
Rescigno, T. N., 1985, Phys. Rev. A **31**, 607.
Rinneberg, H., and J. Neukammer, 1982, J. Phys. B **15**, L825.
Rinneberg, H., and J. Neukammer, 1983, Phys. Rev. A **27**, 1779.
Robicheaux, F., 1989, J. Chem. Phys. **91**, 708.
Robicheaux, F., 1991, Phys. Rev. A **43**, 5946.
Robicheaux, F., 1993, Phys. Rev. A **48**, 4162.
Robicheaux, F., and B. Gao, 1991, Phys. Rev. Lett. **67**, 3066.
Robicheaux, F., and B. Gao, 1993, Phys. Rev. A **47**, 2904.
Robicheaux, F., and C. H. Greene, 1992, Phys. Rev. A **46**, 3821.
Robicheaux, F., and C. H. Greene, 1993a, Phys. Rev. A **47**, 1066.
Robicheaux, F., and C. H. Greene, 1993b, Phys. Rev. A **47**, 4908.
Robicheaux, F., and C. H. Greene, 1993c, Phys. Rev. A **48**, 4429.
Robicheaux, F., and C. H. Greene, 1993d, Phys. Rev. A **48**, 4441.
Robicheaux, F., R. P. Wood, and C. H. Greene, 1994, Phys. Rev. A **49**, 1866.
Rodberg, L. S., and R. M. Thaler, 1967, *The Quantum Theory of Scattering* (Academic, New York).
Roig, R. A., 1975, J. Phys. B **8**, 2939.
Rose, S. J., N. C. Pyper, and I. P. Grant, 1978, J. Phys. B **11**, 755.
Ross, M. H., and G. L. Shaw, 1961, Ann. Phys. (N.Y.) **13**, 147.
Ross, S. C., and Ch. Jungen, 1994, Phys. Rev. A **50**, 4618.
Roussel, F., M. Cheret, L. Chen, T. Bolzinger, G. Spiess, J. Hare, and M. Gross, 1990, Phys. Rev. Lett. **65**, 3112.
Ruščić, B., and J. Berkowitz, 1983, Phys. Rev. Lett. **50**, 675.
Ruščić, B., J. P. Greene, and J. Berkowitz, 1984a, J. Phys. B **17**, L79.
Ruščić, B., J. P. Greene, and J. Berkowitz, 1984b, J. Phys. B **17**, 1503.
Rydberg, R. J., 1889, K. Svenska Vetensk. Akad. Handl. **23**, 11.
Sadeghpour, H. R., 1991, Phys. Rev. A **43**, 5821.

Sadeghpour, H. R., and M. Cavagnero, 1993, J. Phys. B **26**, L171.
Sadeghpour, H. R., and C. H. Greene, 1990, Phys. Rev. Lett. **65**, 313.
Sadeghpour, H. R., C. H. Greene, and M. Cavagnero, 1992, Phys. Rev. A **45**, 1587.
Sakimoto, K., 1986, J. Phys. B **19**, 3011.
Samson, J. A. R., Y. Shefer, and G. C. Angel, 1986, Phys. Rev. Lett. **56**, 2020.
Sánchez, I., H. Bachau, and E. Cormier, 1995, J. Phys. B **28**, 2867.
Saraph, H. E., 1978, Comput. Phys. Commun. **15**, 247.
Schinn, G. W., C. J. Dai, and T. F. Gallagher, 1991, Phys. Rev. A **43**, 2316.
Schneider, B. I., 1975, Chem. Phys. Lett. **31**, 237.
Schneider, B. I., 1981, Phys. Rev. A **24**, 1.
Schneider, B. I., 1995, in *Computational Methods for Electron-Molecule Collisions*, edited by W. Huo and F. Gianturco (Plenum, New York), p. 273.
Schwinger, J., 1947, Phys. Rev. **72**, 742.
Scott, N. S., and P. G. Burke, 1980, J. Phys. B **13**, 4299.
Scott, P., A. E. Kingston, and A. Hibbert, 1983, J. Phys. B **16**, 3945.
Seaton, M. J., 1955, C. R. Acad. Sci. **240**, 1317.
Seaton, M. J., 1958, Mon. Not. R. Astron. Soc. **118**, 504.
Seaton, M. J., 1966, Proc. Phys. Soc. London **88**, 801.
Seaton, M. J., 1969, J. Phys. B. **2**, 5.
Seaton, M. J., 1983, Rep. Prog. Phys. **46**, 167.
Seaton, M. J., 1987a, J. Phys. B **20**, 6363.
Seaton, M. J., 1987b, in *Recent Studies in Atomic and Molecular Processes*, edited by A. E. Kingston (Plenum, New York), p. 29.
Seipp, I., and K. T. Taylor, 1994, J. Phys. B **27**, 2785.
Seng, M., M. Halka, K.-D. Heber, and W. Sandner, 1995, Phys. Rev. Lett. **74**, 3344.
Shahabi, S., A. F. Starace, and T. N. Chang, 1984, Phys. Rev. A **30**, 1819.
Shorer, P., 1980, J. Phys. B **13**, 2921.
Siegert, A. J. F., 1939, Phys. Rev. **56**, 750.
Slater, J. F., F. H. Read, S. E. Novick, and W. C. Lineberger, 1978, Phys. Rev. A **17**, 201.
Smith, F. T., 1960, Phys. Rev. **118**, 349.
Smith, M. T., K. T. Taylor, and C. W. Clark, 1992, J. Phys. B **25**, 3985.
Smith, S. J., and G. Leuchs, 1987, Adv. At. Mol. Phys. **24**, 157.
Sobel'man, I. I., 1972, *An Introduction to the Theory of Atomic Spectra* (Pergamon, New York).
Sohl, J. E., Y. Zhu, and R. D. Knight, 1990, J. Opt. Soc. Am. B **7**, 9.
Starace, A. F., 1982, in *Corpuscles and Radiation in Matter*, Hanbuch der Physik 31, edited by W. Mehlhorn (Springer, Berlin), p. 1.
Starace, A. F., and L. Armstrong, Jr., 1976, Phys. Rev. A **13**, 1850.
Starace, A. F., and G. L. Webster, 1979, Phys. Rev. A **19**, 1629.
Stephens, J. A., and C. H. Greene, 1995, J. Chem. Phys. **102**, 1579.
Stephens, J. A., and V. McKoy, 1989, Phys. Rev. Lett. **62**, 889.
Stephens, J. A., and V. McKoy, 1992, J. Chem. Phys. **97**, 8060.
Sugar, J., and C. Corliss, 1985, J. Phys. Chem. Ref. Data **14**, Suppl. 2.
Sun, J.-Q., 1989, Phys. Rev. A **40**, 7355.
Sun, J.-Q., and K. T. Lu, 1988, J. Phys. B **21**, 1957.
Sun, J.-Q., K. T. Lu, and R. Beigang, 1989, J. Phys. B **22**, 2887.
Tang, J. Z., S. Watanabe, M. Matsuzawa, and C. D. Lin, 1992, Phys. Rev. Lett. **69**, 1633.
Tayal, S. S., 1988, Phys. Rev. A **38**, 729.
Tayal, S. S, and P. G. Burke, 1987, J. Phys. B **20**, 4715.
Taylor, K. T., and D. W. Norcross, 1986, Phys. Rev. A **34**, 3878.
Taylor, H. S., and L. D. Thomas, 1972, Phys. Rev. Lett. **28**, 1091.
Teichmann, T., and E. P. Wigner, 1952, Phys. Rev. **87**, 123.
Telmini, M., M. Aymar, and J-M. Lecomte, 1993, J. Phys. B **26**, 233.
Temkin, A., 1962, Phys. Rev. **126**, 130.
Tessman, J. R., A. H. Kahn, and W. Shockley, 1953, Phys. Rev. **92**, 890.
Thumm, U., and W. D. Norcross, 1991, Phys. Rev. Lett **67**, 3495.
Thumm, U., and W. D. Norcross, 1992, Phys. Rev. A **45**, 6349.
Tomkins, F. S., and B. Ercoli, 1967, Appl. Opt. **6**, 1299.
Tran, N. H., P. Pillet, R. Kachru, and T. F. Gallagher, 1984, Phys. Rev. A **29**, 2640.
Tully, J. A., M. J. Seaton, and K. A. Berrington, 1990, J. Phys. B **23**, 3811.
Ueda, K., K. Ito, Y. Sato, and T. Namioka, 1990, Phys. Scr. **41**, 75.
Vaeck, N., M. Godefroid, and J. E. Hansen, 1988, Phys. Rev. A **38**, 2830.
van der Hart, H., C. Laughlin, and J. E. Hansen, 1993, Phys. Rev. Lett. **71**, 1506.
van der Meulen, P., M. O. Krause, C. D. Caldwell, S. B. Whitfield, and C. A. Lange, 1992, Phys. Rev. A **46**, 2468.
van der Meulen, P., M. O. Krause, and C. A. Lange, 1992, J. Phys. B **25**, 97.
van Leeuwen, R., M. Aymar, W. Ubachs, and W. Hogervorst, 1996, J. Phys. B **29**, 1007.
van Leeuwen, R., W. Ubachs, and W. Hogervorst, 1994, J. Phys. B **27**, 3891.
van Leeuwen, R., W. Ubachs, W. Hogervorst, M. Aymar, and E. Luc-Koenig, 1995, Phys. Rev. A **52**, 4567.
Victor, G. A., and C. Laughlin, 1972, Chem. Phys. Lett. **14**, 74.
Walter, C. W., and J. R. Peterson, 1992, Phys. Rev. Lett. **68**, 2281.
Walton, D. S., B. Peart, and K. T. Dolder, 1970, J. Phys. B **3**, L148.
Walton, D. S., B. Peart, and K. T. Dolder, 1971, J. Phys. B **4**, 1343.
Wang, Q., and C. H. Greene, 1989, Phys. Rev. A **40**, 742.
Wang, Q., and C. H. Greene, 1991a, Phys. Rev. A **44**, 1874.
Wang, Q., and C. H. Greene, 1991b, Phys. Rev. A **44**,
Wang, X., and W. E. Cooke, 1993, Phys. Rev. A **47**, 1778.
Wang, X., J. G. Story, and W. E. Cooke, 1991, Phys. Rev. A **43**, 3535.
Wannier, G., 1953, Phys. Rev. **90**, 817.
Watanabe, S., 1982, Phys. Rev. A **25**, 2074.
Watanabe, S., 1986, J. Phys. B **19**, 1577.
Watanabe, S., U. Fano, and C. H. Greene, 1984, Phys. Rev. A **29**, 177.
Watanabe, S., and C. H. Greene, 1980, Phys. Rev. A **22**, 158.
Watanabe, S., and H. Komine, 1991, Phys. Rev. Lett. **67**, 3227.
Watson, D. K., 1988, Adv. At. Mol. Phys. **25**, 221.
Werij, H. G. C., C. H. Greene, C. E. Theodosiou, and A. Gallagher, 1992, Phys. Rev. A **46**, 1248.
Wheeler, J. A., 1937, Phys. Rev. **52**, 1107.

Whittaker, E. T., and G. N. Watson, 1927, *A Course of Modern Analysis* (Cambridge University, Cambridge).
Wigner, E. P., 1946a, Phys. Rev. **70**, 15.
Wigner, E. P., 1946b, Phys. Rev. **70**, 606.
Wigner, E. P., 1955, Phys. Rev. **98**, 145.
Wigner, E. P., and L. Eisenbud, 1947, Phys. Rev. **72**, 29.
Willke, B., and M. Kock, 1991, Phys. Rev. A **43**, 6433.
Willke, B., and K. Kock, 1993, J. Phys. B **26**, 1129.
Wintgen, D., and H. Friedrich, 1986, J. Phys. B **19**, 991.
Wintgen, D., and H. Friedrich, 1987, Phys. Rev. A **35**, 1628.
Wood, R. P., and C. H. Greene, 1994, Phys. Rev. A **49**, 1029.
Wood, R. P., C. H. Greene, and D. J. Armstrong, 1993, Phys. Rev. A **47**, 229.
Wynne, J. J., and J. A. Armstrong, 1979, IBM J. Res. Dev. **23**, 490.
Xu, E. Y., Y. Zhu, O. C. Mullins, and T. F. Gallagher, 1986, Phys. Rev. A **33**, 2401.
Xu, E. Y., Y. Zhu, O. C. Mullins, and T. F. Gallagher, 1987, Phys. Rev. A **35**, 1138.
Yang, C. N., 1948, Phys. Rev. **74**, 764.
Yih, T. S., H.-H. Wu, H. T. Chan, C.-C. Chu, and B. P. Pong, 1989, Chin. J. Phys. **27**, 136.
Zakrzewski, J., K. Dupret, and D. Delande, 1995, Phys. Rev. Lett. **74**, 522.
Zare, R. N., 1988, *Angular Momentum* (Wiley, New York).
Zeippen, C. J., 1995, Phys. Scr. T **58**, 43.
Zhou, B., and C. D. Lin, 1995, Phys. Rev. A **51**, 1286.
Zhu, Y., E. Y. Xu, and T. F. Gallagher, 1987, Phys. Rev. A **36**, 3751.
Zilitis, V. A., 1977, Opt. Spectrosc. **43**, 603.